Mechanisms for the Formation and Degradation of Microplastic: Results from Accelerated Weathering Studies

Dissertation

zur Erlangung des akademischen Grades
einer Doktorin der Naturwissenschaften (Dr. rer. nat.)
in der Bayreuther Graduiertenschule
für Mathematik und Naturwissenschaften
an der Universität Bayreuth

vorgelegt von

Nora Meides
geboren in Daun

Bayreuth, 2023

'If we knew what we were doing
it would not be called research, would it?'
Albert Einstein

Die vorliegende Arbeit wurde in der Zeit von September 2019 bis Oktober 2022 in Bayreuth am Lehrstuhl für Makromolekulare Chemie I unter Betreuung von Herrn Professor Dr. Peter Strohriegl angefertigt.

Vollständiger Abdruck der von der Bayreuther Graduiertenschule für Mathematik und Naturwissenschaften (BayNAT) der Universität Bayreuth genehmigten Dissertation zur Erlangung des akademischen Grades einer Doktorin der Naturwissenschafen (Dr. rer. nat.).

Dissertation eingereicht am: 16.11.2022
Zulassung durch das Leitungsgremium: 22.11.2022
Wissenschaftliches Kolloquium: 28.02.2023

Amtierender Direktor: Prof. Dr. Hans Keppler

Prüfungsausschuss:

Prof. Dr. Peter Strohriegl (Gutachter)
Prof. Dr. Stefan Peiffer (Gutachter)
Prof. Dr. Seema Agarwal (Vorsitz)
Dr. Magdalena Mair

Contents

List of Abbreviations

MP	microplastic
SMP	secondary microplastic
NP	nanoplastic
PS	polystyrene
PE	polyethylene
LDPE	low-density polyethylene
PP	polypropylene
PHB	polyhydroxybutyrate
PET	poly(ethylene-therephtalate)
PCL	poly(ϵ-caprolactone)
PBAT	poly(butylene adipate-co-terephthalate)
PLA	polylactic acid
PES	polyethylene succinate
PHA	polyhydroxyalkanoate
PA	polyamide
Mt	million tonnes
h	hours
cm	centimeter
mm	millimeter
µm	micrometer
nm	nanometer
UV	ultraviolet
KJ/mol	kilojoule per mole
MW	molecular weight

MWD	molecular weight distribution
M_n	number-average molecular weight, in g/mol or kg/mol
2D	two-dimensional
3D	three-dimensional
O_2	molecular oxygen
H_2O	water
CO	carbon monoxide
DPE	Polymer Egineering
MCI	Macromolecular Chemistry I
GPC	gel-permeation chromatography
NMR	nuclear magnetic resonance
multiCP	multi cross polarization
MAS	magic angle spinning
SEM	scanning electron microscopy
SEM-EDX	scanning electron microscopy and energy-dispersive X-ray spectroscopy
FT-IR	Fourier-transform infrared spectroscopy
ATR	attenuated total reflectance
DSC	differential scanning calorimetry
XRD	X-ray diffraction
THF	tetrahydrofuran
MALDI-TOF	matrix-assisted laser desorption ionization time-of-flight mass spectrometry
MC	Monte Carlo
T_g	glass-transition temperature
T_m	melting temperature
LDH	lactate dehydrogenase
ImKC	Immortalized mouse Kupffer cells

EU	European Union
SAPEA	Science Advice for Policy by European Academies
CRC	collaborative research center

Glossary

aging weathering, however the term aging inclues annealing, thus in context to environmental compartments the term weathering is preferred (Andrady & Koongolla, 2022). 11

bio-based polymers fully or partially based on biologically-available resources, however may or may not be classified as biodegradable or compostable (Di Lorenzo & Androsch, 2019). 22, 26

bioassimilation conversion of a polymeric item to biomass (Laycock et al., 2017). 26

bioavailability property of being physically and chemically accessible to the action of cells and enzymes released by them (Laycock et al., 2017). 26

bioavailable status of a plastic item that can be processed by cells (Laycock et al., 2017). 26

biodegradability 'plastic biodegradation is the microbial conversion of all its organic constituents to carbon dioxide, new microbial biomass and mineral salts under oxic conditions, or to carbon dioxide, methane, new microbial biomass and mineral salts under anoxic conditions' (SAPEA, 2020). 22, 26

biodegradable polymers may be based on renewable resources (bio-based) or non-renewable resources (fossil-based). In the first case, they are based on naturally available resources, but can not be found as polymers in nature. In the second case they are based on non-renewable resources (and maybe partly on renewable resources), however they are still classified as being biodegradable. Both types belong to the category of *synthetic biodegradable polymers* (Jiang et al., 2012). 26

biodisintegration disintegration resulting from the action of cells (Laycock et al., 2017). 26

bioerosion faster degradation at the surface than inside resulting from biodegradation (Laycock et al., 2017). 26

biofragmentation fragmentation of a polymeric item due to the action of cells (Laycock et al., 2017). 26

biomass material of biological origin excluding material embedded in geological formation or transformed to fossil (Laycock et al., 2017). 26

biomineralization mineralization caused by cell-mediated phenomena (Laycock et al., 2017). 26

compostable property of a plastic that undergoes biological degradation during composting to yield carbon dioxide, water, inorganic compounds, and biomass at a rate consistent with other known compostable materials and leaves no visually distinguishable or toxic residues (Laycock et al., 2017). 26

degradation 'a deleterious change in the chemical structure, physical properties, or appearance of the polymer, which may result from chemical cleavage of the macromolecules forming a polymeric item, regardless of the mechanism of chain cleavage' (Laycock et al., 2017). 8

fossil-based polymers fully based on fossil fuels (crude oil), but may or may not be biodegradable (Di Lorenzo & Androsch, 2019). 26

naturally-occurring polymers directly derived from biomass, including those modified chemically, such as starches, modified starches, chitin, chitosan, cellulose, cellulose acetate, and natural rubber (Di Lorenzo & Androsch, 2019). 20, 26

weathering The combined effect of solar UV radiation, high temperatures, and mechanical stresses acting in concern to bring about degradation in the environment (Andrady & Koongolla, 2022). 11

List of Figures

1 Summary

Among various environmental issues, posing a problem to our planet's ecosystems, the plastic pollution has become a topic of increasing global concern. Plastic plays an indispensable role in our lives, owing to its durability, versatility, lightweight, and low cost. A rising demand in plastic results in increasing volumes of waste and mismanagement, which entails large amounts of plastic being distributed in natural compartments. Once exposed, they subjected to a variety of environmental stressors, provoking degradation.

The initiator of degradation are typically abiotic impacts. Solar UV-irradiation, temperature, the presence of water, humidity, and mechanical stress lead to changes in the polymer's physical and chemical composition, modifying the material characteristics. This provokes embrittlement, fragmentation, and the formation of secondary particles. With dimensions < 1 mm, they are referred to as microplastic (MP).

Plastic and especially MP are ubiquitous. Research to date has rarely addressed the connection between degradation, fragmentation, and MP formation in dependence of time. The aim of this thesis is to fill this knowledge gap by thoroughly investigating the degradation of different polymer systems via accelerated-controlled weathering.

The first paper investigates amorphous polystyrene (PS) as tensile bars and particles, exposed to accelerated weathering for 3200 hours (two years of outdoor weathering). Samples were taken at 13 time intervals and changes in molecular weight, particle size, tensile strength, surface characteristics, and chemical composition investigated. A new method to quantify chemical defects was developed via ^{13}C multi cross polarization (multiCP) nuclear magnetic resonance (NMR) spectroscopy (paper 4). The correlation of all data enabled the development of a two-stage degradation model. Stage I involves surface abrasion from irradiation and mechanical impact on the outer surface. Stage II involves fragmentation by embrittlement, provoked by the decreasing molecular weight. Within 3200 hours, 500 secondary particles are released from fragmentation.

The second paper focuses on low-density polyethylene (LDPE) as a semi-crystalline polymer system. LDPE particles and tensile bars were exposed to accelerated weathering, whilst monitoring physical and chemical changes. Due to the semi-crystalline character, changes in crystallinity were additionally investigated via differential scanning calorimetry (DSC), X-ray diffraction (XRD), and solid-state ^{13}C NMR. The two-stage PS degradation model is applicable for semi-crystalline LDPE as well, however needs to be expanded by a third stage: nanoparticle formation and agglomeration. Fragmentation of LDPE led to the release of 14,000 secondary particles.

The third paper addresses the degradation of semi-crystalline polypropylene (PP) powder, additionally containing unknown stabilizers, we could identify as Irgafos® 168 and Irganox® 1010. To examine their direct influence, Soxhlet extraction from another PP batch was performed, and both batches were exposed to accelerated weathering. Com-

parison of both experiments revealed a stabilization period of 350 hours, where no degradation could be tracked for stabilized PP. Once the stabilizers are consumed, degradation sets in rapidly. Non-stabilized PP shows a rapid disintegration, progressing according to our model. On a long-term view, the influence of these stabilizers is negligible. Within approximately two years of outdoor weathering, one PP particle releases as much as 100,000 particles.

The fourth study of this thesis (unpublished) compares outdoor weathering of PS, LDPE, and PP to long-term laboratory degradation. All three polymer systems were exposed to natural weather conditions for two years. Samples were drawn monthly, and the data compared to accelerated weathering. While the mechanisms of degradation are the same, the time scales vary between all three systems. This study highlights, that degradation and fragmentation is largely dependent on the polymer characteristics, influencing its susceptibility towards temperature. This especially applies to the fragmentation rate, which is linked to the formation of secondary MP particles.

The fourth publication included in this study, is a methodology paper describing the ^{13}C multiCP NMR approach we developed to investigate the chemical defects in weathered polymers. ^{13}C multiCP NMR is a bulk-sensitive method and able to provide quantitative data. This method was used for the investigation of PS, LDPE, and PP, the first three publications of this thesis.

The fifth publication is a case study investigating the toxicological affect of weathered PS beads to murine macrophages. Non-weathered and weathered PS beads were exposed to the cells, and their cytotoxic potential investigated. Our results show, that there are distinct differences between weathered and non-weathered PS particles, highlighting the necessity to focus on realistic environmental samples, e.g., weathered, not pristine.

In summary, this thesis includes a variety of new insights into the environmental degradation of three polymers commonly found as plastic waste in nature: PS, LDPE, and PP. We thoroughly investigated the degradation and fragmentation behaviors using accelerated, laboratory-controlled weathering, as well as outdoor, natural weathering. We were able to develop a degradation model, and to calculate fragmentation rates, giving a numerical approximation for the formation of secondary MP particles. Our data fills some knowledge gaps, and provides a relevant basis for further research in this field.

2 Zusammenfassung

Unter den zahlreichen Umweltproblematiken, welche die Ökosysteme unseres Planeten belasten, hat sich Plastikverschmutzung zu einer globalen, besorgniserregenden Thematik entwickelt. Plastik spielt in unserem täglichen Leben eine unersetzliche Rolle, besonders durch seine Beständigkeit, Vielseitigkeit, das geringe Gewicht und den niedrigen Preis. Die steigene Nachfrage führt auch zum Erzeugnis großer Mengen an Abfall und zu unsachgemäßer Entsorgung, was ermöglicht, dass Plastik in die Umwelt gelangt. Dort wird es einer Vielzahl an Umweltfaktoren ausgesetzt, die den Abbau begünstigen.

Die Initiatoren für Degradation sind typischerweise abiotische Bedingungen. Sonneneinstrahlung (UV), Temperatur, Wasser und mechanische Beanspruchung führen zu physikalischen und chemischen Modifikationen, wodurch sich die Materialeigenschaften ändern. Dies führt zu Versprödung, Fragmentierung und der Bildung von sekundären Partikeln. Bei einer Größe < 1 mm werden diese Partikel als MP bezeichnet.

Plastik und besonders MP sind ubiquitär. Bisherige Forschung hat sich kaum mit den Zusammenhängen zwischen Abbau, Fragmentierung und der MP-Bbildung in Abhängigkeit von der Expositionsdauer befasst. Das Ziel dieser Arbeit ist es, diese Wissenslücke zu schließen, indem der Abbau verschiedener Polymersysteme durch beschleunigte, kontrollierte Alterung ausgiebig untersucht wurde.

Die erste Publikation befasst sich mit amorphem Polystyrol (PS) in Form von Zugstäben und Partikeln, welche über 3200 Stunden (zwei Jahre Außenbewitterung) beschleunigter Bewitterung ausgesetzt wurden. Zu 13 Zeitintervallen wurden Proben entnommen und Änderungen in Molekulargewicht, Größe, der Zugfestigkeit, Oberflächeneigenschaften und chemischen Zusammensetzung untersucht. Eine neue Methode zur Quantifizierung chemischer Defekte wurde mittels ^{13}C multiCP NMR (Kernspinresonanz-) Spektroskopie entwickelt (4. Publikation). Durch Korrelation aller Daten entwickelten wir ein zweistufiges Degradationsmodell. Stufe I beinhaltet Oberflächenabrieb durch UV-Strahlung und mechanischem Eintrag. Stufe II die Fragmentierung durch Versprödung. In 3200 Stunden werden durch Fragmentierung 500 sekundäre MP Partikel freigesetzt.

Die zweite Publikation konzentriert sich auf low-density Polyethylen (LDPE) als teilkristallines Polymersystem. PE-Partikel und Zugstäbe wurden beschleunigter Bewitterung ausgesetzt, sowie die physikalischen und chemischen Veränderungen verfolgt. Aufgrund der teilkristallinen Struktur wurden Kristallinitätsänderungen zusätzlich mittels DSC (dynamische Differenzkalorimetrie), XRD (Röntgendiffraktometrie) und ^{13}C NMR untersucht. Das zweistufige Modell ist auch auf teilkristallines PE übertragbar, muss jedoch um Stufe III erweitert werden: Nanopartikelbildung und Agglomeration. Die Fragmentierung von PE führt zur Freisetzung von 14.000 sekundären MP Partikeln.

Die dritte Publikation befasst sich mit dem Abbau von teilkristallinem Polypropylen (PP), das zusätzlich unbekannte Stabilisatoren enthält, die wir als Irgafos® 168 und Irganox® 1010 identifizieren konnten. Um ihren direkten Einfluss zu untersuchen, wurde ein weiterer PP Batch mittels Soxhlet-Extraktion aufgereinigt, und anschließend beide Batches beschleunigter Bewitterung ausgesetzt. Der direkte Vergleich ergab eine Stabilitäts-Phase von 350 Stunden, in welcher für additiviertes PP kein Abbau verfolgt werden konnte. Sobald die Additive verbraucht sind, setzt die Degradation zügig ein. Additivfreies PP hingegen weist umgehende Degradation, gemäß unseres dreistufigen Modells, auf. Langfristig ist der Einfluss dieser Additive allerdings vernachlässigbar. Innerhalb von 3200 Stunden beschleunigter Alterung werden von einem PP-Partikel bis zu 100.000 sekundäre Partikel freigesetzt.

Die vierte, bisher unveröffentlichte Studie vergleicht die Außenbewitterung von PS, PE und PP mit Langzeit-Laborbewitterung. Alle drei Polymere wurden zwei Jahre lang natürlichem Wetter ausgesetzt. Eine monatliche Probennahme erfolte, sowie ein Vergleich der Daten mit der beschleunigten Bewitterung. Während die Abbaumechanismen dieselben sind, variieren die Zeitskalen zwischen allen drei Polymertypen zwischen beschleunigter und natürlicher Bewitterung. Diese Studie verdeutlicht, dass Abbau und Fragmentierung weitestgehend von den Eigenschaften des Polymers abhängen, welche auch die Anfälligkeit gegenüber Temperaturschwankungen beeinflussen. Dies gilt insbesondere für die Fragmentierungsrate und die Bildung sekundärer MP-Partikel.

Die vierte Veröffentlichung ist ein Methodenpaper, das die ^{13}C multiCP NMR Methodik beschreibt, welche wir zur Quantifizierung chemischer Defekte entwickelt haben. ^{13}C multiCP NMR ist eine volumenempfindliche Methode, die quantitative Daten liefern kann. Diese Methode wurde in den ersten drei Veröffentlichungen dieser Arbeit an PS, PE und PP angewendet.

Die fünfte Veröffentlichung addressiert die toxikologische Wirkung von bewitterten PS-Kügelchen auf mausartige Makrophagen. Unbewitterte und bewitterte PS-Kügelchen wurden den Zellen ausgesetzt und ihr zytotoxisches Potential untersucht. Unsere Ergebnisse zeigen, dass es deutliche Unterschiede zwischen bewitterten und nicht bewitterten PS-Partikeln gibt, was die Notwendigkeit sich auf realistische Umweltproben zu konzentrieren, z.B. bewittert, verdeutlicht.

Zusammenfassend enthält diese Dissertation eine Vielzahl neuer Einblicke in den Abbau von drei Polymeren, PS, PE und PP, die häufig als Müll in der Natur vorkommen. Wir haben das Abbau- und Fragmentierungsverhalten mit beschleunigter, im Labor kontrollierter Bewitterung, sowie mit natürlicher Außenbewitterung ausführlich untersucht. Die Ergebnisse ermöglichten uns die Entwicklung eines Abbaumodells und die Berechnung von Fragmentierungsraten, was eine numerische Näherung für die Bildung sekundärer MP-Partikel darstellt. Unsere Ergebnisse konnten einige Wissenslücken schließen und liefern eine wichtige Grundlage für weitere Forschungen auf diesem Gebiet.

3 Introduction

The global population has more than tripled in the past 70 years (1950-2020), reaching a total of 7.8 billion people in 2020[128]. This population growth is accompanied by an increase in human consumption[45], and thus a rising demand of non-renewable resources, such as precious metals and fossil fuels (oil, gas). For polymer production, monomers, such as ethylene, propylene, and styrene, are extracted from crude oil and natural gas[60]. As the majority of plastic produced today is still based on fossil fuels, polymer production thus promotes the rising demand in oil and gas[95].

Plastic is everywhere. It is a key part of our everyday lives: from the clothes we wear, the food we buy, the cars we drive, to communication devices, sports, clean water, hygiene, and safety. Plastic is cheap to produce, lightweight, and durable, plastic products are extremely versatile materials[121]. While plastic makes our lives easier in multiple ways, the challenges and issues of our extensive plastic consumption and misuse are accumulating, making petrochemical plastic waste a topic of serious global concern, which can no longer be neglected[97;82;8;56;121].

Single-use products, extensive waste production, and poor waste management strategies have led to the accumulation of large amounts of plastic waste in natural compartments[12;51;108]. Plastic pollution is among the greatest environmental concerns of modern times[108;39;124]. There is even a geological marker for this era: plastiglomerate, a material consisting in a matrix of once-molten plastic, rock fragments, sand grains, shells, and organic matter such as wood[31].

Plastic fragments down to nm-size have been reported from every environmental compartment of the Earth[108;71;63]. The plastic found in nature typically reveals a complex composition, often consists in multi-material compounds, contains additives, stabilizers, dyes, their weathering products, and sorbed contaminants[63]. Factors such as solar radiation, temperature fluctuations, water, and mechanical stress will further modify the structure. A comprehensive understanding of the change in size, chemical composition, and physical properties is crucial in order to draw conclusions on the effects of plastic in the environment.

Current topics of extensive research around the global plastic-issue are finding innovative solutions for sustainable polymers[32], mitigating waste accumulation[18], cleaning of the oceans from marine plastic debris[106], as well as developing approaches to reduce plastic waste production in the first place[93]. Numerous studies have addressed the impacts of plastic and plastic derivatives on the oceans, humans, and plants, concluding that immediate and chronic, mechanical and chemical disruptions can be caused within organisms[82]. Nevertheless, the mitigation of the plastic pollution is proceeding in a very slow manner. Recycling strategies and a proper waste management system are not given in every country, largely affecting waste management and pathways of plastic into the environment. A topic of high potential are sustainable and biodegradable polymers, which are able to degrade under environmentally relevant conditions leading to formation of CO_2 or CH_4, and H_2O[2]. Still, designing biodegradable polymers with ideal properties, while assuring complete biodegradation in diverse environmental compartments, is still extremely challenging, since biodegradation by definition occurs only under certain environmental conditions[11]. There is not a distinct solution to mitigate plastic waste and pollution, it has to be tackled from different directions.

3.1 Plastic in the Environment - Sources

The global plastic production has increased dramatically since the 1950s, when large-scale manufacturing, and the start of 'our plastic age' began[121;139]. Since then, and up to 2015, a total of 8300 million tonnes (Mt) of primary plastic material (polymer resin, synthetic fibers, and additives) have been produced[51], with an annual growth until 2019 (figure 1)[96;94].

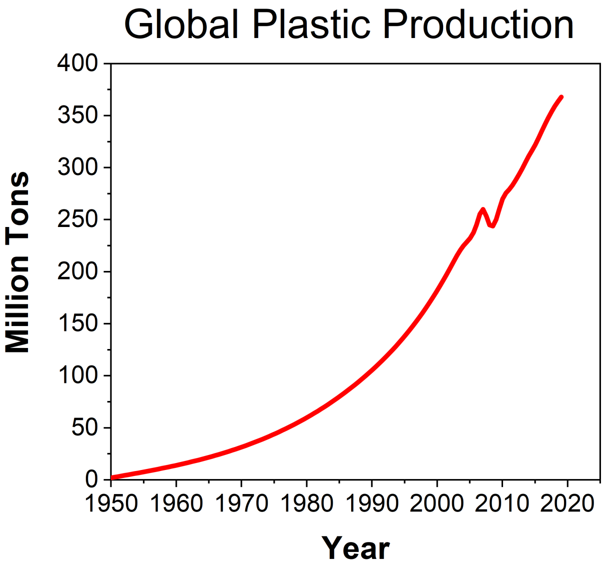

Figure 1: Development of the global plastic production in million tons from 1950-2019. Data source: Geyer et al.[51].

The life span of plastic products produced nowadays varies between 1-50 years. Thus, not all plastic made within one year is also discarded in the same year of production[96]. In Europe in the year 2020, 55 Mt of plastic were produced and 30 Mt of post-consumer waste were collected[96]. Owing to the large percentage of plastic produced for single-use products, especially packaging, which makes up ca. 40 %, the European waste production is extremely high (figure 2[95]). Within Europe, Germany is the country with the largest plastic post-consumer waste production (5.3 Mt in 2018[95]).

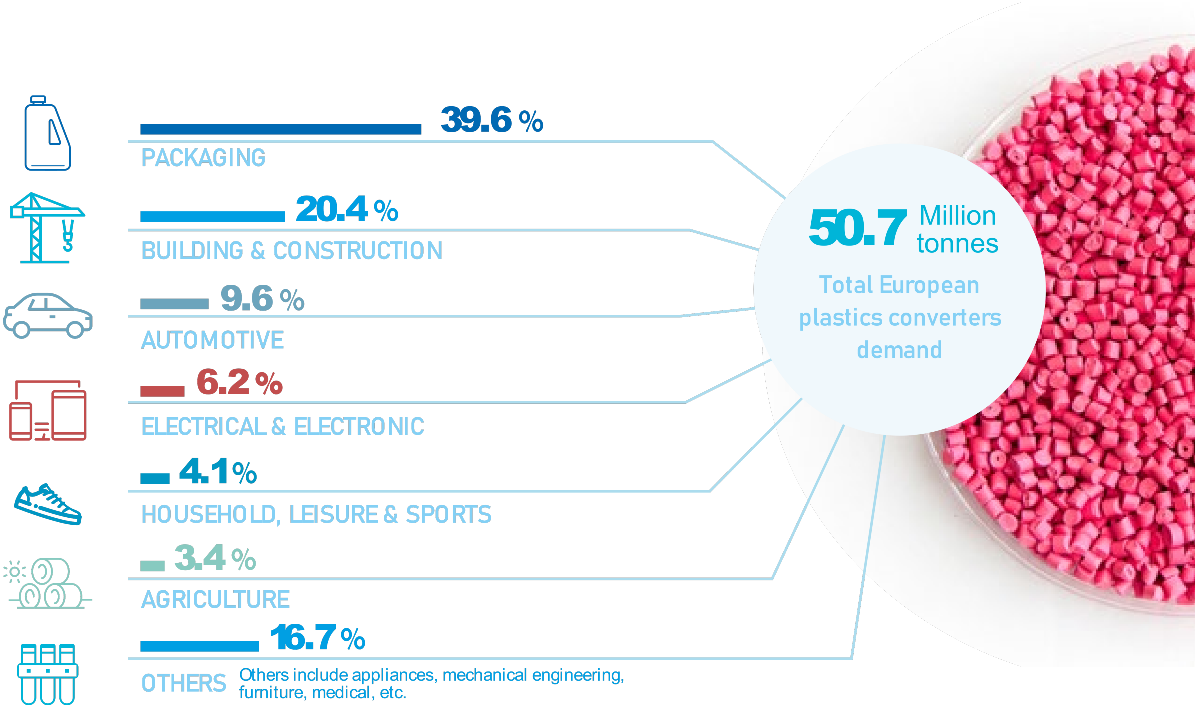

Figure 2: Plastic demand by segment for Europe (EU28+NO/CH) in 2019. Image source: PlasticsEurope[95].

Recycling methods and incineration of plastic waste have not been established at considerable scales before 1980[51]. While the end-of-life management of plastic waste has been improved over the years, still in 2020 in Europe only 35 % was recycled, 42 % used for energy recovery, and 23 % was sent to landfills[96]. 8 % of the plastic waste collected in 2020 were exported from the EU into other countries[114], and are ultimately declared as *recycled*. Unfortunately, even this data needs to be interpreted with caution. Recent studies by Bishop et al.[15] and Jambeck et al.[65] have shown, that a large proportion of plastic waste exported for recycling ends up as mismanaged waste either on land or in the ocean. By aggregation of data on PE waste flows in 2017, Bishop et al.[15] were able to model the fate of PE exported for recycling from Europe. Based on their data, 31 % of PE exported for recycling is not actually recycled, but either incinerated or put into landfills. This is due to the poor waste management infrastructure of the importing, typically low- or middle-income countries, where the average mismanaged waste fraction is 68 %[65;15;78]. As of this, Bishop et al.[15] estimated, that approximately 3 % of all exported plastic waste ultimately enters the oceans, a number being up to three orders of magnitude higher than previously assumed[65]. Once in the environment, plastic materials may be extremely persistent, taking up to hundreds of years until they degrade[61;107].

3.2 Plastic Degradation - Origin of Microplastic

When exposed in natural compartments, plastic is subjected to several environmental stress factors via biotic or abiotic mechanisms, ultimately leading to degradation (figure 3)[58]. As a consequence, the size, shape, color, and chemical composition are modified, affecting the physical characteristics of the material, the interaction with organisms, and the distribution within the different compartments[50;7;118].

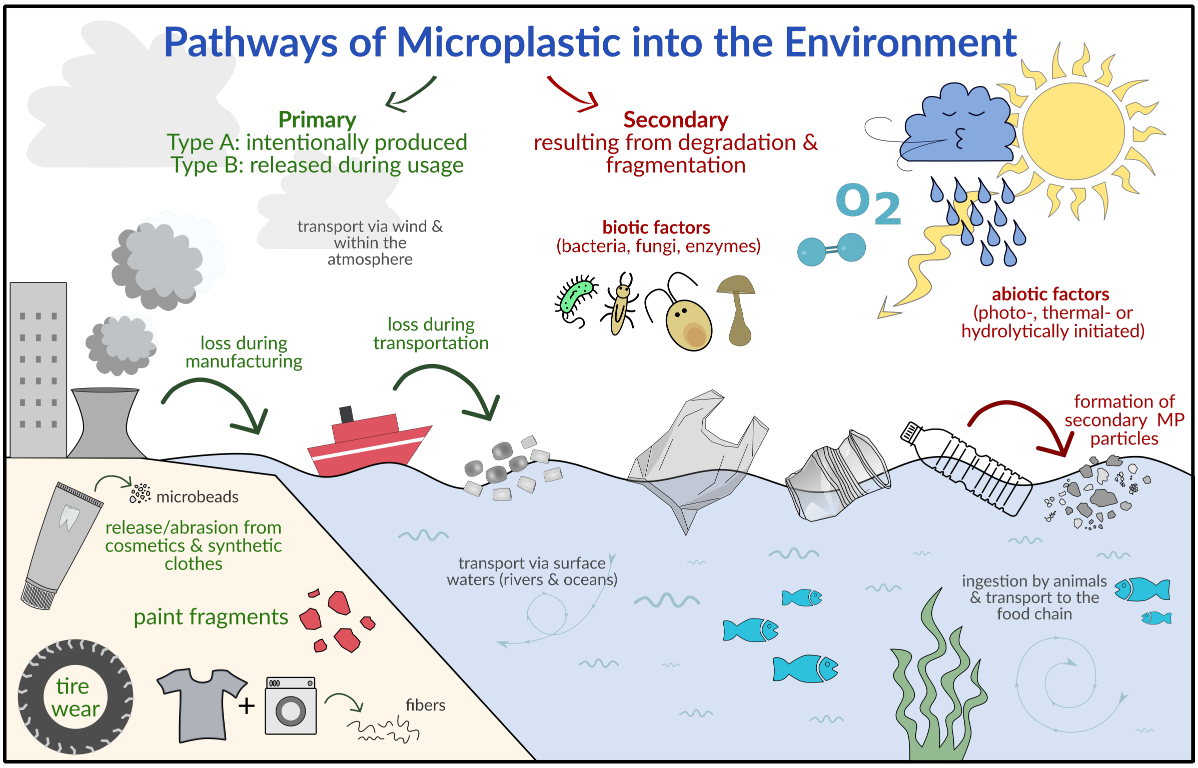

Figure 3: A variety of possible pathways for primary or secondary microplastic (SMP) to enter the environment, as well as ways of transport within the environment.

Plastic debris is usually referred to as macroplastic, however distinct definitions are still a matter of debate[57;44]. Recently, Hartmann et al.[57] suggested, that from a nomenclature point of view the SI prefixes for length should be used, defining nanoplastic (NP): 1 to < 1000 nm in diameter, microplastic (MP): 1 to < 1000 µm, mesoplastic: 1 to < 10 mm, and macroplastic: 1 cm and larger. In this work, this nomenclature is adapted to a great extent.

Upon exposure to environmental stress factors enabling degradation, such as UV-light and mechanical impact, fragmentation of larger plastic material is triggered, and secondary particles in macro-, micro-, and nanometer-scale are produced (figure 3)[8]. While numerically, there is a greater abundance of MP in natural compartments than there is of large plastic items, MP in general constitutes far less to the entire plastic mass found within oceans[23]. However, not all MP found in the environment is produced from degradation. Two classes of MP are distinguished, primary MP and SMP[30]. While definitions regarding MP are still somewhat inconsistent and not standardized to date, the following paragraphs are largely oriented on the classification suggested by the Fraunhofer Institute for Environmental, Safety, and Energy Technology UMSICHT[14].

3.2.1 Primary Microplastic

Primary MP can be divided into type-A and type-B[14;6]. Type-A is intentionally produced in a size from 1 to < 1000 µm for specific applications, while type B is released as MP during use of a product (figure 3).

Primary MP type-A is commonly found within personal care and cosmetic products, where the particles serve as abrasives. Examples are beads in facial and body scrubs (figure 4), toothpaste, shower gel, makeup, glitter, and others[55;43;129;80;119]. There is also primary MP manufactured for industrial purposes, e.g., abrasives to blast-clean surfaces, laser-powder for three-dimensional (3D) printing, or as pellets, beads or powder, being the raw material used for further processing like molding[47;14].

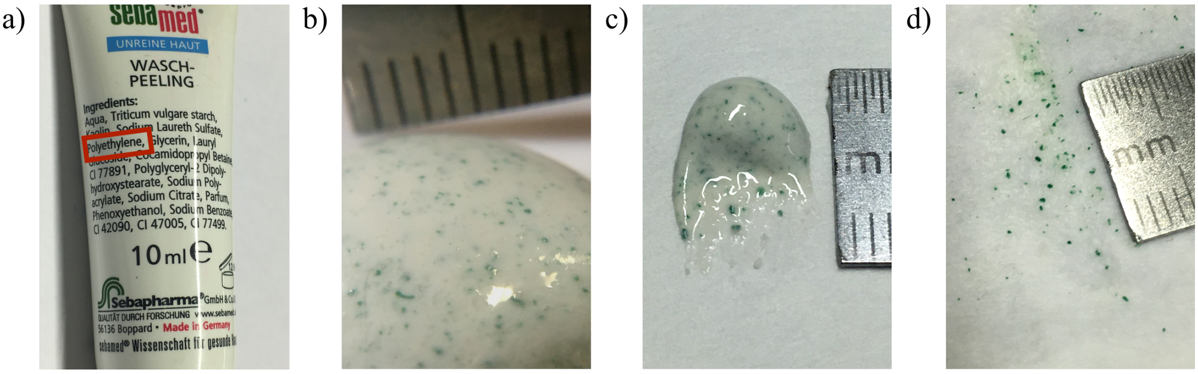

Figure 4: Primary MP in facial peeling. a) Ingredient list of the product containing polyethylene. b)-c) the scrub contains green particles < 1 mm in size, which are visible with bare eye. d) Filtered particles from the facial peeling.

Pathways of primary MP type-A into the environment depend on their area of application. Particles from industrial use are commonly accidentally released during manufacturing or transport on land or at sea[119;8]. Especially around industrial plastic production areas, or close to cities, there is an accumulated number of particles found in the surrounding soil, water or atmosphere[72;126;10;74].

Primary MP type-A from cosmetic products (figure 4) enters the environment via wastewater from domestic or industrial drainage systems[33]. While most waste water treatment plants are able to remove up to 99.9 % of the MP from the wastewater streams, a large proportion of particles (ca. 20 %) will remain within the secondary sewage sludge[52]. These sludge soils are commonly used as fertilizer. Within the European Union (EU), up to 5 Mt of sludge are distributed on farm land every year[74], and thus accumulated within soils. While there are certain demands considering the quality of these sewage sludges (e.g., heavy metals), there are only few limitations regarding their use as fertilizer, resulting in MP-contamination of soils. In Germany, within three years it is permitted to dispense up to 5 tonnes of sludge per hectare[25].

Another source of primary MP type-A into soils and water from agriculture are polymer-based pesticides[36;134;111]. These so-called 'smart polymeric systems' enable the controlled release of pesticides, herbicides, and agrochemicals, based on interaction of pesticides with synthetic or natural polymers[111]. Upon degradation of the polymer, these chemicals are successively released into the environment. In this way, they may fulfill their purpose punctually, e.g., inside plants or organisms, and in a controlled and continuous manner[111;36]. Although these MP are the consequence of degradation, their intentional purpose and exposure classifies them as *primary*.

Primary MP type-A have been a matter of debate in recent years, which has caused the emergence of regulations in some countries. In Germany, according to the consumer protection service, MP in personal care products does not pose a health risk, and consequently there is no justification for a ban[138]. Nevertheless, companies themselves have chosen to voluntarily omit the use of synthetic polymers within their products[55], following the consumer's demands.

Primary MP type-B are particles released during the use of polymer products[14;6]. Examples are the abrasion of synthetic textile fibers, tire wear, paint, wear down of plastic running tracks, artificial turf, and rubber roads[14;6;58]. According to recent studies, paint fragments are often overlooked or excluded. Still, they make up one of the most abundant types of MP, alongside fibers and tire wear, to be found within the ocean[46;125;127]. The transition between the MP-formation being a consequence of degradation, or a consequence of use is vague and debated. However, since these particles are released during use of a product, they are referred to as *primary*.

Sources of primary MP type-B into the environment are mainly wear-off during use. Tire wear is transported into waterways via runoff or by wind through the atmosphere[125]. Main sources of paint fragments originate from coastal structures or boats. Fibers typically result from textile abrasion during wearing or washing. Browne et al.[24] experimentally determined, that polyester products can shed > 1900 fibers in one wash. These fibers are then accumulated in waste water and sewage sludge fertilizer, as previously mentioned[74]. The most abundant type of polymer fibers found in coastal waters from 18 different shore lines on six continents were polyester (56 %) and acrylic (23 %)[24].

3.2.2 Secondary Microplastic

Plastic particles having reached sizes between 1 to < 1000 µm as a consequence of degradation, and subsequent fragmentation of larger plastic debris by environmental forces, are referred to as SMP (figure 3)[57;8;6]. Compared to primary MP, SMP are far more abundant within oceans[8;9].

While degradation can be triggered during use of the plastic products (primary MP type-B), the dominating source of SMP is degradation within natural compartments. The exposure to several environmental stress factors will affect the polymer structure, resulting in a modification of the chemical and physical properties. Exposure to sunlight will particularly affect the material stability, enhancing embrittlement, leading to fragmentation, and formation of smaller particles, as can be seen in figure 5[50].

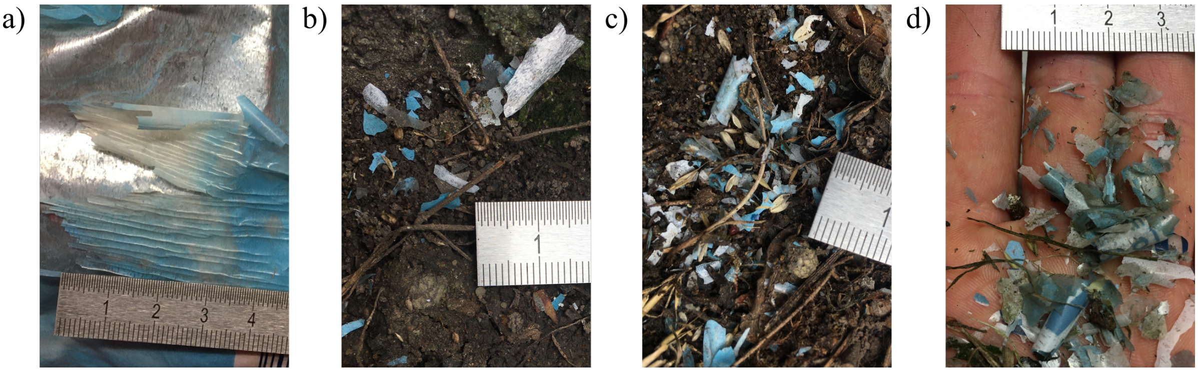

Figure 5: a) Cooler bag found on the terrace of the MCI building at the University of Bayreuth. The bag has most likely been exposed to outdoor weathering conditions for 1-2 years, the material embrittled and fragmentation led to SMP particle formation. b)-d) Meso- and microplastic particles from the cooler bag in various sizes, found on the soil around the bag.

Transfer of SMP can thus be direct, from degradation on-site, or indirect, from transportation in between compartments[30]. Additionally, SMP can result from primary MP, from the influence of weathering. Throughout this thesis, the term *weathering* is preferred over *aging*, due to minor deviations within their definitions (see also Glossary).

SMP can be extremely diverse in material and composition. Mismanaged waste in natural compartments can comprise any polymer type or size. Degradation and fragmentation affect macro- as well as MP. A decreasing size facilitates transportation within environmental compartments or ingestion by small animals or filter-feeders[38]. Ingestion however, is largely dependent on the size of the plastic and the size of the organisms. The smaller the plastic fragment is, the larger will the variety of organisms be, which are able to ingest these fragments[48]. Further, a smaller size will also facilitate translocation from the gut into the circulatory system, enhance interaction with cells or become assimilated into tissues[22;48;73;87]. Small MP particles, accumulating in lower trophic level organisms, may easily be transported within food chains, and ultimately be consumed by humans[76].

With decreasing size, further pathways of transportation gain relevance, e.g., atmospheric transport of airborne particles. This is relevant, as particle diameters < 10 µm are considered a concern for human respiratory health[81]. With decreasing size, the physical characteristics of the particles, and thus their interaction with one another and other environmental particles will also change. This is of even greater significance considering particles in the nm-range (nanoplastic).

3.2.3 Nanoplastic

Microplastic can further degrade into pieces smaller than 1 µm, referred to as NP[57]. While no NP has yet been detected in environmental samples[64], only in recent years, the scientific community has acknowledged the presence of NP in the environment[16].

Finding NP in natural samples is plausible, but also uncertain due to a variety of challenges in sampling, separation, and detection[64]. In addition, the individual characterization of NP is very demanding, since the majority of analytical technology relies on bigger sizes and higher sample quantities. As a consequence, the abundance of NP in environmental samples, their effect on plants, living organisms, and their fate in the natural environment is rarely studied to date[64].

As of their small size, not only detection and analysis is challenging, their physicochemical behaviors, and biological interactions also largely differ from MP[117]. NP have a strong tendency to agglomerate and hetero-agglomerate with colloidal organic matter or natural inorganic colloids[117;64]. As a consequence, no free NP is expected to be available within natural samples (e.g., surface waters). Knowledge gaps on NP are still large, thus to date no distinct conclusions can be drawn on the occurrence, persistence, reactivity, toxicity, transport, fate, and risks of NP on plants, animals, humans, and ecosystems.

3.3 Mechanisms of Plastic Degradation

As mentioned in the previous chapter, SMP and NP result from degradation and fragmentation of larger plastic material. Mismanaged waste ending up in natural compartments is exposed to a multitude of environmental stress factors, which are separated into two dominating pathways: abiotic and biotic degradation[58;26;50;28].

3.3.1 Abiotic Degradation

Abiotic degradation can proceed either via physical or chemical mechanisms. Physical modifications will affect the morphology of the polymer material, leading to abrasion, cracking, and embrittlement, typically proceeding from the surface into the bulk. Chemical alterations will affect the molecular level, and include changes such as chain-scission, molecular weight reduction, oxidation, recombination, and the formation as well as accumulation of degradation products[28]. Although they represent two different types of processes, physical and chemical mechanisms are linked to one-another, showing strong inter-dependencies.

Chemical degradation generally proceeds in three steps: 1) initiation of the reaction, 2) propagation, and 3) termination. The chemical degradation reaction is initiated either by exposure to UV-radiation (photolytical), heat (thermal) or water (hydrolytical)[50]. Once initiated, chemical and physical degradation proceed simultaneously. A progressing chemical degradation provokes embrittlement, which in turn will facilitate physical degradation, such as surface and bulk cracking, fragmentation, and formation of MP and NP. In this thesis, photo-initiated abiotic degradation is paramount, thus thermal and hydrolytical-initiation will not be discussed.

Initiation

The initiation step is induced by the absorption of light. In natural environments the exposure to sunlight is the main factor triggering polymer degradation. The energy of photons from the UV-A (280-315 nm) and UV-B area (315-400 nm) is sufficiently high to break chemical bonds, namely carbon-carbon (C-C) bonds (375 KJ/mol) and C-H bonds (420 KJ/mol)[112;140]. Photo-initiation however relies on the presence of chromophoric, light-absorbing groups in the polymeric material. In PS, as an exemplary polymer system, there is a phenyl chromophore in each repeating unit (phenyl ring). Upon irradiation, the energy of the photons causes bond-cleavage and abstraction of a H-atom, resulting in formation of a low molecular weight H-radical and an alkyl macroradical (reaction 1)[140]. These radicals are highly reactive. As they are constantly in search for a binding partner, radical-forming reactions induce an auto-catalytic progression of the reaction, also referred to as the propagation step[112].

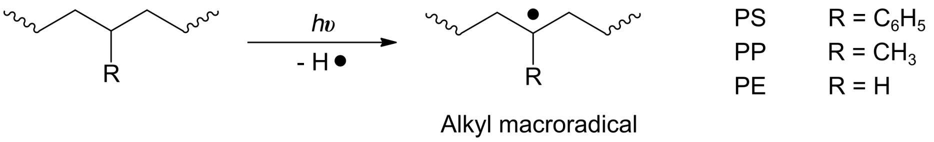

Reaction 1: Initiation step of polymer degradation. Upon exposure to sunlight ($h\nu$), a H-atom is abstracted from the polymer backbone, leading to formation of an alkyl macroradical. PS = polystyrene, PP = polypropylene, PE = polyethylene.

Not every polymer absorbs light. Polyolefins, e.g., PP and polyethylene (PE), are fully saturated, and do not contain any chromophoric groups within their structure. They are thus expected to be inert towards photo-initiation theoretically, yet they are susceptible and readily photodegrade. This is ascribed to the presence of impurities or structural abnormalities within the macromolecular structure[53;50].

Propagation

The propagation step involves reaction of the alkyl macroradicals with molecular oxygen (O_2), thus the presence of O_2 is essential for progression of the degradation (reaction 2). O_2 is incorporated into the chain, leading to formation of a peroxy macroradical (step I). This peroxy radical will further abstract a H-atom from another chain, which leads to the formation of a hydroperoxide, and again an alkyl macroradical[4;112].

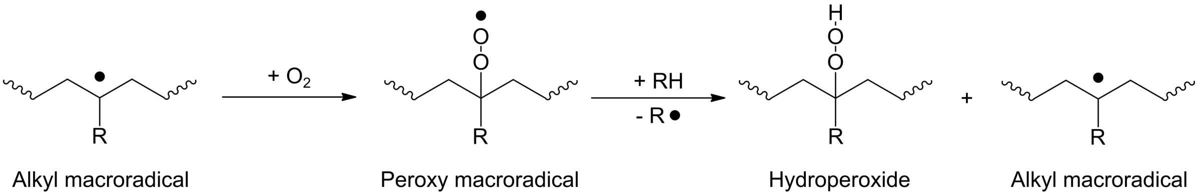

Reaction 2: Propagation step I, the alkyl macroradical reacts with O_2, forming a peroxy macroradical which abstracts another H-atom to form hydroperoxide.

Hydroperoxides represent the first molecular reaction product resulting from the photo-initiated oxidation process. However, they represent an unstable intermediate. As they are also photolabile, they may undergo homolysis upon further exposure to light, leading to the extraction of a hydroxyl-group, and thus formation of an alkoxy macroradical and a hydroxyl radical (reaction 3)[140]. Further, they may extract a H-atom from one and the extraction of a hydroxyl-group from another hydroperoxide, ultimately leading to the formation of a peroxy and an alkoxy macroradical, and release of water (H_2O) (reaction 3)[140].

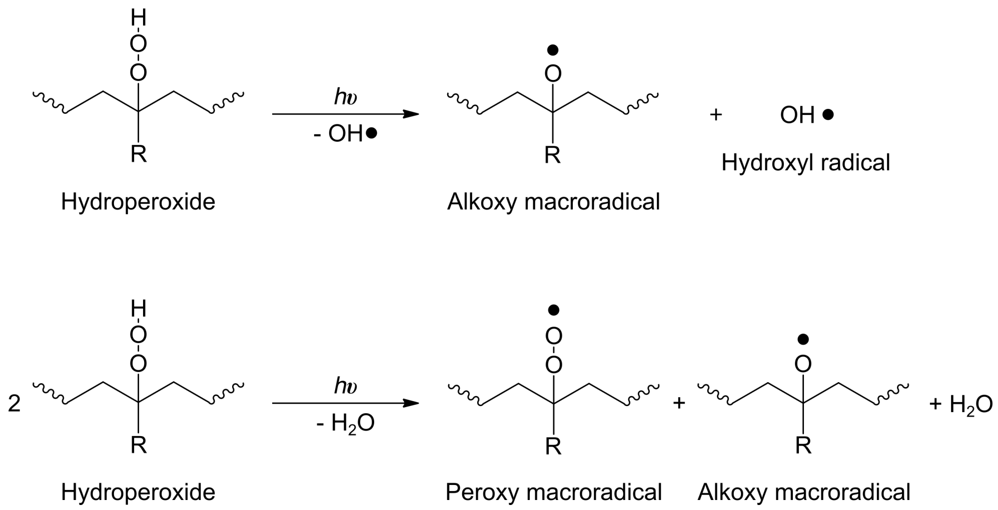

Reaction 3: Propagation step II, possible pathways of hydroperoxides to photodecompose.

The propagation step is extremely complex with many smaller side reactions taking place. While O_2 is essential for the first propagation reaction, it is not inevitably necessary for many of the subsequent reactions[54]. Alkyl macroradicals may also be formed by reaction of the polymer chain with a hydroxyl radical (reaction 4). Abstraction of a H-atom from another chain will release H_2O. Further, the alkoxy macroradicals from step II, (reaction 3) may also abstract a H-atom from another chain, resulting in formation of alkyl macroradicals and alcohol (reaction 4).

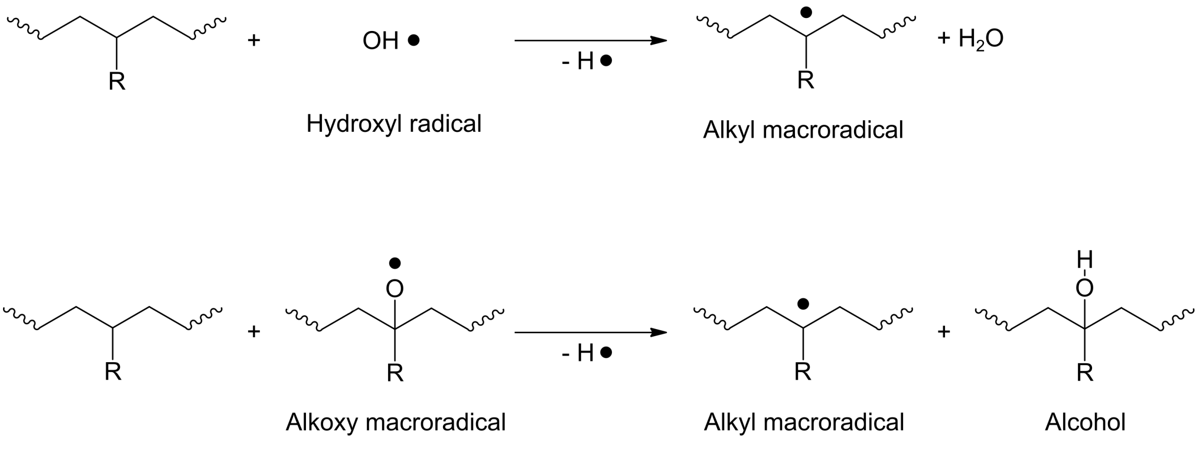

Reaction 4: Propagation step III, possible reaction pathways of polymer chains with radicals.

The propagation reactions include an on-going process of hydroperoxide-formation and -degradation. Propagation step IV involves another major degradation step, characterizing polymer break-down. Alkoxy radicals are susceptible to β-cleavage, where breaking up of C-C bonds leads to fission of the backbone (chain-scission), generating further radicals which contribute to the reaction. β-cleavage leads to a decrease in molecular weight, enhancing embrittlement and polymer fragmentation[4;112;140;28]. Functional groups formed in this step are ketones and aldehydes (reaction 5).

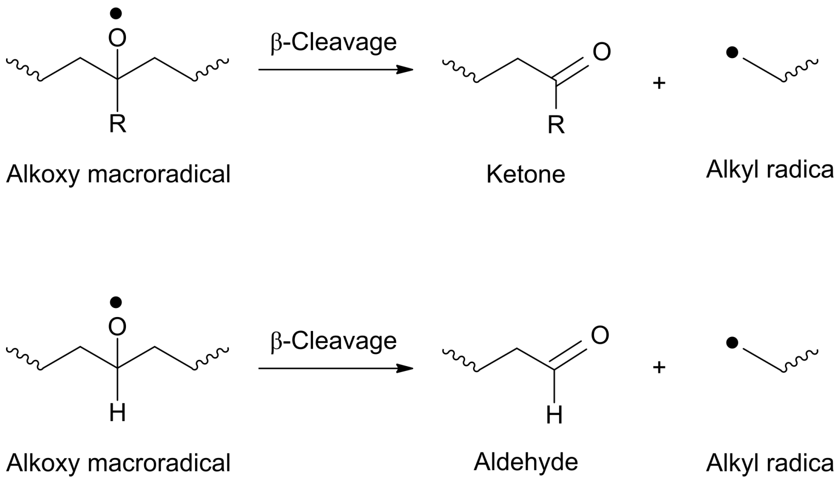

Reaction 5: Propagation step IV, alkoxy macroradicals are susceptible to β-cleavage, leading to formation of ketones and aldehydes.

Accumulating oxygen-containing reaction products within the polymeric structure enhances the photodegradability. Carbonyl-compounds like ketones, resulting from polymer degradation, are chromophoric groups, which absorb light, facilitating and accelerating polymer break-down[4;112].

Ketone degradation proceeds through two major radical-forming reactions called Norrish type I (reaction 6) and Norrish type II (reaction 7), the latter leading to chain-scission via β-cleavage, further reducing the molecular weight of the polymer[140;54]. Both Norrish reactions are photo-initiated.

Norrish I (reaction 6) will produce two radical intermediates via α-cleavage of the ketone, forming an acyl and alkyl radical. The acyl radical may further react with O_2 resulting in carbonyl compounds which will form alkyl peroxyl radicals (reaction 6). The acyl radical may also release carbon monoxide (CO) forming yet another alkyl radical[54].

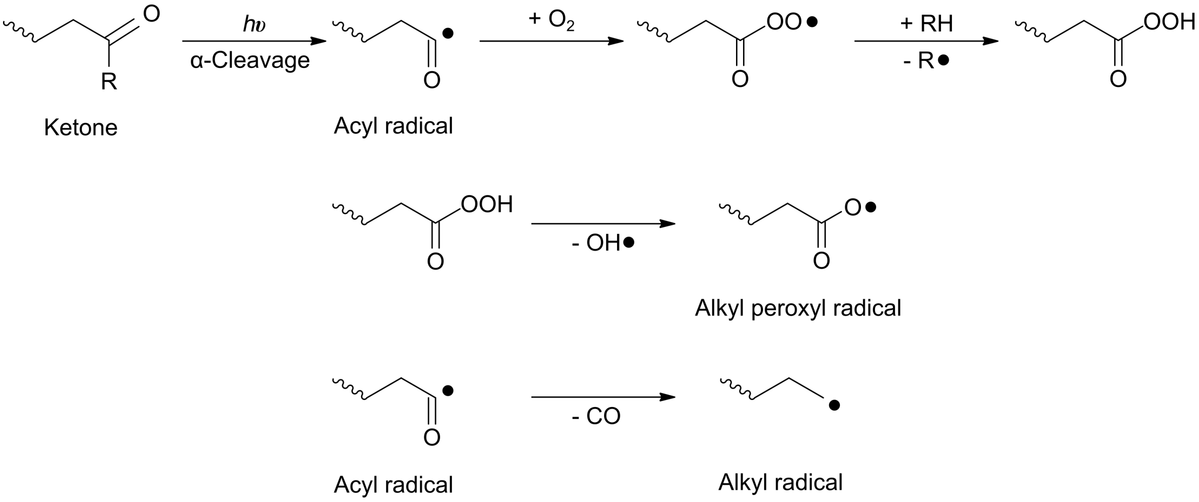

Reaction 6: Ketones are photolabile, thus exposure to UV can lead to radical formation without chain-cleavage (Norrish I).

Norrish II reactions will lead to backbone-scission via β-cleavage (reaction 7). Penetration of UV leads to H-transfer from the backbone to the carbonyl group, β-cleavage then results in formation of an olefin and a methyl ketone[54]. For PS, the H-transfer within Norrish II involves ring-opening of the phenyl ring and subsequent backbone-cleavage via β-scission[112].

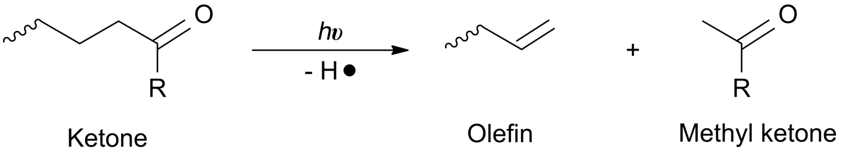

Reaction 7: Exposure to UV may also lead to radical formation with chain-cleavage (Norrish II), which results in a reduction of the molecular weight.

Termination

The final step of photodegradation is the termination step, involving radical recombination reactions leading to the formation of inactive products. Numerous reactive intermediates, formed from initiation or during propagation, are involved in the termination reactions. Disproportionation and crosslinking are the dominating mechanisms[112]. During the final termination reactions, the reactive species, which are the driving force during propagation, completely disappear. Carboxylic acids are among the final inert end products forming[8].

Termination reactions may involve the alkyl macroradicals from the initiation step. Via crosslinking of two alkyl macroradicals, propagation is omitted, and the molecular weight (MW) increased (reaction 8)[54].

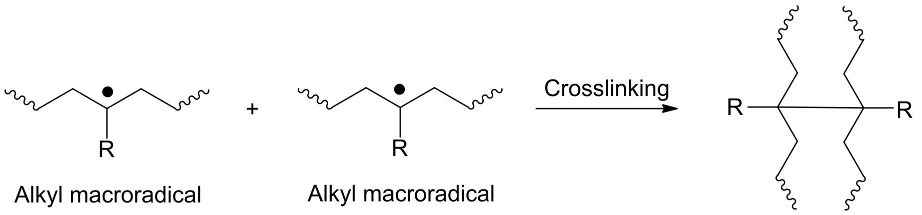

Reaction 8: Crosslinking of alkyl macroradicals resulting in an increase in MW.

Crosslinking may also affect peroxy and alkyl macroradicals, as given in reaction 9.

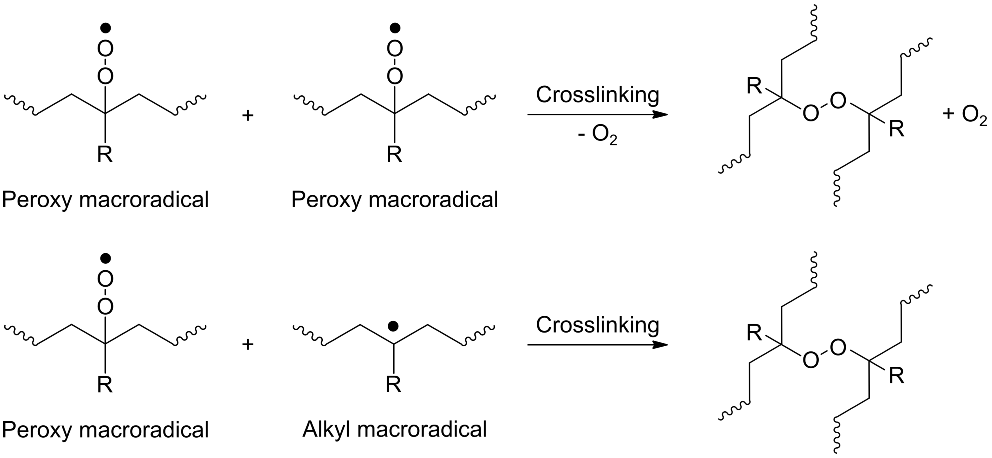

Reaction 9: Crosslinking of peroxy and alkyl macroradicals.

Alkyl radicals may be affected by disproportionation resulting in formation of an olefin and an inactive chain-end (reaction 10). Alkyl radical recombination leads to formation of an alkyl chain.

Reaction 10: Disproportionation of alkyl radicals.

Finally, carboxylic acids are formed from alkyl peroxyl radicals abstracting a H-atom from another chain or from acyl radicals reacting with hydroxyl radicals (reaction 11)[54].

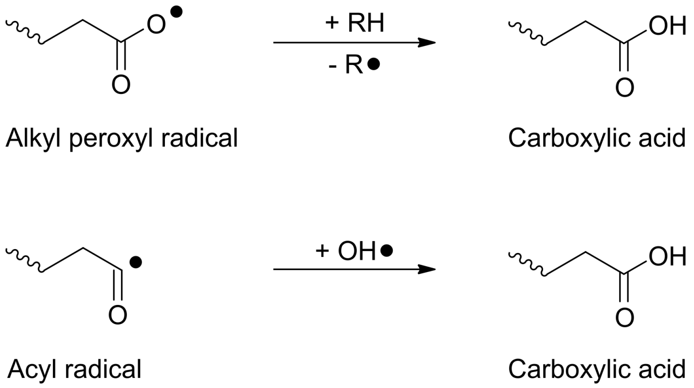

Reaction 11: Formation of carboxylic acids as inert end-products.

Despite crosslinking, the polymer chains themselves remain susceptible to photo-initiated degradation, with on-going weathering, the MW is thus continuously decreased and low-MW-compounds accumulate[54]. The repairing mechanisms of crosslinking can thus account for some of the damage being done, however, with chromophoric groups accumulating, chain-scission will dominate over crosslinking, consequently shifting the entire molecular weight distribution (MWD) to lower values[110].

Degradation Rates

The rate at which plastic materials will degrade is strongly dependent on the intensity of single parameters, such as UV-irradiation, temperature, and O_2-availability. A higher UV-intensity will accelerate chemical degradation[110;54;41]. Temperature will strongly increase the general reaction rate (Arrhenius relationship), as with every 10 °C temperature increase, the reaction rate is said to double[112;9]. This however, will only apply to the propagation reaction, as the first step of photooxidation, the initiation via photons, is unaffected by elevated temperatures.

In environmental settings with high temperature and UV-irradiation, polymers will degrade faster than in cooler compartments with a lower UV dose[41;9]. A typical setting for outdoor exposure of polymers is Florida in the United States of America. This is due to the subtropical weather: a high UV-intensity along with high annual UV activity, high temperatures, abundant rainfall, and high humidity[59;92].

3.3.2 Biodegradable Polymers and Biodegradation

Biodegradation or biotic degradation is the microbial conversion of all organic constituents to carbon dioxide (CO_2, under aerobic conditions), or methane (CH_4, under anaerobic conditions), new biomass, and mineral salts[105]. Within the category of biodegradable polymers there are two groups: naturally-occurring polymers and synthetic biodegradable polymers.

Naturally-Occurring Polymers

There are numerous molecules of large molecular weight, which are naturally-occurring, and consequently also able to naturally degrade. Examples are starch, cellulose (polysaccharides, figure 6), proteins, DNA, sugar, and many more[99;34]. Naturally-occurring polymers typically derive from 1) plant, 2) animal or 3) microbial sources, representing three sub-groups[99].

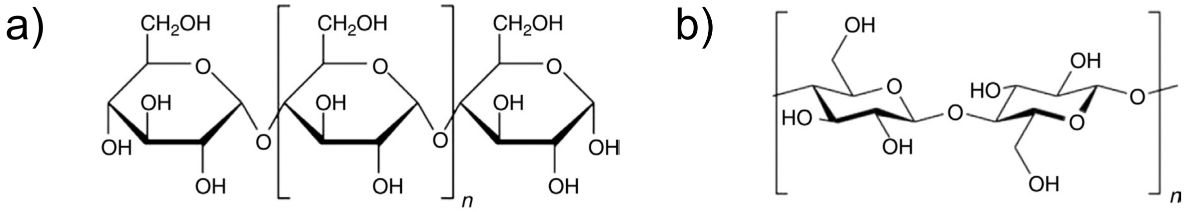

Figure 6: Chemical structures for a) starch and b) cellulose, representing two naturally-occurring polymers. Graphic modified from Jiang and Zhang[67].

Starch is produced by plants for the storage of energy. For commercial use, it is isolated from feedstock such as potato, wheat, rice or corn as granules[68;34]. Owing to its poor processability, stability, and mechanical properties, native starch is typically chemically modified and starch-composites are produced[83]. Starch-based polymers may be used for short-lived applications such as packaging or as cupboard, paper, paint, in cosmetics, and pharmaceuticals[34].

Cellulose is a structural element in the fiber walls of plants[13]. Unlike starch, cellulose has a high thermal stability and elastic modulus, therefore natural cellulose-based materials (e.g., wood, hemp, cotton) can be used as they are[34;13]. To improve its properties, cellulose can also be chemically modified. Typical applications are within the food, drug, medical, cosmetic, and hygiene sector[13].

Natural polymers are biogenic, abundant, and renewable, which has made them regain a lot of interest in recent years. Their use is a common approach to minimize the dependency on crude oil, while additionally designing more sustainable polymers[69]. Natural polymers are generally used as a component to synthesize modern biodegradable materials via blending, derivation or graft copolymerization[83].

Synthetic Biodegradable Polymers

Synthetic polymers in general are produced and designed by humans as the result of decades of research[105]. Synthetic biodegradable polymers represent a category therein, next to the group of synthetic non-biodegradable polymers. Synthetic polymers may be fully or partially based on biologically-available resources, they are thus named *bio-based* polymers. Conversely, fossil-based polymers are fully based on fossil fuels (petrochemicals). Polymers from both subgroups may or may not be biodegradable. Due to frequent confusion concerning the terms *bio-based* and *biodegradable*, figure 7 shows the connection and differences between both, based on the European Commission[40].

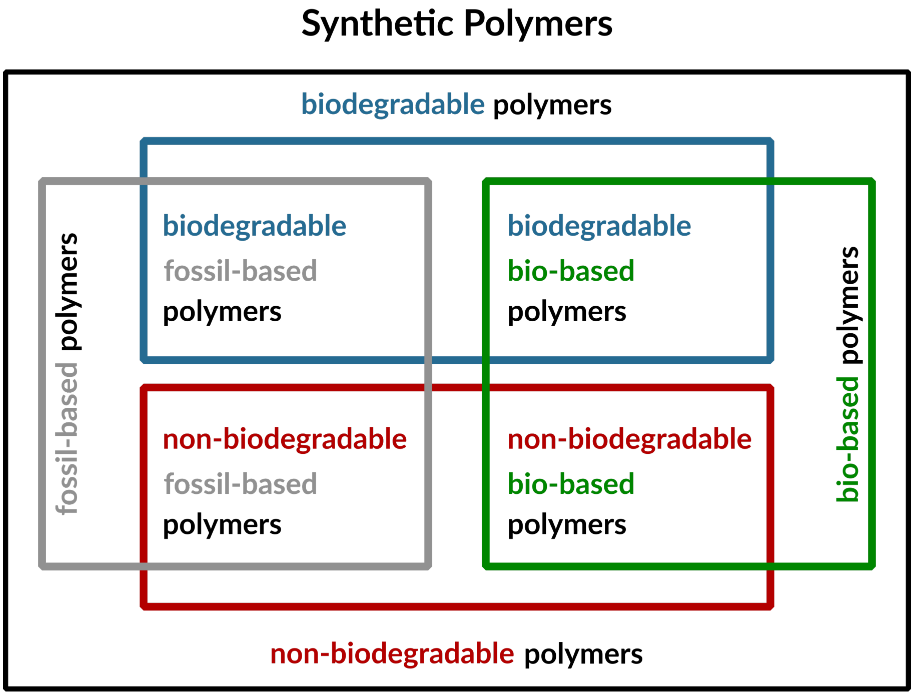

Figure 7: Graphic overview of synthetic polymers and the interrelation between bio-based, fossil-based, biodegradable, and non-biodegradable polymers. Graphic modified from the European Commission[40].

The term *biodegradable* means a polymer is able to degrade from the action of naturally-occurring microorganisms, such as algae, fungi or bacteria[77]. Biodegradability can be further divided into aerobic and anaerobic biodegradation. According to the definitions given by the Science Advice for Policy by European Academies (SAPEA)[105], 'plastic biodegradation is the microbial conversion of all its organic constituents to carbon dioxide, new microbial biomass, and mineral salts under oxic conditions, or to carbon dioxide, methane, new microbial biomass, and mineral salts under anoxic conditions'[105].

Examples of bio-based and biodegradable polymers are polyhydroxyalkanoate (PHA) or polylactic acid (PLA), the latter being typically used as compostable garbage bags (figure 8). Examples for fossil-based, biodegradable polymers are poly(ϵ-caprolactone) (PCL) ($[C_6H_{10}O_2]_n$) or polyethylene succinate (PES) ($[C_6H_8O_4]_n$)[103;77;3]. The majority of commercially-available, synthetic biodegradable plastics are polyesters, such as PLA ($[C_3H_4O_2]_n$), PCL, polyhydroxybutyrate (PHB) ($[C_4H_6O_2]_n$), and the copolymer poly(butylene adipate-co-terephthalate) (PBAT).

Polyesters contain ester units, which are prone to chemical hydrolysis (action of only H_2O) or enzymatic hydrolysis (action of H_2O and enzymes)[135]. Aliphatic polyesters are biodegradable under natural conditions. Ester-bonds also occur in nature and the enzymes, which are able to degrade these bonds, are ubiquitous in a variety of living organisms, such as bacteria and fungi. While aromatic polyesters (e.g., poly(ethylene-therephtalate) (PET)) have long been considered as non-biodegradable, PET-degrading enzymes such as PETase from *Ideonella sakaiensis* are now commonly used to study the enzymatic degradation of PET[89].

Figure 8: PLA bag labeled as 100 % compostable according to the DIN regulation.

Although bio-based polymers seem to have a great potential of replacing commodity polymers, such as PP or PE, there are still numerous challenges in need of elaboration, especially concerning the biodegradability itself. Biodegradable polymers are not meant to be discarded as waste into nature, but designed in order to facilitate the biodegradability in industrial compost plants[2]. Nevertheless, biodegradable polymers are not completely biodegradable under any circumstances in any natural environment, but require specific conditions or several parameters to be fulfilled at the same time, e.g., sufficient moisture, microbial interaction, and an optimal temperature in a medium with ideal pH[90]. In natural environments, these conditions are usually not met over a sufficiently long time scale to enable complete biodegradation. In industrial composting plants however, ideal conditions can be reached and held, in order to assure biodegradation in a short amount of time. Consequently, the term *biodegradable* is a definition according to the European Norm EN 13432[35], which is extremely misleading for the average consumer. Within this norm, a material is defined as being biodegradable (or compostable, e.g., figure 8), if within 12-weeks time 90 % of the starting material is fragmented into particles < 2 mm in size, and within 6 months time 90 % is mineralized. However, it is not further defined, what happens to the remaining 10 %. A recent study has investigated how well compostable bags degrade in an industrial compost plant[115]. The authors were able to detect a large proportion of MP being of biodegradable plastic origin, within the final compost intended as fertilizer for agriculture and gardening[115]. The use of these MP-polluted fertilizers thus enables the entering into the natural environment, further contributing to the MP-pollution, rather than having positive effects[115].

Applications for biodegradable polymers are within the agricultural, the medical sector, as well as for consumer goods, and food packaging[86]. For agricultural applications, biodegradable polymers may be used as mulch films, for designing slow release fertilizers, pesticides, or plant bots or bags (figure 8)[2;3]. Especially within this sector, biodegradable polymers are of special interest, considering the large proportion of non-soil degradable polymer fragments, which contribute substantially to the MP pollution in soils[74].

Big advantages of designing bio-based polymers are that their components are economical, readily available, and supposedly non-toxic[13;99]. Considering the striving for CO_2-neutrality, increasing prices of oil and gas, and non-renewable resource depletion, the development and application of sustainable technologies is crucial. Bio-based and biodegradable polymers are becoming topics of growing industrial, economic, and scientific interest, with Europe leading in terms of research and development[74;69]. If biodegradable polymers are the solution to mitigate the MP issue, is still a matter of debate. The general mechanisms of biodegradation have been widely studied on different biodegradable polymers in recent years[84;3;29;143;90;135;77]. Nevertheless, the correlation of biodegradation to MP-formation, as well as MP-elimination via biodegradation, are still poorly understood[90;103;77]. Additionally, degradation products accumulating from biodegradation have also been reported to pose potential risks[135]. Further studies are necessary, nevertheless, polymers made from renewable resources are considered to be a step into the right direction[2].

Biodegradation

As previously described for abiotic degradation, biodegradation will also result in a modification of the chemical and physical properties of a polymer, but can also lead to complete metabolism, and conversion into CO_2 and biomass in the presence of O_2, or CH_4 and biomass in the absence of O_2[105]. In general, biodegradation can be divided into three steps. The first involves the colonization of microorganisms on the surface (biofilm formation) and the release of enzymes (figure 9, Step 1). The second step includes depolymerization of the macromolecules into smaller molecules (oligomers, monomers) via hydrolysis or oxidation from the enzymes (figure 9, Step 2). The final step involves mineralization of these small molecules by incorporation of the polymer carbon into biomass or release as CO_2 (figure 9, Step 3)[143].

Depending on the molecule structure, the step of depolymerization (step 2) may proceed via two processes: enzymatic hydrolysis or enzymatic oxidation[84]. Both result in chain scission, which involves the formation of lower molecular weight oligomers, dimers, and monomers[103;90;113]. Characteristics of step 2 are consequently a rapid decrease in molecular weight accompanied by only minor weight loss[86].

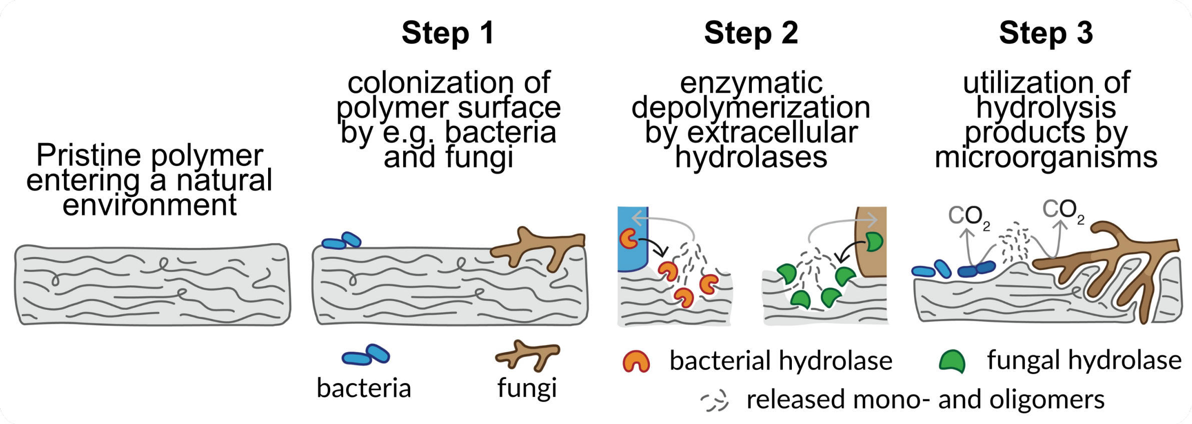

Figure 9: Schematic drawing of the three-step biodegradation process. Step 1 is the colonization of microorganisms on the surface of the polymer. Step 2 is the depolymerization and formation of low-molecular-weight compounds. Step 3 is the conversion of these low-molecular-weight oligomers or monomers into CO_2 and biomass. Graphic modified from Sander[103].

The final step includes microbial uptake and utilization of the remaining low-molecular weight fragments for energy production. This step is characterized by a slower decrease in molecular weight and extensive weight loss, as ca. 50 % of the polymer is converted into its monomer and into CO_2[86]. In laboratory experiments, the amount of CO_2 being produced can be quantitatively determined. This enabling the calculation of the percentage of biodegradation, a value typically used to quantify this process[2].

Biodegradation can either proceed from the surface into the bulk, or directly affect the bulk. Bulk degradation may also proceed after surface degradation. Which process is prevalent depends on the polymer thickness and the degradation mechanisms[77]. In the case of bulk degradation, a decrease in molecular weight from chain-scission occurs before a mass loss is recorded. This is observed with chemical hydrolysis, requiring a high rate of water diffusion (figure 10).

Polymers, which may be affected by this are PLA and PCL[77;84]. Chemical hydrolysis in the absence of microbes however, proceeds via abiotic, rather than biotic impact. In a natural setting, enzymatic hydrolysis is prevalent, where the enzymes act as a catalyst for the degradation reactions[84]. Exemplarily for PLA, water and enzymes attack the ester group in the backbone, water is absorbed, followed by cleavage of the ester bond, as displayed in figure 10.

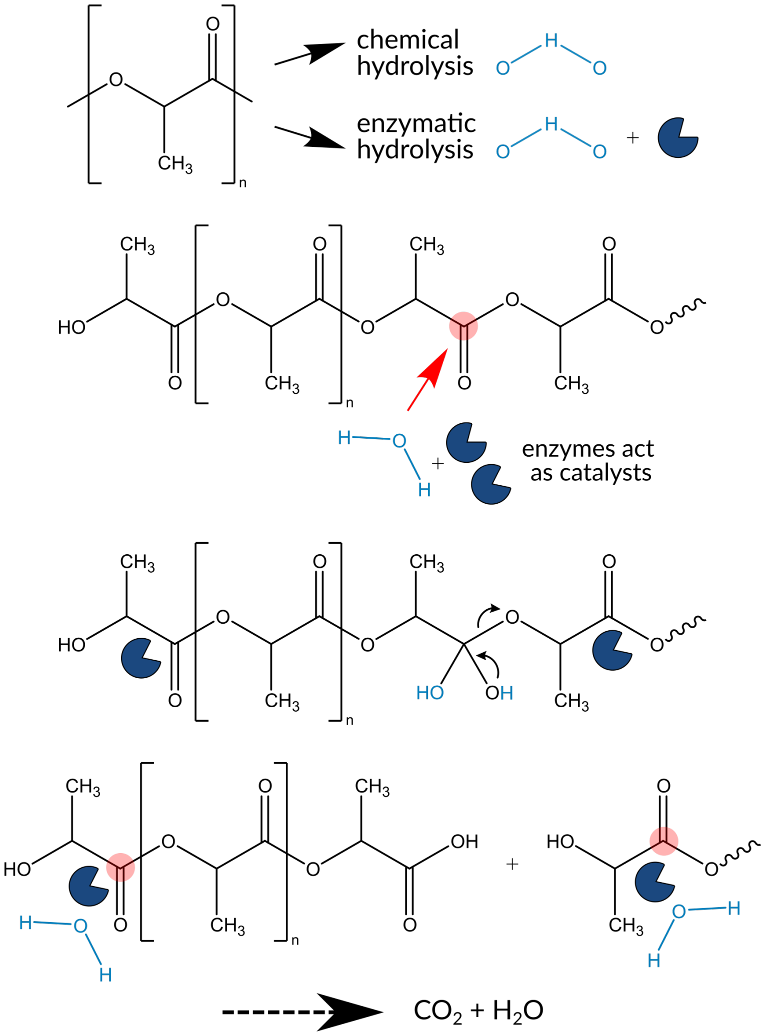

Figure 10: Hydrolysis mechanism on the example of PLA chain scission. Enzymes, and H_2O will attack the ester bond within the chain and lead to chain cleavage, which reduces the molecular weight. Complete enzymatic mineralization will lead to the formation of CO_2 and H_2O.

The low-molecular weight fragments are further degraded into monomers, which are ultimately metabolized into CO_2 and H_2O[86]. Below the example of PLA is given:

$$
\begin{aligned}
&PLA_{\ high\ MW} \ \xrightarrow{H_2O}\ PLA_{\ low\ MW} \\
&PLA_{\ low\ MW} \ \xrightarrow{H_2O\ +\ microorganisms}\ lactic\ acid\ (monomer) \\
&lactic\ acid\ (monomer) \ \xrightarrow{H_2O\ +\ microorganisms}\ CO_2\ +\ H_2O
\end{aligned}
\tag{3.1}
$$

Similar as previously mentioned for abiotic degradation, biodegradation and its rates also depend on the prevalent conditions, the combination and severity of parameters such as temperature, moisture, O_2-availability, pH, humidity, bio-surfactants, microorganisms, and enzyme concentration[2;77]. Under natural, environmental conditions, abiotic parameters such as sunlight, wind, and wind speed can accelerate the degradation rate and the mechanisms acting on degrading[2]. Biodegradation typically proceeds faster for low-molecular-weight, more-hydrophilic, and more-amorphous polymers, as biodegradation preferentially affects the amorphous domains over the crystalline[86].

Commercial synthetic polymers with a C-C backbone (such as PE, PP, PS) are resistant towards biodegradation, owing to their hydrophobicity and their high molecular weight[97]. However, they may become susceptible towards biotic impact, once abiotic degradation has sufficiently modified and deteriorated the material, causing a lowering of the molecular weight, and the formation of functional groups, such as carbonyl compounds[97;116;90]. It further needs to be considered, that an interplay of abiotic and biotic mechanisms is common in natural environments, and that both factors may affect the polymer successively or synergistically[77].

A list of definitions described within this section along with further definitions on the topic of *biodegradation* are given within the glossary, referring to Laycock et al.[77]. The following terms are described: naturally-occurring polymers, bio-based polymers, fossil-based polymers, biodegradable polymers, biodegradability, bioassimilation, bioavailability, bioavailable, biodisintegration, bioerosion, biofragmentation, biomass, biomineralization, compostable.

3.4 Weathering of Plastic

Most plastic found in the environment has been exposed to extensive weathering via abiotic and biotic impacts (figure 5). Consequently, it is crucial to understand how weathering affects the chemical and physical properties of plastic in both macro- and micrometer scales. From the analysis, conclusions can be drawn concerning the toxicity and the potential negative impacts weathered plastic materials in the environment may have on the ecosystems, living organisms, and humans.

In order to investigate the details of weathered plastic, there are two approaches. One is to sample plastic objects from the environment, which have been exposed to natural weathering. These environmental plastic samples can then be identified and investigated. The second approach is to artificially weather plastic samples under precisely chosen, modifiable laboratory conditions in order to reconstruct the weathering procedure. Both approaches have advantages and disadvantages, which will be discussed in the upcoming sections.

3.4.1 Naturally-Weathered Samples

Collecting weathered plastic or MP directly from the environment delivers realistic sample material, which represents the material living organisms and ecosystems are exposed to (figure 5). The weathering conditions are not enhanced or accelerated, but have acted in real-time. Investigating naturally-weathered samples is powerful, delivering real data and results. Nevertheless, naturally-weathered samples are also extremely complex to investigate due to various reasons.

Polymer products used for everyday purposes, which accumulate in natural environments, typically consist of a mixture of the polymer itself along with different chemical additives, such as stabilizers, plasticizers, pigments, flame retardants, or antioxidants[85]. This makes the pristine composition of the polymer product extremely complex already, without weathering being involved. Upon exposure to abiotic and biotic impacts, the polymer and its additives are modified, adding even more complexity to the sample matrix. Stabilizers are often not chemically-bound to the polymer, and may leach out of the system or diffuse within the polymer matrix. All of these individual components are detectable within various methods, overlying and influencing the main information about the polymers themselves[91].

What the polymer experiences, and how it weathers, highly depends on the environment and mechanisms it is exposed to. Natural weathering conditions (e.g., temperature, humidity, light) fluctuate daily and annually, while biotic and abiotic degradation act simultaneously[26]. The plastic item may be transferred from one compartment to another, experiencing distinct changes in the prevalent conditions. Leaching and diffusion of polymer additives are controlled by solubility of the additive in the surrounding media and the diffusion coefficients of the additive-polymer system[21]. Owing to this complexity, up to current research it has not yet been possible to give details on the life-cycle and environmental impact a naturally weathered plastic object may have experienced[104]. Dating of macro litter has been reported to be possible in various studies via printed dates on food containers, logos, design or indicators for production year[42;27;102]. While an approach for MP-dating via additive-identification was suggested by Lechthaler et al.[79], no data on age-determination of environmental MP has yet been reported. Without knowing the time of exposure, the degradation rates, stability, and persistence of plastic in the environment is hard to predict.

Another challenge of analyzing environmental plastic samples is understanding the influence of single parameters. Fluctuating conditions and the simultaneous action of different abiotic and biotic impacts makes it hard or even impossible to distinguish the individual effects. An approach to investigate simple, but natural conditions is the outdoor exposure of well-defined materials, as displayed in figure 11.

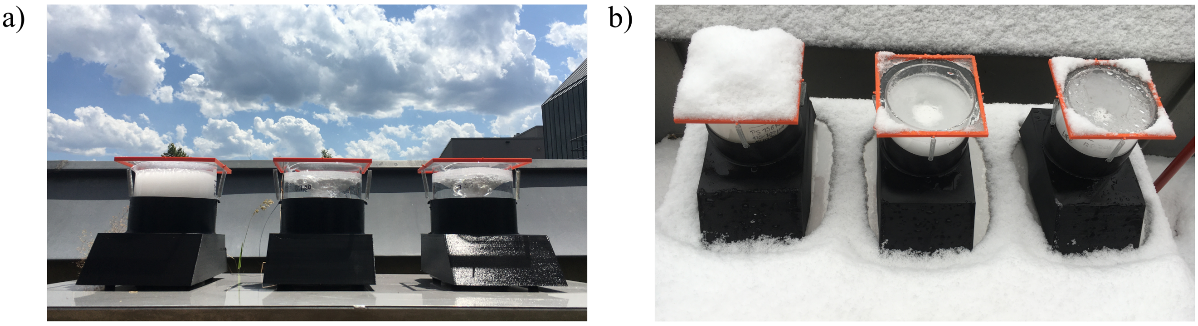

Figure 11: Outdoor weathering at the department MCI during a) summer, and b) winter. The seasonal fluctuation of solar radiation and temperature are evident, a) representing long days of sunshine during the summer months, b) showing gray, cloudy weather, and snow-covered samples during winter.

Controlled outdoor weathering enables a step by step determination of individual effects on degradation (e.g., seasonal fluctuations), while keeping the weathering mechanisms naturally realistic. This compromise between fully natural and fully controlled exposure brings along many advantages. Nevertheless, outdoor experiments are poorly reproducible, since the actual weather is very variable. Further, natural weathering is a very slow process, demanding long time scales to assure sufficient degradation[9;17].

3.4.2 Laboratory-Accelerated Weathering

To overcome the time issue, laboratory-accelerated weathering is a powerful tool to mimic polymer degradation to the same extent, as reached with natural weathering, but consuming less time. A weathering chamber (Q-SUN Xe-3) from Q-Lab is displayed in figure 12. Single parameters can be varied, added or excluded, which enables to draw direct conclusion on the effect these individual parameters have on polymer weathering. Additionally, a more precise control and continuity of temperature and radiation intensity is assured, less fluctuation implying more reliable data[9;98;61;17].

Figure 12: a) Q-Sun Xe-3 weathering test chamber for controlled, accelerated laboratory weathering. Images in b)-c) show the inside of the test chamber, which is equipped with mirrors. Photograph in c) by Christian Wißler.

Nevertheless, real natural settings are challenging to imitate, as a variety of different processes act simultaneously, requiring individual monitoring in a laboratory-controlled setup. Additionally, the intensities need to be chosen carefully in order to assure a realistic imitation. With accelerated weathering, conditions are often kept permanent (e.g., 24-hour irradiation), and elevated (e.g., temperatures > 25 °C) which will unavoidably hinder other processes to act simultaneously. For instance, a higher irradiation dose will also lead to elevated temperatures. Even if both are kept in a realistic range, it may be challenging to grow a biofilm or involve living organisms, as they will most likely not withstand the increased temperature and irradiation[136]. At a certain severity, intensified accelerated weathering thus also has some limitations.

Accelerated weathering is widely used in the industry, especially for service life prediction, durability, development of additives, e.g., to improve aging resistance[98;109]. For industrial use, accelerated weathering aims at improving materials in order to achieve ideal performance and longevity, thus the main kinetics of polymer degradation have been extensively studied for the past 50 years[9]. The focus on environmental issues has only developed with growing concerns towards plastic debris, MP-pollution, and their consequences for the environment and its inhabitants[8;30;62].

3.5 The Microplastic Issue

Plastic is produced on a large-scale since the 1950s, being a breakthrough invention[51]. Reusable products like cutlery and dishes were replaced by single-use items, saving time, work, and stress. Nowadays, a world without plastic is unimaginable and unrealistic. The problems single-use production and its extensive waste generation entail, have long been overlooked. Plastic consumption is now seen from a more critical point of view, and has even emerged to becoming a topic of global concern[133]. While polymer degradation studies started with the large-scale production of plastic[1], the term *microplastic* has yet only first been used in the year 2004 by Thompson et al.[120].

Numerous studies have since investigated the impacts of MP in the environment, leading to an almost exponential increase in scientific publications including the term *microplastic* in the last years[17]. Up to date, a variety of negative effects have been concluded. Depending on the size (section 3.2.2), MP can be ingested by animals[30;121] and retained in the gut, where the accumulation is said to lead to suffocation, malnutrition, and starvation (figure 13)[22;5;131;130]. Another recent study by Kwon et al.[75] suggests a potential risk of small MP to lead to cell death of microglial cells (macrophages of the central nervous system) in murine and human brains. Oxidative stress, immunological responses, neurotoxicity, trans-generational toxicity, genomic instability, reproductive abnormalities, and disruption of the endocrine system have been reported[5;142]. The toxicity of additives or other leaching chemicals, and the sorption behavior of chemicals on MP is commonly investigated, yet still debated[123;88;133].

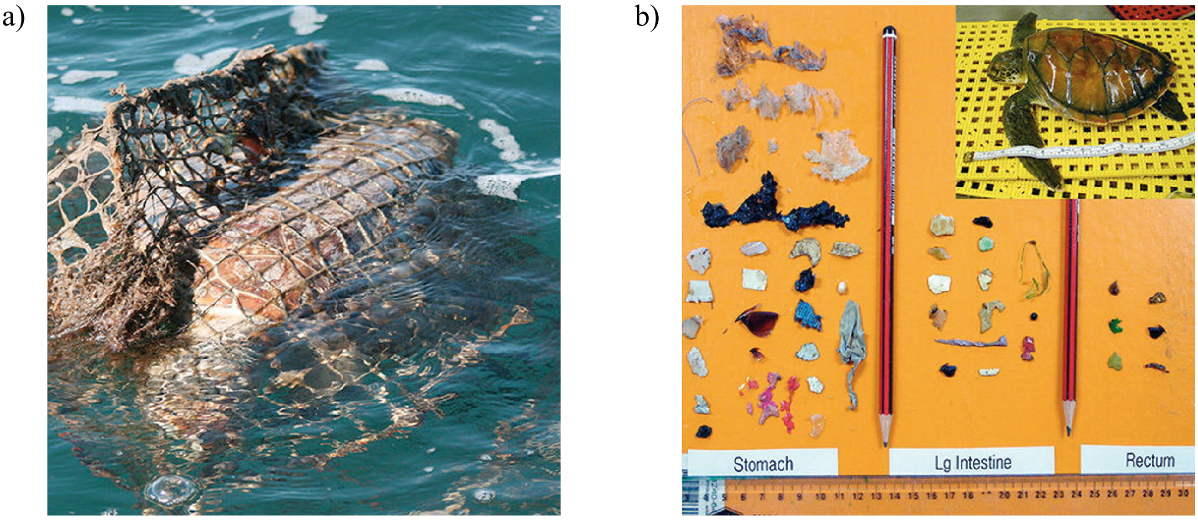

Figure 13: a) Image of a juvenile green turtle *Chelonia mydas* trapped within a discarded crab trap. b) several plastic fragments which were recovered from the gut of a juvenile green turtle (image courtesy Kathy Townsend). Reprinted with permission from Vegter et al.[130]. Copyright© 2014 Inter-Research.

In summary, there is still a knowledge deficiency on specific consequences of MP on the environment and its inhabitants. Many questions regarding how harmful MP are for ecosystems and humans still can not be precisely answered. While the majority of studies typically addresses toxicity of MP or aged MP impacting the health and fitness of individual species, correlations to a larger scale of communities or ecosystems is currently still lacking[88]. Additionally, a big focus is often put on the size of the MP, rather than on their composition. A recent study by Brehm et al.[20] on the example of the water mussel *Dreissena bugensis* demonstrates, that mussels cannot distinguish between natural or MP particles during their filtration. The uptake of different polymers (PS, PLA, polyamide (PA), PET) was comparable to the uptake of the mussel shell control fragments. The authors suggest that the increased toxicity observed from PET particle uptake does not correlate to the size of the fragments, but to the composition. Analysis of the PET revealed the presence of anthranilamide, anthranilonitrile, and butylated hydroxytoluene, chemicals which are toxic to aquatic organisms[20].

Laboratory studies investigating biological effects, transport or migration of MP are often executed with pristine, non-aged particles. In environmental settings, samples are however much more complex. A recent study by Ramsperger et al.[100] has shown, that pristine PS beads from different manufacturers reveal distinct differences in monomer content, ζ-potentials, and surface charge densities. These characteristics largely influence the particle-cell interaction, supporting the necessity to sufficiently characterize all kinds of particles[100;66]. This particularly also applies to plastic or MP recovered from natural compartments, which is extremely diverse. Consequently, it is crucial to understand the individual polymer systems (aged, non-aged), their compositions, characteristics, and behaviors as a function of environmental exposure and weathering, before drawing conclusions on their impacts, especially those of aged MP particles, on animals, plants, humans, and ecosystems.

4 Challenges

Polymer degradation and the kinetics of photooxidation have been thoroughly studied, thus the main mechanisms are well understood[49;1;19]. The focus however has mainly been on polymer performance and economic benefits[37]. Investigations around MP, its presence, behaviors, characteristics, and consequences are numerous to date, nevertheless, MP-studies are still a fairly new field in science, bearing a variety of challenges.

MP sources into environmental compartments are manifold, and so is MP in general. It may be of primary or secondary origin[119;8]. The size, shape, color, and composition of plastic products is wide-ranging, as polymers are constructed to remain undamaged under certain conditions. Since plastic products are extremely diverse to begin with, their MP counterparts are at least as complex. Environmentally weathered plastic has always experienced some kind of degradation[132]. In order to produce environmentally-relevant laboratory experiments, realistic sizes, concentrations, shapes, and compositions need to be chosen[101;137].

To reduce the complexity, many laboratory experiments are performed with non-aged polymer materials[141], which may also substantially differ in properties[100]. It is thus even more necessary to thoroughly characterize the characteristics of all aged and non-aged plastic or MP. A severe hurdle within MP studies is the lacking of standardization. To begin with, the exact size-definition of MP is currently still disputed, and a variety of different classifications are published[44;57;47]. There are no standard methods for sampling, preparation, and analytical investigation[57;8;122]. Macroscopic plastic litter is easier to collect, MP particles however, are typically sampled with sieves or nets of varying sizes, often excluding small fractions[8]. Variations within the sampling method, preparation, and the analytical techniques will fundamentally effect the results and conclusions. Consequently, comparison of different studies is often limited[17].

Polymer degradation studies rarely address the complex interplay of embrittlement, fragmentation, and MP particle formation. Additionally, reliable data on fragmentation rates, and thus on the formation of SMP is scarce[8;70]. Actual numbers and the abundance of MP particles in the environment can only be estimated, currently hindering a proper numerical modeling for the life cycle of plastic objects in natural compartments[17].

MP research is not only of scientific relevance, it has become a global topic of public interest. One of the frequently asked questions posed by society and consumers is if MP are dangerous and toxic for the natural environment, plants, animals, and humans. In order to provide answers to the questions arising, it is crucial to understand the fundamentals of MP formation and degradation. In order to acquire reliable and reproducible data using well-defined and controllable parameters, laboratory-controlled accelerated weathering is a tool preferentially used[9].

5 Objectives

This thesis was prepared in the sub-project C01, which is part of the collaborative research center (CRC) 1357 *microplastic* at the University of Bayreuth. In the sub-project C01, three working groups are involved. A big advantage of the CRC 1357 is the very close cooperation of interdisciplinary projects from the fields of biology, geosciences, chemistry, and physics. Within the CRC 1357, consistent definitions are used and uniform materials produced. This allows for a comparison of individual studies within the CRC, and overcomes some of the most challenging difficulties previously mentioned.

Within the scope of this thesis, multiple laboratory-controlled accelerated weathering studies were performed with the focus of particle degradation, fragmentation, and the formation of SMP particles. Accelerated weathering was performed using an industrially-available weathering chamber, which is commonly used within the automobile industry. A protocol was developed, tested, and maintained over all of the following studies, enabling the comparability. Initially, the polymer materials were relatively primitive in composition (pristine PS, free of stabilizers). In each study, macroscopic tensile bars and microscopic particles were exposed simultaneously, the weathering conditions were kept simple and controllable. The combination of materials and methods was chosen in a way that the experiments can be easily reproduced, expanded, and complexioned.

The general aim of the publications included in this thesis was to investigate the degradation of the chosen polymer systems in a very detailed manner using a broad variety of analytical techniques ranging from the surface into the bulk of the materials, and from optical investigation down to the atomic level. Analysis was performed as a function of exposure time, allowing for detailed conclusions on the interplay of polymer degradation, fragmentation, MP formation, and the influence of geometry, individual weathering parameters, and polymer type.

The first three publications involve thorough degradation protocols of the polymers PS, PE, and PP. For amorphous PS and semi-crystalline LDPE, the observations and conclusions drawn from particles and tensile bar weathering were processed into general degradation models. A new approach for solid-state NMR spectroscopic analysis enabled the quantitative determination of functional groups evolving from photooxidation. Further, numerical values for the release of SMP particles forming from degradation, could be calculated.

We increased the sample complexity with every study, starting with amorphous, stabilizer-free PS, followed by semi-crystalline LDPE and semi-crystalline, stabilized PP. The correlation of all results enabled the development of a two-stage particle degradation model for amorphous PS, which could be extended by a third stage after investigation of the semi-crystalline polymer systems LDPE and PP. Fragmentation rates could be calculated for all three polymers, following particle size investigations over the entire experiment duration, which corresponds to approximately two years of outdoor weathering.

To verify our results from accelerated weathering in terms of degradation mechanisms and rates, we further performed outdoor exposure of the same polymer systems over a time scale of two years.

During outdoor weathering, samples were drawn monthly, then processed and analyzed in the same manner as the accelerated experiments. Correlation of the data sets from laboratory and natural weathering confirmed, that the mechanisms of simulated solar radiation and natural sunlight are the same. Discrepancies were noted in the time scales of degradation and fragmentation, which vary for each polymer individually.

In order to quantitatively investigate the polymer defects forming from photo-initiated oxidation, we developed a new method using multiCP ^{13}C NMR spectroscopy. This approach enables the determination of small quantities of defects up to 1 % in samples with a natural abundance of ^{13}C. Ideal parameters were elaborated using PS enriched with ^{13}C at the α-position to 23 %. The quantitative multiCP method was utilized for the accelerated and the outdoor experiments, and the proportion of functional groups investigated in a qualitative manner.

Lastly, we performed a case study using spherical PS beads exposed to laboratory weathering for different time intervals up to 600 hours (h). The effect of weathered and pristine PS on the cellular response of murine macrophages was investigated using biological essays, transcriptome analysis, and metabolic pathway prediction. Our results demonstrate a significant difference within the celluar response towards weathered and non-weathered PS particles. This study further highlights the necessity of a profound characterization of all kinds of MP particles prior to performing further experiments.

This thesis includes a total of five publications and one manuscript, to be submitted. The conclusions from our studies deliver a profound basis of how polymers degrade under abiotic impact, how fragmentation is correlated to the extent of degradation, and how SMP particles are formed.

References

[1] B. Achhammer, M. Reiney, L. Wall, and F. Reinhart. Study of degradation of polystyrene by means of mass spectrometry. *Journal of Polymer Science*, 8(5): 555–571, 1952.

[2] S. Agarwal. Biodegradable polymers: Present opportunities and challenges in providing a microplastic-free environment. *Macromolecular Chemistry and Physics*, 221(6):2000017, 2020.

[3] T. Ahmed, M. Shahid, F. Azeem, I. Rasul, A. A. Shah, M. Noman, A. Hameed, N. Manzoor, I. Manzoor, and S. Muhammad. Biodegradation of plastics: current scenario and future prospects for environmental safety. *Environmental Science and Pollution Research*, 25(8):7287–7298, 2018.

[4] S. Al-Malaika. Oxidative degradation and stabilisation of polymers. *International Materials Reviews*, 48(3):165–185, 2003. doi: 10.1179/095066003225010218.

[5] C. G. Alimba and C. Faggio. Microplastics in the marine environment: current trends in environmental pollution and mechanisms of toxicological profile. *Environmental toxicology and pharmacology*, 68:61–74, 2019.

[6] L. An, Q. Liu, Y. Deng, W. Wu, Y. Gao, and W. Ling. Sources of microplastic in the environment. In *Microplastics in Terrestrial Environments*, pages 143–159. Springer, 2020.

[7] A. L. Andrady. Microplastics in the marine environment. *Marine Pollution Bulletin*, 62(8):1596–1605, 2011.

[8] A. L. Andrady. The plastic in microplastics: A review. *Marine Pollution Bulletin*, 119(1):12–22, 2017.

[9] A. L. Andrady and B. Koongolla. Degradation and fragmentation of microplastics. In *Plastics and the Ocean: Origin, Characterization, Fate, and Impacts*, pages 227–268. Wiley Online Library, 2022.

[10] K. Ashton, L. Holmes, and A. Turner. Association of metals with plastic production pellets in the marine environment. *Marine Pollution Bulletin*, 60(11): 2050–2055, 2010.

[11] A. R. Bagheri, C. Laforsch, A. Greiner, and S. Agarwal. Fate of so-called biodegradable polymers in seawater and freshwater. *Global Challenges*, 1(4): 1700048, 2017.

[12] D. K. Barnes, F. Galgani, R. C. Thompson, and M. Barlaz. Accumulation and fragmentation of plastic debris in global environments. *Philosophical transactions of the royal society B: biological sciences*, 364(1526):1985–1998, 2009.

[13] F. Z. Benabid and F. Zouai. Natural polymers: Cellulose, chitin, chitosan, gelatin, starch, carrageenan, xylan and dextran. *Algerian Journal of Natural Products*, 4 (3):348–357, 2016.

[14] J. Bertling, R. Bertling, and L. Hamann. Kunststoffe in der Umwelt: Mikro- und Makroplastik. 2018. URL `https://publica.fraunhofer.de/entities/publication/97906872-d1ee-401e-a639-492f3c239952/details`.

[15] G. Bishop, D. Styles, and P. N. L. Lens. Recycling of european plastic is a pathway for plastic debris in the ocean. *Environment International*, 142:105893, 2020.

[16] F. Blancho, M. Davranche, H. E. Hadri, B. Grassl, and J. Gigault. Nanoplastics identification in complex environmental matrices: Strategies for polystyrene and polypropylene. *Environmental Science & Technology*, 55(13):8753–8759, 2021.

[17] M. P. Born and C. Brüll. From model to nature - a review on the transferability of marine (micro-) plastic fragmentation studies. *Science of the Total Environment*, 811:151389, 2022. doi: 10.1016/j.scitotenv.2021.151389.

[18] S. B. Borrelle, J. Ringma, K. L. Law, C. C. Monnahan, L. Lebreton, A. McGivern, E. Murphy, J. Jambeck, G. H. Leonard, M. A. Hilleary, et al. Predicted growth in plastic waste exceeds efforts to mitigate plastic pollution. *Science*, 369(6510): 1515–1518, 2020.

[19] F. Bottino, G. Di Pasquale, and A. Pollicino. Studies on polymer surface photooxidation. *Recent Research Development in Polymer Scienence*, pages 203–210, 1998.

[20] J. Brehm, M. V. Wilde, L. Reiche, L.-C. Leitner, B. Petran, M. Meinhart, S. Wieland, S. Ritschar, M. Schott, J.-P. Boos, S. Frei, H. Kress, J. Senker, A. Greiner, T. Fröhlich, and C. Laforsch. In-depth characterization revealed polymer type and chemical content specific effects of microplastic on dreissena bugensis. *Journal of Hazardous Materials*, 437:129351, 2022.

[21] J. H. Bridson, E. C. Gaugler, D. A. Smith, G. L. Northcott, and S. Gaw. Leaching and extraction of additives from plastic pollution to inform environmental risk: A multidisciplinary review of analytical approaches. *Journal of Hazardous Materials*, 414:125571, 2021.

[22] M. A. Browne, A. Dissanayake, T. S. Galloway, D. M. Lowe, and R. C. Thompson. Ingested microscopic plastic translocates to the circulatory system of the mussel, Mytilus edulis (L.). *Environmental Science & Technology*, 42(13):5026–5031, 2008.

[23] M. A. Browne, T. S. Galloway, and R. C. Thompson. Spatial patterns of plastic debris along estuarine shorelines. *Environmental Science & Technology*, 44(9): 3404–3409, 2010.

[24] M. A. Browne, P. Crump, S. J. Niven, E. Teuten, A. Tonkin, T. Galloway, and R. Thompson. Accumulation of microplastic on shorelines woldwide: sources and sinks. *Environmental Science & Technology*, 45(21):9175–9179, 2011.

[25] Bundesministerium der Justiz. Verordnung über die Verwertung von Klärschlamm, Klärschlammgemisch und Klärschlammkompost (Klärschlammverordnung - AbfKlärV), 2020. URL `https://www.gesetze-im-internet.de/abfkl_rv_2017/BJNR346510017.html`.

[26] L. Cai, J. Wang, J. Peng, Z. Wu, and X. Tan. Observation of the degradation of three types of plastic pellets exposed to uv irradiation in three different environments. *Science of the Total Environment*, 628:740–747, 2018.

[27] A. Cau, A. Bellodi, D. Moccia, A. Mulas, C. Porcu, A. Pusceddu, and M. C. Follesa. Shelf-life and labels: A cheap dating tool for seafloor macro litter? Insights from MEDITS surveys in Sardinian sea. *Marine Pollution Bulletin*, 141:430–433, 2019.

[28] A. Chamas, H. Moon, J. Zheng, Y. Qiu, T. Tabassum, J. H. Jang, M. Abu-Omar, S. L. Scott, and S. Suh. Degradation rates of plastics in the environment. *ACS Sustainable Chemistry & Engineering*, 8(9):3494–3511, 2020. doi: 10.1021/acssuschemeng.9b06635.

[29] S. Chinaglia, M. Tosin, and F. Degli-Innocenti. Biodegradation rate of biodegradable plastics at molecular level. *Polymer Degradation and Stability*, 147:237–244, 2018.

[30] M. Cole, P. Lindeque, C. Halsband, and T. S. Galloway. Microplastics as contaminants in the marine environment: a review. *Marine Pollution Bulletin*, 62(12): 2588–2597, 2011.

[31] P. L. Corcoran and K. Jazvac. The consequence that is plastiglomerate. *Nature Reviews Earth & Environment*, 1(1):6–7, 2020.

[32] R. M. Cywar, N. A. Rorrer, C. B. Hoyt, G. T. Beckham, and E. Y.-X. Chen. Bio-based polymers with performance-advantaged properties. *Nature Reviews Materials*, pages 1–21, 2021.

[33] J. G. Derraik. The pollution of the marine environment by plastic debris: a review. *Marine Pollution Bulletin*, 44(9):842–852, 2002.

[34] M. L. Di Lorenzo and R. Androsch. *Thermal properties of bio-based polymers*. Springer, 2019.

[35] DIN EN 13432:2000-12. Verpackung - Anforderungen an die Verwertung von Verpackungen durch Kompostierung und biologischen Abbau - Prüfschema und Bewertungskriterien für die Einstufung von Verpackungen, Deutsche Fassung, EN 13432:2000, 2000. URL `https://dx.doi.org/10.31030/9010637`.

[36] S. Dubey, V. Jhelum, and P. Patanjali. Controlled release agrochemicals formulations: a review. *Journal of Scientific & Industrial Research*, 70:105–112, 2011.

[37] N. Emanuel and A. L. Buchachenko. *Chemical physics of polymer degradation and stabilization*, volume 1. VNU Science Press, 1987.

[38] R. E. Engler. The complex interaction between marine debris and toxic chemicals in the ocean. *Environmental Science & Technology*, 46(22):12302–12315, 2012. doi: 10.1021/es3027105.

[39] M. Eriksen, L. C. Lebreton, H. S. Carson, M. Thiel, C. J. Moore, J. C. Borerro, F. Galgani, P. G. Ryan, and J. Reisser. Plastic pollution in the world's oceans: more than 5 trillion plastic pieces weighing over 250,000 tons afloat at sea. *PloS one*, 9(12):e111913, 2014.

[40] European Commission. Scientific opinion: Biodegradability of plastics in the open environment, 2020. URL `https://op.europa.eu/en/publication-detail/-/publication/0c0d6267-433a-11eb-b27b-01aa75ed71a1`.

[41] A. Fairbrother, H.-C. Hsueh, J. H. Kim, D. Jacobs, L. Perry, D. Goodwin, C. White, S. Watson, and L.-P. Sung. Temperature and light intensity effects on photodegradation of high-density polyethylene. *Polymer Degradation and Stability*, 165:153–160, 2019.

[42] J. Falk-Andersson, Z. Tairova, T. T. Drægni, and M. L. Haarr. Methods for determining the geographical origin and age of beach litter: Challenges and opportunities. *Marine Pollution Bulletin*, 172:112901, 2021.

[43] L. S. Fendall and M. A. Sewell. Contributing to marine pollution by washing your face: microplastics in facial cleansers. *Marine Pollution Bulletin*, 58(8):1225–1228, 2009.

[44] J. Frias and R. Nash. Microplastics: Finding a consensus on the definition. *Marine Pollution Bulletin*, 138:145–147, 2019. doi: 10.1016/j.marpolbul.2018.11.022.

[45] E. Ganivet. Growth in human population and consumption both need to be addressed to reach an ecologically sustainable future. *Environment, Development and Sustainability*, 22(6):4979–4998, 2020.

[46] C. C. Gaylarde, J. A. B. Neto, and E. M. da Fonseca. Paint fragments as polluting microplastics: A brief review. *Marine Pollution Bulletin*, 162:111847, 2021.

[47] GESAMP Joint Group of Experts on the Scientific Aspects of Marine Environmental Protection. Sources, fate and effects of microplastics in the marine environment. *Journal Series GESAMP Reports and Studies*, (90):96 p., 2015. URL `http://www.gesamp.org/publications/reports-and-studies-no-90`.

[48] GESAMP Joint Group of Experts on the Scientific Aspects of Marine Environmental Protection. Proceedings of the gesamp international workshop on assessing the risks associated with plastics and microplastics in the marine environment. *Journal Series GESAMP Reports and Studies*, (103):60 p., 2020. URL `http://www.gesamp.org/site/assets/files/2136/rs103e-1.pdf`.

[49] G. Geuskens, D. Baeyens-Volant, G. Delaunois, Q. Lu-Vinh, W. Piret, and C. David. Photo-oxidation of polymers-i: a quantitative study of the chemical reactions resulting from irradiation of polystyrene at 253.7 nm in the presence of oxygen. *European polymer journal*, 14(4):291–297, 1978.

[50] B. Gewert, M. M. Plassmann, and M. MacLeod. Pathways for degradation of plastic polymers floating in the marine environment. *Environmental science: processes & impacts*, 17(9):1513–1521, 2015.

[51] R. Geyer, J. R. Jambeck, and K. L. Law. Production, use, and fate of all plastics ever made. *Science Advances*, 3(7):e1700782, 2017.

[52] E. A. Gies, J. L. LeNoble, M. Noël, A. Etemadifar, F. Bishay, E. R. Hall, and P. S. Ross. Retention of microplastics in a major secondary wastewater treatment plant in vancouver, canada. *Marine Pollution Bulletin*, 133:553–561, 2018.

[53] N. Grassie and G. Scott. *Polymer degradation and stabilisation.* CUP Archive, 1988.

[54] G. Grause, M.-F. Chien, and C. Inoue. Changes during the weathering of polyolefins. *Polymer Degradation and Stability*, page 109364, 2020.

[55] C. Guerranti, T. Martellini, G. Perra, C. Scopetani, and A. Cincinelli. Microplastics in cosmetics: Environmental issues and needs for global bans. *Environmental Toxicology and Pharmacology*, 68:75–79, 2019.

[56] J. N. Hanun, F. Hassan, and J.-J. Jiang. Occurrence, fate, and sorption behavior of contaminants of emerging concern to microplastics: Influence of the weathering/aging process. *Journal of Environmental Chemical Engineering*, 9(5):106290, 2021.

[57] N. B. Hartmann, T. Hueffer, R. C. Thompson, M. Hasselloev, A. Verschoor, A. E. Daugaard, S. Rist, T. Karlsson, N. Brennholt, M. Cole, and M. P. Herrling. Are we speaking the same language? Recommendations for a definition and categorization framework for plastic debris. *Environmental Science & Technology*, 53(3):1039–1047, 2019. doi: 10.1021/acs.est.8b05297.

[58] C. Hernández-Sánchez, J. González-Sálamo, C. Ortega-Zamora, G. Jiménez-Skrzypek, and J. Hernández-Borges. Microplastics: an emerging and challenging research field. *Current Analytical Chemistry*, 17(7):894–901, 2021.

[59] G. Hill, C. Moreira, F. Huynh, A. Trufasila, F. Ly, R. Lloyd, H. Sawal, and C. J. Wallis. Correlation of a temperate UV-weathering cycle to outdoor exposure for the determination of the environmental instability of polyethylene films using HT-GPC analysis. *Polymers*, 13(4):591, 2021.

[60] S. H. Hong, W. J. Shim, and M. Jang. Chemicals associated with marine plastic debris and microplastics: Analyses and contaminant levels. In *Microplastic Contamination in Aquatic Environments*, pages 271–315. Elsevier, 2018.

[61] A. A. Horton, A. Walton, D. J. Spurgeon, E. Lahive, and C. Svendsen. Microplastics in freshwater and terrestrial environments: evaluating the current understanding to identify the knowledge gaps and future research priorities. *Science of the Total Environment*, 586:127–141, 2017.

[62] T. Hüffer, A.-K. Weniger, and T. Hofmann. Sorption of organic compounds by aged polystyrene microplastic particles. *Environmental Pollution*, 236:218–225, 2018.

[63] N. P. Ivleva. Chemical analysis of microplastics and nanoplastics: Challenges, advanced methods, and perspectives. *Chemical Reviews*, 121(19):11886–11936, 2021.

[64] I. Jakubowicz, J. Enebro, and N. Yarahmadi. Challenges in the search for nanoplastics in the environment-a critical review from the polymer science perspective. *Polymer Testing*, 93:106953, 2021.

[65] J. R. Jambeck, R. Geyer, C. Wilcox, T. R. Siegler, M. Perryman, A. Andrady, R. Narayan, and K. L. Law. Plastic waste inputs from land into the ocean. *Science*, 347(6223):768–771, 2015.

[66] J. Jasinski, M. V. Wilde, M. Voelkl, V. Jérôme, T. Froehlich, R. Freitag, and T. Scheibel. Tailor-made protein corona formation on polystyrene microparticles and its effect on epithelial cell uptake. *Applied Materials & Interfaces*, 2022.

[67] L. Jiang and J. Zhang. Biodegradable polymers and polymer blends. *Handbook of Biopolymers and Biodegradable Plastics: Properties, Processing and Applications*, pages 109–128, 2012.

[68] T. Jiang, Q. Duan, J. Zhu, H. Liu, and L. Yu. Starch-based biodegradable materials: Challenges and opportunities. *Advanced Industrial and Engineering Polymer Research*, 3(1):8–18, 2020.

[69] G. John, S. Nagarajan, P. K. Vemula, J. R. Silverman, and C. Pillai. Natural monomers: A mine for functional and sustainable materials–occurrence, chemical modification and polymerization. *Progress in Polymer Science*, 92:158–209, 2019.

[70] F. Julienne, N. Delorme, and F. Lagarde. From macroplastics to microplastics: Role of water in the fragmentation of polyethylene. *Chemosphere*, 236:124409, 2019.

[71] N. Kalogerakis, K. Karkanorachaki, G. Kalogerakis, E. I. Triantafyllidi, A. D. Gotsis, P. Partsinevelos, and F. Fava. Microplastics generation: onset of fragmentation of polyethylene films in marine environment mesocosms. *Frontiers in Marine Science*, 4:84, 2017.

[72] S. Kernchen, M. G. Löder, F. Fischer, D. Fischer, S. R. Moses, C. Georgi, A. C. Nölscher, A. Held, and C. Laforsch. Airborne microplastic concentrations and deposition across the weser river catchment. *Science of the Total Environment*, 818:151812, 2022.

[73] A. A. Koelmans, P. E. Redondo-Hasselerharm, N. H. Nor, V. N. de Ruijter, S. M. Mintenig, and M. Kooi. Risk assessment of microplastic particles. *Nature Reviews Materials*, 7(2):138–152, 2022.

[74] M. Kumar, X. Xiong, M. He, D. C. W. Tsang, J. Gupta, E. Khan, S. Harrad, D. Hou, Y. S. Ok, and N. S. Bolan. Microplastics as pollutants in agricultural soils. *Environmental Pollution*, 265(Part A):114980, 2020. doi: 10.1016/j.envpol.2020.114980.

[75] W. Kwon, D. Kim, H.-Y. Kim, S. W. Jeong, S.-G. Lee, H.-C. Kim, Y.-J. Lee, M. K. Kwon, J.-S. Hwang, J. E. Han, et al. Microglial phagocytosis of polystyrene microplastics results in immune alteration and apoptosis in vitro and in vivo. *Science of The Total Environment*, 807:150817, 2022.

[76] E. A. Laws. *Environmental toxicology: selected entries from the encyclopedia of sustainability science and technology*. Springer Science & Business Media, 2012.

[77] B. Laycock, M. Nikolić, J. M. Colwell, E. Gauthier, P. Halley, S. Bottle, and G. George. Lifetime prediction of biodegradable polymers. *Progress in Polymer Science*, 71:144–189, 2017.

[78] L. Lebreton and A. Andrady. Future scenarios of global plastic waste generation and disposal. *Palgrave Communications*, 5(1):1–11, 2019.

[79] S. Lechthaler, V. Esser, H. Schüttrumpf, and G. Stauch. Why analysing microplastics in floodplains matters: Application in a sedimentary context. *Environmental Science: Processes & Impacts*, 23(1):117–131, 2021.

[80] K. Lei, F. Qiao, Q. Liu, Z. Wei, H. Qi, S. Cui, X. Yue, Y. Deng, and L. An. Microplastics releasing from personal care and cosmetic products in china. *Marine Pollution Bulletin*, 123(1-2):122–126, 2017.

[81] J. M. Levermore, T. E. Smith, F. J. Kelly, and S. L. Wright. Detection of microplastics in ambient particulate matter using raman spectral imaging and chemometric analysis. *Analytical Chemistry*, 92(13):8732–8740, 2020.

[82] C.-T. Lin, M.-C. Chiu, and M.-H. Kuo. A mini-review of strategies for quantifying anthropogenic activities in microplastic studies in aquatic environments. *Polymers*, 14(1):198, 2022.

[83] D. Lu, C. Xiao, and S. Xu. Starch-based completely biodegradable polymer materials. *Express polymer letters*, 3(6):366–375, 2009.

[84] N. Lucas, C. Bienaime, C. Belloy, M. Queneudec, F. Silvestre, and J.-E. Nava-Saucedo. Polymer biodegradation: Mechanisms and estimation techniques–a review. *Chemosphere*, 73(4):429–442, 2008.

[85] H. Luo, Y. Zhao, Y. Li, Y. Xiang, D. He, and X. Pan. Aging of microplastics affects their surface properties, thermal decomposition, additives leaching and interactions in simulated fluids. *Science of The Total Environment*, 714:136862, 2020.

[86] T. Maharana, B. Mohanty, and Y. Negi. Melt-solid polycondensation of lactic acid and its biodegradability. *Progress in polymer science*, 34(1):99–124, 2009.

[87] M. Mahmoudi, K. Azadmanesh, M. A. Shokrgozar, S. W. Journeay, and S. Laurent. Effect of nanoparticles on the cell life cycle. *Chemical reviews*, 111(5): 3407–3432, 2011.

[88] D. J. Marchant, J. Jones, G. Zemelka, O. Eyice, and P. Kratina. Do microplastics mediate the effects of chemicals on aquatic organisms? *Aquatic Toxicology*, 242: 106037, 2022.

[89] T. Menzel, S. Weigert, S. Gagsteiger, Y. Eich, S. Sittl, G. Papastavrou, H. Ruckdäschel, V. Altstädt, and B. Höcker. Impact of enzymatic degradation on the material properties of poly(ethylene terephthalate). *Polymers*, 13(3885), 2021.

[90] S. Miri, R. Saini, S. M. Davoodi, R. Pulicharla, S. K. Brar, and S. Magdouli. Biodegradation of microplastics: better late than never. *Chemosphere*, 286:131670, 2022.

[91] J. N. Möller, M. G. Löder, and C. Laforsch. Finding microplastics in soils: a review of analytical methods. *Environmental Science & Technology*, 54(4):2078–2090, 2020.

[92] C. Moreira, R. Lloyd, G. Hill, F. Huynh, A. Trufasila, F. Ly, H. Sawal, and C. Wallis. Temperate UV-Accelerated Weathering Cycle Combined with HT-GPC Analysis and Drop Point Testing for Determining the Environmental Instability of Polyethylene Films. *Polymers*, 13(14):2373, 2021.

[93] L. K. Ncube, A. U. Ude, E. N. Ogunmuyiwa, R. Zulkifli, and I. N. Beas. An overview of plastic waste generation and management in food packaging industries. *Recycling*, 6(1):12, 2021.

[94] PlasticsEurope. Plastics - the facts 2016, an analysis of european plastics production, demand and waste data, 2016. URL `https://plasticseurope.org/knowledge-hub/plastics-the-facts-2016/`.

[95] PlasticsEurope. Plastics - the facts 2020: An analysis of european plastics production, demand and waste data, 2020. URL `https://plasticseurope.org/knowledge-hub/plastics-the-facts-2020/`.

[96] PlasticsEurope. Plastics - the facts 2021, an analysis of european plastics production, demand and waste data, 2021. URL `https://plasticseurope.org/knowledge-hub/plastics-the-facts-2021/`.

[97] A. Priya, K. Dutta, and A. Daverey. A comprehensive biotechnological and molecular insight into plastic degradation by microbial community. *Journal of Chemical Technology & Biotechnology*, 97(2):381–390, 2022.

[98] J. Qin, J. Jiang, Y. Tao, S. Zhao, W. Zeng, Y. Shi, T. Lu, L. Guo, S. Wang, X. Zhang, et al. Sunlight tracking and concentrating accelerated weathering test applied in weatherability evaluation and service life prediction of polymeric materials: A review. *Polymer Testing*, 93:106940, 2021.

[99] S. Rajeswari, T. Prasanthi, N. Sudha, R. P. Swain, S. Panda, and V. Goka. Natural polymers: A recent review. *World Journal of Pharmacy and Pharmaceutical Sciences*, 6:472–494, 2017.

[100] A. F. Ramsperger, J. Jasinski, M. Völkl, T. Witzmann, M. Meinhart, V. Jérôme, W. P. Kretschmer, R. Freitag, J. Senker, A. Fery, H. Kress, T. Scheibel, and C. Laforsch. Supposedly identical microplastic particles substantially differ in their material properties influencing particle-cell interactions and cellular responses. *Journal of Hazardous Materials*, 425:127961, 2021.

[101] U. Rozman and G. Kalčíková. Seeking for a perfect (non-spherical) microplastic particle–the most comprehensive review on microplastic laboratory research. *Journal of Hazardous Materials*, 424:127529, 2022.

[102] P. G. Ryan. Land or sea? What bottles tell us about the origins of beach litter in Kenya. *Waste Management*, 116:49–57, 2020.

[103] M. Sander. Biodegradation of polymeric mulch films in agricultural soils: Concepts, knowledge gaps, and future research directions. *Environmental Science & Technology*, 53(5):2304–2315, 2019. doi: 10.1021/acs.est.8b05208.

[104] T. Sang, C. J. Wallis, G. Hill, and G. J. Britovsek. Polyethylene terephthalate degradation under natural and accelerated weathering conditions. *European Polymer Journal*, 136:109873, 2020.

[105] SAPEA, Science Advice for Policy by European Academies. Biodegradability of plastics in the open environment, 2020. URL `https://sapea.info/topic/biodegradability-of-plastics/`.

[106] E. Schmaltz, E. C. Melvin, Z. Diana, E. F. Gunady, D. Rittschof, J. A. Somarelli, J. Virdin, and M. M. Dunphy-Daly. Plastic pollution solutions: emerging technologies to prevent and collect marine plastic pollution. *Environment International*, 144:106067, 2020.

[107] K. Schuhen, D. He, and Y. E. Luo. Microplastics in terrestrial environments: emerging contaminants and major challenges. *Analytical and Bioanalytical Chemistry volume*, 413:6199–6200, 2021.

[108] J. Seay and M. E. Ternes. A review of current challenges and legal advances in the global management of plastic waste. *Clean Technologies and Environmental Policy*, pages 1–8, 2022.

[109] Y. Shi, J. Qin, Y. Tao, G. Jie, and J. Wang. Natural weathering severity of typical coastal environment on polystyrene: Experiment and modeling. *Polymer Testing*, 76:138–145, 2019. doi: 10.1016/j.polymertesting.2019.03.018.

[110] A. V. Shyichuk and J. R. White. Analysis of chain-scission and crosslinking rates in the photo-oxidation of polystyrene. *Journal of applied polymer science*, 77(13), 2000.

[111] A. Sikder, A. K. Pearce, S. J. Parkinson, R. Napier, and R. K. O'Reilly. Recent trends in advanced polymer materials in agriculture related applications. *ACS Applied Polymer Materials*, 3(3):1203–1217, 2021.

[112] B. Singh and N. Sharma. Mechanistic implications of plastic degradation. *Polymer Degradation and Stability*, 93(3):561–584, 2008.

[113] D. Sol, A. Laca, A. Laca, and M. Díaz. Approaching the environmental problem of microplastics: Importance of WWTP treatments. *Science of the Total Environment*, 740:140016, 2020.

[114] Statista. Industries & Markets, Plastic waste in Europe, 2021. URL `https://www.statista.com/study/56285/plastic-waste-in-europe/`.

[115] T. Steiner, Y. Zhang, J. N. Möller, S. Agarwal, M. G. Löder, A. Greiner, C. Laforsch, and R. Freitag. Municipal biowaste treatment plants contribute to the contamination of the environment with residues of biodegradable plastics with putative higher persistence potential. *Scientific Reports*, 12(1):1–14, 2022.

[116] E. Syranidou, K. Karkanorachaki, F. Amorotti, A. Avgeropoulos, B. Kolvenbach, N.-Y. Zhou, F. Fava, P. F.-X. Corvini, and N. Kalogerakis. Biodegradation of mixture of plastic films by tailored marine consortia. *Journal of Hazardous Materials*, 375:33–42, 2019.

[117] A. Ter Halle and J. F. Ghiglione. Nanoplastics: A complex, polluting terra incognita. *Environmental Science & Technology*, 55(21):14466–14469, 2021.

[118] A. Ter Halle, L. Ladirat, M. Martignac, A. F. Mingotaud, O. Boyron, and E. Perez. To what extent are microplastics from the open ocean weathered? *Environmental Pollution*, 227:167–174, 2017.

[119] R. C. Thompson. Microplastics in the marine environment: sources, consequences and solutions. In *Marine Anthropogenic Litter*, pages 185–200. Springer, Cham, 2015.

[120] R. C. Thompson, Y. Olsen, R. P. Mitchell, A. Davis, S. J. Rowland, A. W. John, D. McGonigle, and A. E. Russell. Lost at sea: where is all the plastic? *Science*, 304(5672):838–838, 2004.

[121] R. C. Thompson, S. H. Swan, C. J. Moore, and F. S. vom Saal. Our plastic age. *Philosophical Transactions of the Royal Society B: Biological Sciences*, 364(1526): 1973–1976, 2009.

[122] A. Tirkey and L. S. Upadhyay. Microplastics: An overview on separation, identification and characterization of microplastics. *Marine Pollution Bulletin*, 170: 112604, 2021.

[123] F. G. Torres, D. C. Dioses-Salinas, C. I. Pizarro-Ortega, and G. E. De-la Torre. Sorption of chemical contaminants on degradable and non-degradable microplastics: Recent progress and research trends. *Science of the Total Environment*, 757: 143875, 2021.

[124] P. S. Tourinho, V. Kočí, S. Loureiro, and C. A. van Gestel. Partitioning of chemical contaminants to microplastics: Sorption mechanisms, environmental distribution and effects on toxicity and bioaccumulation. *Environmental Pollution*, 252:1246–1256, 2019.

[125] A. Turner. Paint particles in the marine environment: An overlooked component of microplastics. *Water Research X*, 12:100110, 2021.

[126] A. Turner and L. Holmes. Occurrence, distribution and characteristics of beached plastic production pellets on the island of Malta (central Mediterranean). *Marine Pollution Bulletin*, 62(2):377–381, 2011.

[127] A. Turner, C. Ostle, and M. Wootton. Occurrence and chemical characteristics of microplastic paint flakes in the North Atlantic Ocean. *Science of The Total Environment*, 806:150375, 2022.

[128] United Nations Department of Economic and Social Affairs, Population Division. Global Population Growth and Sustainable Development, 2021. URL `https://www.un.org/development/desa/pd/sites/www.un.org.development.desa.pd/files/undesa_pd_2022_global_population_growth.pdf`.

[129] G. S. Ustabasi and A. Baysal. Occurrence and risk assessment of microplastics from various toothpastes. *Environmental Monitoring and Assessment*, 191(7):1–8, 2019.

[130] A. C. Vegter, M. Barletta, C. Beck, J. Borrero, H. Burton, M. L. Campbell, M. F. Costa, M. Eriksen, C. Eriksson, A. Estrades, et al. Global research priorities to mitigate plastic pollution impacts on marine wildlife. *Endangered Species Research*, 25(3):225–247, 2014.

[131] M. Wagner and S. Lambert. *Freshwater microplastics: emerging environmental contaminants?* Springer Nature, 2018.

[132] W. R. Waldman and M. C. Rillig. Microplastic research should embrace the complexity of secondary particles. *Environmental Science & Technology*, 13(54), 2020.

[133] F. Wang, C. S. Wong, D. Chen, X. Lu, F. Wang, and E. Y. Zeng. Interaction of toxic chemicals with microplastics: a critical review. *Water Research*, 139:208–219, 2018.

[134] J. Wang, X. Liu, Y. Li, T. Powell, X. Wang, G. Wang, and P. Zhang. Microplastics as contaminants in the soil environment: a mini-review. *Science of the Total Environment*, 691:848–857, 2019.

[135] X.-F. Wei, A. J. Capezza, Y. Cui, L. Li, A. Hakonen, B. Liu, and M. S. Hedenqvist. Millions of microplastics released from a biodegradable polymer during biodegradation/enzymatic hydrolysis. *Water Research*, page 118068, 2022.

[136] P. Weihs, A. W. Schmalwieser, and G. Schauberger. UV effects on living organisms. In *Environmental Toxicology*, pages 609–688. Springer, 2013.

[137] J. S. Weis and K. H. Palmquist. Reality check: experimental studies on microplastics lack realism. *Applied Sciences*, 11(18):8529, 2021.

[138] Wissenschaftliche Dienste Deutscher Bundestag. Sachstand, Mikroplastik in Kosmetika, Rechtliche Rahmenbedingungen, 2016. URL `https://www.bundestag.de/resource/blob/476046/f7081582453e6aa9a4b7b2e8be3d0a0f/wd-7-115-16-pdf-data.pdf`.

[139] V. Yarsley and E. Couzens. Plastics middlesex. *Britain: Penguin Books Limited*, page 152, 1945.

[140] E. Yousif and R. Haddad. Photodegradation and photostabilization of polymers, especially polystyrene. *SpringerPlus*, 2(1):1–32, 2013.

[141] K. Zhang, A. H. Hamidian, A. Tubić, Y. Zhang, J. K. H. Fang, C. Wu, and P. K. S. Lam. Understanding plastic degradation and microplastic formation in the environment: A review. *Environmental Pollution*, page 116554, 2021.

[142] Y. Zhang, S. Wang, V. Olga, Y. Xue, S. Lv, X. Diao, Y. Zhang, Q. Han, and H. Zhou. The potential effects of microplastic pollution on human digestive tract cells. *Chemosphere*, 291:132714, 2022.

[143] M. T. Zumstein, A. Schintlmeister, T. F. Nelson, R. Baumgartner, D. Woebken, M. Wagner, H.-P. E. Kohler, K. McNeill, and M. Sander. Biodegradation of synthetic polymers in soils: Tracking carbon into CO_2 and microbial biomass. *Science Advances*, 4(7):eaas9024, 2018.

6 List of Publications

The following published articles and one manuscript, are included within this thesis:

Paper 1 *Reconstructing the Environmental Degradation of Polystyrene by Accelerated Weathering*
Nora Meides, Teresa Menzel, Björn Poetzschner, Martin G. J. Löder, Ulrich Mansfeld, Peter Strohriegl, Volker Altstädt, and Jürgen Senker
Environmental Science & Technology **2021**, 55, 12, 7930-7938.

Paper 2 *Degradation of low-density polyethylene to nanoplastic particles by accelerated weathering*
Teresa Menzel, Nora Meides, Anika Mauel, Ulrich Mansfeld, Winfried Kretschmer, Meike Kuhn, Eva M. Herzig, Volker Altstädt, Peter Strohriegl, Jürgen Senker, Holger Ruckdäschel
Science of the Total Environment **2022**, 154035, 0048-9697.

Paper 3 *Quantifying the fragmentation of polypropylene upon exposure to accelerated weathering*
Nora Meides, Anika Mauel, Teresa Menzel, Jürgen Senker, Volker Altstädt, Holger Ruckdäschel, Peter Strohriegl
Microplastics & Nanoplastics **2022**, 2:23.

Paper 4, manuscript ready for submission *Environmental degradation of polystyrene, polyethylene, and polypropylene - a comparison of natural and accelerated weathering*
Nora Meides, Anika Mauel, Teresa Menzel, Wolfgang Babel, Jürgen Senker, Volker Altstädt, Holger Ruckdäschel, Peter Strohriegl

Paper 5 *Quantification of photooxidative defects in weathered microplastics using ^{13}C multiCP NMR spectroscopy*
Anika Mauel, Björn Pötzschner, Nora Meides, Renée Siegel, Peter Strohriegl, Jürgen Senker
RSC Advances **2022**, 12, 10875-10885.

Paper 6 *Pristine and artificially-aged polystyrene microplastic particles differ in regard to cellular response*
Matthias Völkl, Valérie Jérôme, Alfons Weig, Julia Jasinski, Nora Meides, Peter Strohriegl, Thomas Scheibel, Ruth Freitag
Journal of Hazardous Materials **2022**, 435, 128955.

7 Synopsis

Within this thesis, three of the most abundant polymer systems, found as plastic litter within the natural environment, were chosen for experiment and analysis: PS, LDPE, and PP. All three systems were exposed to laboratory-controlled, accelerated simulated weathering for 3200 h, and investigated for changes in their physical and chemical characteristics as a function of exposure time. A graphical overview of the individual papers of this thesis is given in figure 14. A total of 13 samples were drawn at different time intervals, and then analyzed with a variety of methods to allow for a thorough characterization as a function of increasing exposure time. Intervals of sampling were at 24, 50, 100, 200, 400, 600, 800, 1200, 1600, 2000, 2400, 2800, and 3200 h.

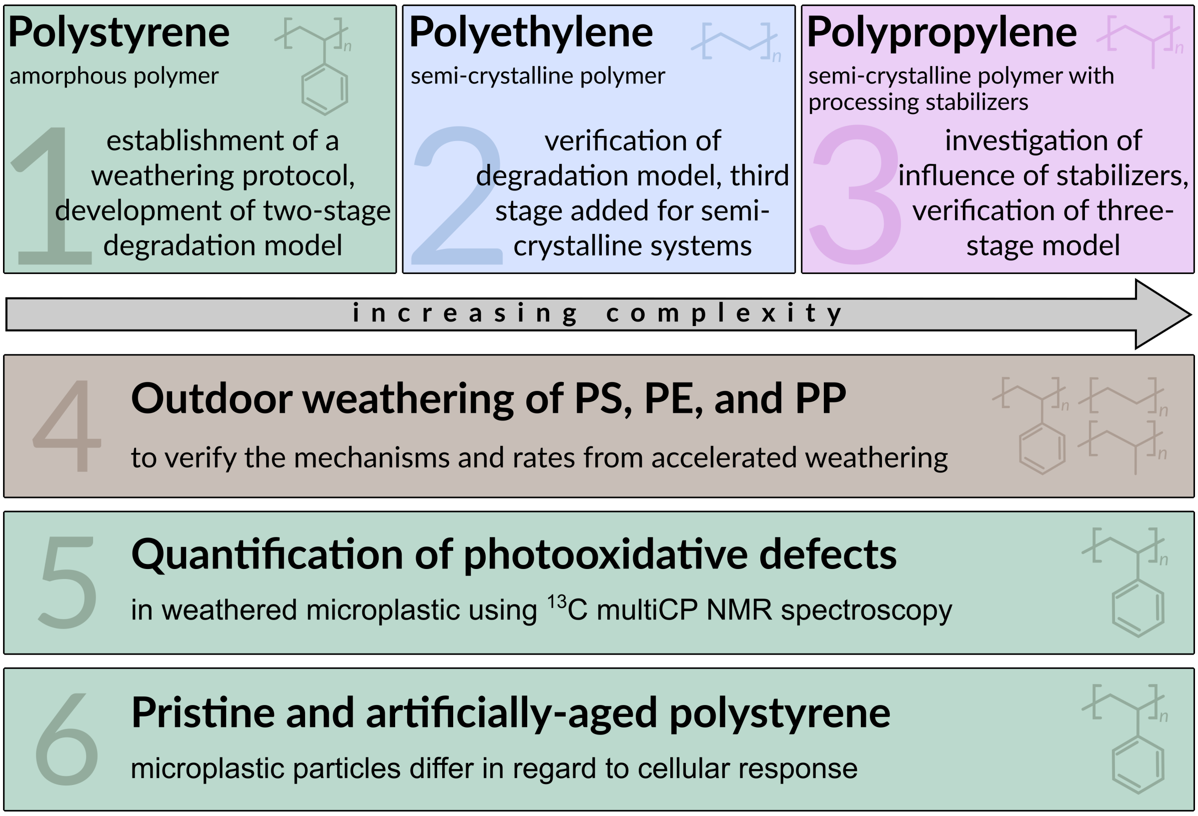

Figure 14: Overview of the thesis. Paper 1: development of a weathering protocol and two-stage degradation model for PS. Paper 2: transfer of conclusions to semi-crystalline LDPE. Paper 3: investigation of semi-crystalline PP containing a processing stabilizer. Paper 4: exposure of PS, LDPE, and PP to natural, outdoor weathering to verify the mechanisms and rates from accelerated weathering. Paper 5: development of a quantification method for photooxidative defects using ^{13}C multiCP NMR spectroscopy. Paper 6: Pristine and artificially-aged PS MP particles differ in regard to their cellular response.

7.1 Polystyrene - an amorphous polymer system

The first part of the thesis is based on polystyrene, an amorphous polymer with no additives besides 600 ppm zinc stearate, representing a very basic and simple system (chapter 8.1). For long-term accelerated weathering, a commercially-available PS (PS 158 N) delivered from INEOS Styrolution Group (Frankfurt am Main, Germany) was purchased. With the first experiment, we aimed at establishing the weathering protocol, analytical procedures, and a degradation model for amorphous polymer systems.
Tensile bars and particles were prepared from PS 158 N and placed into the weathering chambers located at the departments Polymer Egineering (DPE) and MCI at the University of Bayreuth. Samples were drawn at the above previously time intervals and characterized individually. Results from both geometries were compared in order to investigate the influence of geometry on the degradation mechanisms and time scales, as well as to link the degradation rates of both, macroscopic tensile bars and microscopic particles.

Particle degradation in previously published literature is based merely on estimations, and numeric data for secondary particle production is rarely studied[2;11]. To investigate particle degradation in our studies, the particle size evolution was measured with increasing exposure time. For this a Microtrac FlowSync Particle Size Analyzer (Microtrac Retsch GmbH, Haan, Germany) was used. This instrument works with laser diffraction (3 lasers and 2 detectors) coupled with dynamic image analysis, thus delivers two-dimensional (2D)-images of the particle sample, and various numerical values obtained from the measured size distribution. In the particle size development, two trends can be observed: during the first 600 h of exposure, the particle size decreases linearly. From 600 h onward, it evolves in an exponential manner. To determine changes in the surface morphology, optical microscopy as well as scanning electron microscopy (SEM) were executed for chosen samples. Within the first 400 h, the particle SEM images show that particle surfaces seem to become smoother and rounded off. We attribute this effect to degradation being a surface effect within the first weathering stage. Photooxidation initiated by simulated UV irradiation along with soft mechanical impact from stirring result in a modification of the particle surface. We classified these observations as the first weathering stage for particles, namely surface abrasion (figure 15).

Polymer degradation is typically accompanied by a decrease in MW. Photooxidation propagation step IV (reaction 5) involves β-cleavage, where breaking up of C-C bonds leads to fission of the backbone, and thus a reduction of the MW. These reactions can also be retraced via gel-permeation chromatography (GPC)-measurements, where MWs, and MWDs can be determined. For PS tensile bars and particles, the MW decreases with increasing weathering, the initially long, linear polymer chains are cleaved, resulting in shorter chains. Crosslinking reactions are common, as described in section 3.3.1, and indicated with red dots in figure 15.
The MW reduction of the particles seems to proceed slower than the MW-reduction of tensile bars. To explain this, it is important to consider the effect of mechanical

impact. The macroscopic tensile bars do not experience any mechanical influence, but continuous simulated solar radiation and intervals of simulated rain (18 min of spray within 120 min of irradiation), which is not comparable to stirring (e.g., particle-particle, particle-beaker, and particle-stirring device collisions). While the bars are thoroughly irradiated from one side (which is ultimately sampled and analyzed), the particles experience irradiation, surface degradation, and mechanical stress. With on-going exposure, the weathered surface material becomes increasingly brittle, develops a crack-pattern, and is ultimately abraded by mechanical impact. This is a continuing process, where surface material is constantly degraded and abraded, exposing non-weathered material from the bulk. As the particle size decreases, this effect is accelerated, which is represented by the exponential trend in particle size decrease. We interpret this turnover in the particle degradation mechanisms (surface to bulk), as the second stage of particle degradation (figure 15).

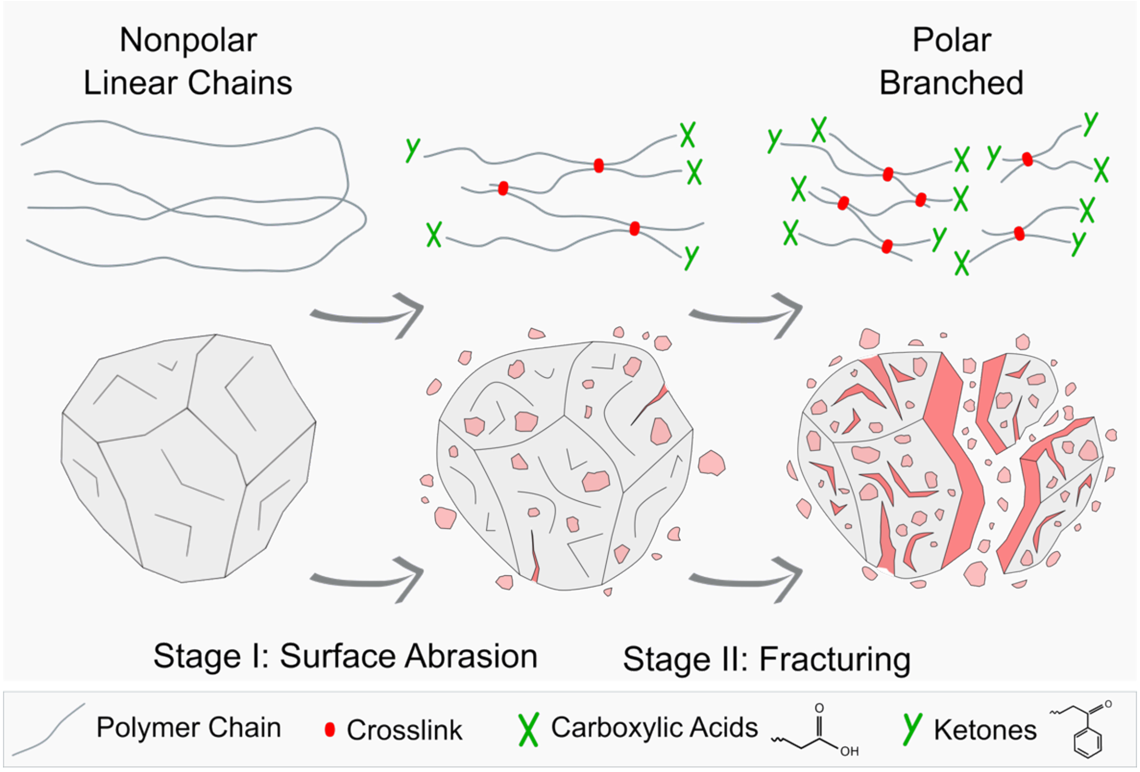

Figure 15: Two-stage degradation model for amorphous PS MP particles exposed to the environmental stress factors solar radiation and mechanical stress[13].

Photooxidation does not only lead to a reduction in MW, but also to the incorporation of O_2 from the formation of oxygen-containing functional groups (chapter 3.3.1, e.g., carboxylic acids, figure 15). To further investigate the alteration from weathering as a function of the sample depth with exposure time, scanning electron microscopy

and energy-dispersive X-ray spectroscopy (SEM-EDX) measurements were performed, revealing the O/C-ratio from the surface down to 100 µm. The results support the modification of the chemical composition, and the accumulation of oxygen-bearing functional groups. At 2000 h, the O/C ratio has increased from 0.005 to 0.15 at a depth of 30 µm. This highly weathered and oxidized area is further referred to as the photooxidative zone *d*.
Stage II is dominated by particle fracturing. From the progression of the photooxidative zone into deeper layers, embrittlement is provoked. Whole particles break up as mechanical forces continue to trigger collision. As a consequence, large numbers of SMP particles are formed ranging down to sizes < 1 µm. From the average particle size determined analytically, the secondary particle production could be calculated. For PS, we were able to calculate that from one mother particle, approximately 500 SMP particles are released during our experimental runtime (calculation in chapter 8.1). These SMP particles are thoroughly oxidized and polar, their polymer chains are short and highly branched (figure 15).

As described in detail within section 3.3.1, photo-initiated degradation, as we perform in our weathering setup, leads to radical formation, and subsequent reactions with ambient O_2. Our observations from SEM-EDX measurements and the development of the photooxidative zone *d* thus correlate well to the literature. Qualitative and semi-quantitative investigations of oxygen-containing functional groups are typically performed using Fourier-transform infrared spectroscopy (FT-IR). To provide a complementary method for the quantification of polymer defects, we developed a new method to investigate and quantify functional groups via solid-state ^{13}C multiCP NMR spectroscopy. Details of this method have also been published in an analytical paper, which is presented in section 7.5.

7.2 Low-density polyethylene - a semi-crystalline polymer system

The second part of the thesis focuses on a slightly more complex system, a semi-crystalline LDPE (Lupolen 1800p) from LyondellBasell Industries (chapter 8.2). With the results from our first study, we expressed the assumption, that our two-stage degradation model is valid for predicting the abiotic degradation and mechanisms of other commodity polymers with a C-C backbone[13]. We used the semi-crystalline LDPE system to verify that the assumptions made also apply for polymers with increased complexity. The experimental framework of LDPE weathering remains the same as previously described for PS. This further ensures a confirmation of our weathering protocol and the transferability to other polymers. The increase in complexity required the expansion of analytical techniques by additionally including measurements regarding the evolution of crystallinity upon weathering.

In general, particle degradation proceeds in a similar manner, compared to PS. Within stage I, both particle size measurements and SEM images reveal the same observations:

a linear decrease in particle size accompanied by a smoothening and rounding of the surfaces. Stage I, namely surface abrasion, is comparable to amorphous PS. Simultaneously, the molecular weight decreases, indicating chain-scission via β-cleavage, as previously described (chapter 3.3.1). Profound differences however, lie within the semi-crystalline character and the low glass-transition temperature (T_g) of LDPE[7;9].

Crystallinity

Semi-crystalline polymers consist in chains being amorphous (disordered), as well as crystalline (ordered). Figures 16 and 17 graphically display the evolution of LDPE polymer chains upon weathering. Degradation affects the amorphous and crystalline domains differently, the amorphous chains are much more prone to degradation than the crystalline. Thus, the amorphous chains are continuously cleaved, leading to further formation of functional chain end-groups (green dots).

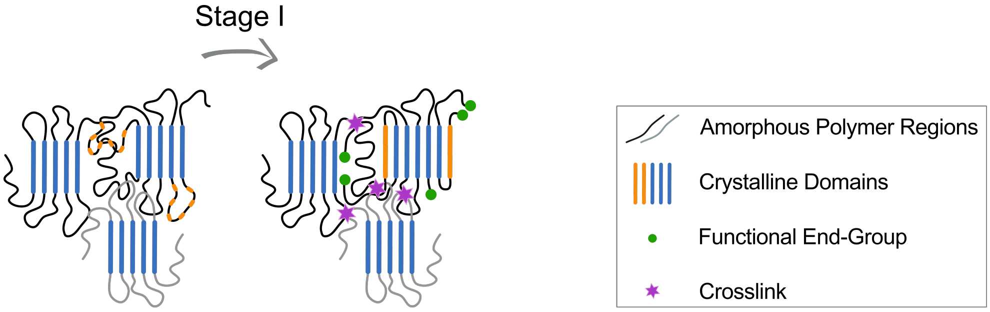

Figure 16: LDPE on the molecular chain level, made of amorphous as well as crystalline domains. Within stage I of degradation, amorphous domains are preferentially degraded, leading to chain-scission and the formation of functional end-groups (green dots). Crosslinking may occur (purple stars). Molecular rearrangement leads to the formation of new crystalline domains (orange).

Meanwhile, crosslinking may occur (purple stars) leading to a slight increase in MW, but since chain-scission happens at a faster rate than crosslinking, the overall MW decreases. Cleaved chains will reorganize in an ordered manner, forming crystalline domains, indicated with blue (original) and orange (reorganized) bars in figure 16.

In order to track the changes in crystallinity, DSC measurements were performed. With increasing weathering, the degree of crystallinity increases with a linear trend from 40 % to 70 %. This observation was verified via solid-state NMR spectroscopy, where very similar values were observed.

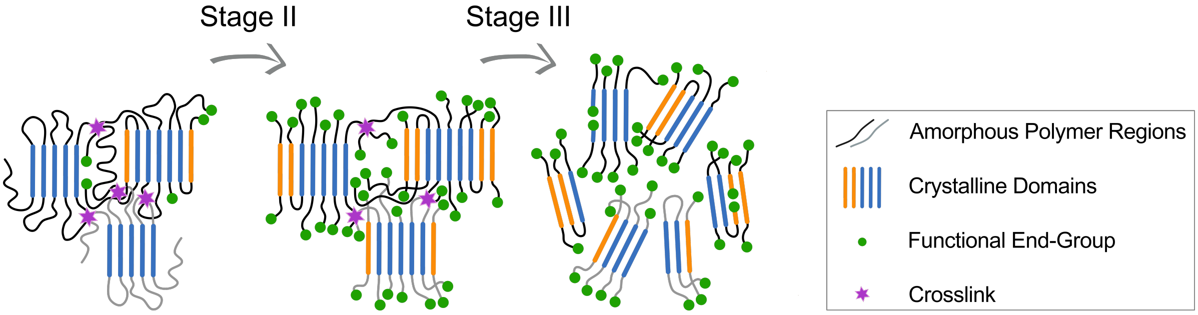

Figure 17: As weathering proceeds (stage II), the degradation of amorphous domains is continued. Further functional chain end-groups are accumulating, and crystalline domains are formed at the expense of amorphous regions. In the final stage III of degradation, crystallites are also affected from photooxidation, leading to disintegration.

To get insights into the size of the crystalline domains and their evolution, XRD-measurements were performed. Within the first stages of weathering, the size of the crystalline domains increases from 13 to 20 nm (stage I-II), then reaches a plateau. With on-going weathering (stage II), the process of chain-scission and molecular chain reorganization is intensified (figure 17). In the final stage III, the crystalline domain size, determined from XRD, decreases again, indicating that these domains are also affected by degradation. This final, third stage of weathering, observed for semi-crystalline LDPE, is new compared to amorphous PS, where we identified only two-stages of degradation (figure 15).

Glass-transition temperature T_g

Another difference of LDPE to PS is the T_g, which is defined as the temperature, at which the polymer chains start to exhibit macromolecular mobility within the molecular structure. For PS, $T_g = \sim 100$ °C[14], which displays a temperature well above the experimental temperature (55 °C). For LDPE however, the T_g is below 0 °C[7;9], meaning the polymer chains are very flexible, and may easily rearrange at our experimental temperature.

This fact supports the observations made for fragmentation of particles. We do not observe crack-formation and propagation, as we did for PS. Crack-patterns are also absent within the bar surfaces at that point of weathering, where the tensile strength already indicates embrittlement. Our explanation for this are surface healing effects, which are possible due to the chain mobility LDPE has at our experimental temperature. Crack-formation is compensated up to a certain point, where the amorphous domains are sufficiently depleted, resulting in a decrease of tie-molecules and entanglement. From this point on, a direct disintegration of the particles sets in, leading to formation of smaller SMP particles (figure 18).

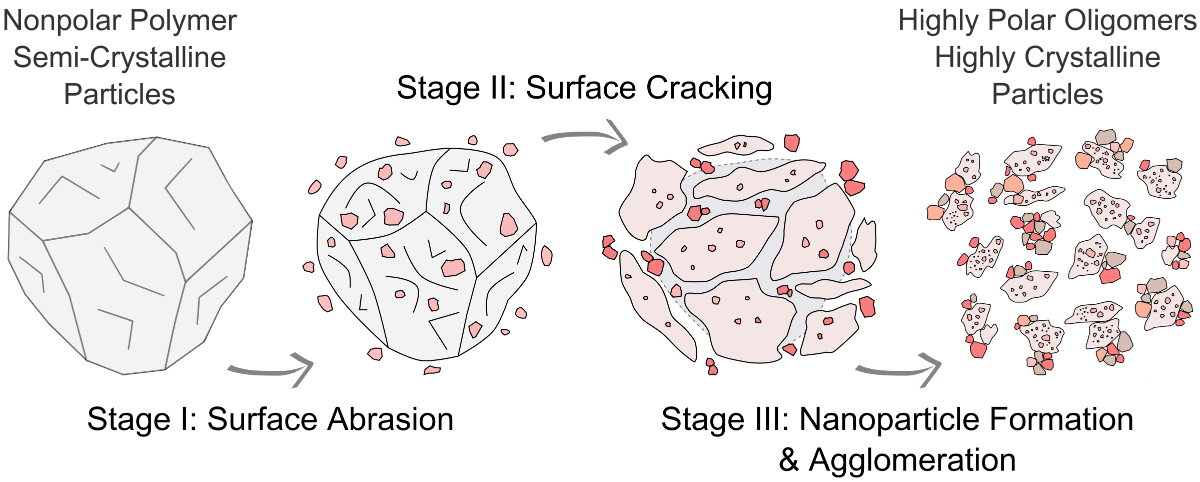

Figure 18: Degradation of LDPE on the particle level. Stage I: surface abrasion, stage II is dominated by surface cracking, where bigger flakes are directly taken off, and no cracks are observed within particles, but direct disintegration. Stage III represents the intensification, fragmentation continues, leading to the formation of nanoparticles. Their small size and high surface-to-volume-ratio leads to agglomeration.

This is also very evident within the particle size analysis. The transition from linear to exponential, so the transition from stage I to stage II, correlates well with the observations made for PS. The exponential trend, however, shows a much faster time constant $\tau_{\,LDPE}$ being 537 h, and $\tau_{\,PS}$ 930 h. LDPE particles thus disintegrate more rapidly than PS particles do, ultimately resulting in a far lower average particle size after 3200 h of weathering ($\oslash$ $\text{PS}_{3200\ h} = 20$ µm; $\oslash$ $\text{LDPE}_{3200\ h} = 8$ µm). The final stage III observed for LDPE is new, and has not been observed for PS. This stage is dominated by further fragmentation and the formation of many small, nanometer (nm)-sized particles. While they are not resolved within the numerical particle size analysis, due to agglomeration effects (figure 18), they are clearly visible in SEM images. This third stage is also evident in the crystallinity measurements, where it is dominated by disintegration of crystalline domains. We assume, that in stage III, the NP are highly crystalline, polar, short-chained oligomers with a high proportion of oxygen-bearing functional groups. The data obtained from DSC, NMR, and XRD measurements correlate well.

Using the same approach as for PS, we were able to calculate the fragmentation rate of LPDE. Within 3200 h of weathering, one mother particle (190 µm) releases 14,000 SMP particles in total. This rate largely exceeds the rate calculated for PS (500 SMP particles), and highlights the fact, that fragmentation is largely dependent on the polymer and its material characteristics. Our particle model, developed for amorphous polymers, is adaptable for semi-crystalline polymers, however, a third stage needed to be added, considering that crystallinity strongly influences the fragmentation behavior.

7.3 Polypropylene - a semi-crystalline polymer system containing stabilizers

For the third part of the thesis, the polymer system PP (Moplen HP 526J, Lyondell-Basell) was chosen (chapter 8.3). This PP grade remains with having semi-crystalline character, yet adds another component of complexity to the analytical investigations. As indicated by the manufacturer[10], standard processing stabilizers are added. Thus, the third experiment was performed with a semi-crystalline, additivated polymer system. Weathering was executed in the same manner as previously reported, with a special focus on the influence of the stabilizers present. The degradation behavior was correlated to the exposure time. Within this study, exclusively particles were investigated.

To elucidate the effect of stabilizers on the degradation of PP, we performed a Soxhlet extraction with tetrahydrofuran (THF) at 80 °C for 14 days. This PP fraction, supposedly without stabilizer, was subsequently also exposed to simulated solar radiation using the known protocol. Since the actual stabilizers included within PP HP 526J are not given, we performed further purification steps with the THF residue after Soxhlet extraction. Via column chromatography, multiple fractions were recovered and further analyzed with matrix-assisted laser desorption ionization time-of-flight mass spectrometry (MALDI-TOF) and liquid-state ^{1}H NMR spectroscopy.

PP particles with and without stabilizer

All samples taken from the experiments with and without stabilizer, were analyzed in the same way as previously reported. Particle size analysis, molecular weight distributions, development of crystallinity, as well as the proportions of functional groups accumulating were determined as a function of exposure time.

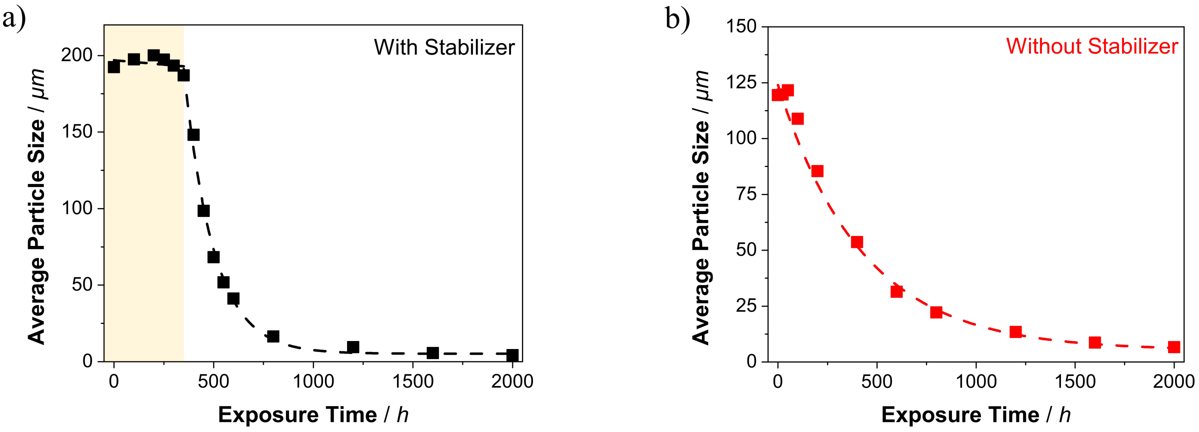

Figure 19: Average particle size as a function of exposure time a) for PP with stabilizer, and b) for PP without stabilizer.

For PP with stabilizer, no changes are observed within the first 350 h of weathering. This applies for the average particle size (figure 19), degree of crystallinity, melting temperature (T_m), and MWD. PP without stabilizer, however, shows rapid changes in all of these values from 50 h on. This first stage of seeming stability highlights the influence of the stabilizers on polymer degradation.

Identification of the stabilizers

The stabilizer composition is not given in detail by the manufacturer. The THF-residue, recovered after Soxhlet extraction, was purified and then analyzed via MALDI-TOF MS, liquid-state ^{31}P, and ^{1}H NMR spectroscopy. Two stabilizers could be identified.

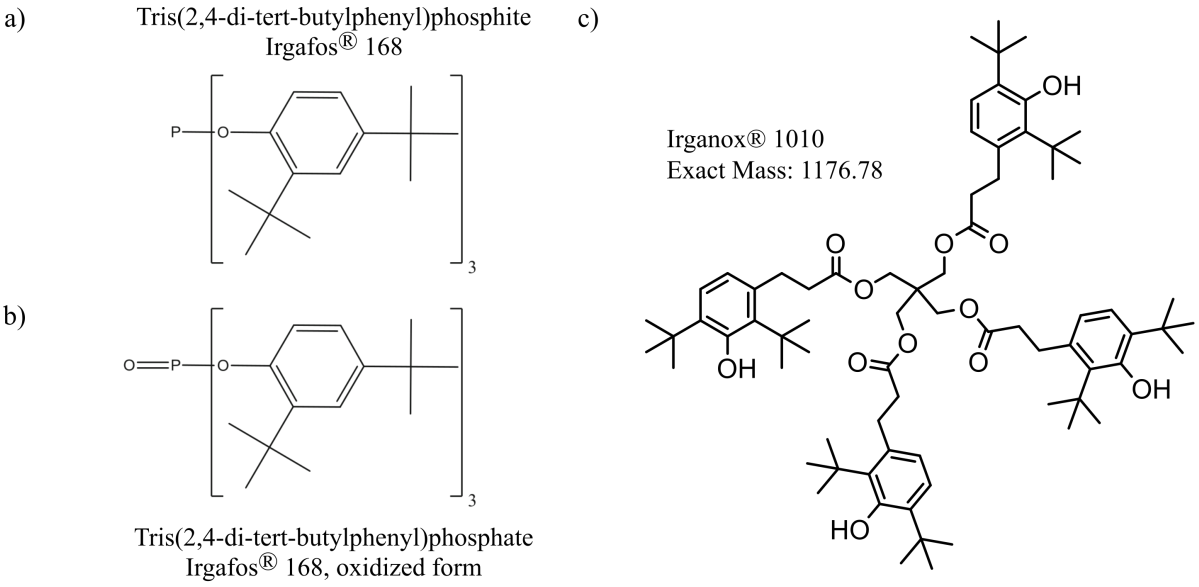

Figure 20: Chemical structures of a) Irgafos® 168, b) its oxidized form, and c) Irganox® 1010.

The MS spectra obtained from MALDI-TOF measurements could be precisely assigned to Irgafos® 168 (tris(2,4-di-tert-butylphenyl)phosphite, figure 20a). The dominant peaks however, correspond to the oxidized species (tris(2,4-di-tert-butylphenyl)phosphate, figure 20b), as given in the literature[5;16]. The observations could be supported with ^{31}P NMR spectroscopy. The second stabilizer could be assigned to Irganox® 1010. We could not identify oxidation products or the initial molecule (1176 g/mol, figure 20c), but only low molecular weight fragments (< 800 g/mol). Here too, the presence of Irganox® 1010 could be verified via liquid-state ^{1}H NMR spectroscopy.

Irgafos® 168 and Irganox® 1010 are primary and secondary antioxidants, thus they hinder oxidation of the polymer, which may be induced during processing. Although they are no UV-stabilizing agents, they still deactivate peroxy radicals and hydroperoxides, which are also formed during the initiation step of photooxidation.

The PP grade chosen for this study contains stabilizers, complicating degradation by a further parameter. Nevertheless, we found a possibility to **1)** extract and **2)** identify the stabilizers, **3)** directly compare stabilized and non-stabilized PP, and **4)** draw conclusions on the effect of the stabilizers on degradation.

Our semi-crystalline particle model, developed for LDPE, is also adaptable to PP. The additional stage III is observed here too, however stage I happens so much faster, it is hardly visible within the data trends. We attribute the rapid onset of degradation to the polymer structure of PP. Every second carbon in the chain is a tertiary C-atom, leaving the single H-atoms very prone to abstraction. Stable radicals, and subsequently peroxides and alcohols are formed[6]. Using our quantitative multiCP solid-state NMR approach, we were able to identify and quantify these compounds, where elevated values of peroxides and alcohols were noted, supporting our theory.

For PP, the mechanisms of degradation are the same as for LDPE, however the rates differ. Despite the distinct differences within the first 400 h of weathering, comparing stabilized and non-stabilized particles, the long-term degradation proceeds with similar, exponential trends. After 3200 h the data for particle size, molecular weight, crystallinity, and also the proportion of chemical groups forming are within the same range. The stabilizer thus only effects the first two stages of weathering.

Fragmentation however, is more pronounced for PP, than what was observed for LDPE. The final sample drawn has an average particle size of 4 µm, largely differing from the size of the starting material ($\sim$ 190 µm). For PP, we were able to calculate, that a total number of 100,000 SMP particles were formed as a result of fragmentation. This number is higher by one order of magnitude compared to LDPE. Additionally, nanometer-sized particles are also resolved within SEM images, where NP adhere to the surface of larger particles. Stage III of NP formation and agglomeration is thus the same as previously determined for LDPE.

Comparing all three studies, we verified our degradation model, which was first established for amorphous PS, and then adapted to semi-crystalline polymers (LDPE and PP). We conclude, that fragmentation and the formation of SMP particles largely depends on the polymer type and its properties. Fragmentation was smallest for PS, and highest for PP, where not only the semi-crystalline character, but also the polymer structure plays an important role.

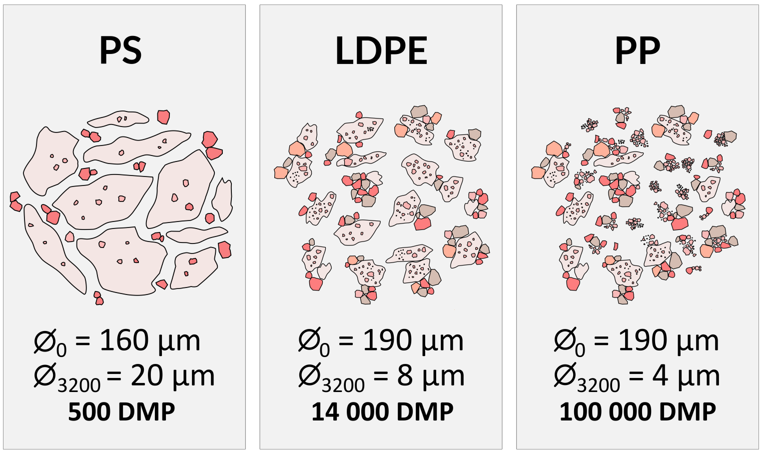

Figure 21: Fragmentation leads to formation of large amounts of SMP particles. Average particle sizes of the reference material (0 h), and particles after 3200 h as well as particle production for PS, LDPE, and PP.

Besides the formation of large amounts of SMP particles, we were able to additionally trace the formation of NP particles. These however, are not present as free particles, as they agglomerate due to their high surface-to-volume ratio, and surface charge. Our experimental conclusions support the observations made within environmental samples, were free secondary NP particles are challenging to observe and detect[3;17].

7.4 Outdoor weathering of PS, LDPE, and PP to verify the mechanisms and rates from accelerated weathering

Within the fourth part of the thesis, all three polymer systems previously described (PS, LDPE, PP) where exposed to natural weathering outside on a rooftop at the University of Bayreuth (chapter 8.4). The weathering parameters correspond to the natural outdoor conditions in Bayreuth, and were recorded using the data from the weather station of the Botanical Garden at the University of Bayreuth, which is located within ∽ 500 meters from our experiments. This outdoor degradation procedure was run over a total test duration of 1.5 years, supposedly corresponding to 2400 h of accelerated weathering in our laboratory setup.

The general aim of this study was to verify, that despite the elevated irradiance and temperature conditions of our weathering chamber, the mechanisms remain the same as they will be in an outdoor setting. Outdoors, natural sunlight and its varying intensity, along with temperature fluctuations of day, night, weather, and seasons will decelerated the degradation process. Comparison of the data obtained from both experiments, enables us to check the applicability of our conclusions and the developed models for the environmental degradation of PS, LDPE, and PP.

All three polymer systems degrade upon exposure to outdoor weathering, revealing trends that are very similar to those observed from accelerated weathering. Exemplarily, figure 22 a) displays the average particle size of PS as a function of exposure time in days/months. First, the trend evolves as a linear decrease, then shifts to an exponential decay. The molecular weight number-average molecular weight, in g/mol or kg/mol (M_n) in figure 22 b) decreases continuously, starting with the first month of exposure. The only plateau in the trend resembles the winter months with short days and low UV-activity. After 1.5 years the M_n has reached a value of 14,700 g/mol, which is almost identical to accelerated weathering (14,800 g/mol after 2000 h).

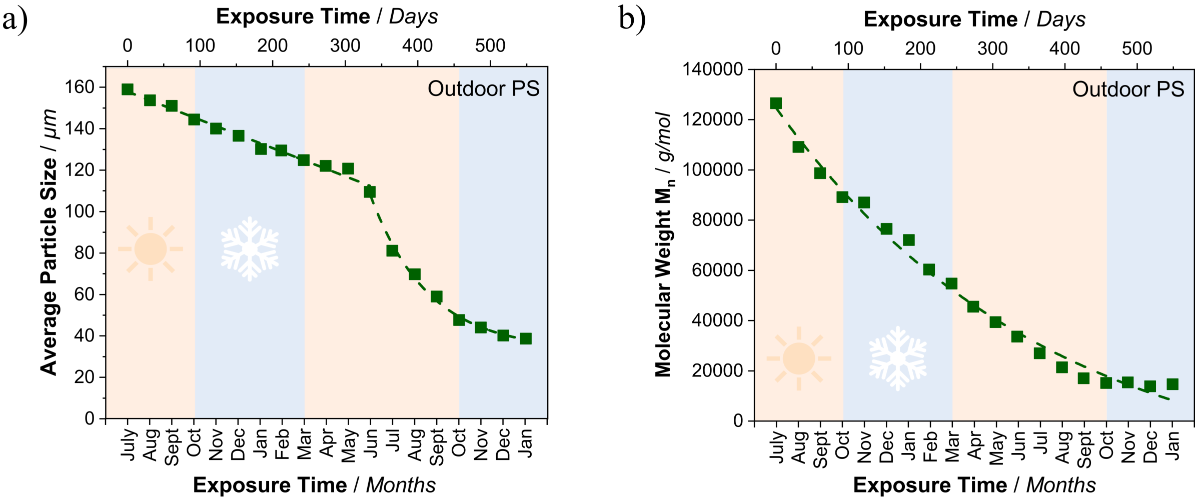

Figure 22: Average particle size as a function of exposure time a), and molecular weight M_n in b) for PS particles exposed to outdoor weathering for 1.5 years (July 2020-January 2022).

Similar conclusions can be drawn when comparing the semi-crystalline polymers LDPE and PP. The trends of the particle size, molecular weight, and the thermal characteristics correlate nicely. Further, the influence of the stabilizers present in PP are also evident. Solid-state ^{13}C NMR measurements were also performed on chosen samples of all three experiments. The spectra verify that the main defects forming from degradation are peroxides, ketones, carboxylic acids, vinylidenes, and alcohols.

The trends and mechanisms obtained from outdoor degradation are largely comparable to those from accelerated-laboratory weathering. While the mechanical characteristics, trends, and the chemical evolution is very similar between both settings, the time scales show some deviations. This can largely be traced back to a) lower temperatures, specifically affecting LDPE and PP, b) fluctuations in irradiance, and c) seasonal fluctuations in temperature, irradiance, and the sunshine duration between the summer and the winter months.

7.5 Quantification of photooxidative defects in weathered MP using ^{13}C multiCP NMR spectroscopy

Conventional approaches for the identification of polymer defects developing upon degradation are FT-IR or attenuated total reflectance (ATR) FT-IR, and Raman spectroscopy. Both are very sensitive methods, nevertheless, they are surface-dependent, and FT-IR is also influenced by fluorescence[4]. While the carbonyl index typically derived from FT-IR delivers semi-quantitative values, a lack of standardization leaves the comparability between multiple studies questionable[1].

Using multiCP (cross-polarization) as a calibration method for quantitative solid-state ^{13}C NMR spectroscopy, is a method previously introduced by Johnson and Schmidt-Rohr[8]. This method was also applied for the quantification of polymer defects within our previous studies on PS, LDPE, and PP, however weak signals and long measuring times hindered a thorough quality assessment. Using PS as polymer system, the multiCP approach was optimized and adapted (chapter 8.5). For this, PS was synthesized and ^{13}C-enriched by 23 % at the α-position. The ^{13}C-enriched PS was also exposed to accelerated laboratory weathering and subsequently analyzed at different exposure times for the formation of polymer defects (e.g., peroxides, carboxylic acids, ketones, alcohols).

The ^{13}C-enrichment allowed for a markedly higher sensitivity along with a measurement time reduction by a factor of ~ 400[12]. In figure 23, a ^{13}C CP MAS NMR spectrum of PS with ^{13}C in natural abundance (red) is plotted along with a spectrum of PS, ^{13}C-enriched by 23 %. Both samples were exposed to simulated solar radiation for 2400 h. The three significant PS peaks, which can also be seen in the reference PS spectrum (inset figure 23), are assigned to the aliphatic backbone (I, II at 35 to 50 ppm), the aromatic ipso carbon (III at 145 ppm), and the aromatic CH units (IV, V, VI at 128 ppm) of the phenyl rings.

This study enabled to investigate the influence of essential parameters in order to find the ideal conditions for samples with ^{13}C in natural abundance. Although PS is the system which was investigated here, most photooxidative defects arising will originate at the α-position. The experimental parameters are thus transferable to other polymer systems.

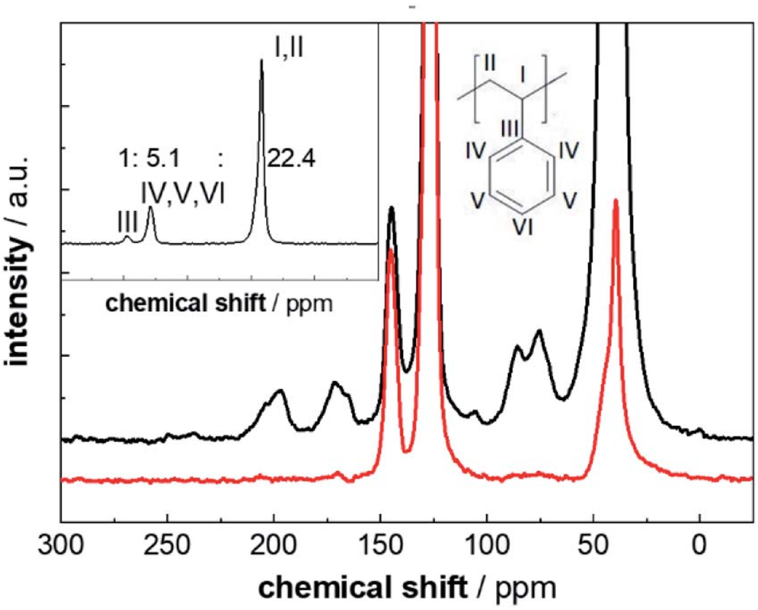

Figure 23: Comparison of ^{13}C CP MAS NMR spectra of PS enriched by 23 % at the α-position (black), and PS in natural abundance (red) of the particle samples weathered for 2400 h. Inset: ^{13}C multiCP MAS spectrum of pristine ^{13}C-enriched PS[12].

In this publication I performed weathering of the PS reference particles, with ^{13}C in natural abundance, as well as PS enriched in ^{13}C, both for different exposure times. Anika Mauel and Björn Pötzschner performed NMR measurements, and optimized the method. Renée Siegel supported the NMR measurements.

7.6 Case study: Comparison of pristine and artificially weathered PS MP in regard to their cellular response

The final part of this thesis addresses a topic previously mentioned within the challenges in section 4 (chapter 8.6). Various experimental studies regarding potential toxic effects of MP particles are performed using pristine, non-weathered materials[20;15;19], which do not reflect realistic samples of environmental relevance. Thus, in our final study, we investigated the influence of weathered versus non-weathered PS micro particles on murine macrophages.

For the experiment, 2 µm PS micro beads (Polyscience Europe GmbH, Eppenheim, Germany) were exposed to our standard weathering protocol for 200, 400, and 600 h, corresponding to 43, 86, and 130 days of natural weathering. Since the chemical changes introduced upon weathering were thoroughly studied for PS in our previous study (chapter 7.1), the focus was put on the surface characteristics (ζ-potential, size distribution, and SEM imaging), and on investigating the effects of weathering on a biological level. For this purpose, the cellular responses of the murine liver macrophage cell line

Immortalized mouse Kupffer cells (ImKC) were investigated at the level of metabolic activity, the membrane integrity, reactive oxygen species formation, genotoxicity, and inflammatory response.

Physically, the aged PS beads showed a exposure time-dependent decrease in particle size along with a decrease in the ζ-potential. On a biological level, both types of particles are similarly taken up by the cells. Nevertheless, the pristine and shortly aged particles ($PS_{pristine}$-PS_{43}) showed a higher pro-inflammatory response, while the long-time weathered particles (PS_{130}) revealed increased cytotoxic effects on the cells. In addition to changes within the composition of the particles (e.g., the accumulation of oxygen-containing functional groups), the shape of the particles also changed. Sharp edges, which are formed from fragmentation after 130 d, can also damage the plasma membrane of the cells. This leads to an increased release of the intracellular enzyme lactate dehydrogenase (LDH), which could be detected for the sample exposed for 130 d.

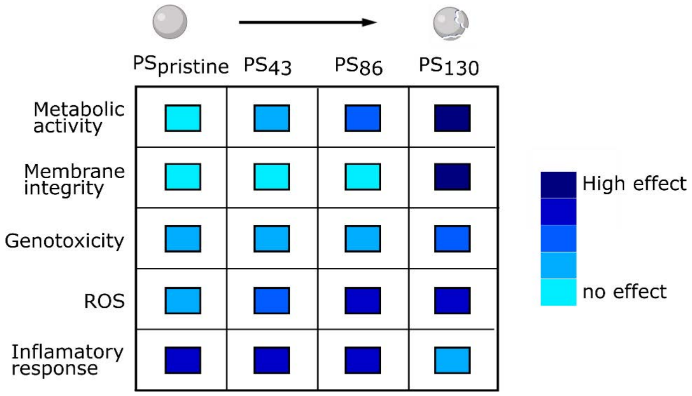

Figure 24: Overview of the biological/noxious effects of $PS_{pristine}$ versus $PS_{weathered}$ for 43, 86 or 130 days[18].

In summary, both particles (pristine and weathered) showed interaction with ImKC cells, however the interactions differ in terms of their cytotoxic potential. While the $PS_{pristine}$ particles show no effect regarding the metabolic activity, they bear a higher inflammatory potential (figure 24). The weathered particles however, show increased cytotoxic effects, while bearing a lower inflammatory potential. We assume, that the shape (e.g., rough edges) plays a major role in regard to the noxiousness. Considering that MP in the environment mostly consist in SMP, which have formed from fragmentation of larger plastic debris, sharp edges are very common.

Our results reveal the distinct differences between weathered and non-weathered PS particles on the cellular response, highlighting the necessity to focus on the effects of realistic samples, bearing those physicochemical characteristics of MP in the environment.

Within this publication, I performed weathering of PS beads for different exposure times. Julia Jasinski provided particle characterization and confocal microscopy. Alfons Weig analyzed the RNA sequencing data. Matthias Völkl, Alfons Weig, and Valérie Jérôme analyzed the data and created the figures.

Within this thesis, we first thoroughly investigated the simulated environmental degradation of the polymer systems PS, LDPE, and PP. We established degradation models for the fragmentation of macro- and microplastic into SMP particles, and traced the formation of NP. With each study, we increased the complexity, and verified our conclusions previously drawn. For PS, LDPE, and PP the general degradation mechanisms are very similar, however fragmentation is largely material-dependent. The formation of SMP particles was numerically determined for all three polymer systems, revealing that the fragmentation rates (Fr) differ according to: $\mathrm{Fr}_{PS} < \mathrm{Fr}_{LDPE} < \mathrm{Fr}_{PP}$.

We further performed outdoor weathering experiments, using the same polymer systems, to verify that accelerated weathering is a suitable tool to investigate polymer degradation in a reasonable time scale. Additionally, we established a new method to quantify the defect proportions arising upon degradation. For this, quantitative multiCP solid-state ^{13}C NMR spectroscopy is used. Lastly, we investigated the cytotoxic potential for PS beads weathered according to our protocol. Comparing weathered and non-weathered PS samples, both show cellular responses, however the aged particles bear a higher cytotoxic potential on murine macrophages than the pristine particles do.

References

[1] J. Almond, P. Sugumaar, M. N. Wenzel, G. Hill, and C. Wallis. Determination of the carbonyl index of polyethylene and polypropylene using specified area under band methodology with atr-ftir spectroscopy. *e-Polymers*, 20(1):369–381, 2020.

[2] M. P. Born and C. Brüll. From model to nature - a review on the transferability of marine (micro-) plastic fragmentation studies. *Science of the Total Environment*, 811:151389, 2022. doi: 10.1016/j.scitotenv.2021.151389.

[3] H. Cai, E. G. Xu, F. Du, R. Li, J. Liu, and H. Shi. Analysis of environmental nanoplastics: Progress and challenges. *Chemical Engineering Journal*, 410:128208, 2021.

[4] S. F. Chabira, M. Sebaa, and C. G'sell. Oxidation and crosslinking processes during thermal aging of low–density polyethylene films. *Journal of Applied Polymer Science*, 124(6):5200–5208, 2012.

[5] K. Fouyer, O. Lavastre, and D. Rondeau. Direct monitoring of the role played by a stabilizer in a solid sample of polymer using direct analysis in real time mass spectrometry: the case of Irgafos 168 in polyethylene. *Analytical Chemistry*, 84 (20):8642–8649, 2012.

[6] G. Grause, M.-F. Chien, and C. Inoue. Changes during the weathering of polyolefins. *Polymer Degradation and Stability*, page 109364, 2020.

[7] J. Han, R. H. Gee, and R. H. Boyd. Glass transition temperatures of polymers from molecular dynamics simulations. *Macromolecules*, 27(26):7781–7784, 1994.

[8] R. L. Johnson and K. Schmidt-Rohr. Quantitative solid-state ^{13}C NMR with signal enhancement by multiple cross polarization. *Journal of Magnetic Resonance*, 239: 44–49, 2014.

[9] M. D. Lechner, E. H. Nordmeier, B. J. Schmitt, K.-H. Hahn, C. Lennartz, and R. Heering. Das Makromolekül als Festkörper und als Schmelze. In *Makromolekulare Chemie*, pages 429–641. Springer, 2014.

[10] LyondellBasell. Technical Data Sheet Lupolen 1800P: Low Density Polyethylene, 2021. URL `https://productsafety.lyondellbasell.com/DirectRequest?ResponseTypeGuid=f1e32c20-d810-4db0-b25e-8e23a59f3733&ProductGuid=28be098e-bb34-4bb8-a683-894ea1c1751e`.

[11] K. Mattsson, F. Björkroth, T. Karlsson, and M. Hassellöv. Nanofragmentation of expanded polystyrene under simulated environmental weathering (thermooxidative degradation and hydrodynamic turbulence). *Frontiers in Marine Science*, 7:1252, 2021.

[12] A. Mauel, B. Pötzschner, N. Meides, R. Siegel, P. Strohriegl, and J. Senker. Quantification of photooxidative defects in weathered microplastics using ^{13}C multiCP NMR spectroscopy. *RSC advances*, 12(18):10875–10885, 2022.

[13] N. Meides, T. Menzel, B. Poetzschner, M. G. J. Löder, U. Mansfeld, P. Strohriegl, V. Altstaedt, and J. Senker. Reconstructing the environmental degradation of polystyrene by accelerated weathering. *Environmental Science & Technology 55*, (12):7930–7938, 2021. URL `10.1021/acs.est.0c07718`.

[14] J. Rieger. The glass transition temperature of polystyrene: results of a round robin test. *Journal of Thermal Analysis and Calorimetry*, 46(3-4):965–972, 1996.

[15] U. Rozman and G. Kalčíková. Seeking for a perfect (non-spherical) microplastic particle–the most comprehensive review on microplastic laboratory research. *Journal of Hazardous Materials*, 424:127529, 2022.

[16] C. Schwarzinger, S. Gabriel, S. Beißmann, and W. Buchberger. Quantitative Analysis of Polymer Additives with MALDI-TOF MS Using an Internal Standard Approach. *Journal of the American Society for Mass Spectrometry*, 23(6):1120–1125, 2012. doi: 10.1007/s13361-012-0367-1.

[17] A. Ter Halle and J. F. Ghiglione. Nanoplastics: A complex, polluting terra incognita. *Environmental Science & Technology*, 55(21):14466–14469, 2021.

[18] M. Völkl, V. Jérôme, A. Weig, J. Jasinski, N. Meides, P. Strohriegl, T. Scheibel, and R. Freitag. Pristine and artificially-aged polystyrene microplastic particles differ in regard to cellular response. *Journal of Hazardous Materials*, 435:128955, 2022.

[19] J. S. Weis and K. H. Palmquist. Reality check: experimental studies on microplastics lack realism. *Applied Sciences*, 11(18):8529, 2021.

[20] K. Zhang, A. H. Hamidian, A. Tubić, Y. Zhang, J. K. H. Fang, C. Wu, and P. K. S. Lam. Understanding plastic degradation and microplastic formation in the environment: A review. *Environmental Pollution*, page 116554, 2021.

8 Publications and Manuscripts

Individual Contributions to the Publications

In the upcoming section, the individual contributions of each author to the publications included within this thesis are given in detail. The work that I have contributed to each publication was performed at the chair Macromolecular Chemistry I at the University of Bayreuth between September 2019 and September 2022.

Paper 1:
Reconstructing the Environmental Degradation of Polystyrene by Accelerated Weathering
Environmental Science & Technology 2021, 55, 12, 7930-7938.
Nora Meides, Teresa Menzel, Björn Poetzschner, Martin G.J. Löder, Ulrich Mansfeld, Peter Strohriegl, Volker Altstädt, Jürgen Senker

For this publication, I established a weathering protocol for particle weathering in water. I performed the weathering experiments of the PS particles, sample extraction and preparation, measured and evaluated the particle size, and measured the GPC measurements of particles and tensile bars, including evaluation of the particle data. Further, I investigated the particle characteristics via SEM with the aid of M.H. and U.M. Evaluation of the images of particles was done by myself. Finally, I visualized the two-stage degradation model using the software Inkscape. I also designed the graphical abstract for this publication. T.M. performed weathering of tensile bars and tensile testing. B.P. conducted Monte Carlo simulations and NMR measurements. U.M. performed SEM and SEM-EDX measurements. I wrote a large proportion of the manuscript with T.M., especially the introduction and results and discussion part. T.M., B.P., and myself each wrote the materials and methods part of our individual methods. M.L., P.S., J.S., and V.A. supported us with writing and finalizing the manuscript. We were all involved in the final discussions. P.S., J.S., and V.A. supervised the project. I completed the final formatting of the manuscript. J.S. and P.S. are both corresponding authors.

Paper 2:
Degradation of low-density polyethylene to nanoplastic particles by accelerated weathering
Science of the Total Environment 2022, 826, 154035, 0048-9697.
Teresa Menzel, Nora Meides, Anika Mauel, Ulrich Mansfeld, Winfried Kretschmer, Meike Kuhn, Eva M. Herzig, Volker Altstädt, Peter Strohriegl, Jürgen Senker, Holger Ruckdäschel

In this publication, I performed weathering of LDPE particles, particle sample extraction and preparation. Further, I measured the average particle size and size distributions, as well as investigated the thermal properties via DSC measurements. With the help of M.H. and U.M., we analyzed the particle characteristics via SEM. I performed the image evaluation and editing. Finally, I designed the three-stage degradation model using the software Inkscape. T.M. conducted weathering of tensile bars, DSC measurements, tensile testing and FT-IR measurements. She further designed the graphical abstract.

A.M. was responsible for NMR measurements, Monte Carlo (MC) simulations and powder XRD measurements. M.K. and E.M.H. performed WAXS measurements of chosen samples. U.M. performed SEM imaging and SEM-EDX measurements of tensile bars, W.K. conducted ^{1}H HT liquid NMR spectroscopy and HT GPC measurements. T.M., A.M., and myself wrote the manuscript. H.R., V.A., P.S., and J.S. supported the discussions and helped finalizing the manuscript. H.R., V.A., P.S., and J.S. are supervisors of the project, H.R., and J.S. are corresponding authors.

Paper 3:
Quantifying the fragmentation of polypropylene upon exposure to accelerated weathering
Microplastics and Nanoplastics, 2022, 2:23.
Nora Meides, Anika Mauel, Teresa Menzel, Volker Altstädt, Holger Ruckdäschel, Jürgen Senker, Peter Strohriegl

In this publication I performed the Soxhlet extraction of PP particles, weathering of PP with and without additive, sample extraction and preparation. Further, I performed the purification of the stabilizer residue, and analysis of the residue via MALDI-TOF mass spectrometry. For identification of the stabilizer, I performed a further weathering experiment of reference stabilizer compounds, and subsequent MALDI-TOF measurements to identify the stabilizer. For particle characterization, I performed average particle size and particle distribution measurements, DSC measurements for thermal characteristics. M.H. and U.M. helped with SEM imaging, I performed the evaluation and processing of the SEM images. A.M. performed solid-state ^{13}C NMR spectroscopy, and liquid-state ^{1}H and ^{31}P NMR spectroscopy. W.K. measured the molecular weight of both PP experiments via HT GPC. I wrote the manuscript, supported by A.M., T.M., P.S., H.R., V.A., and J.S., all authors joined the discussions and helped finalizing the manuscript. P.S., H.R., V.A., and J.S. are supervisors of the project, P.S. is corresponding author.

Paper 4:
Environmental degradation of polystyrene, polyethylene, and polypropylene - a comparison of natural and accelerated weathering
Manuscript ready for submission.
Nora Meides, Anika Mauel, Teresa Menzel, Wolfgang Babel, Volker Altstädt, Holger Ruckdäschel, Jürgen Senker, Peter Strohriegl

In this manuscript, I performed the outdoor weathering experiment of all three polymers over a total experimental duration of 1,5 years. I further established the weathering setup enabling outdoor exposure. I also performed the cryo-cooled experiments in the accelerated weathering chamber. I managed the monthly sample extraction, sample preparation, particle size and size distribution measurements. I performed GPC measurements and data evaluation of PS, as well as DSC measurements and data evaluation of LDPE and PP. Further, I prepared the plots of the weather data from the ecological botanical garden (data provided by W.B.). HT GPC measurements of LDPE and PP were performed by W.K., A.M. was responsible for the ^{13}C solid-state NMR measurements. I wrote the manuscript with the help of A.M., T.M., P.S., J.S.; V.A., and H.R.

are supervisors of the project and helped finalize the manuscript and joined the discussions. P.S. is corresponding author.

Paper 5:
Quantification of photooxidative defects in weathered microplastics using ^{13}C multiCP NMR spectroscopy
RSC Advances, 2022, 12, 10875-10885.
Anika Mauel, Björn Pötzschner, Nora Meides, Renée Siegel, Peter Strohriegl, Jürgen Senker

In this publication I performed accelerated weathering on the PS particles for different exposure times, as well as particle preparation (filtering and drying). Further, I performed GPC-measurements, data evaluation and wrote the experimental parts to my experiments and measurements. A.M. and B.P. planned and executed the ^{13}C multiCP NMR measurements and developed an ideal setup to achieve best results for multiCP experiments. A.M., B.P., R.S., and J.S. wrote the manuscript, P.S. and myself read the final manuscript and supported the revision process until final publication.

Paper 6:
Pristine and artificially-aged polystyrene microplastic particles differ in regard to cellular response
Journal of Hazardous Materials, 2022, 435, 128955.
Matthias Völkl, Valérie Jérôme, Alfons Weig, Julia Jasinski, Nora Meides, Peter Strohriegl, Thomas Scheibel, Ruth Freitag

In this publication I performed accelerated weathering on the particles for different exposure times. I also wrote proportions of the manuscript in the introduction section, the methods part, was involved within the discussion part and also during the revision process. M.V., V.J., A.W., J.J., T.S., and R.F. designed all further experiments. M.V. performed most of the cell-based experiments. J.J. provided particle characterization and confocal microscopy. A.W. analyzed the RNA sequencing data. M.V., A.W., and V.J. analyzed all further data and created the figures. M.V., V.J., A.W., P.S., T.S., and R.F. wrote the manuscript. V.J., A.W., T.S., P.S., and R.F. reviewed and edited the manuscript and supervised during the experiments.

8.1 Reconstructing the Environmental Degradation of Polystyrene by Accelerated Weathering.

Environmental Science & Technology
pubs.acs.org/est
Article

Reconstructing the Environmental Degradation of Polystyrene by Accelerated Weathering

Nora Meides,[#] Teresa Menzel,[#] Björn Poetzschner,[#] Martin G. J. Löder, Ulrich Mansfeld, Peter Strohriegl,[*] Volker Altstaedt, and Jürgen Senker[*]

Cite This: *Environ. Sci. Technol.* 2021, 55, 7930−7938
Read Online
ACCESS | Metrics & More | Article Recommendations | Supporting Information

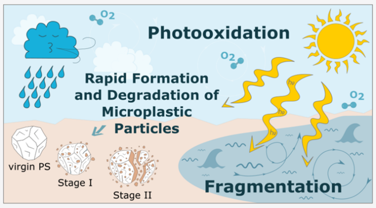

ABSTRACT: The fragmentation of macro- into microplastics (MP) is the main source of MP in the environment. Nevertheless, knowledge about degradation mechanisms, changes in chemical composition, morphology, and residence times is still limited. Here, we present a long-term accelerated weathering study on polystyrene (PS) tensile bars and MP particles using simulated solar radiation and mechanical stress. The degradation process was monitored by gel permeation chromatography (GPC), scanning electron microscopy (SEM), energy-dispersive X-ray (EDX), ^{13}C magic-angle spinning (MAS) NMR spectroscopy, tensile testing, and Monte Carlo simulations. We verified that degradation proceeds in two main stages. Stage I is dominated by photooxidation in a near-surface layer. During stage II, microcrack formation and particle rupturing accelerate the degradation. Depending on the ratio and intensity of the applied stress factors, MP degradation kinetics and lifetimes vary dramatically and an increasing amount of small MP fragments with high proportions of carboxyl, peroxide, and keto groups is continuously released into the environment. The enhanced surface area for adsorbing pollutants and forming biofilms modifies the uptake behavior and interaction with organisms together with potential ecological risks. We expect the proposed two-stage model to be valid for predicting the abiotic degradation of other commodity plastics with a carbon−carbon backbone.

KEYWORDS: *microplastics, polymer degradation, photooxidation, two-stage degradation model, quantitative ^{13}C MAS NMR spectroscopy, Monte Carlo simulations, microcrack formation, particle fragmentation*

■ INTRODUCTION

A multitude of plastic applications led to an exponentially growing global plastic production over the last 70 years and reached almost 360 million tons in 2018.[1] About 60% of the global plastics production consists of single-use commodity plastics with an aliphatic backbone like polypropylene (PP), polyethylene (PE), and polystyrene (PS).[1−5] If current production and waste management trends continue, roughly 12 billion tons of plastic waste is assumed to accumulate in natural environments and landfills by 2050.[6] Once in the environment, plastics lead to potentially severe consequences for sea- and wildlife with inestimable long-term implications for the world's ecosystems.[7−10] In particular, microplastics (MP), defined as plastic fragments smaller than 5 mm,[11] are environmental contaminants of increasing scientific and public concern, as plastics are expected to persist for ages due to their high durability and low biodegradability and thus accumulate in the environment.[12] Due to their small size, MP harbor a high risk of entering terrestrial and aquatic food chains on the basis of the food web.[13,14] The ecological risks are suspected to increase with decreasing MP particle size, in tandem with a growing surface-to-volume ratio, which enlarges the surface area of a particle.[15]

Meanwhile, the presence of MP is verified in every environmental compartment.[16,17] Its majority originates from abrasion during usage, weathering, and fragmentation of larger commodity plastic items into so-called secondary MP.[16] Although a basic understanding of the processes underlying fragmentation is present, detailed mechanistic knowledge of the physicochemical processes of the degradation chain under environmental conditions is lacking. However, this knowledge is imperative to enable a reliable risk assessment, to develop mitigation measures and efficient strategies for future handling of the MP challenge.

Several analytical techniques are available that can be used to follow the degradation of polymers. To reach molecular resolution, gel permeation chromatography (GPC) is commonly used. GPC provides information on the molecular weight distribution (MWD) and is thus sensitive to chain scissions and cross-linking.[16,18,19] For a chemically resolved

Received: November 28, 2020
Revised: May 1, 2021
Accepted: May 4, 2021
Published: May 21, 2021

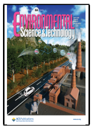

fingerprint of the polymer defects, Fourier transform infrared (FTIR) spectroscopy is often applied.[20,21] However, attenuated total reflection (ATR)-FTIR spectroscopy is surface-dependent, making the quantification of defect concentrations challenging.[20] Nuclear magnetic resonance (NMR) spectroscopy is a bulk method and provides quantitative amounts of degradation products.[22,23] Its element selectivity increases the distinguishability between the individual defect types, further enhanced by selective isotopic labeling.[22] As such, solid- and liquid-state ^{13}C NMR spectroscopic studies of PP,[24,25] PE,[26−29] PS,[30,31] and other common polymers[32−34] are used to monitor the intermediates and final chain defects.

The degradation of commodity plastics, mostly investigated for PE and PP,[2−5] is commonly attributed to a complex interplay of photooxidation, mechanical stress,[35−37] and recently also biotic degradation.[38,39] The radical-driven photooxidation leads to continuous chain scissions of the polymer backbone and subsequent formation of hydroxy, peroxo, keto, carboxy, and vinyl defects.[21,24,25,28] In parallel, cross-linking of polymer chains by radical recombination occurs.[40] Previous studies report that the distribution of defects is inhomogeneous in depth relative to the sample volume.[16] This results in regions with varying properties like polarity and durability, which in turn are supposed to facilitate fragmentation of the plastic objects by surface ablation and rupturing.[16,41,42] Despite these general ideas for the degradation, central aspects regarding time and length scales as well as defect concentrations must be clarified. In particular, the interaction between chemical composition and stress-induced particle breakup is not yet understood.

Therefore, we conducted a comprehensive accelerated weathering study of commercial PS to follow the abiotic degradation processes from macroscopic to atomic length scales. PS is one of the most abundant polymer types to be found as macro- and microplastic litter in aquatic, marine, and soil environments.[18,43] Compared to PP and PE, the degradation of PS MP is significantly less well investigated and mainly limited to rather short time scales.[31,44−46] By combining accelerated weathering experiments on two sets of samples, we strive to resolve the influence of two main abiotic environmental stress factors: (i) solar radiation and (ii) mechanical stress like shear forces and abrasion. We weathered macroscopic PS tensile bars and 160 μm PS particles in water in a commercial weathering chamber that allows us to enhance the natural weathering conditions artificially. While the bar's surfaces were subjected only to simulated solar radiation, the particles were also exposed to moderate mechanical stress by constant stirring. The abiotic degradation of the PS samples was monitored by a variety of analytical techniques such as GPC, scanning electron microscopy (SEM), SEM-energy-dispersive X-ray (EDX), particle size analysis, and mechanical testing. In addition, we used solid-state ^{13}C magic-angle spinning (MAS) NMR spectroscopy to develop a quantitative picture of the degradation products and chain defects as a function of exposure time. Further, Monte Carlo (MC) simulations of the chain degradation allowed us to link the GPC and NMR spectroscopic data. This approach led to a comprehensive degradation model for PS under the influence of simulated solar radiation and mechanical stress.

■ EXPERIMENTAL SECTION

Materials, Methods, and the Accelerated Weathering Test. A commercially available PS (Styrolution PS 158N) manufactured by INEOS Styrolution Group (Frankfurt am Main, Germany) was used to produce both tensile bars and MP particles. The number- and weight average molecular weights (M_n and M_w) as well as the dispersity ($Đ = M_w/M_n$) determined by GPC were M_n = 125 000 g/mol, M_w = 281 000 g/mol, and $Đ$ = 2.25. PS 158N is a standard PS type and contains no additives besides 600 ppm of zinc stearate, according to the manufacturer. For tensile bar weathering experiments, ISO 527-2 type 1A tensile bars were prepared by injection molding (Arburg Allrounder 470H 1000-170, Arburg GmbH, Loßburg, Germany). For particle weathering experiments, the pellets were ground using an Ultra Centrifugal Mill ZM 200 (Retsch GmbH, Haan, Germany) and sieved with an Alpine Air Jet Sieve E200 LS (Hosokawa Alpine AG, Augsburg, Germany) to 125−200 μm sized particles.

Tensile bars and particles were exposed to controlled accelerated weathering conditions in the industrial test chamber Q-SUN XE-3 (Q-LAB Corporation, Westlake, OH). The irradiation source is composed of three xenon arc lamps emitting radiation similar to natural sunlight due to the Daylight-Q filter system filtering radiation with wavelengths smaller than 295 nm (emission spectrum in Figure S1). In both experiments, irradiance was set to 60 W/m^2 at 300−400 nm and relative humidity to 50%. The irradiance corresponded to 594 W/m^2 total irradiance (Table S1). Compared to an average mid-European irradiation of 114 W/m^2, the irradiance in the chamber was 5-fold enhanced (Figure S2 and Table S1).

Weathering conditions for the bars corresponded to the ISO 4892-2:2011 standard with a chamber temperature of 38 °C. Spray periods of 18 min with deionized water within a 120 min irradiation cycle were applied. Ten samples (five for mechanical testing and five for analytical measurements) of tensile bars were taken for analysis after 0, 200, 400, 800, 1000, 1400, and 2000 h. For particle weathering, 20 g of the PS powder was constantly stirred in a quartz glass-covered beaker in 600 mL of deionized water (55 °C) using a poly(tetrafluoroethylene) (PTFE)-coated magnetic stirrer at 150 rpm. Particle samples were taken for analysis after 0, 24, 50, 100, 200, 400, 600, 800, 1200, 1600, 2000, 2400, 2800, and 3200 h. Per MP sample, 1−2 g of particles were taken from the MP−water dispersion, filtered with a suction filter, and dried at 40 °C in a vacuum oven. These sample amounts represented a sufficiently large ensemble for reproducible averaging.

A detailed description of the experimental conditions for GPC, SEM, SEM-EDX measurements, particle size analysis, mechanical testing, solid-state NMR spectroscopy, and Monte Carlo simulations is given in the Supporting Information (SI).

■ RESULTS

Particle Weathering. In the case of particle weathering in water, simulated solar exposure and mechanical stress by stirring led to a decrease in particle size (Figure S5). Quantitative particle size measurements show that the decrease in particle size is combined with the broadening of the particle size distributions (Figure 1a). The average particle size of the reference sample is ∼160 μm, with particle distribution ranging from ∼100 to 300 μm. It was observed that 2000 h of weathering, however, led to a decrease in the average particle size down to 50 μm with particle sizes ranging from ∼10 to 200 μm (Figure 1a). During the first 600 h of weathering, we observed a linear decay in size (Figure 1b). From 600 h onward, the trend evolves exponentially ($\propto \exp(-t/\tau)$) with a time constant (τ) of 930 h. The particle breakdown accelerates

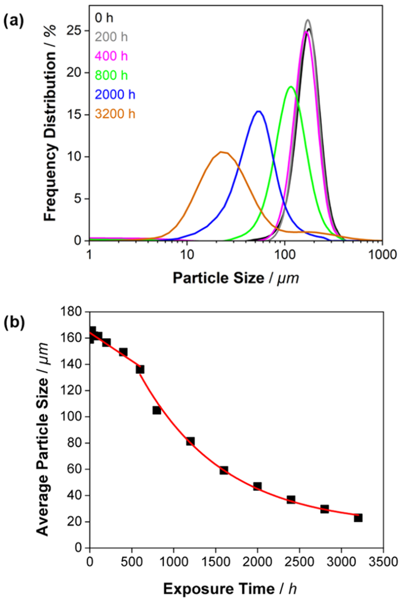

Figure 1. (a) Selected particle size distributions of PS particles for exposure times between 0 and 3200 h. (b) Average particle sizes as a function of exposure time. Full data is given in Table S2 and Figure S6.

and the particle size reaches 20 μm at 3200 h. For samples weathered for 2000 h and longer, the formation of a tail toward large particle sizes is visible within the particle size distributions (Figures 1a and S6). This effect is attributed to agglomeration effects as a consequence of the increased surface area and polarity.

Within the first 400 h of exposure, the primarily angular particles developed smooth surfaces and rounded shapes. Further, thin platelet-shaped fragments were ablated from the particle surfaces (Figure 2a,b). Prominent fractures and deep microcracks become visible beyond 800 h (Figure 2c,d). After 2400 h of exposure, fragments <1 μm were observed due to particle disintegration (Figure 2d, yellow arrows). They are not resolved within the particle size analysis since they adhere to larger particles.

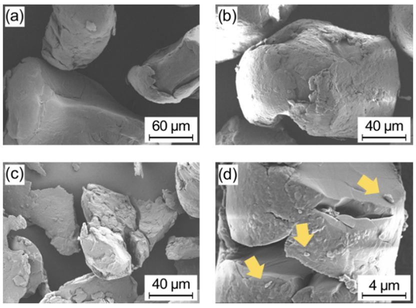

Figure 2. SEM micrographs of (a) virgin particles at 0 h of exposure, (b) rounded particles after 400 h of exposure, (c) fractured particles after 800 h, and (d) the fractured surfaces of a particle after 2400 h of exposure. Arrows in (d) indicate <1 μm sized fragments on the particle surface.

For the dark control experiment (same experimental setup, but no simulated solar radiation), no changes in the particle size were observed. The complete data set is given in Table S3 and Figures S7 and S8.

Tensile Bar Weathering. Weathering of the tensile bars with periods of water spraying and constant simulated solar radiation led to PS-typically yellowing,[45] an optical loss of transparency and gloss (Figure S9). However, on a microscopic scale, no influence on the surface texture was detectable up to an exposure time of 400 h (Figure S10). From 800 h onward, we observed the first microcracks. They developed in a preferred direction (Figure 3a), possibly due to the polymer orientation during injection molding. As the exposure time increased, further cracks appeared perpendicular to the previous ones. This led to an even finer surface and more regular texture (Figure 3b). This regularity is the dominant surface effect with prolonged weathering >1400 h (Figure 3c,d) and no further variation in the surface texture was observed.

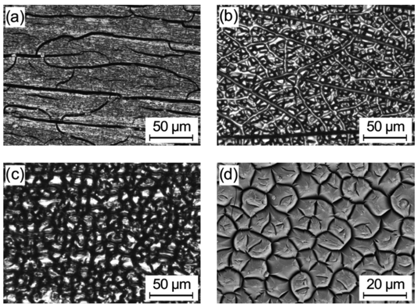

Figure 3. Optical micrograph images of PS bar surfaces for different exposure times: (a) 800 h with microcracks, (b) 1000 h with finer surface texture, and (c) 1400 h with regular surface texture supported by a (d) SEM micrograph of the same sample with higher resolution. (Additional microscope images are given in Figure S10.)

For the determination of a depth profile of the photooxidation, SEM-EDX line scan measurements were carried out on weathered surfaces after exposure times of 800 and 2000 h (Figure 4a). The reference sample shows a constant O/C ratio of approx. 0.005, independent of the sample depth. This value reflects the solubility of O_2 in PS. In the case of the weathered samples, the O/C ratio is significantly increased up to a sample depth of 30 μm. With increasing distance from the surface, the oxygen content decreases in an exponential manner, approaching the value of the reference sample. This indicates the chemical uptake of O_2 by photooxidation, further referred to as the photooxidative zone *d*.

A characteristic value to display PS embrittlement is the elongation at break (ε_B) (Figure 4b). For short exposure times, we observed an increase in ε_B. This observation on weathered PS was already reported elsewhere[47] and is probably due to cross-linking, leading to a temporarily improved entanglement. For longer exposure times, ε_B decreases again and reaches a plateau at about 800 h and roughly 60% of the initial value.

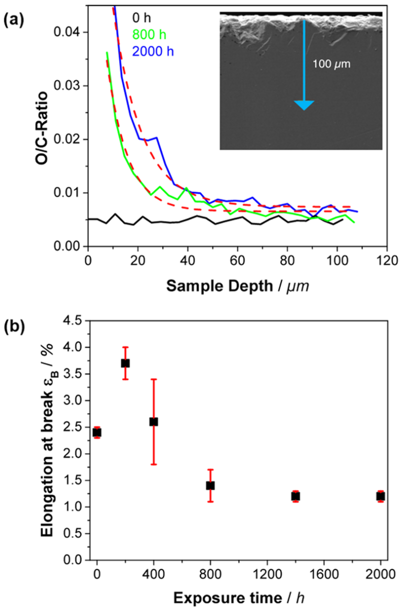

Figure 4. (a) Graphical plot of the O/C ratio versus the sample depth of PS bars for the reference sample (black), materials weathered for 800 h (green) and 2000 h (blue) determined by SEM-EDX measurements. The dashed red lines represent a guide for the eye. The SEM micrograph displays the line scan from the weathered surface to the inside of the sample. (b) Effect of weathering on the elongation at break ε_B, determined by tensile tests.

The rapid drop indicates the ductile-to-brittle transition. In addition, the formed microcracks act as initial breaking points on the surface of samples.

Evolution of Chain Defects. The molecular weight distributions (MWDs) for the weathered tensile bars and particles were determined by GPC measurements and are given in Figure 5a, together with the corresponding number average molecular weights (M_n) and dispersities (Đ) (Figures 5b and S11). Regardless of the sample geometry, a shift of the MWDs to lower values was observed with increasing exposure time. For the bar surface, M_n decreases from 125 000 to 2900 g/mol within 2000 h. M_n of the particles decreases to 5400 g/mol within 3200 h. Furthermore, the distributions broaden continuously as reflected in an increase of Đ from 2 to 4 (Figure 5b and Tables S4 and S5). For exposure times longer than 800 h, the surface of the bars degrades faster compared to the particles. For the dark control experiment, no changes in MWD, M_n, and Đ were observed (Table S6 and Figure S12).

To reproduce the experimental MWDs of the particles, MC simulations were performed on the degradation of a polymer chain ensemble subjected to chain scissions and cross-linking. The dispersity of the measured spectra (Figure 5c) could be matched almost perfectly by adjusting the cross-link probability P_{cl} twice. At an M_n of 44 000 g/mol, P_{cl} changed from 0.250 to 0.290 and again to 0.305 when M_n reached 15000 g/mol. We attribute the small increase in P_{cl} to an increase in mobility, as the polymer chains become shorter in the course of the degradation. The resulting simulated MWDs (Figure 5d) reproduce very well the observed MWDs for similar M_n values. From the simulations, we conclude that an average particle sample developed a cross-link density of 1.4% and 3.2% of chain scissions per repeating unit (RU) for an exposure time of 3200 h.

Solid-state ^{13}C cross-polarization (CP) MAS NMR spectra of the tensile bar's surface layer and the particles are shown in Figure 6a,b. For reference PS (0 h, black line), three prominent peaks are visible, which are assigned to the aliphatic backbone (35−50 ppm), the aromatic ipso carbon (128 ppm), and the aromatic CH units (145 ppm) of the phenyl rings. Smaller signals between 0 and 30 ppm are attributed to the additive zinc stearate. With increasing exposure time, several additional peaks typical for peroxide (III, 77 ppm), carboxyl (II, 172 ppm), and ketone (I, 201 ppm) groups emerged (Figure 6a) as a consequence of the photooxidation (Figure S13a). Based on liquid-state NMR measurements (Figure S13b), the ketone resonance was assigned to end-chain ketones only. Due to the stabilization of the radicals on the aliphatic carbon in the α position to the phenyl rings, the peroxide units are expected to be preferentially located at the methine carbons. We attribute this to the stabilization of benzyl radicals. For both sample geometries, the intensity of the defect resonances increases with exposure time, with markedly higher intensities for the tensile bar surfaces (Figure 6a,b).

As CP experiments are not necessarily quantitative in terms of intensity ratios, calibration is needed. Therefore, quantitative multi-CP spectra were recorded for the selected samples of both sample suites, and a correction factor c_i for each resonance was derived with values between 0.68 and 0.92 (Table S7 and Figure S14). This procedure is reliable since all spectra were recorded with identical experimental conditions (further discussion is given in the SI on page 14). From the spectral intensities (Tables S9 and S10), the proportion of the respective chemical groups, with respect to the total number of RUs in the polymers, were calculated (see Section 2.2.8 in the SI). The result is shown in Figure 6c for the bar surfaces and the particle samples. By calculating the typical molecular weight of a single polymer chain (Figure S4) from the number of end groups (Figure 6c) and correlating these values to M_n of the observed MWDs, the lower limit of the cross-link density was derived (see Section 2.2.8). In accordance with the spectral intensities, the proportion of the degradation products is higher by a factor of about 3 for the bar surface materials. Nevertheless, weathering experiments for both suites follow a similar linear trend up to exposure times of 1400 h for bars and 1600 h for particles. For longer exposures, a saturation effect is observed for the peroxide and carboxyl groups as well as for the cross-link density in the case of the bars, while the ketone defect proportion continues to increase linearly (Figure 6c). For the particles, no saturation was observed except for the peroxide units. Compared to the tensile bars, the turning point is shifted with 2000 h to larger values. The trend for the ketone proportions implies an induction period, most likely originating from the weak signal-to-noise ratio for this resonance for short weathering times.

The total proportion of end groups (ketone and carboxyl groups), the derived cross-link densities for the NMR, and the simulations of the GPC data follow similar trends (Figures 6d and S15), with the absolute values of the simulations being systematically smaller by a factor of ≈1.8. We attribute the smaller defect content observed for the GPC data to the relatively simple model used for the simulations, which, e.g.,

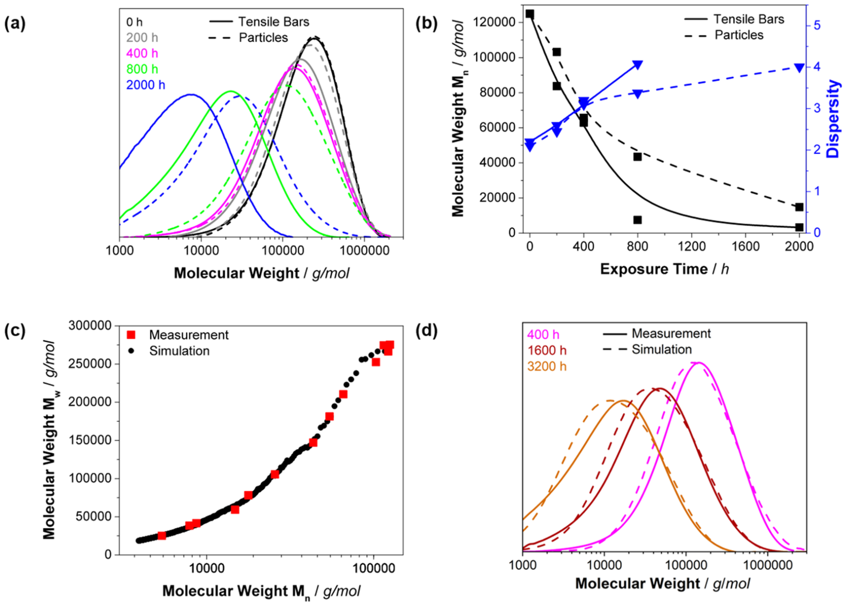

Figure 5. (a) MWD for tensile bar surfaces (solid lines) and particles (dashed lines) for exposure times between 0 and 2000 h. The MWD is cut at 1000 g/mol due to the limited resolution of the column set at low MW. (b) Graph of M_n (black) and $Đ$ (blue) as a function of exposure time for bar surfaces (continuous lines) and particles (dashed lines). $Đ$ for the tensile bar sample at 2000 h cannot be determined due to the limited resolution of the columns. (c) M_w over M_n of the MC simulation (black dots) compared to the measured values (red squares). (d) Comparison of simulated (dashed lines) and measured (solid lines) MWD for particles of selected exposure times. Full data are given in Tables S4 and S5.

omits end groups created without dividing the macromolecules into individual objects. For both methods, chain scissions were observed to occur more frequently by factors of 1.6 (NMR) and 2.4 (simulation) compared to cross-links. Thus, on average, 67% chain scissions and 33% cross-links take place.

■ DISCUSSION

For this study, PS tensile bars and PS particles were subjected to accelerated weathering under laboratory-controlled conditions, focusing on two main abiotic environmental stress factors—simulated solar radiation and mechanical forces induced by stirring. The tensile bars were only exposed to radiation without mechanical stress. They developed a depth profile with an exponential character for the proportion of the photooxidation degradation products (Figure 4a). For exposure times of 800 and 2000 h, the photooxidative zone d did not reach beyond a near-surface layer of ~30 μm in depth. This agrees well with the results published by Audouin et al.,[47] reporting the thickness of this near-surface layer to be independent of the exposure time.

The content of polar carboxyl, peroxide, and keto groups within d increases linearly along with the cross-link density as a function of the exposure time (Figure 6a,c). Therefore, the initially nonpolar and linear PS chains turn gradually into increasingly polar and branched oligomers (Figure 7 top). For the bar surfaces, M_n decreases from 125 000 to 3300 g/mol within 2000 h (Figure 5a,b). This corresponds to an average oligomer with roughly 32 RUs and 16 polar groups. On average, five short chains with six RUs are linked in at least four positions and form a highly branched molecule. At this stage, we expect the oligomers to become too short and polar to further degrade in the same manner. This is evident by the saturation of the contents of carboxyl groups, peroxide units, and cross-links (Figure 6c). We assume that at this stage, the chain lengths become short enough and the polarity high enough to make the oligomers water soluble. As previously reported, the high oxygen content might also facilitate the complete decomposition and the release of carbon dioxide.[46]

After an initial rise in ductility (Figure 4b), due to increased entanglement as a result of continuous cross-linking, the simultaneous growth of chain defects embrittles PS for exposure times larger than 200 h. In addition, the observed M_n reaches values smaller than the critical molecular weight M_c of roughly 34 000 g/mol for PS,[48] suggesting that the macromolecules become too short for an effective entanglement. The ductile-to-brittle transition is displayed by a drop in the ultimate elongation at break (Figure 4b). At a threshold reached between 400 and 800 h, microcracks appear on the tensile bar surfaces (Figure 3a) due to this embrittlement. The first cracks are predominantly aligned along the injection molding direction because of the polymer orientation during processing.[49] With increasing exposure, further cracks develop transversely to the previous ones forming a regular pattern (Figure 3). These patterns enclose regions with the material of increased polarity. The resulting texture resembles the patterns formed by spinodal dewetting of a polar fluid with high surface tension on a hydrophobic surface.[50,51] Thus, we attribute this effect to the difference in polarity between the degraded surface layer and the mostly unaffected PS bulk. Once the first cracks in the near-surface layer appear, their propagation into

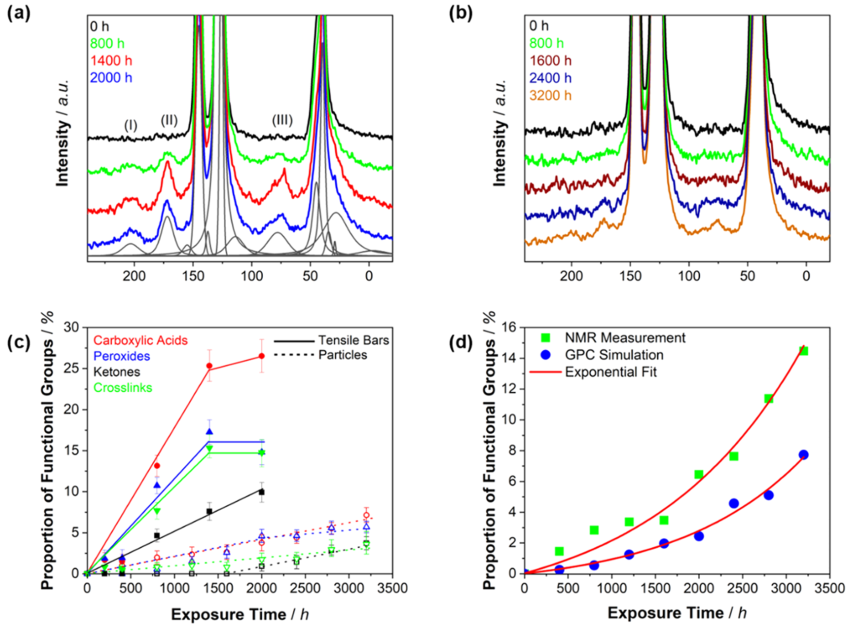

Figure 6. ^{13}C CP MAS NMR spectra of (a) the tensile bar's surface layer with marked functional groups: (I) ketones, (II) carboxylic acids, and (III) peroxides and (b) the particles for different exposure times. The individual spectra are normalized and shifted horizontally for a better overview. Exemplarily, the refinement of the ^{13}C NMR spectrum for the 2000 h tensile bar is shown in gray lines in (a). Further information regarding the fitting procedure is given in Section 2.2.6 and Table S8 in the SI. (c) The derived proportions of functional groups and cross-links with respect to the number of RUs are depicted for tensile bars (full symbols and solid lines) and particles (open symbols and dashed lines) as a function of exposure time. The lines are a guide for the eye. (d) The sum of the proportions of the end group and cross-link densities for the NMR measurement (green squares) and the GPC simulation data (blue circles) of the particles. Exponential fits ($\propto \exp(-t/\tau)$; red lines) are shown with time constants (τ) of 1700 (NMR measurement) and 1450 h (GPC simulations).

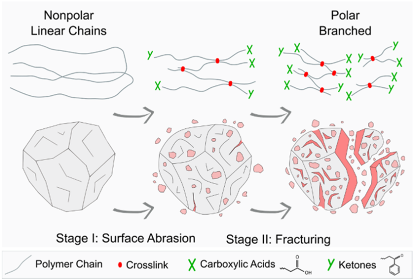

Figure 7. Two-stage degradation model for microplastic particles exposed to the environmental stress factors solar radiation and mechanical stress.

the bulk is facilitated.[53] We expect the appearance of these cracks to mark the beginning of a second macroscopic degradation mechanism.

In contrast to the tensile bars, the MP particles are exposed to both factors solar radiation and moderate mechanical stress by turbulent stirring. The particles decrease slowly and linearly in size for short exposure times, resulting from the abrasion of smaller fragments from the particle surfaces (Figures 1b and 2b). We refer to this period as stage I. Based on the particle size measurements, degradation stage I is associated with an exposure period between 0 and 400 h. Andrady[16] refers to stage I as "fragmentation by surface ablation." He suggests that this stage is driven by mechanical forces such as wave action, abrasion with sand, and contact with animals.[42] We monitored the influence of only mechanical stress and performed a dark control experiment. The particles were subjected to moderate mechanical stress by stirring under identical conditions, as described above, but in the absence of simulated solar radiation. In the dark, the particles do not change their morphologies and sizes at all (Figures S7 and S8), meaning that the decrease of molecular weight, induced by irradiation, is a prerequisite for abrasion as observed during stage I.

For exposure times >800 h, cracks become visible on the particle surfaces (Figure 2c) and fracturing of particles into smaller fragments occurs (Figure 7). From this point onward, the particle size decreases exponentially from 130 to 20 μm within 2400 h and thus breakdown is accelerated (Figure 1b). We refer to this time regime as stage II. The observed exponential decrease of the average particle size is correlated to an exponential increase of the defect proportions (Figure 6c). This is caused by the continuous formation of new particle surfaces upon particle breakup, subsequently exposed to radiation. The observed difference of 65% between the time constants of the trends of the particle sizes and the defect proportions (NMR spectroscopic and GPC data) is in accordance with a stochastic and thus asymmetric particle breakdown (Figures 1b and 6d). This additionally matches the increasing disparity of the particle sizes (Figure 1a). Assuming the MP particles as spheres, their average volume (160 μm diameter and 2 145 000 μm^3 volume) decreases by 99.8% to 4200 μm^3 and approximately 500 small daughter particles with an average diameter of 20 μm are released from one single particle of the starting material.

The lower defect proportions observed for the particle experiments compared to the bars (Figure 6c) correlate with the proposed two-stage degradation model (Figure 7). Additionally, due to geometry factors, the particles are exposed to less solar radiation on average. For short exposure times, only a surface layer with a thickness of approximately 30 μm, corresponding to the determined photooxidative zone d, is affected by degradation and ablation. With the occurrence of microcracks, additional surfaces and secondary particles participate in the photooxidation process. Photooxidation and particle rupturing repeat themselves until the average particle size is smaller than depth d. After 3200 h of exposure, an average particle is smaller than d and consists of oligomers with an M_n of 5600 g/mol, 54 RUs, 8 polar groups, and at least 3 cross-links between the PS chains with an average length of 18 RUs. For the degradation of both tensile bars and MP particles, chain scissions and cross-links were observed to occur in a ratio of 2:1.

Although this study used laboratory-controlled weathering conditions, the design of the two experimental settings, the sample geometries, and the derived two-stage model allow for drawing conclusions of abiotic MP degradation in natural environments. The weathering experiments of PS bars with simulated solar radiation and alternating rain and dry phases mimic natural conditions on land, where mechanical stress might be almost absent. In contrast, for MP at rivers, oceans, coastlines, and beaches, collisions with its environment become increasingly important. In our experiments, only moderate mechanical stress is applied, which can be compared to MP floating in rivers or oceans. We do not consider the effect of harsh mechanical stress induced by collisions with pebbles or sand,[52] which mimics the swash zone and leads to a strong decrease in particle size within a short time. We thus reconstructed this scenario by stirring PS particles in a water column and exposing them to simulated solar radiation with the same intensities as used for the tensile bar experiment. The acceleration factor of the set laboratory weathering conditions, with respect to natural weathering, was extrapolated based on the experimental conditions. An experimental runtime of 2400 h (100 days) is comparable to 1.5 years of outdoor weathering in the area of Central Europe (see Table S1).

The two-stage model implies that MP objects degrade much slower in natural environments where mechanical impacts occur less frequently and with less force. Deposition on land, where mechanical stress is mainly governed by wind, approaches these conditions, in particular, in more shielded compartments. Here, the narrow photooxidative zone remains intact for longer times. For the limiting case of no mechanical stress, the zone degrades homogeneously into increasingly smaller and more polar macromolecules, finally dissolving or decomposing into carbon dioxide.[46] The cycle starts again by the degradation of the next near-surface layer. As a consequence, roughly every two years a zone of 30 μm is degraded, leading to MP lifetimes of several tens of years under these conditions. With more collisions, typical for beaches and coastlines, as well as shear stress of turbulent flows in rivers and oceans, the lifetime becomes much shorter, as fracturing of MP objects after an induction period (stage II) continually creates fresh surfaces. Our results suggest that fracturing occurs in cycles, which might become as short as half a year, speeding up the MP degradation exponentially.

At rivers, oceans, beaches, and coastlines, MP fracturing already produces an increasing amount of small MP particles, on the order of a few tens of micrometers, at an early stage of the degradation process.[54] Based on our data, out of one MP particle, on average, 500 small daughter particles are released during an estimated environmental lifetime of 1.5 years. As these particles are partially oxidized by the degradation and thus are hydrophilic, biofilm formation by bacteria and other microbes[55,56] and the uptake by microorganisms are facilitated.[57,58] MP degradation products enter the food web early and thus interact almost instantaneously with flora and fauna.[57,59] Due to the high degree of oxidation and the presence of peroxide groups, a negative impact on organisms is likely.[59,60] As the original MP objects act as a reservoir, a constant level of potentially harmful particles is maintained over a time period of up to several tens of years, depending on how intense the solar radiation is and how often MP is subjected to mechanical stress.[61]

In addition to the environmental stress factors selected for this laboratory study (solar radiation and mechanical stress), we expect several other factors like biofilm formation, biodegradation, temperature fluctuations, harsh mechanical grinding, oxygen fugacity, salinity, and more to affect MP degradation in the environment. Recent studies of biodegradation on weathered PS films have demonstrated that once exposed to abiotic degradation, marine consortia can further participate in the degradation process, leading to a reduction in molecular weight and sample weight.[38,39] Stronger mechanical stresses might also lead to faster particle fragmentation. Efimova et al.[52] highlighted the significant size reduction of various polymer samples by interaction with marine pebbles, mimicking the swash zone on beaches in a laboratory environment. Biofilm formation, temperature, and oxygen fugacity influence the penetration of solar radiation, the oxygen diffusion, and thereby the reaction rate of the photooxidation. A recent study reported different degradation rates for plastic pellets (PS, PP, and PE) in ultrapure water and simulated seawater.[44] Salinity changes the solubility of the degradation products as well as the surface tension of the particle−water interfaces and thus the microcrack formation. Within the scope of the current work, these environmental stress factors could not be addressed and will be the subject of forthcoming studies. Although these parameters modify the lifetimes, sizes, and chemical composition of the generated MP particles, we are confident that the main abiotic degradation mechanisms of the derived two-stage model—photooxidation and fragmentation—are generic for all commodity plastics with aliphatic backbones. Thus, we envision being able to model the abiotic degradation of common MP within light-exposed aquatic and terrestrial environmental compartments in the future.

■ ASSOCIATED CONTENT

Supporting Information

The Supporting Information is available free of charge at https://pubs.acs.org/doi/10.1021/acs.est.0c07718.

Additional information on analytical methods such as GPC; SEM; EDX; ^{13}C MAS NMR spectroscopy; tensile testing; particle size analysis; and Monte Carlo simulations (PDF)

■ AUTHOR INFORMATION

Corresponding Authors

Peter Strohriegl − *Department of Macromolecular Chemistry I, University of Bayreuth, 95447 Bayreuth, Germany;* Email: peter.strohriegl@uni-bayreuth.de

Jürgen Senker − *Department of Inorganic Chemistry III, University of Bayreuth, 95447 Bayreuth, Germany;* orcid.org/0000-0002-7278-7952; Email: Juergen.senker@uni-bayreuth.de

Authors

Nora Meides − *Department of Macromolecular Chemistry I, University of Bayreuth, 95447 Bayreuth, Germany*

Teresa Menzel − *Department of Polymer Engineering, University of Bayreuth, 95447 Bayreuth, Germany*

Björn Poetzschner − *Department of Inorganic Chemistry III, University of Bayreuth, 95447 Bayreuth, Germany*

Martin G. J. Löder − *Department of Animal Ecology I, University of Bayreuth, 95447 Bayreuth, Germany;* orcid.org/0000-0001-9056-8254

Ulrich Mansfeld − *Bavarian Polymer Institute, University of Bayreuth, 95447 Bayreuth, Germany*

Volker Altstaedt − *Department of Polymer Engineering, University of Bayreuth, 95447 Bayreuth, Germany*

Complete contact information is available at: https://pubs.acs.org/10.1021/acs.est.0c07718

Author Contributions

[#]N.M., T.M., and B.P. contributed equally to this work.

Notes

The authors declare no competing financial interest.

■ ACKNOWLEDGMENTS

The authors would like to thank Lisa Weber for sample preparation; Florian Meichsner, Philip Schmode, and Jutta Failner for GPC measurements; Kristian Schweimer for liquid-state NMR spectra; Martina Heider and Annika Pfaffenberger for SEM; and Werner Koehler for stimulating discussions. This work was funded by the German Research Foundation (DFG)—project number 391977956—SFB 1357 Microplastics, subproject C01.

■ REFERENCES

(1) PlasticsEurope. Plastics—The Facts 2019. An Analysis of European Plastics Production, Demand and Waste Data. https://www.plasticseurope.org/en/resources/publications/1804-plastics-facts-2019.

(2) Julienne, F.; Delorme, N.; Lagarde, F. From macroplastics to microplastics: Role of water in the fragmentation of polyethylene. *Chemosphere* **2019**, *236*, No. 124409.

(3) Da Costa, J. P.; Nunes, A. R.; Santos, P. S.; Girao, A. V.; Duarte, A. C.; Rocha-Santos, T. Degradation of polyethylene microplastics in seawater: Insights into the environmental degradation of polymers. *J. Environ. Sci. Health, Part A: Toxic/Hazard. Subst. Environ. Eng.* **2018**, *53*, 866−875.

(4) Rajakumar, K.; Sarasvathy, V.; Chelvan, A. T.; Chitra, R.; Vijayakumar, C. T. Natural weathering studies of polypropylene. *J. Polym. Environ.* **2009**, *17*, 191−202.

(5) Schoolenberg, G. E. A fracture mechanics approach to the effects of UV-degradation on polypropylene. *J. Mater. Sci.* **1988**, *23*, 1580−1590.

(6) Geyer, R.; Jambeck, J. R.; Law, K. L. Production, use, and fate of all plastics ever made. *Sci. Adv.* **2017**, *3*, No. e1700782.

(7) Chae, Y.; An, Y. J. Current research trends on plastic pollution and ecological impacts on the soil ecosystem: A review. *Environ. Pollut.* **2018**, *240*, 387−395.

(8) de Souza Machado, A. A.; Kloas, W.; Zarfl, C.; Hempel, S.; Rillig, M. C. Microplastics as an emerging threat to terrestrial ecosystems. *Global Change Biol.* **2018**, *24*, 1405−1416.

(9) Galloway, T. S.; Cole, M.; Lewis, C. Interactions of microplastic debris throughout the marine ecosystem. *Nat. Ecol. Evol.* **2017**, *1*, No. 0116.

(10) Lambert, S.; Wagner, M. Microplastics Are Contaminants of Emerging Concern in Freshwater Environments: An Overview. *Freshwater Microplastics*; Springer: Cham, 2018; pp 1−23.

(11) Frias, J. P. G. L.; Nash, R. Microplastics: finding a consensus on the definition. *Mar. Pollut. Bull.* **2019**, *138*, 145−147.

(12) Law, K. L.; Morét-Ferguson, S. E.; Goodwin, D. S.; Zettler, E. R.; DeForce, E.; Kukulka, T.; Proskurowski, G. Distribution of surface plastic debris in the eastern Pacific Ocean from an 11-year data set. *Environ. Sci. Technol.* **2014**, *48*, 4732−4738.

(13) Setälä, O.; Fleming-Lehtinen, V.; Lehtiniemi, M. Ingestion and transfer of microplastics in the planktonic food web. *Environ. Pollut.* **2014**, *185*, 77−83.

(14) Huerta Lwanga, E.; Mendoza Vega, J.; Ku Quej, V.; Chi, J. dlA.; Sanchez del Cid, L.; Chi, C.; Escalona Segura, G.; Gertsen, H.; Salánki, T.; van der Ploeg, M.; Koelmans, A. A.; Geissen, V. Field evidence for transfer of plastic debris along a terrestrial food chain. *Sci. Rep.* **2017**, *7*, No. 14071.

(15) Cole, M.; Lindeque, P.; Halsband, C.; Galloway, T. S. Microplastics as contaminants in the marine environment: a review. *Mar. Pollut. Bull.* **2011**, *62*, 2588−2597.

(16) Andrady, A. L. The plastic in microplastics: A review. *Mar. Pollut. Bull.* **2017**, *119*, 12−22.

(17) Eerkes-Medrano, D.; Thompson, R. C.; Aldridge, D. C. Microplastics in freshwater systems: a review of the emerging threats, identification of knowledge gaps and prioritisation of research needs. *Water Res.* **2015**, *75*, 63−82.

(18) Andrady, A. L. Persistence of Plastic Litter in the Oceans. In *Marine Anthropogenic Litter*; Bergmann, M.; Gutow, L.; Klages, M., Eds.; Springer: Berlin, 2015; pp 57−72.

(19) Bottino, F. A.; Cinquegrani, A. R.; Di Pasquale, G.; Leonardi, L.; Pollicino, A. Chemical modifications, mechanical properties and surface photo-oxidation of films of polystyrene (PS). *Polym. Test.* **2004**, *23*, 405−411.

(20) Shim, W. J.; Hong, S. H.; Eo, S. E. Identification methods in microplastic analysis: a review. *Anal. Methods* **2017**, *9*, 1384−1391.

(21) Shi, Y.; Qin, J.; Tao, Y.; Jie, G.; Wang, J. Natural weathering severity of typical coastal environment on polystyrene: Experiment and modeling. *Polym. Test.* **2019**, *76*, 138−145.

(22) Schmidt-Rohr, K.; Spiess, H. W. *Multidimensional Solid-State NMR and Polymers*; Academic Press: San Diego, 1998.

(23) Johnson, R. L.; Schmidt-Rohr, K. Quantitative solid-state 13C NMR with signal enhancement by multiple cross polarization. *J. Magn. Reson.* **2014**, *239*, 44−49.

(24) Vaillant, D.; Lacoste, J.; Dauphin, G. The oxidation mechanism of polypropylene: contribution of 13C-NMR spectroscopy. *Polym. Degrad. Stab.* **1994**, *45*, 355−360.

(25) Mowery, D. M.; Assink, R. A.; Derzon, D. K.; Klamo, S. B.; Clough, R. L.; Bernstein, R. Solid-state 13C NMR investigation of the oxidative degradation of selectively labeled polypropylene by thermal aging and γ-irradiation. *Macromolecules* **2005**, *38*, 5035−5046.

(26) Horii, F.; Zhu, Q.; Kitamaru, R.; Yamaoka, H. Carbon-13 NMR study of radiation-induced crosslinking of linear polyethylene. *Macromolecules* **1990**, *23*, 977−981.

(27) Assink, R. A.; Celina, M.; Dunbar, T. D.; Alam, T. M.; Clough, R. L.; Gillen, K. T. Analysis of hydroperoxides in solid polyethylene by MAS 13C NMR and EPR. *Macromolecules* **2000**, *33*, 4023−4029.

(28) Chabira, S. F.; Sebaa, M.; G'sell, C. Oxidation and crosslinking processes during thermal aging of low-density polyethylene films. *J. Appl. Polym. Sci.* **2012**, *124*, 5200−5208.

(29) Hsu, Y. C.; Truss, R. W.; Laycock, B.; Weir, M. P.; Nicholson, T. M.; Garvey, C. J.; Halley, P. J. The effect of comonomer concentration and distribution on the photo-oxidative degradation of linear low-density polyethylene films. *Polymer* **2017**, *119*, 66−75.

(30) Pop, M.; Traian, S.; Daraban, L.; Fechete, R. 13C NMR Study of Gamma Irradiated Polystyrene. *Stud. Univ. Babes-Bolyai, Chem.* **2011**, *56*, 129−134.

(31) Prasad, A. V.; Singh, R. P. Photooxidative degradation of styrenic polymers: 13C-NMR and morphological changes upon irradiation. *J. Appl. Polym. Sci.* **1998**, *70*, 637−645.

(32) Mkhatresh, O. A.; Heatley, F. A. 13C NMR Study of the Products and Mechanism of the Thermal Oxidative Degradation of Poly (ethylene oxide). *Macromol. Chem. Phys.* **2002**, *203*, 2273−2280.

(33) Ronagh-Baghbani, M.; Ziaee, F.; Bouhendi, H.; Ziaie, F. Crosslinking investigation of polybutadiene thermal degradation by carbon-13 nuclear magnetic resonance. *Polym. Degrad. Stab.* **2011**, *96*, 1805−1811.

(34) Wang, Y.; Xu, L.; Wang, M.; Pang, W.; Ge, X. Structural identification of polyacrylonitrile during thermal treatment by selective 13C labeling and solid-state 13C NMR spectroscopy. *Macromolecules* **2014**, *47*, 3901−3908.

(35) Gewert, B.; Plassmann, M. M.; MacLeod, M. Pathways for Degradation of Plastic Polymers Floating in the Marine Environment. *Environ. Sci.: Processes Impacts* **2015**, *17*, 1513−1521.

(36) Fairbrother, A.; Hsueh, H. C.; Kim, J. H.; Jacobs, D.; Perry, L.; Goodwin, D.; White, C.; Watson, S.; Sung, L. P. Temperature and light intensity effects on photodegradation of high-density polyethylene. *Polym. Degrad. Stab.* **2019**, *165*, 153−160.

(37) Song, D.; Gao, J.; Lu, L.; Li, X. Evaluation of service life of polystyrene in tropical marine environment by principal component analysis. *Adv. Mater. Sci. Eng.* **2015**, *2015*, No. 604935.

(38) Syranidou, E.; Karkanorachaki, K.; Amorotti, F.; Franchini, M.; Repouskou, E.; Kaliva, M.; Vamvakaki, M.; Kolvenbach, B.; Fava, F.; Corvini, F. F.-X.; Kalogerakis, N. Biodegradation of weathered polystyrene films in seawater microcosms. *Sci. Rep.* **2017**, *7*, No. 17991.

(39) Syranidou, E.; Karkanorachaki, K.; Amorotti, F.; Avgeropoulos, A.; Kolvenbach, B.; Zhou, N. Y.; Fava, F.; Corvini, P. F.-X.; Kalogerakis, N. Biodegradation of mixture of plastic films by tailored marine consortia. *J. Hazard. Mater.* **2019**, *375*, 33−42.

(40) Shyichuk, A. V.; White, J. R. Analysis of chain-scission and crosslinking rates in the photo-oxidation of polystyrene. *J. Appl. Polym. Sci.* **2000**, *77*, 3015−3023.

(41) White, J. R. *Polymer Weathering: Mechanisms of Degradation and Failure*, Proceedings of the 9th Brazilian Polymer Congress, 2007.

(42) Corcoran, P. L.; Biesinger, C. M.; Grifi, M. Plastics and beaches: a degrading relationship. *Mar. Pollut. Bull.* **2009**, *58*, 80−84.

(43) Browne, M. A.; Galloway, T. S.; Thompson, R. C. Spatial Patterns of Plastic Debris along Estuarine Shorelines. *Environ. Sci. Technol.* **2010**, *44*, 3404−3409.

(44) Cai, L.; Wang, J.; Peng, J.; Wu, Z.; Tan, X. Observation of the degradation of three types of plastic pellets exposed to UV irradiation in three different environments. *Sci. Total Environ.* **2018**, *628−629*, 740−747.

(45) Dinoop lal, S.; Sunil, J. T.; Rajesh, C. Solid-phase photodegradation of polystyrene by nano TiO2 under ultraviolet radiation. *Environ. Nanotechnol., Monit. Manage.* **2019**, *12*, No. 100229.

(46) Ward, C. P.; Armstrong, C. J.; Walsh, A. N.; Jackson, J. H.; Reddy, C. M. Sunlight converts polystyrene to carbon dioxide and dissolved organic carbon. *Environ. Sci. Technol. Lett.* **2019**, *6*, 669−674.

(47) Audouin, L.; Langlois, V.; Verdu, J.; De Bruijn, J. C. M. Role of oxygen diffusion in polymer ageing: kinetic and mechanical aspects. *J. Mater. Sci.* **1994**, *29*, 569−583.

(48) Dobkowski, Z. Determination of critical molecular weight for entangled macromolecules using the tensile strength data. *Rheol. Acta* **1995**, *34*, 578−585.

(49) Ehrenstein, G. W.; Engel, L.; Klingele, H.; Schaper, H. *SEM of Plastics Failure: REM von Kunststoffschäden*; Hanser Publishers, 2011.

(50) Jeevahan, J.; Chandrasekaran, M.; Joseph, G. B.; Durairaj, R. B.; Mageshwaran, G. Superhydrophobic surfaces: a review on fundamentals, applications, and challenges. *J. Coat. Technol. Res.* **2018**, *15*, 231−250.

(51) Xie, R.; Karim, A.; Douglas, J. F.; Han, C. C.; Weiss, R. A. Spinodal dewetting of thin polymer films. *Phys. Rev. Lett.* **1998**, *81*, 1251.

(52) Efimova, I.; Bagaeva, M.; Bagaev, A.; Kileso, A.; Chubarenko, I. P. Secondary Microplastics Generation in the Sea Swash Zone With Coarse Bottom Sediments: Laboratory Experiments. *Front. Mar. Sci.* **2018**, *5*, No. 313.

(53) Awaja, F.; Zhang, S.; Tripathi, M.; Nikiforov, A.; Pugno, N. Cracks, microcracks and fracture in polymer structures: Formation, detection, autonomic repair. *Prog. Mater. Sci.* **2016**, *83*, 536−573.

(54) Song, Y. K.; Hong, S. H.; Eo, S.; Han, G. M.; Shim, W. J. Rapid Production of Micro-and Nanoplastics by Fragmentation of Expanded Polystyrene Exposed to Sunlight. *Environ. Sci. Technol.* **2020**, *54*, 11191−11200.

(55) Zettler, E. R.; Mincer, T. J.; Amaral-Zettler, L. A. Life in the "plastisphere": microbial communities on plastic marine debris. *Environ. Sci. Technol.* **2013**, *47*, 7137−7146.

(56) Kirstein, I. V.; Kirmizi, S.; Wichels, A.; Garin-Fernandez, A.; Erler, R.; Löder, M.; Gerdts, G. Dangerous hitchhikers? Evidence for potentially pathogenic Vibrio spp. on microplastic particles. *Mar. Environ. Res.* **2016**, *120*, 1−8.

(57) Imhof, H. K.; Ivleva, N. P.; Schmid, J.; Niessner, R.; Laforsch, C. Contamination of beach sediments of a subalpine lake with microplastic particles. *Curr. Biol.* **2013**, *23*, R867−R868.

(58) Imhof, H. K.; Rusek, J.; Thiel, M.; Wolinska, J.; Laforsch, C. Do microplastic particles affect Daphnia magna at the morphological, life history and molecular level? *PLoS One* **2017**, *12*, No. e0187590.

(59) Engler, R. E. The complex interaction between marine debris and toxic chemicals in the ocean. *Environ. Sci. Technol.* **2012**, *46*, 12302−12315.

(60) Avio, C. G.; Gorbi, S.; Regoli, F. Plastics and microplastics in the oceans: from emerging pollutants to emerged threat. *Mar. Environ. Res.* **2017**, *128*, 2−11.

(61) Song, Y. K.; Hong, S. H.; Jang, M.; Han, G. M.; Jung, S. W.; Shim, W. J. Combined effects of UV exposure duration and mechanical abrasion on microplastic fragmentation by polymer type. *Environ. Sci. Technol.* **2017**, 4368−4376.

Reprinted with permission from Environmental Science & Technology 2021, 55, 12, 7930–7938.

Supplementary material: `https://doi.org/10.1021/acs.est.0c07718`

8.1.1 Supplementary Material: Reconstructing the Environmental Degradation of Polystyrene by Accelerated Weathering.

Supporting Information

Reconstructing the Environmental Degradation of Polystyrene by Accelerated Weathering

Nora Meides,[1,†] Teresa Menzel,[2,†] Björn Poetzschner,[3,†] Martin G.J. Löder,[4] Ulrich Mansfeld,[5] Peter Strohriegl,[1,*] Volker Altstaedt,[2] Jürgen Senker[3,*]

[1] Department Macromolecular Chemistry I, University of Bayreuth, Universitätsstraße 30, 95447 Bayreuth, Germany
[2] Department Polymer Engineering, University of Bayreuth, Universitätsstraße 30, 95447 Bayreuth, Germany
[3] Department Inorganic Chemistry III, University of Bayreuth, Universitätsstraße 30, 95447 Bayreuth, Germany
[4] Department Animal Ecology I, University of Bayreuth, Universitätsstraße 30, 95447 Bayreuth, Germany
[5] Bavarian Polymer Institute, University of Bayreuth, Universitätsstraße 30, 95447 Bayreuth, Germany

[†] These authors contributed equally to this work

[*] corresponding author: Juergen.senker@uni-bayreuth.de; peter.strohriegl@uni-bayreuth.de

List of Figures

List of Tables

Table S6: Average molecular weight (M_n and M_w) and dispersity (Đ) from GPC measurements of the control dark experiment.

Table S7: Correction factors of the individual resonances derived from the quantitative NMR spectra.

Table S8: Deconvolution parameters for the 2000 h CP PS plate spectrum. Peak 1, 2 and 9 resemble the ketone, carboxy and peroxide resonance, respectively.

Table S9: Intensities of the resonances obtained from the deconvolution procedure for the 13C CP MAS NMR spectra of the PS particles.

Table S10: Intensities of the resonances obtained from the deconvolution procedure for the 13C CP MAS NM spectra of PS tensile bars.

2. Experimental

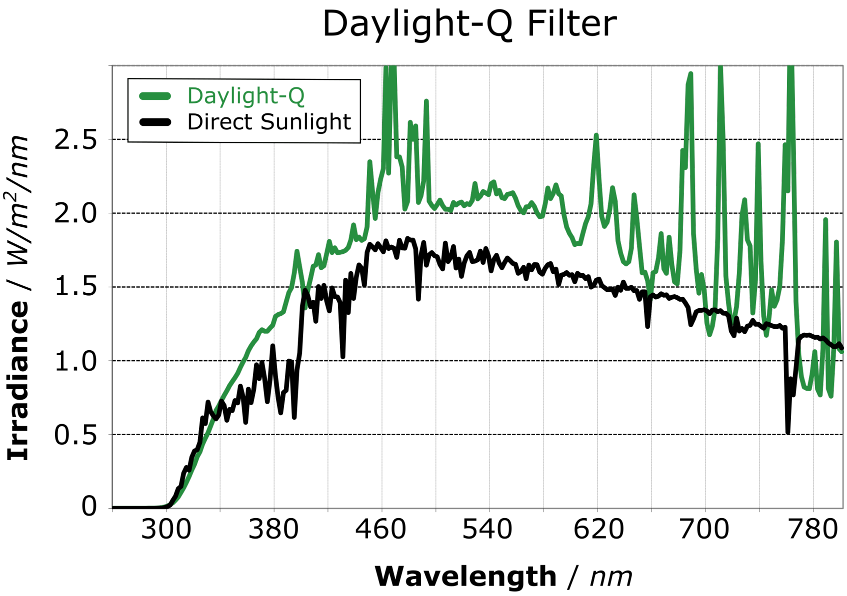

Figure S1 Q-SUN daylight-Q filter compared to direct sunlight. Modified from Q-Lab Corporation, 2014, Technical Bulletin LX-5060, A Choice of Filters for Q-Sun Xenon Test Chambers.

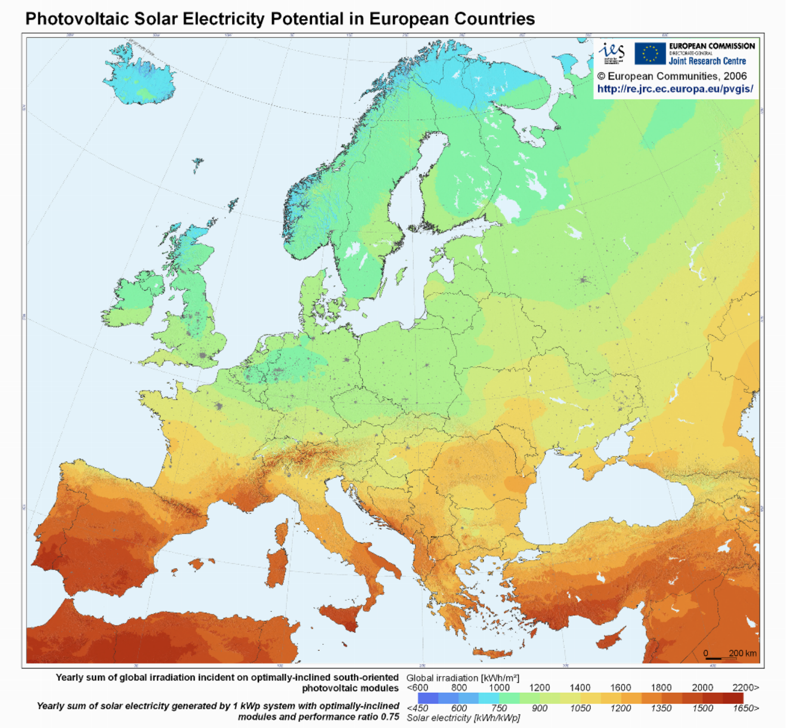

Figure S2 Global Irradiation in kWh/m^2 and Solar Electricity Potential in Europe. Source: European Commission.

Table S1 Calculation of total irradiance in the Q-SUN Xe-3 weathering chamber as well as the acceleration factor for Central Europe.

Calculation of total irradiance in Q-SUN Xe-3 chamber		
Calculation factor (according to Q-Lab, GER)	9.9	-
Lamp settings	60	W/m^2
Total irradiance in Q-SUN Xe-3 chamber	594.17	W/m^2
Acceleration factor of Q-SUN Xe-3 chamber compared to Central Europe		
Solar irradiance per year (Central Europe)	1000	kWh/m^2
Hours per year	8765	h
Solar irradiance Central Europe	114	W/m^2
Acceleration factor of Q-SUN Xe-3 chamber	5.2	-

2.2.1 Dark Control Particle Experiment

Non-irradiated powder and bars served as reference material. In addition, the impact of mechanical stress on PS particles from stirring was monitored by a dark control experiment. The same sample setup, as previously described, was used. 20 g of PS powder was constantly stirred in a quartz glass-covered beaker within 600 ml of deionized water (55°C) using a PTFE coated magnetic stirrer at 150 rpm. To ensure complete darkness, the experiment was run inside a dark chamber. Samples were taken in the same intervals as the UV experiment, and processed and analyzed equally.

2.2.2 Gel Permeation Chromatography (GPC)

Measurements of the MWD were performed via GPC using a Waters gel permeation chromatography set equipped with a 515 HPLC Pump, 2707 Autosampler, 2414 Refractive Index Detector and 2998 Photodiode Array Detector (Waters GmbH, Eschborn, Germany). The column set consisted in a guard column (ResiPore Guard, 5 x 0.75 cm, particle size 3 µm) and two separation columns (ResiPore Guard, 30 x 0.75 cm, particle size 3 µm). Tetrahydrofuran (THF) was used as the mobile phase and calibration was performed using narrow distributed PS standards. A sample volume of 100 µl (1 mg/ml) was measured with a flow rate of 0.5 ml/min at ca. 30°C. 1,2-dichlorobenzene was used as internal standard.

Tensile bars for GPC analysis were prepared by removing the near-surface layer to an approximate thickness of 0.05 mm with a scalpel. For GPC analyses of tensile bars and particles, 2 mg were dissolved in 2 ml THF and filtered with a 0.2 µm syringe filter. M_n, M_w and Đ were determined using the software EMPOWER 3 (Waters).

2.2.3 Scanning Electron Microscopy (SEM) and Energy-dispersive X-ray spectroscopy (EDX)

For visualizing surface changes of the bars and particles during accelerated weathering, field-emission scanning electron microscopy (FESEM) was performed with a Zeiss LEO 1530 (Carl Zeiss Microscopy GmbH, Jena, Germany) and a Zeiss ULTRA PLUS (Carl Zeiss Microscopy GmbH, Jena, Germany), each at an acceleration voltage of 3 kV.

Energy-dispersive X-ray spectroscopy (EDX) for determination of the carbon to oxygen ratio was performed on a FEI Quanta FEG 250 at 5 kV equipped with a 100 mm^2 Thermo Fisher UltraDry EDX detector and an Everhart-Thornley electron detector. To prepare the tensile bars, a block of the sample was cut normal to the weathered surface with a glass knife using an ultramicrotome. Tensile bars and particles were coated with a thin layer of platinum by a Cressington 208 HR sputter coater using an argon plasma.

2.2.4 Particle Size Analysis

Particle size distributions of each sample were measured using a Microtrac FlowSync Particle Size Analyzer (Microtrac Retsch GmbH, Haan, Germany). This instrument uses laser diffraction (3 lasers and 2 detectors) coupled with dynamic image analysis. Measurements were run as wet analysis using deionized water as the mobile phase. 2-5 mg of particles were added to 2 ml of 5 wt.-% $Na_4P_2O_7$ and a few droplets of Tween® 20 detergent to avoid aggregation. This mixture was poured into the water-filled measuring cell and diluted with 200 ml water. A 60 second ultrasound treatment (40 kHz) was further performed to ensure complete suspension of the particles. The values display the average of three measurements (Tabs. S2 and S3).

2.2.5 Mechanical Testing

Tensile testing of 1A type tensile bars was performed according to ISO 527-2 using a universal testing machine (Zwick Z020, ZwickRoell GmbH & Co. KG, Ulm, Germany) with an extensometer. The values for the elongation at break (ε_B) are averaged from five replicates for each exposure time.

2.2.6 Solid-State NMR Spectroscopy

All ^{13}C CP MAS NMR spectroscopic experiments were acquired with a Bruker Avance-III HD spectrometer operating at a B_0 field of 9.4 T. The ^{13}C (ν_0 = 100.6 MHz) MAS NMR spectra were obtained with a ramped ^{1}H-^{13}C cross polarization (CP) experiment using a commercial 3.2 mm triple resonance probe (Bruker). The spectra were recorded with a spinning frequency of 20 kHz and a contact time of 2.0 ms. The corresponding nutation frequency υ_{nut} for the ^{13}C channel was set to 50 kHz while for the ^{1}H channel the nutation frequency was varied linearly from 26 kHz to 53 kHz. During acquisition, proton broadband decoupling with a spinal-64 sequence (υ_{nut} (^{1}H) = 70 kHz) was applied. All ^{13}C NMR spectra were referenced to tetramethylsilane (TMS) using the secondary standard adamantane. The spectra were deconvoluted with the simulation package SOLA included in Topspin 3.2. To obtain quantitative spectral intensities, we used a multi-pulse CP sequence (Fig. S3).[1] For this sequence, several CP blocks (contact time 500 µs, υ_{nut} (^{13}C) = 50 kHz, 40 kHz $\leq \upsilon_{nut}$ (^{1}H) $\leq$ 55 kHz) are applied, separated by a time t_z of 3 s to allow for the proton spins to relax. The $(90°)_{-x}$ pulses at the end and the beginning of each CP block were set to 2.5 µs (^{1}H) and 3.8 µs (^{13}C).

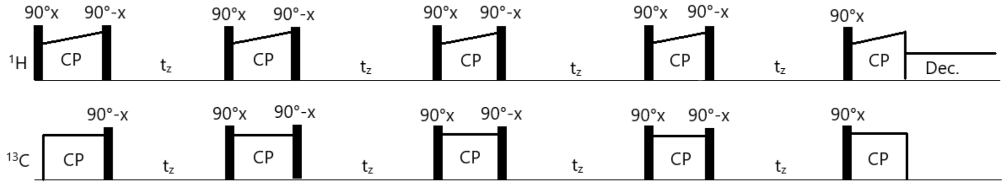

Figure S3 Quantitative multi-CP sequence[1] for determining quantitative intensities for otherwise non-integrable CP MAS NMR spectroscopic experiments. The individual CP blocks are separated by a time t_z. During this time, the carbon and proton signal is stored in z-direction using $(90°)_{-x}$ pulses on both channels at the end of each CP block. The time t_z is short enough to leave the carbon magnetization unchanged due to the long ^{13}C spin-lattice relaxation times. A further $(90°)_x$ pulse turns the magnetization back to the xy-plane and the next CP block is applied. After several blocks, the ^{13}C magnetization of the nuclei belonging to different chemical sites saturates and a quantitative spectrum is obtained.

All ^{13}C MAS NMR spectra were refined using the Sola fitting program included in Topspin 3.6. It applies a pseudo-Voigt function for each resonance (equation given below) with A being the amplitude, w the Gauss/Lorentz ratio, b the broadening and x_0 the isotropic chemical shift of the resonance.

$$f(x) = A * \left[(1-w)\frac{2b}{4\pi(x-x_0)^2+b^2} + w\,\frac{\sqrt{4ln2}}{\sqrt{\pi}b}\,e^{-\frac{4ln2}{b^2}(x-x_0)^2}\right]$$

As Sola does not provide certainty intervals for the individual refinement parameters, we determined the errors for the peak intensities for the polymer defects (ketone, carboxy and peroxide groups) by varying the amplitudes of the resonances, but making sure that the modified simulated line shapes still match the observed ones within the signal-to-noise-ratio, thus keeping the refinement in an acceptable range. The errors of the defect proportions were then derived by applying error propagation.

2.2.7 Simulation of Molecular Weight Distributions of Weathered PS

MC simulations of the degradation were conducted in MatLab R2009b using the experimental MWD of reference PS with 23500 initial polymer chains, represented by their molecular mass, to provide a sufficient statistic. For every timestep, either

one chain scission in a chain or one crosslink between two chains was carried out. The occurrence of these two processes was randomly selected within the adjustable probabilities for crosslinks P_{cl} and for chain scissions $P_{cs} = 1 - P_{cl}$. In case of chain scissions, a randomly chosen polymer chain was cut at a random position within the chain, resulting in two chains with reduced molecular weight. To avoid the formation of soluble decomposition products, which cannot be detected in the GPC experiments, chains shorter than or equal to 3 PS repeating units (RUs, M = 312 g/mol) were rejected from the cutting process. In case of crosslinking, two chains were randomly chosen and combined by addition of their molecular weights. If one chain was randomly selected twice, crosslinking occurs within the same chain, which does not change the molecular weight for this step. This procedure was repeated until we reached a MWD comparable to the experimental distribution for the longest exposure time. The crosslink density is defined as the total number of performed crosslinks, divided by the total number of RUs. The proportion of end groups corresponds to the total number of chain scissions, multiplied by two and divided by the total number of RUs for all chains.
The code is available on request.

2.2.8 Calculation of Defect Proportions

To calculate the proportion of the chemical groups of ketones, carboxylic acids and peroxides, one first has to calculate the proportion of styrene RUs (p_{ru}) relative to the proportion of the defects. This is given by

$$p_{ru} = [1 - (8*I_k) - (2*I_c) - (8*I_p)]/8 \qquad (1)$$

while I_k is the relative intensity of the ketone resonance, I_c of the carboxylic acid resonance and I_p of the peroxide resonance on the total spectral intensity (normalized to 1). From the total intensity, one has to subtract 8-times the intensity of the ketone resonance intensity, since one ketone group contains 8 carbon atoms. Analogously the carboxylic acid group contains 2 and the peroxide group contains 8 carbons. The result is the total spectral intensity of carbons from the styrene RUs. This divided by 8, since one styrene RU contains 8 carbons, gives the relative proportion of styrene RUs. The absolute proportion of the ketone (ap_k), carboxylic acid (ap_c) and peroxide groups (ap_p) is then given by

$$\begin{aligned} ap_k &= I_k/(p_{ru} + I_k + I_c + I_p) \qquad (2)\\ ap_c &= I_c/(p_{ru} + I_k + I_c + I_p)\\ ap_p &= I_p/(p_{ru} + I_k + I_c + I_p) \end{aligned}$$

since the ratio of the different groups is $I_k : I_c : I_p : p_{ru}$. The absolute proportions are plotted in Fig. 6c.

From the NMR and GPC data, the minimal average number of crosslinks per macromolecule can be calculated.
First, one defines an average mass M_{NMR} (dependent on the weathering time t), which is the average mass of individual polymer chains when crosslinks are not considered, e.g. if three chains are crosslinked together. M_{NMR} is given by the average individual mass of the three chains, averaged over the whole sample (Fig. S4).
Further, the average polymer mass derived from the GPC experiments, which includes polymer structures with crosslinks, is defined as M_{GPC} (see Tab. S5 and Fig. S11). We neglect the change of the average mass per RU M_{ru} with weathering, and assume that the average mass equals the mass of the PS RU (104.15 g/mol). Even for a large amount of degradation products, like in our experiments, this is valid within ± 3 %, since the averaged molecular weight of the degradation products with respect to their proportion in the degraded polymer is similar to the molecular weight of the styrene RUs. It is then obvious that is must hold

$$M_{NMR} = M_{GPC}/(cl+1) \qquad (3)$$

while cl is the minimum average number of crosslinks per molecule.

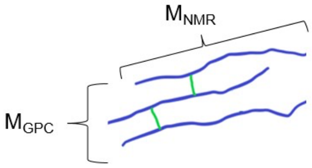

Figure S4 Illustration of the definition of M_{NMR} and M_{GPC}. The blue lines represent individual polymer chains, the green lines represent crosslinks.

Now we consider the proportion of end groups. EG_A should be the proportion of all end groups on the total number of RUs, EG_N the proportion of new emerged end groups, due to the weathering, and EG_0 the proportion of end groups at the beginning of the experiment, without weathering. It holds

$$EG_A = EG_N + EG_0 \ . \tag{4}$$

The proportion of new end groups EG_N is given by the NMR results and is the sum of the proportion of ketone and carboxylic end groups:

$$EG_N = ap_k + ap_c \tag{5}$$

EG_0 is given by the average polymer mass at the beginning

$$EG_0 = 2 * \frac{M_{ru}}{M_{GPC0}} \ , \tag{6}$$

whereby M_{GPC0} is the average molecular weight without weathering. The factor of 2 occurs because every chain contains 2 end groups. Thus, the proportion of all end groups EG_A can be calculated. However, EG_A itself is linked to the average NMR molecular weight M_{NMR} (s. above) via

$$EG_A = 2 * \frac{M_{ru}}{M_{NMR}} \ . \tag{7}$$

Combining equations (3) and (7) the minimal average number of crosslinks per macromolecule cl can be calculated. This over the total number or RUs per macromolecule is defined as the crosslink density, as shown in Fig. 6c.

3. Results

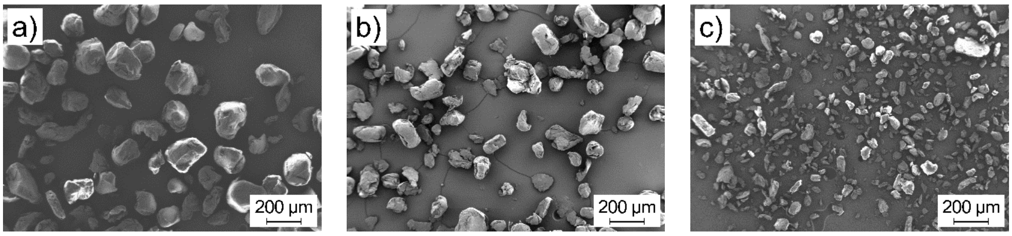

Figure S5 SEM micrographs of PS particles. a) Reference material, b) 800 h and c) 2000 h of exposure and mechanical stress by stirring.

Table S2 Average particle size values of all particle samples. Measurement 1-3 are displayed, values of all three measurements are averaged.

Particle Size Data – Simulated Solar Radiation				
Weathering Time	**Measurement 1**	**Measurement 2**	**Measurement 3**	**Average Size**
hours	*µm*	*µm*	*µm*	*µm*
0	160.1	159.5	159.8	159.8
24	164.3	164.6	164.2	164.4
50	162.8	162.9	164.0	163.2
100	161.2	160.9	161.8	161.3
200	156.6	156.5	155.9	156.3
400	153.4	152.2	151.2	152.3
600	139.5	138.5	138.1	138.7
800	111.8	111.4	110.6	111.3
1200	93.42	88.92	87.77	90.04
1600	63.99	63.50	63.39	63.63
2000	50.42	50.20	50.08	50.23
2400	34.72	34.32	34.49	34.51
2800	29.91	29.58	29.52	29.67
3200	22.81	22.56	21.42	22.26

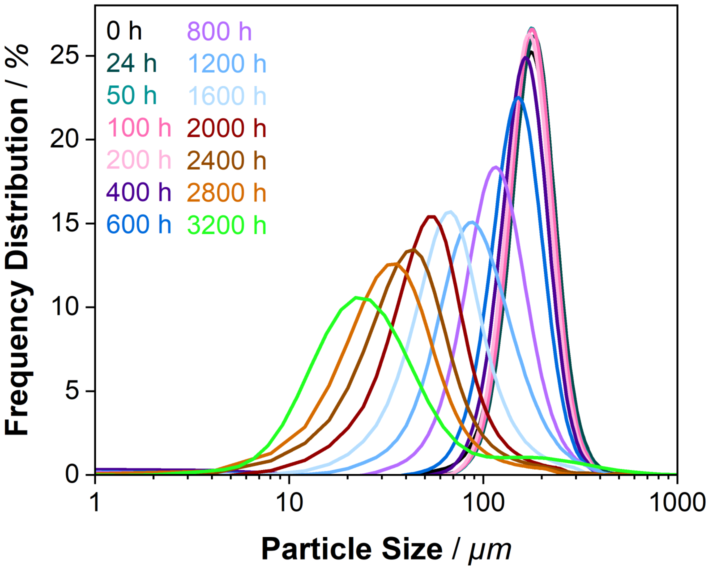

Figure S6 Particle size distribution of PS particles from 0 - 3200 h of weathering.

Table S3 Average particle size values of all particle samples from the dark control experiment. Measurement 1-3 are displayed, values of all three measurements are averaged.

Particle Size Data – Dark Control Experiment				
Experiment Runtime	**Measurement 1**	**Measurement 2**	**Measurement 3**	**Average Size**
hours	*μm*	*μm*	*μm*	*μm*
0	158.2	158.6	158.9	158.6
24	158.9	158.1	158.5	158.5
50	150.0	151.0	150.3	150.4
100	152.4	153.5	151.6	152.5
200	152.3	152.7	153.1	152.7
400	150.6	150.7	150.6	150.6
600	151.9	153.8	155.7	153.8
800	155.7	155.7	156.4	155.9
1200	154.3	154.6	154.3	154.4
1600	152.8	151.9	152.1	152.2
2000	153.2	153.2	153.4	153.3
2400	152.5	153.0	153.9	153.1
2800	156.0	156.1	156.0	156.0
3200	151.3	152.0	151.8	151.7

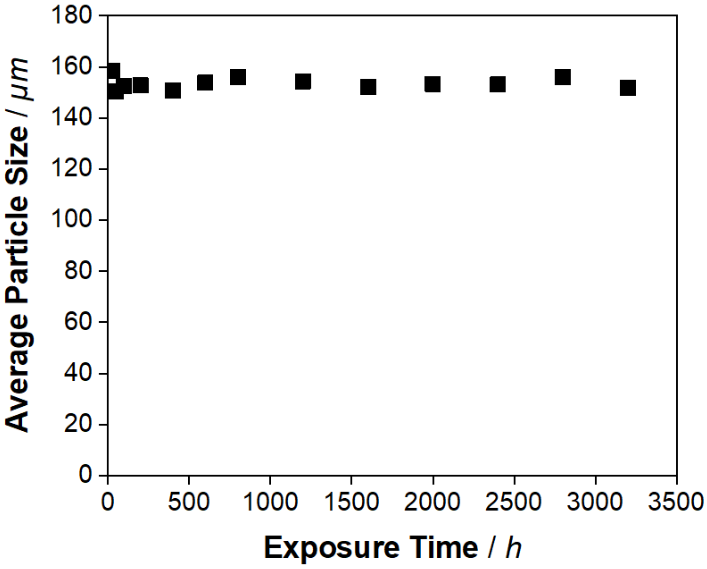

Figure S7 Average particle size of the dark control experiment. The average particle size does not change with increasing experiment duration, as observed for the weathering experiment (Fig. 1b).

219

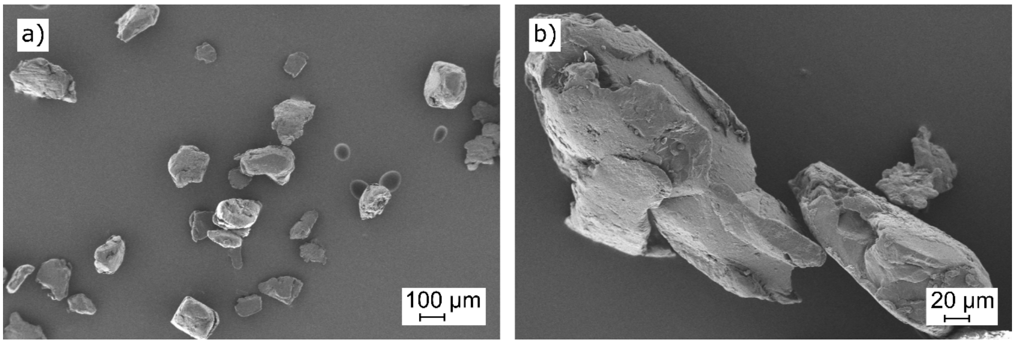

Figure S8 SEM images of particles from the dark control PS experiment after 2000 h. a) Overview of multiple particles at 50x magnification and b) particles at 250x magnification showing their surface characteristics. They are not rounded and show no signs of degradation.

220

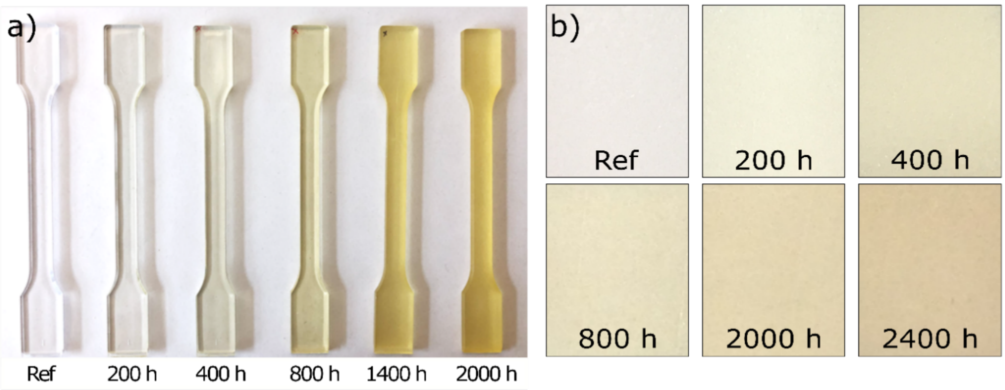

Figure S9 Optical changes showing distinct yellowing with increasing simulated solar radiation of a) Tensile bar PS samples and b) PS particles.

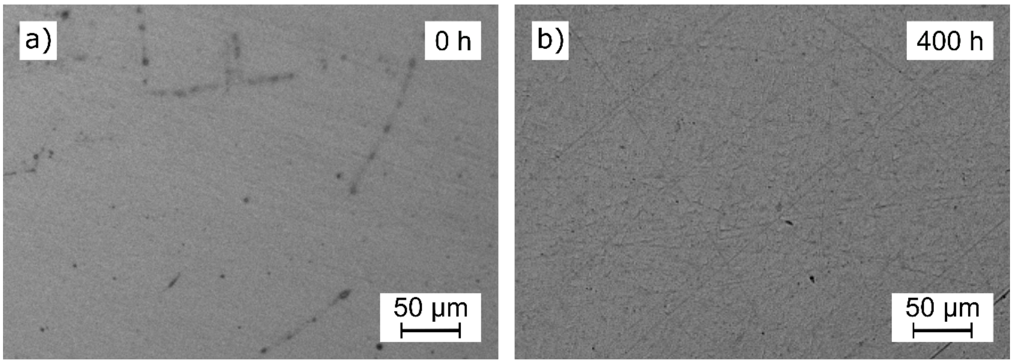

Figure S10 a) Optical microscopy image displaying the surface characteristics of a bar surface at 0 h. b) Optical microscopy image of a bar surface after 400 h of weathering. No change in surface morphology can be observed until this stage.

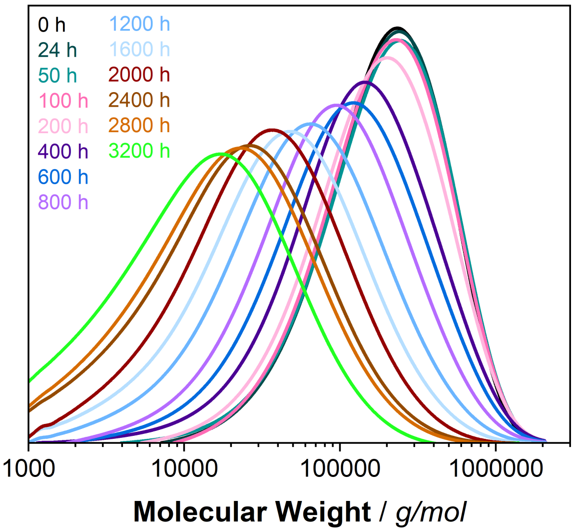

Figure S11 Molecular weight distribution for all samples that were taken from the particle PS experiment (0-3200 hours).

Table S4 Average molecular weight (Mn and Mw) in g/mol and dispersity (Đ) from GPC measurements as a function of the weathering time for both PS tensile bar surface material and PS particle samples.

Weathering Time [h]	Tensile Bars			Particles		
	M_n [g/mol]	**M_w** [g/mol]	Đ	**M_n** [g/mol]	**M_w** [g/mol]	Đ
0	125000	281000	2.25	125000	281000	2.25
200	83700	220600	2.63	103200	252600	2.45
400	62900	195800	3.07	65700	210300	3.20
800	7500	30500	3.87	43500	147000	3.38
1400	7900	29000	3.67			
2000	2900	7300		14800	59200	4.01

Table S5 Average molecular weight (M_n and M_w) in g/mol and dispersity (Đ) from GPC measurements as a function of the weathering time from 0 to 3200 hours of simulated solar exposure for PS particle samples.

GPC Data – Simulated Solar Radiation			
Weathering Time	**M_n**	**M_w**	**Đ**
hours	*g/mol*	*g/mol*	
0	125000	281000	2.25
24	125100	275300	2.20
50	114900	274600	2.39
100	122200	270200	2.21
200	103200	252600	2.45
400	65730	210300	3.20
600	54450	181400	3.33
800	43470	147000	3.38
1200	25670	105500	4.11
1600	17800	78100	4.40
2000	14800	59200	4.01
2400	8700	41600	4.79
2800	7900	36400	4.62
3200	5400	25100	4.64

226

Table S6 Average molecular weight (M_n and M_w) in g/mol and dispersity (Đ) from GPC measurements of the control dark experiment.

GPC Data – Dark Control Experiment			
Experiment Runtime	**M_n**	**M_w**	**Đ**
hours	*g/mol*	*g/mol*	
0	125000	281000	2.25
24	114600	273700	2.39
50	113100	273100	2.41
100	117700	269700	2.29
200	117200	267700	2.28
400	112900	276100	2.45
600	106200	260400	2.45
800	95800	236600	2.47
1200	106300	270600	2.54
1600	117800	274600	2.33
2000	118700	269100	2.27
2400	108700	252800	2.33
2800	110300	253100	2.29
3200	104600	248200	2.37

227

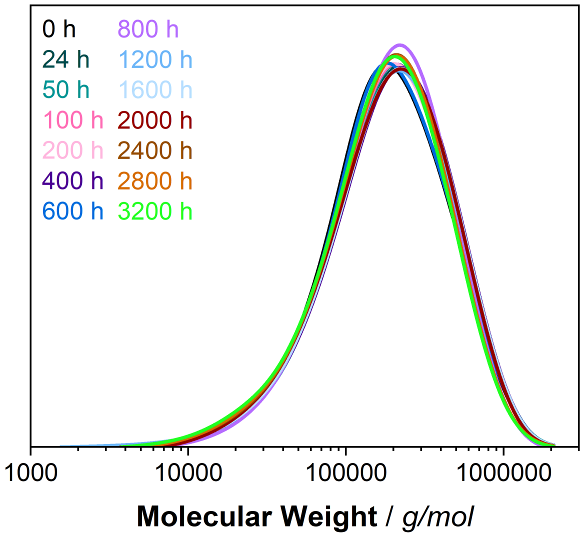

Figure S12 Molecular weight distribution for all samples from the dark control experiment.

228

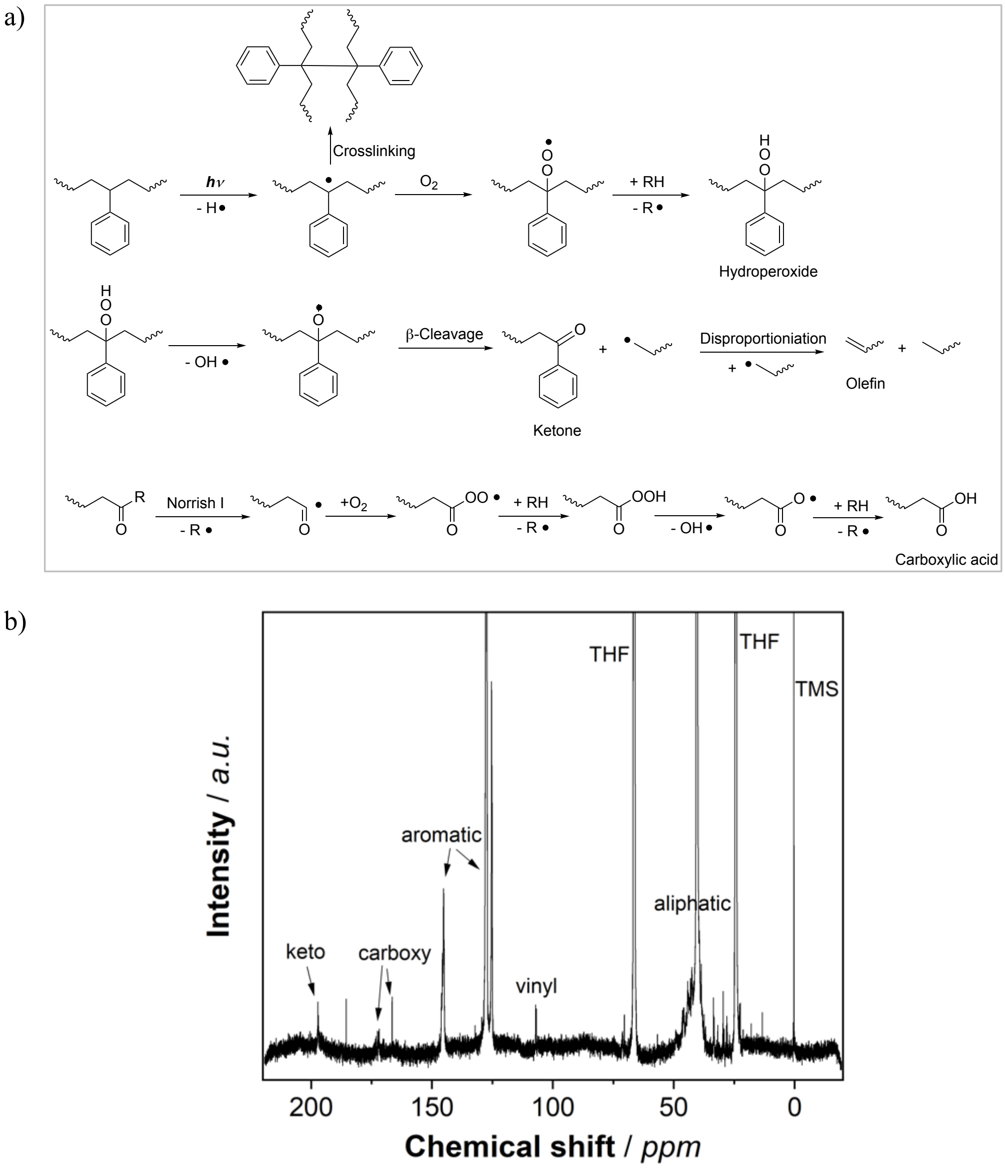

Figure S13 a) Mechanism for the formation of crosslinks, hydroperoxides, keto groups, olefins and carboxylic acids during the photooxidation of PS b) Liquid-state NMR spectrum of ^{13}C enriched (α position) PS in THF. The resonances of carboxy, keto and vinyl groups are visible. Only one keto resonance is detectable at 197 ppm, indicating that mainly end chain keto groups and no in chain keto groups evolve during degradation.

Table S7 Correction factors of the individual resonances derived from the quantitative NMR spectra.

	c_{ketone}	$c_{carboxylic\ acid}$	$c_{peroxide}$
Plate surface	0.75	0.92	0.70
Particles	0.70	0.80	0.68

To further corroborate the validity of the quantitative CP measurements, the derived intensities for the resonances for the ipso carbon, the aromatic CH groups as well as the aliphatic CH/CH_2 units were compared the ones derived with single pulse excitation and the expected intensity ratio of 1:5:2. The intensity ratios for the SP NMR spectrum of the tensile bars weathered for 2000 h amounts to 0.97:5:2.18. The ratios from the quantitative CP NMR spectra are 1.05:5:1.9 for the particle sample

(3200 h) and 0.99:5:2.13 for the tensile bar sample (2000 h). The small deviations show the accuracy of the quantitative experiments. Due to the broadband excitation profile of the SP and CP experiments, we are confident that also the intensities of the ketone, carboxy and peroxide resonances, are quantitative. For the latter a crosscheck using a SP NMR experiment is not possible due to the long spin-lattice relaxation times ($T_1 > 50$ s), limited measurement times and thus poor signal-to-noise ratios for the defects.

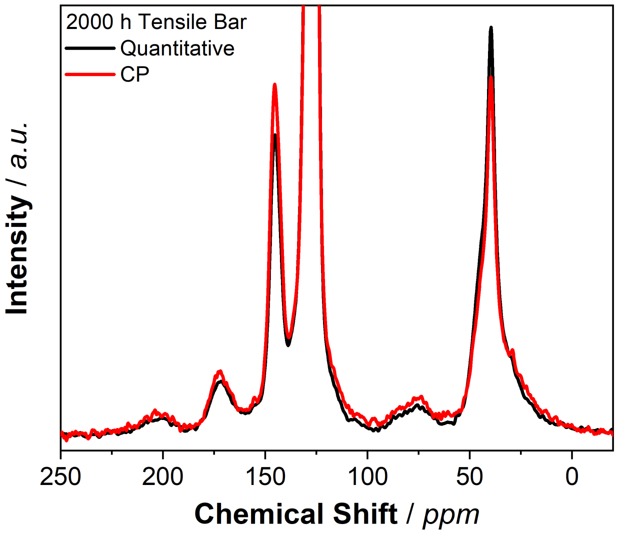

Figure S14 Comparison of a quantitative (black) and normal cp (red) spectrum for the 2000 h bar surface sample. Both spectra are normalized to the intensity of the main aromatic resonance at 130 ppm. The measurement time of the quantitative spectrum was 4 days compared to 1 day for the normal cp spectrum.

Table S8 Deconvolution parameters for the 2000 h CP PS plate spectrum. Peak 1, 2 and 9 resemble the ketone, carboxy and peroxide resonance, respectively. The intensities are normalized to the intensity of peak 6 (main aromatic resonance). The errors in brackets for resonances 1, 2 and 9 were derived based on varying the signal intensity within the signal-to-noise-ratio (see section 2.2.6).

peak	**chemical shift**	**intensity**	**G/L ratio**	**broadening**
1	203.88	42.6 (6.0)	0.5	1705
2	172.11	96.0 (7.0)	0.45	1202
3	155.37	16.2	0.59	870
4	145.23	213.0	1.00	632
5	137.55	11.7	0.47	385
6	127.86	1000	0.20	497
7	125.92	139.7	1.00	331
8	122.40	54.9	0.47	1992
9	75.56	70.7 (7.0)	0.67	2027
10	45.88	119.7	0.15	750
11	39.67	204.0	0.22	477
12	34.19	15.7	0.00	534
13	29.38	4.9	0.51	164
14	26.64	132.9	0.20	2005
15	0.94	77.6	0.50	4500

Table S9 Intensities of the resonances obtained from the deconvolution procedure for the ^{13}C CP MAS NMR spectra of the PS particles. Additionally, the estimated errors for the defects derived as described in section 2.2.6 are given. The term "quant." refers to the ^{13}C MAS NMR spectrum obtained with quantitative CP. The hyphen marks resonances which could not be detected with sufficient accuracy.

Weathering time / h	**aromatic CH**	**aromatic C_{ipso}**	**aliphatic**	**ketone**	**ketone error**	**carboxy**	**carboxy error**	**peroxide**	**peroxide error**
3200 quant.	1062	222	407	8.5	1	16.5	1	13	1
3200	1217	297	423	14	3	24	3	22	2
2800	1178	304	427	10.5	2	18	2	21	3
2400	1190	273	427	5	3	14	2	17	2.5
2000	1077	269	400	3	2	11	3	15.5	2.5
1600	1086	247	397	-	-	7.5	2.5	8.5	2
1200	1196	311	441	-	-	7.5	2.5	5.5	2
800	1237	341	445	-	-	6.5	2.5	2	2
400	1235	328	457	-	-	3.5	3	-	-
0	1248	337	455	-	-	-	-	-	-

Table S10 Intensities of the resonances obtained from the deconvolution procedure for the ^{13}C CP MAS NM spectra of PS tensile bars. Additionally, the estimated errors for the defects derived as described in section 2.2.6 are given. The term "quant." refers to the ^{13}C MAS NMR spectrum obtained with quantitative CP. The hyphen marks resonances which could not be detected with sufficient accuracy.

Weathering time / h	**aromatic CH**	**aromatic C_{ipso}**	**aliphatic**	**ketone**	**ketone error**	**carboxy**	**carboxy error**	**peroxide**	**peroxide error**
2000 quant.	1176	232	399	32	5	86	6	48	5
2000	1168	227	345	43	6	94	7	71	7
1400	1167	246	370	35	6	89	7	82	7
800	1146	267	397	17	3	39	5	43	4.5
400	1164	312	379	-	-	4	3	7	4.5
200	1150	300	375	-	-	4.3	3	6.5	4.5
0	1248	337	455	-	-	-	-	-	-

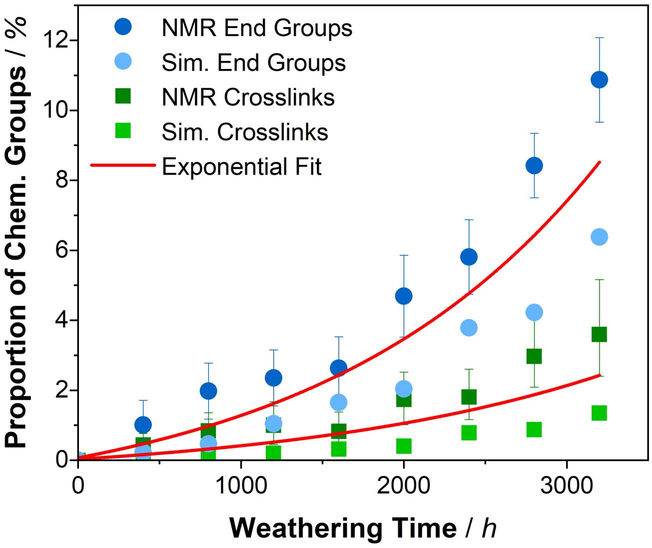

Figure S15 Proportion of end groups (red) and crosslink density (green) as a function of weathering time from the NMR data and the MC simulations. The lines are guides for the eyes.

Supplementary References

1. Johnsen, R. L.; Schmidt-Rohr, K. Quantitative solid-state 13C NMR with signal enhancement by multiple cross polarization. *Journal of Magnetic Resonance* **2014**, 239, 44-49.

8.2 Degradation of Low-Density Polyethylene to Nanoplastic Particles by Accelerated Weathering.

Science of the Total Environment 826 (2022) 154035

Contents lists available at ScienceDirect

Science of the Total Environment

journal homepage: www.elsevier.com/locate/scitotenv

Degradation of low-density polyethylene to nanoplastic particles by accelerated weathering

Teresa Menzel [a,1], Nora Meides [b,1], Anika Mauel [c,1], Ulrich Mansfeld [d], Winfried Kretschmer [e], Meike Kuhn [f], Eva M. Herzig [f], Volker Altstädt [a], Peter Strohriegl [b], Jürgen Senker [c,*], Holger Ruckdäschel [a,*]

[a] *Department of Polymer Engineering, University of Bayreuth, Universitätsstraße 30, 95447 Bayreuth, Germany*
[b] *Department of Macromolecular Chemistry I, University of Bayreuth, Universitätsstraße 30, 95447 Bayreuth, Germany*
[c] *Department of Inorganic Chemistry III, University of Bayreuth, Universitätsstraße 30, 95447 Bayreuth, Germany*
[d] *Bavarian Polymer Institute, University of Bayreuth, Universitätsstraße 30, 95447 Bayreuth, Germany*
[e] *Department of Inorganic Chemistry II, University of Bayreuth, Universitätsstraße 30, 95447 Bayreuth, Germany*
[f] *Dynamics and Structure Formation - Herzig Group, Institute of Physics, University of Bayreuth, Universitätsstraße 30, 95447 Bayreuth, Germany*

HIGHLIGHTS

- Knowledge on environmental degradation from macro- to microplastic is lacking.
- Long-term, accelerated laboratory weathering of semi-crystalline LDPE
- Combining a multitude of analytical methods on a macro- and microscopic scale
- Development of a three-stage degradation model for semi-crystalline polymers
- Nanoplastic particles visualized, strongly adhering to microplastic particles

GRAPHICAL ABSTRACT

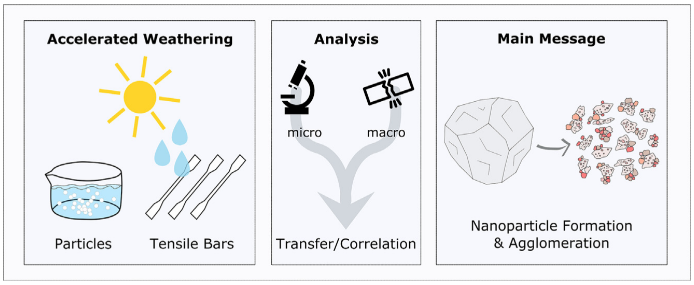

ARTICLE INFO

Article history:
Received 9 December 2021
Received in revised form 25 January 2022
Accepted 16 February 2022
Available online 22 February 2022

Editor: Dimitra A. Lambropoulou

Keywords:
Microplastic
Agglomeration
Surface fragmentation
Three-stage model
Semi-crystalline
Polymer chain defects

ABSTRACT

When plastics enter the environment, they are exposed to abiotic and biotic impacts, resulting in degradation and the formation of micro- and nanoplastic. Microplastic is ubiquitous in every environmental compartment. Nevertheless, the underlying degradation processes are not yet fully understood. Here, we studied the abiotic degradation of commonly used semi-crystalline, low-density polyethylene (LDPE) in a long-term accelerated weathering experiment combining several macro- and microscopic methods. Based on our observations, the degradation of LDPE proceeds in three stages. Initially, LDPE objects are prone to abrasion, followed by a period of surface cracking. A large number of secondary particles with a high degree of crystallinity are formed, with sizes down to the nanometer scale. These particles consist of highly polar oligomers leading to agglomeration in the final stage. We therefore suppose that weathered microplastic and nanoplastic particles will attach to colloidal environmental matter. This offers an explanation for the absence of free nanoplastic particles in natural samples.

---

[*] Corresponding authors.
E-mail addresses: juergen.senker@uni-bayreuth.de (J. Senker), holger.ruckdaeschel@uni-bayreuth.de (H. Ruckdäschel).
[1] These authors contributed equally to this work.

http://dx.doi.org/10.1016/j.scitotenv.2022.154035

1. Introduction

The global plastic waste generation has exceeded 300 million tons annually since 2015. With almost one third, polyethylene (PE) represents the largest share (Geyer et al., 2017). The combination of easy processing, chemical resistance, and a low price makes PE a good candidate for various applications. High-density PE (HDPE), consisting of slightly branched polymer chains, is used for both long-term applications e.g., pipes, tubes, and short-term applications like milk and shampoo bottles. In contrast, highly branched low-density PE (LDPE) is mainly used for cheap consumer goods (reusable bags, trays, agricultural films, food packaging) with a lifetime of less than one year. Due to the steadily increasing demand for packaging, PE is one of the most abundant polymers worldwide. Consequently, PE is ubiquitous in marine and terrestrial environments (Andrady, 2011; Bishop et al., 2020; Da Costa et al., 2018; Engler, 2012) due to improperly disposed plastic waste or littering. Once entering the environment, abiotic and biotic impacts lead to progressive degradation, fragmentation, and the formation of micro- and nanoplastic particles (Bishop et al., 2020; Da Costa et al., 2018; Fairbrother et al., 2019; Julienne et al., 2019; Meides et al., 2021).

Recently, microplastic (MP) and nanoplastic (NP) have been defined by their largest dimension, ranging from 1 μm to <1000 μm and 1 nm to <1000 nm, respectively. These include various polymer types (thermoplastics, thermosets, elastomers, inorganic/hybrids) and shapes (spherical, cylindrical, spheroidal, fragments, films, fibers) (Hartmann et al., 2019). The small particle size facilitates transport and distribution in environmental compartments. Therefore, MP can be easily transported by surface waters to larger water bodies or by wind in the atmosphere (Laermanns et al., 2021; Lehmann et al., 2021; Liu et al., 2019; Petersen and Hubbart, 2021; Wright et al., 2020; Zhou et al., 2018). Environmental samples collected from aquatic and terrestrial compartments and investigated in various studies contain a multitude of polymers. Due to their use as cheap consumer goods, PE, polypropylene (PP), and polystyrene (PS) (Hu et al., 2018; Morét-Ferguson et al., 2010; Wilber, 1987; Xu et al., 2020) are prominent among the plastics found in nature.

The environmental degradation of PE has been extensively studied (Biale et al., 2021; Da Costa et al., 2018; Fernández-González et al., 2021; Gewert et al., 2018; Maria et al., 2011; Ojeda et al., 2011). In natural compartments, PE is exposed to several environmental stress factors often interfering with each other. In order to reduce the complexity and to better understand the influence of single stress parameters, laboratory experiments with a reduced parameter space are beneficial. Although biodegradation of PE has recently been discussed (Jeon et al., 2021), the complete conversion of a plastic carbon source to metabolites is not supposed to result in MP (Ghatge et al., 2020; Sander, 2019). Thus, abiotic degradation is more likely responsible for progressive deterioration of the physical and chemical structure, leading to fragmentation and resulting in the formation of MP particles. Recent weathering studies analyze chemical and morphological changes (Canopoli et al., 2020; Fernández-González et al., 2021; Martínez-Romo et al., 2015; Ojeda et al., 2011), study the evolution of crystallinity and brittleness (Garvey et al., 2020; Ojeda et al., 2011), investigate soluble oligomers (Biale et al., 2021; Gewert et al., 2018) and additive leaching (Suhrhoff and Scholz-Böttcher, 2016). A wide range of weathering sources, from natural to simulated solar radiation, as well as a variety of different lamps, intensities, and exposure times were used. Environmental samples, as well as pristine polymers with varying geometries (films, powders, pellets, or pipes), and commercial disposables with a complex multilayer composition have been investigated in these studies making comparisons challenging.

To simplify the complexity of environmental conditions, we designed a laboratory-controlled experiment that allows us to study the interaction between two prominent degradation mechanisms and their impact on the progressive deterioration of LDPE. The first mechanism is photooxidation. Photo-initiated radical reactions lead to either crosslinking or chain-scissions, the latter introducing oxygen-containing functional groups (Fotopoulou and Karapanagioti, 2017). The initial oxidation step is the formation of peroxides, followed by generation of alcohols, ketones, or aldehydes (Chabira et al., 2008; Grause et al., 2020; Mowery et al., 2005). The latter can be further oxidized to carboxylic acids (Fig. S8). Upon weathering, the long and nonpolar PE chains gradually transform into increasingly polar oligomers, which eventually become soluble (Biale et al., 2021; Gewert et al., 2018). The second mechanism is physical degradation by mechanical stress. Changes in crystallinity and brittleness lead to particle fragmentation and rupturing. This, in turn, produces a large number of small, defect-rich particles during weathering (Garvey et al., 2020; Meides et al., 2021).

The interplay between the two mechanisms was recently studied for amorphous PS. It was shown that PS degrades in two stages. The first stage is characterized by surface abrasion, followed by particle fragmentation in the second stage (Meides et al., 2021). Once degradation by photooxidation has reduced the molecular weight sufficiently, the sample embrittles and the turnover to stage II is initiated. It is an open question whether LDPE degradation proceeds in the same manner for two reasons: First, LDPE is semi-crystalline, adding complexity to the degradation processes (Garvey et al., 2020). Second, the glass transition temperature of LDPE is far below typical environmental degradation temperatures, allowing for rapid chain dynamics within the amorphous regions (Han et al., 1994; Lechner et al., 2014; Wool, 2008).

Thus, we conducted a laboratory-controlled long-term accelerated weathering study of semi-crystalline, additive-free LDPE (LyondellBasell, 2021) combing results from two sample geometries. While macroscopic tensile bars were continuously exposed to simulated solar radiation, micrometer-sized particles were additionally subjected to mechanical stress. The study of chemical and morphological changes in both sample geometries allowed us to link the results of the mechanical testing of the tensile bars with LDPE particle degradation. In this way, we were able to bridge a fundamental experimental gap since mechanical testing is not possible for MP particles. This approach allows the development of a model for the degradation of LDPE.

We monitor photooxidative degradation by combining Gel Permeation Chromatography (GPC), ^{13}C Magic-Angle Spinning (MAS) as well as high-temperature (HT) ^{1}H liquid-state Nuclear Magnetic Resonance (NMR) Spectroscopy and Monte Carlo (MC) Simulations. As previously shown (Meides et al., 2021), this combination enables the identification of relevant defects, determining their proportions, and estimating average chain compositions as a function of the weathering time. Energy-Dispersive X-ray Spectroscopy (EDS) adds depth-dependent information, whereas Fourier-Transform Infrared (FTIR) spectroscopy enables the determination of near-surface defects. Using ^{13}C MAS NMR spectroscopy for the main defect characterization has some advantages compared to other frequently used techniques like FTIR and Raman spectroscopy or thermo-analytical approaches such as pyrolysis-gas chromatography–mass spectrometry (Py-GC–MS) (Canopoli et al., 2020; Da Costa et al., 2018; Dong et al., 2020; Fairbrother et al., 2019; Fernández-González et al., 2021; Martínez-Romo et al., 2015; Nava et al., 2021; Ojeda et al., 2011). NMR analysis is non-destructive and provides volume-averaged results for typical photooxidative defects like aldehydes, ketones, carboxylic acids, peroxides, and alcohols. With a multiple cross-polarization (multiCP) experiment, these defects can further be quantified to obtain defect proportions (Johnson and Schmidt-Rohr, 2014; Meides et al., 2021). Chemical changes are correlated to trends for the particle sizes (Particle Size Analyzer, Scanning Electron Microscopy (SEM)), the crystallinity (Differential Scanning Calorimetry (DSC), X-ray Diffraction (XRD)), and the mechanical properties (Tensile Testing). The laboratory-controlled conditions in combination with a broad range of analytical methods allow to probe and link the effects of chemical and physical degradation on various length- and time scales. The derived data thus offer a comprehensive understanding of the environmentally relevant abiotic degradation pathways for semi-crystalline LDPE.

2. Material and methods

2.1. Material

A commercially available, additive-free LDPE (Lupolen 1800P), delivered by LyondellBasell Industries (Basell Polyolefine GmbH, Wesseling, Germany), was used. The initial number- (M_n) and weight-average (M_w) molecular weight is M_n = 36,600 g/mol and M_w = 368,000 g/mol, respectively, the dispersity is $Đ = 10.1$ ($Đ = M_w/M_n$). Pellets were ground with an Ultra Centrifugal Mill ZM 200 (Retsch GmbH, Haan, Germany) and separated into several fractions by sieving with an Alpine Air Jet Sieve E200 LS (Hosokawa Alpine AG, Augsburg, Germany). We used the 125–200 μm fraction for the particle experiment. For the surface experiments, type 1A tensile bars (ISO 527-2) with 4 mm height were injection molded with an Arburg Allrounder 470H 1000-170 (Arburg GmbH, Loßburg, Germany).

2.2. Methods

2.2.1. Accelerated weathering

Particles and tensile bars were placed into a test chamber Q-SUN XE-3 (Q-LAB Corporation, Westlake, OH, USA) equipped with three xenon lamps and a Daylight-Q filter (Fig. S1) and irradiated with 60 W/m^2 (at 300–400 nm), corresponding to a total irradiance of 594 W/m^2. Compared to the average mid-European spectral irradiance, we achieve a five-fold acceleration (Fig. S2, Table S1). Relative humidity was set to 50%, chamber temperature to 38 °C.

For the particle experiment, we weighed 20 g LDPE powder into a quartz glass beaker covered with a quartz-glass lid to enable UV penetration from all sides. LDPE particles were constantly stirred in 600 ml deionized water (55 °C). We used a magnetic stirrer with a PTFE-coated stirring device. A total of 13 samples (1–2 g each) were extracted for analysis between 0 and 3200 h, filtered and dried at 40 °C under vacuum. As the xenon lamps were never switched off, the weathering time is identical to the total irradiation.

For the surface experiment, 80 tensile bars were exposed to weathering conditions according to ISO 4892-2:2011. One weathering cycle of 120 min irradiation includes an 18 min spray period with deionized water. The weathering cycle was repeated until an overall weathering time of 0, 200, 400, 800, 1400, 1600, 2000 and 3200 h was reached, and ten tensile bars were taken for each weathering time for sufficient statistics in tensile testing.

2.2.2. Gel Permeation Chromatography (GPC)

Molecular weight distribution (MWD), M_n, M_w, and Đ for particles and bars were measured via GPC using an Agilent (Polymer Laboratories Ltd.) PL-GPC 220 high-temperature chromatographic unit. The set is equipped with RI and PD detectors and three linear mixed bed and guard columns (Olexis). Analysis was performed at 150 °C (Pasch, 2001) using 1,2,4-trichlorobenzene (TCB) as the mobile phase. The samples were prepared by dissolving 2–3 mg polymer (0.1 wt.-%) in 1.5 ml of the mobile phase solvent (TBC) in an external oven at 150 °C under continuous stirring. The solutions were run without filtration. For the tensile bar surfaces, material from 0–1 mm, 1–2 mm, and 2–3 mm depth was collected by cutting orthogonal to the exposed surface. The molecular weights of the samples were referenced to linear HDPE standards (M_w = 142,000–701,000 g/mol, K = 40,600, and Alpha = 0.725) and were corrected with K and Alpha values for highly branched (high pressure) LDPE (K = 40,600 and Alpha = 0.550).

2.2.3. Scanning Electron Microscopy (SEM) and Energy-dispersive X-ray Spectroscopy (EDS)

For visualizing surface changes, field-emission scanning electron microscopy (FESEM) was performed on particles with a Zeiss ULTRA PLUS (Carl Zeiss Microscopy GmbH, Jena, Germany) at an acceleration voltage of 3 kV and a FEI Quanta 250 (Field Electron and Ion Company, Thermo Fisher Scientific, Hillsboro, USA) high-resolution field emission gun (FEG) scanning electron microscope at 10 kV. The tensile bar surfaces were investigated with a Zeiss ULTRA PLUS (Carl Zeiss Microscopy GmbH, Jena, Germany) at an acceleration voltage of 3 kV. For energy-dispersive X-ray spectroscopy (EDS), a 60 mm^2 Thermo Fisher UltraDry EDS detector was used on a Zeiss LEO 1530 (Carl Zeiss Microscopy GmbH, Jena, Germany) operating at 10 kV. Prior to the investigation, the bars were cut perpendicular to the exposed surface with a glass knife under cryo conditions using an ultramicrotome. Particles and bars were coated with a thin layer of platinum by a Cressington 208 HR sputter coater.

2.2.4. Particle size analysis

Particle size distributions and the average particle size were determined with a Microtrac FlowSync Particle Size Analyzer (Microtrac Retsch GmbH, Haan, Germany) with a lower detection limit of 10 nm. Measurements were performed in deionized water with 2–5 mg of particles, 2 ml of 5 wt.-% $Na_4P_2O_7$, and a few drops of a 2 wt.-% dioctyl sulfosuccinate sodium salt detergent. 60 s of ultrasound at 40 kHz were applied to avoid aggregation. The tabulated values display the average of three measurements (Table S2).

2.2.5. Mechanical testing

The exposed tensile bars were characterized by tensile testing according to ISO 527-2. Therefore, a Zwick Z020 (ZwickRoell GmbH & Co. KG, Ulm, Germany) was equipped with an extensometer. The measured values for the elongation at break (ε_B) were averaged from ten samples taken at each exposure time.

2.2.6. NMR spectroscopy

Liquid-state high-temperature ^{1}H NMR spectra were acquired with a Varian INOVA 300 spectrometer (^{1}H: ν_0 = 300 MHz) at 120 °C. The samples were prepared by dissolving 9–15 mg of the polymer in 0.5 ml $C_2D_2Cl_4$ at 120 °C before measuring. Solid-state ^{13}C MAS NMR spectra were recorded using a Bruker Avance-III HD spectrometer operating at a B_0 field of 9.4 T (^{13}C: ν_0 = 100.6 MHz), a 3.2 mm triple resonance probe (Bruker), and a spinning frequency of 20 kHz. Ramped ^{1}H^{13}C CP experiments were performed with a contact time of 2.0 ms, a ^{13}C nutation frequency ν_{nut} of 54 kHz, a ramped continuous wave (cw) pulse with ν_{nut} varying linearly from 40 kHz to 55 kHz, and ^{1}H spinal-64 decoupling (υ_{nut} (^{1}H) = 88 kHz) during acquisition. Quantitative ^{13}C MAS NMR spectra were obtained with fully relaxed single-pulse excitation (recycle delay 5000 s) for the particle sample weathered for 1600 h and with a multi-pulse CP sequence (Johnson and Schmidt-Rohr, 2014) for particle and surface samples exposed for 3200 h. For the latter, six short CP excitations (contact time: 500 μs, υ_{nut} (^{13}C) = 54 kHz, 40 kHz ≤ υ_{nut} (^{1}H) ≤ 53 kHz) sandwiched between 90° pulses on both channels were used, separated by a delay of 3 s to allow for the proton spin bath to relax. The ^{1}H and ^{13}C 90° pulses were adjusted to 2.5 μs and 3.8 μs, respectively. All spectra were deconvoluted with pseudo-Voigt functions using SOLA included in Topspin 3.6. All ^{1}H and ^{13}C NMR spectra were referenced with respect to tetramethylsilane (TMS).

2.2.7. Differential Scanning Calorimetry (DSC)

To determine the crystallinity of surfaces and particles, DSC measurements were performed on 8–10 mg sample material using a Mettler Toledo DSC 3+ and DSC 1 (Mettler-Toledo GmbH, Gießen, Germany). The surface material of tensile bars was scratched off from 0 to 1 mm depth. The samples were heated with 10 K per minute under N_2-atmosphere from 25 to 200 °C and cooled to 25 °C. An isothermal stage of 5 min was applied in between. The degree of crystallinity χ_c in the first heating cycle was determined with ΔH_m° = 293.6 J/g for a hypothetically 100% crystalline PE (Ojeda et al., 2011). A baseline correction was performed, and the melting peak was integrated using the STARe software. Two samples were measured for each exposure time with identical results.

2.2.8. X-ray Diffraction (XRD)

Powder X-ray diffractograms (PXRD) were measured with $Cu_{K\alpha}$ radiation (λ = 1.54 Å) in Bragg-Brentano geometry on a Panalytical EMPYREAM instrument (Malvern Panalytical GmbH, Kassel, Germany) using flat-plate samples spinning with 0.25 Hz, a 2Θ range of 5–50°, a step size of 0.013° and a PIXcel^{1D} detector. Prior to deconvolution with pseudo-Voigt profiles, air scattering was subtracted from the diffractograms, and a baseline correction was performed. Crystalline domain sizes were estimated with the Scherrer formula (K ~ 1) (Garvey et al., 2020; Scherrer, 1912).

Wide-angle X-ray Scattering (WAXS) was performed on a Xeuss 3.0 instrument (Xenocs SAS, Grenoble, France) with a $Cu_{K\alpha}$ source (λ = 1.54 Å), a Dectris EIGER 2R 1 M detector, and a sample-to-detector distance of 46.1 mm. Scattering experiments were carried out at room temperature under vacuum. The 2D scattering patterns were integrated using the XSACT software to obtain I(Ψ) data. The data were evaluated by analyzing the (110) reflex.

2.2.9. Fourier-Transform Infrared (FTIR) spectroscopy

FTIR spectra were recorded with a PerkinElmer Spectrum 100 (PerkinElmer, Waltham, USA) in attenuated total reflection (ATR) mode. For each sample, four scans between 650 and 4000 cm^{-1} with a resolution of 4 cm^{-1} were accumulated. The maximum peak height of the asymmetric CH stretching vibration at 2915 cm^{-1} was normalized using the Spectrum V.6.3.5 software.

3. Results

In this study, we performed accelerated weathering on LDPE particles and tensile bars. Under controlled abiotic laboratory conditions, both LDPE geometries were subjected to simulated solar radiation and water. While tensile bars were exposed to intervals of rain without mechanical stress, particles were constantly stirred in water and therefore additionally subjected to abrasion. Degradation was monitored using a variety of analytical tools covering macroscopic and atomic length scales.

3.1. Weathering of tensile bars and particles

For LDPE particles weathered in water, the effect of simulated solar radiation in combination with moderate mechanical stress from stirring leads to a decrease in particle size (Fig. 1). The first 400 h result in the formation of smoother surfaces by surface abrasion (Fig. 1a–b). We attribute this to stage I of our degradation model (Fig. 7). From 800 h onwards, smooth surfaces continuously evolve to rather rough shapes, indicating rapid break-up and the transition into stage II of particle fragmentation. However, no cracking of whole particles is observed (Fig. 1c), as in the case of PS (Meides et al., 2021). Particle break-up of LDPE is driven by surface fragmentation. We attribute this to the morphological differences between amorphous PS and semi-crystalline LDPE. Fragments of various sizes are attached to the particle surfaces. After 2000 h of exposure, particles are very small and still have sharp edges (Fig. 1d). The ongoing fragmentation is traceable within SEM images of particle surfaces at high magnification (Fig. 1e–f). Secondary NP particles attach to the surface of larger ones representing stage III.

Quantitative particle size measurements reveal a constant particle size of ~190 μm within the first 400 h, followed by an exponential decrease ($\propto \exp(-t/\tau)$, τ = 537 h), indicating rapid particle disintegration (Fig. 2a, Table S2). From 2000 h onwards, the average particle size reaches a linear plateau. Particle size decrease is accompanied by a broadening of the particle size distribution (Fig. 2b). For the reference sample (0 h), the smallest particles are 80 μm and the largest 420 μm. After 3200 h, the particle

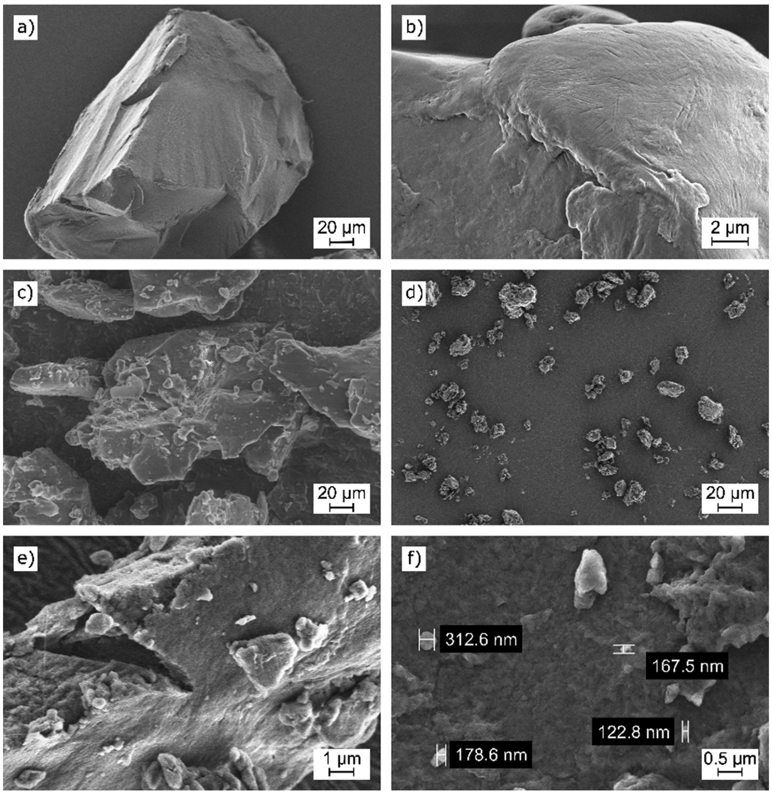

Fig. 1. SEM images of a) an initial particle at 0 h, b) the surface of a rounded particle after 400 h, c) fractured particles after 800 h, and d) fragments of particles after 2000 h of weathering. e) SEM image showing various particles <1 μm on the surface of a larger particle at 2000 h of weathering. f) The diameters of these particles are on the order of a few hundred nanometers.

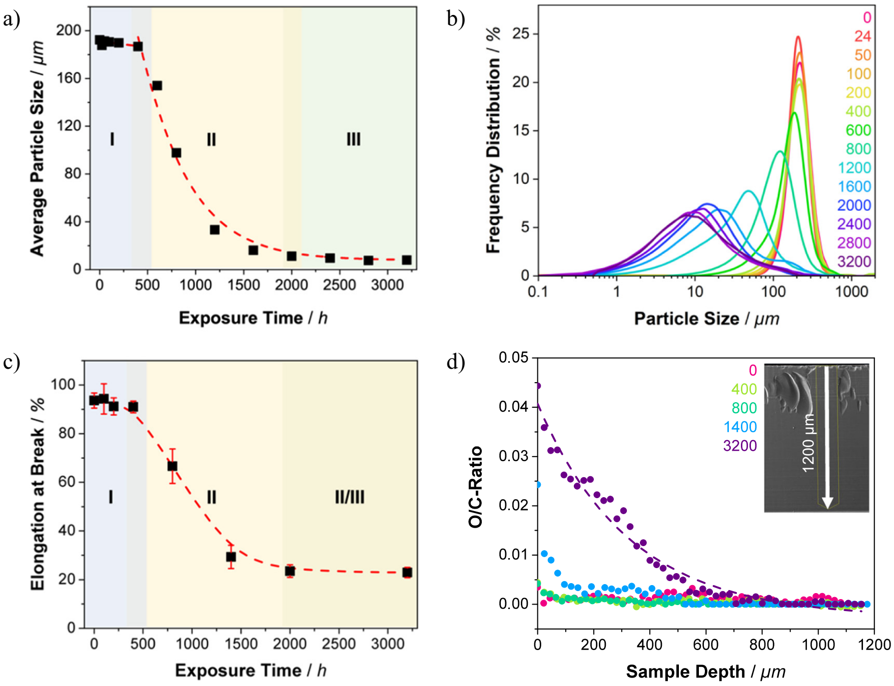

Fig. 2. a) Average particle size values and b) particle size distributions from 0 to 3200 h. c) The elongation at break from 0 to 3200 h for exposed tensile bars. d) The O/C-ratio versus the sample depth for LDPE tensile bars at 0, 400, 800, 1400, and 3200 h exposure determined by SEM-EDS measurements. The bars were cut perpendicular to the exposed surface. The mapping was recorded from the exposed surface 1200 µm into the bulk, as indicated by the arrow in the insert.

sizes range from 0.5 µm to 120 µm. The bimodal character developing at high weathering stages in Fig. 2b is due to agglomeration. This effect becomes clearly visible from 1600 h onwards, masking the continuous decrease of the particle size, visible in the SEM images, and resulting in a plateau of the average particle size (Fig. 2a). These trends define the three stages of particle degradation (Fig. 7). Surface abrasion does not trigger particle size decrease, resulting in consistency up to 400 h. Fragmentation dominates stage II, evident by the exponential decrease from 400 h to 2000 h. In stage III the measured particle sizes remain constant. This is in contrast to the SEM micrographs (Fig. 1e–f), where NP particles adhering to larger particles are clearly traceable, proving an ongoing particle disintegration. The plateau arises since particle disintegration is compensated by particle agglomeration. Despite surfactant addition and ultrasound treatment, aggregates are not disrupted in the particle size measurement, demonstrating strong adhesion. This is caused by the increasing surface-to-volume ratio and surface polarity (Liu et al., 2021; Suresh et al., 2011; Vicentini et al., 2019). Consequently, a large portion of NP particles formed during the later stages of weathering is not detectable in the particle size measurements (Fig. 2a).

Compared to PS (Meides et al., 2021), the fragmentation rate of LDPE is roughly three times higher. 14,000 daughter particles of 8 µm average size are released from one initial particle (190 µm average size) within 3200 h. The number of daughter particles was estimated by comparing the volumes from the 0 h mother particle and the daughter particles (Table S2). 14,000 daughter particles may even be underestimated since with decreasing average size, agglomeration of stage III strongly influences the values determined by particle size measurements (Fig. 2b).

The transition from stage I into stage II, observed for particles, correlates to the trends of the elongation at break determined from tensile bars (Fig. 2c). The elongation at break is a common indicator for embrittlement evolving due to degradation processes (White, 2007). Although it is a bulk-sensitive method, surface defects promote the fracture behavior. The characteristic drop from 95% to 25% (Fig. 2c) indicates embrittlement, correlating to stage II observed from particle weathering. The failure at low strain, from 1400 h onwards, is attributed to the occurrence of microcracks (Fig. 3b–d), facilitating the crack propagation under mechanical load. After 3200 h, the elongation at break has lost 75% of its initial value.

Mechanical embrittlement (Fig. 2c) coincides with the transition from stage I to II around 400 h. However, for LDPE, this does not overlap with the visual surface embrittlement defined by the appearance of microcracks at the surface. First microcracks are only visible after longer exposure times >1400 h (Fig. 3b). This is a fundamental difference to amorphous PS, where mechanical and surface embrittlement correlate (Meides et al., 2021). The microcracks on the LDPE surfaces are preferentially aligned due to the processing by injection molding and subsequent crystallization. This is a consequence of a preferred orientation of the polymer chains and of the crystalline domains, as suggested by 2D WAXS measurements (Fig. S4). With increasing exposure, microcracks grow in length and width, resulting in a more pronounced crack pattern (Fig. 3c). With 3200 h of exposure, the polymer chain orientation has less impact on the crack orientation. Smaller cracks are visible within an orthogonal pattern of microcracks with 10–20 µm width (Fig. 3d). Surface embrittlement is attributed to a progressive depletion of amorphous regions by chain-scission and surface oxidation, resulting in a decrease of tie-molecules and entanglements. This should lead to microcrack formation for exposure times exceeding 400 h. However, microcracks are absent until 1400 h (Fig. 3a–b). This can be explained by considering the semi-crystalline character of LDPE, with a glass transition temperature below 0 °C (Han et al., 1994; Lechner et al., 2014), far below the experiment temperature. Consequently, self-healing

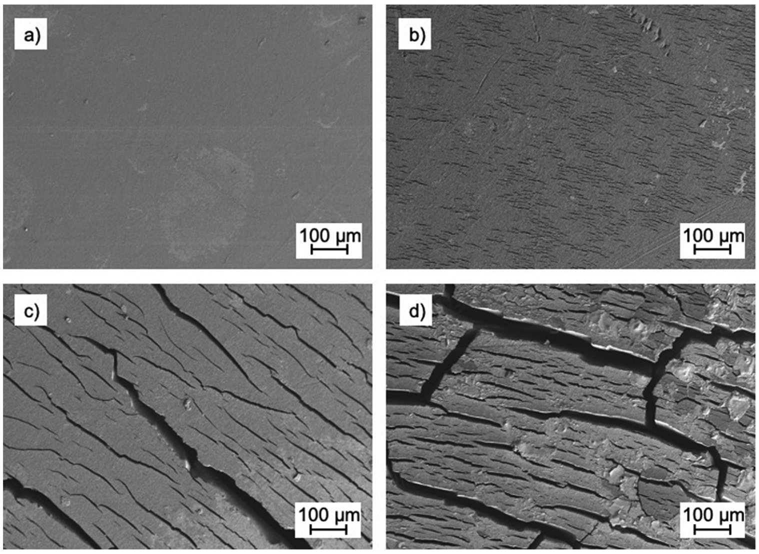

Fig. 3. SEM images of LDPE bar surfaces. a) At 800 h without any surface structure, b) 1400 h with first microcracks, c) 2000 h with growing microcracks, and d) 3200 h with surface structures of an orthogonal crack pattern and microcracks.

by enhanced surface rearrangement seems likely (Kang et al., 2018; Wool, 2008). This effect also applies to particle degradation, where no pronounced particle cracking is observed in the transition from stage I to II (Fig. 1a–d).

To determine the progression of oxygen-containing functional groups as a function of sample depth, the O/C-ratio was determined via SEM-EDS (Fig. 2d). The formation of microcracks increases oxygen uptake reaching a photooxidative zone *d* of almost 100 μm after 1400 h. The composition of *d* is discussed in detail in Section 3.3. The growth of surface cracks in depth and width further enhances oxygen uptake and likely accelerates the degradation progress. Consequently, hindered polymer chain dynamics in combination with microcrack formation enable a progression of *d* into depths of up to ~700 μm by 3200 h (Fig. 2d).

3.2. Development of crystallinity with weathering

Changes in crystallinity for semi-crystalline LDPE particles and surfaces were tracked by DSC, ^{13}C NMR spectroscopy, and XRD measurements. The DSC scans are plotted in Fig. 4a and b. The initial heating curves at 0 h show a broad melting range from ~65 °C to 110 °C. The broad range is attributed to a nonuniform distribution of crystallite sizes (Ehrenstein, 1999). With exposure, the shoulder initially present at lower temperatures shifts to higher temperatures (arrows in Fig. 4a–b, Table S3), and the melting enthalpy increases. This indicates the growth of the smaller crystalline domains into larger domains with higher melting temperatures. The shoulder merges into the main melting peak as weathering proceeds. Both geometries show a similar trend of an increasing degree of crystallinity by ~25% for particles (Fig. 4d) and ~20% for surfaces, as calculated by the integration of the melting peak. However, for surfaces, the process is slightly delayed.

The intensity evolution (Fig. 4c) of the CH_2 ^{13}C NMR resonances of the amorphous (33 ppm) and crystalline (35 ppm) domains (Assink et al., 2001) for particles is in good agreement with the DSC analysis. The downfield resonance (crystalline phase) increases, while the upfield resonance (amorphous phase) decreases. The combination of both results reveals the depletion of amorphous regions, accompanied by an increase of crystallinity. This is in line with previous studies (Garvey et al., 2020; Ojeda et al., 2011; Roy et al., 2007).

XRD measurements allow the estimation of changes in the crystalline domain size during weathering. For both geometries, the full width at half maximum (FWHM) initially decreases, indicating an increase in the average crystalline domain sizes (Figs. 4e, S5, Tables S5–6). The increased molecular motion of shorter chain fragments enhances the rearrangement into crystalline lamellae (Grause et al., 2020). While for the bar surfaces the domain size continuously increases with exposure time, for particles, a plateau with a maximum of ~19 nm is reached (1200 − 2000 h), followed by a slight decrease to 17 nm domain size (2000 − 3200 h). This indicates that the crystalline domains are also affected by disintegration at late stages of weathering (Martínez-Romo et al., 2015; Ojeda et al., 2011). In addition, molecular rearrangements along with a disruption of the lamellar order are supposed to change the physical properties, enhancing oxygen diffusion and subsequently photooxidation (Garvey et al., 2020).

The observations show that chain-scissions occur preferentially within the amorphous domains. Subsequent rearrangements of the fragmented chains allow for the growth of the crystalline domains. As the amorphous regions steadily decline, even crystalline domains are degraded at late stages, resulting in a decreasing average domain size (Fig. 4e). This correlates with the observation of an additional stage III in SEM micrographs, where NP particles are traceable from 2000 h onwards (Fig. 1e–f). We suppose that mechanical forces play a decisive role in stage III. The bars are unaffected from mechanical stress, while the particles are continuously stirred. We assume that the resulting NP particles have a high degree of crystallinity and consist of oligomers with a large proportion of functional groups, formed by oxygen uptake.

3.3. Evolution of chain defects

To assess the degradation on a molecular scale, the evolution of chain defects was investigated via GPC, FTIR and NMR spectroscopy. For both geometries, a shift of the MWD to lower molecular weights is observed (Fig. 5a–b). For particles, the shift is more pronounced compared to bar surfaces, where the decrease in MW proceeds slower. The change in MW is accompanied by an initial growth of Đ until 200 h, followed by a final narrowing of the distribution. This behavior reflects the characteristics of a multi-stage degradation pathway. High degrees of crosslinking are

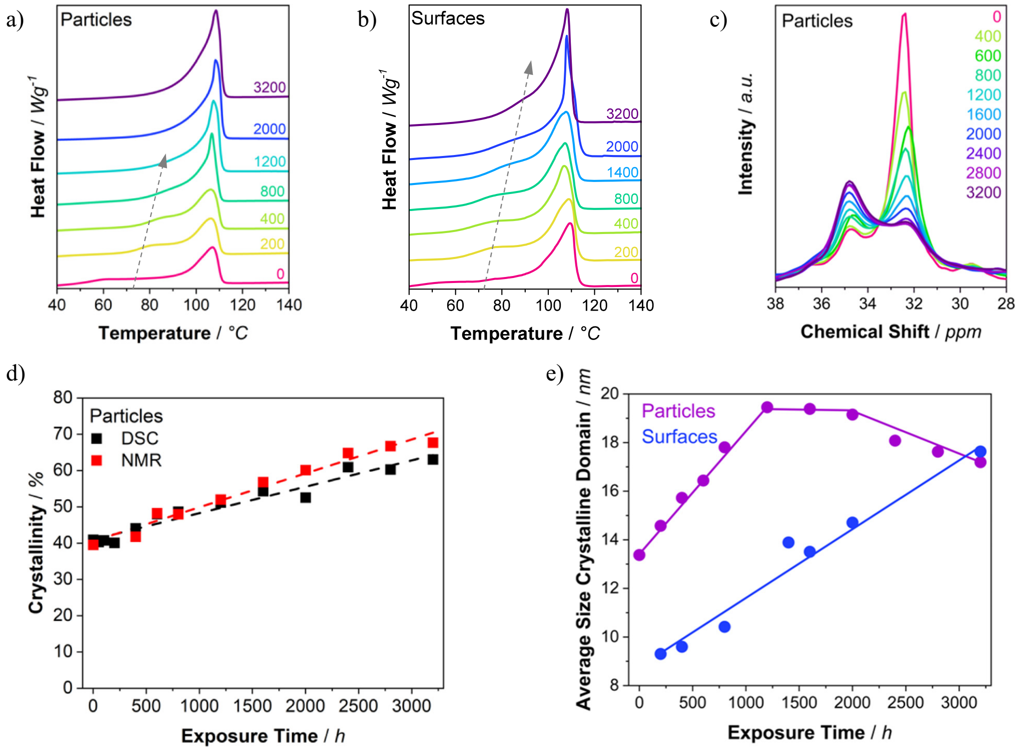

Fig. 4. Heating curves determined from DSC for a) particles and b) tensile bar surfaces for different exposure time intervals. Black arrows indicate the melting shoulder as it merges into the melting peak. c) ^{13}C CP MAS NMR spectra of the particles, normalized to the integral of the backbone signal (integral between 0 and 50 ppm). d) Comparison of trends of crystallinity for particles measured by DSC and NMR and e) qualitative determination of the average size of crystalline domains by XRD for particles and surfaces according to the Scherrer-formula (Scherrer, 1912).

predominantly visible in stage I, indicated by the crossing of the 0 h reference line at high-molecular weights (Shyichuk and White, 2000). This effect is more pronounced for bar surfaces than particles, leading to a stronger increase in Đ (Table S7). Crosslinking declines with the progression of stage I, resulting in a narrowing of the MWD and a decreasing Đ for both geometries. In the literature, this behavior has been reported for polyolefins, where it was attributed to chain-scission in amorphous as well as crystalline domains (Ojeda et al., 2011).

Crosslinking densities and defect proportions were quantified by MC simulations, which reconstruct the experimental particle MWDs. Polymer degradation was simulated using a large ensemble of chains undergoing chain-scissions and crosslinking (SI, page 9). The probability for crosslinking (P_{cl}) was adjusted until the Đ of the measured MWDs could be closely reproduced (Fig. S6). The resulting simulated MWDs are in good agreement with the experimental data (Fig. 5c) and reflect the first two stages of degradation (Fig. 7). During stage I crosslinking and chain-scission occur with almost equal probability ($P_{cl} = 42\%$, $P_{cs} = 58\%$). Between 200 h and 600 h, P_{cl} was reduced in two steps, first to 36.5% and then to 20%, corresponding to the transition to stage II. The first adjustment was performed at M_n of 15,000 g/mol, and the second at M_n of 4750 g/mol. As crosslinking mainly occurs in amorphous regions (Dole, 1979), the rearrangement of amorphous into crystalline units consequently lowers P_{cl} with ongoing weathering. For longer exposure times, P_{cl} remains at 20%. After 3200 h, 1.5% of the repeating units (RUs) developed crosslinks and 8.2% of the RUs contain newly formed end groups due to chain-scission.

For particles and surfaces, defect types were determined via solid-state ^{13}C CP MAS NMR (Fig. 6) and FTIR spectroscopy (Fig. S10). The signals at 35 ppm and 33 ppm were assigned to the crystalline and amorphous CH_2 units of the aliphatic backbone (Assink et al., 2001). Additional weaker signals between 0 and 50 ppm were attributed to the chain architecture of LDPE (Fig. S7) (Chabira et al., 2008). The CH_2 units were additionally identified by their characteristic vibrational bands (Fig. S10). Upon irradiation, signals for carboxylic acids (I, 178 ppm, ν(C=O): ~1714 cm^{-1}), vinylidenes (two carbon signals: II, 141 ppm and III, 117 ppm, ν(CH): 3100 cm^{-1} - 3000 cm^{-1} (shoulder)), peroxides and alcohols (superimposed resonances: IV, 60–90 ppm, ν(OH): 3450 cm^{-1} (broad)) emerge as a result of photooxidation. This matches findings in previous studies for PS and PP (Meides et al., 2021; Mowery et al., 2005, 2007). For both sample geometries, the intensity increases with exposure time.

We use the bulk-sensitive ^{13}C NMR spectroscopy to quantify the defect proportions. For this purpose, the intensity ratios were calibrated with multi-CP experiments (Meides et al., 2021). The most frequent defect types are peroxides and alcohols, followed by carboxylic acids. Olefins play only a minor role (Fig. 6c–d). Ketones and aldehydes (~210 ppm) were not detected in significant quantities. Ketones most likely underwent photolysis via Norrish I and Norrish II reactions (Feldman, 2002), and aldehydes were oxidized to carboxylic acids (Fig. S8). This trend was observed for both sample geometries. The bands for the carboxylic acids are most prominent in the FTIR spectroscopic data, while the resonances for other oxidation products are very weak and partially overlapping. As ATR-FTIR is surface-sensitive, this might imply that carboxylic acids are preferentially formed in near-surface regions. In the NMR spectra, a saturation effect was observed after 2000 h for the alcohol and peroxide proportion in particles, while the other defects increased linearly. The entire proportion of end

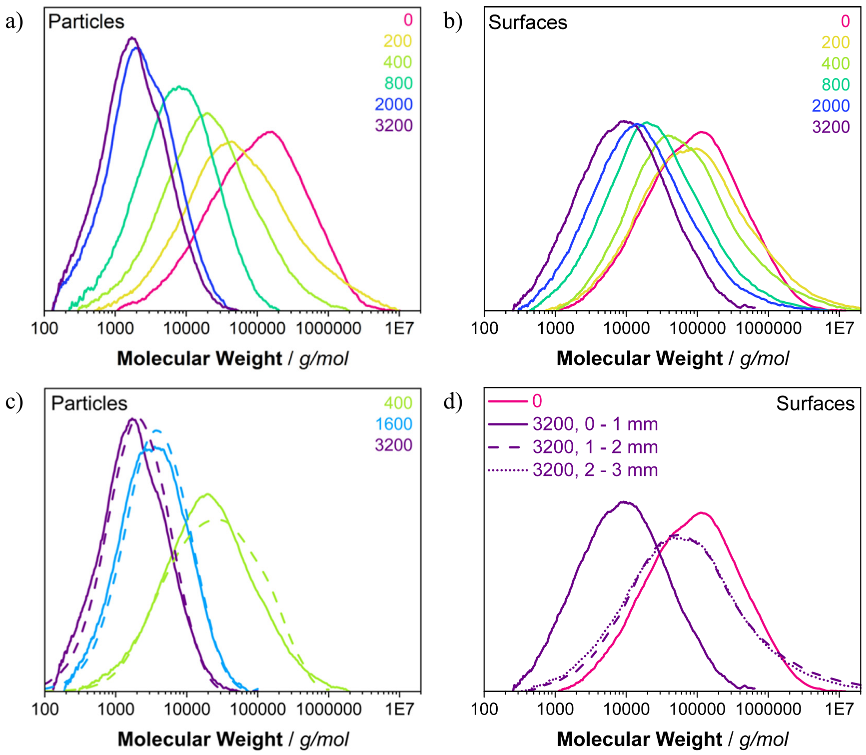

Fig. 5. a) MWD of a) particles and b) tensile bar surface material in 0–1 mm depth. c) Simulated (dashed) vs. experimental (solid) particle MWDs are displayed for exposure times of 400, 1600, and 3200 h. d) MWD for surfaces at 3200 h in 1–2 and 2–3 mm depth compared to the reference material.

groups (keto- and carboxyl groups) and crosslinks are in good agreement with the ones derived from the MC simulations (Fig. 6c, S4). After 3200 h, an average chain in the particle sample consists of 40 RUs with approximately one induced crosslink and 8 polar groups resulting from photooxidation.

In addition, the total amount of oxygen-containing chain defects was analyzed by EDS as a function of the penetration depth from the surface of tensile bars. The accumulation of polar groups leads to a photooxidative zone *d* with a depth of up to 700 μm (Fig. 2d). At 3200 h, the depth-dependent change of the MW of tensile bars was determined via GPC for three layers, with 1 mm thickness each. Although degradation also appears in deeper layers of 1–2 and 2–3 mm, the process is retarded compared to the uppermost layer of 0–1 mm (Fig. 5d). Independent of the depth, the interior between 1 and 3 mm shows a consistent degradation state. This state is comparable to the surface layer between 200 and 400 h of exposure, with its characteristically high degree of crosslinking. Depth-dependent, qualitative ^{1}H HT liquid-state NMR measurements (0–1 mm, 1–2 mm) at 0 h and 3200 h (Fig. S9) validate these findings. The initial sample at 0 h shows the presence of terminal double bonds (α-olefins), while they vanish deeper inside the sample (1–2 mm) after 3200 h. Since unsaturated bonds are more prone to radical formation, their disappearance indicates predominant crosslinking in the absence of oxygen in deeper layers. In contrast, a high number of α-olefins was observed in the top layer (0–1 mm) at 3200 h, as photooxidation and Norrish II reactions are more likely (Fig. S8) (Feldman, 2002). These results demonstrate a deeper penetration of UV-radiation, while oxygen diffusion into the material is limited (Audouin et al., 1994; Celina, 2013). Due to the scarcity of oxygen in 1–3 mm depth, photooxidation only occurred to a marginal extent. Consequently, crosslinking is the predominant radical termination mechanism in deeper layers.

4. Discussion

For semi-crystalline LDPE, three stages of degradation were identified. Stage I (0–400 h) proceeds in a similar manner as for amorphous polymers (e.g., PS) (Meides et al., 2021) and is characterized by surface abrasion (Fig. 7), accompanied by continuous chain-scission and crosslinking. Due to a higher mobility of polymer chains in the amorphous regions ($T_{experiment} \gg T_g$), the crosslinking probability (P_{cl} = 42%) is remarkably high. The difference between amorphous PS and semi-crystalline LDPE on the degradation of surfaces and the fragmentation rate of particles becomes evident with the onset of stage II.

In our experimental weathering simulation, a rapid, exponential decrease in particle size (Fig. 2a) is observed, along with a characteristic drop in the elongation at break (Fig. 2c), marking a decrease in tie molecule density and entanglement, as a consequence of a decrease in MW (Fig. 5a–b). Due to the low T_g of LDPE, self-healing by molecular rearrangements in the amorphous regions prevents microcrack formation during stage II (Figs. 1, 3). With continued weathering, a consistent increase in the degree of crystallinity of ~15% (Fig. 4d) and a growth of the crystalline domains are recorded (Fig. 4e). This leads to stress-induced crack formation on the surfaces, visible from 1400 h onwards (Fig. 3). Large quantities of secondary MP (SMP) particles are formed as stage II proceeds, resulting in 5000 SMP particles with ~11 μm diameter released from one mother particle of ~190 μm after 2000 h (Table S2). This exceeds the number of particles produced under similar conditions for PS (Meides et al.,

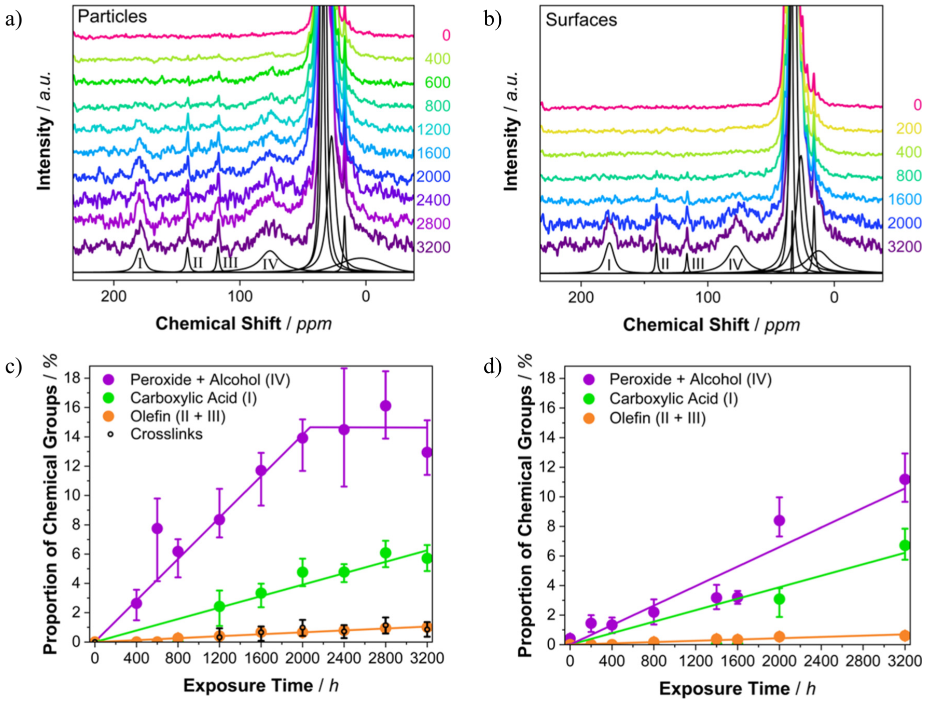

Fig. 6. ^{13}C CP MAS NMR spectra of the a) particles and b) bar surfaces for different exposure times. Upon irradiation, the generation of new signals assigned as signals I (carboxylic acid), II (vinylidene carbon 1), III (vinylidene carbon 2), and IV (peroxide and alcohol) is observed. The spectra are normalized to the integral of the backbone signal (integral between 0 and 50 ppm). The spectra are shifted vertically. Individual fits for the peaks in the spectrum of the particles and surfaces at 3200 h are shown in black. Resulting proportions of functional groups for c) particles and d) bar surfaces. The lines serve as guide to the eye.

2021) by a factor of 10. SMP preferentially consist of mechanically fractured, highly crystalline domains from the surfaces of a mother particle. Thus, LDPE disintegrates via surface cracking instead of bulk cracking observed for amorphous polymers.

As weathering proceeds, amorphous regions are preferably degraded and consequently decrease. The average size of crystalline domains increases by approximately 50% for both geometries, while crystallite growth of particles stagnates (plateau in Fig. 4e). The probability for crosslinking reactions drops to ~20% and thus becomes less likely in stage II. In parallel, polymer chains are more strongly affected by chain-scission (Fig. 5a–b). This results in a high proportion of polar end-groups (Fig. 6a-b), increasing the surface polarity. The high surface-to-volume ratio and polarity of particles result in agglomeration, traceable in the particle size distributions (Fig. 2b) and SEM micrographs (Fig. 1c–f). As weathering proceeds, degradation starts to affect the crystalline domains, resulting in the disintegration of crystallites and finally a reduction of the average crystallite domain size (Fig. 4e). Fragmentation of particles reaches a maximum and NP particles are traceable in SEM micrographs (Fig. 1e–f), where they adhere to larger particles. We assume that these NP particles consist of polar oligomers with a high degree of crystallinity and identify this as stage III in our model (Fig. 7).

In general, the degradation paths in this study are identical for micrometer-sized particles and macroscopic tensile bars, however, bar surface degradation is retarded. Smaller defect proportions are observed for the bar surfaces at 3200 h (Fig. 6c–d) retaining in stage II. Since they are not exposed to mechanical stress, compared to the particles constantly stirred in water, the disintegration of crystalline units is hindered. The absence of mechanical stress results in a highly oxidized top layer, slowly progressing into the sample depth (Fig. 2d). The upper-most surface acts as a protective layer for the sample interior, delaying the overall degradation. The lack of ablation maintains this protective layer. Due to a limited diffusion, the oxygen deficiency leads to the predominance of crosslinking in deeper layers (Fig. 5d). The degradation state at 3200 h in 1–3 mm depth of the tensile bars is similar to the top layer after 200 to 400 h of exposure.

The experimental parameters chosen for our laboratory-controlled studies are clearly defined. Sampling was made in specific time intervals and sufficient sample amounts are obtained, enabling representative measurements with a multitude of analytical tools. Despite the laboratory-controlled conditions, we are confident, that fundamental conclusions on environmental weathering under natural conditions can be drawn from our accelerated weathering results. LDPE particles weathered in water in the presence of moderate mechanical stress are comparable to natural weathering in an aqueous environment, such as rivers or the ocean. LDPE tensile bars are exposed to simulated solar radiation in the absence of mechanical stress, the chosen parameters thus mimic weathering on land.

5. Conclusion

While the basic processes and degradation pathways for LDPE are comparable to PS (Meides et al., 2021), the fracture dynamics and fractionation rates are strongly influenced by its semi-crystalline character. The break-up processes of LDPE proceed via surface fragmentation, a profound difference, significantly increasing the rate of SMP particle production. 14,000 SMP particles are released from one 190 μm-sized mother particle within 3200 h, equivalent to 1.5 years of outdoor weathering in Central Europe (Meides et al., 2021). These SMP have an average particle size of 8 μm.

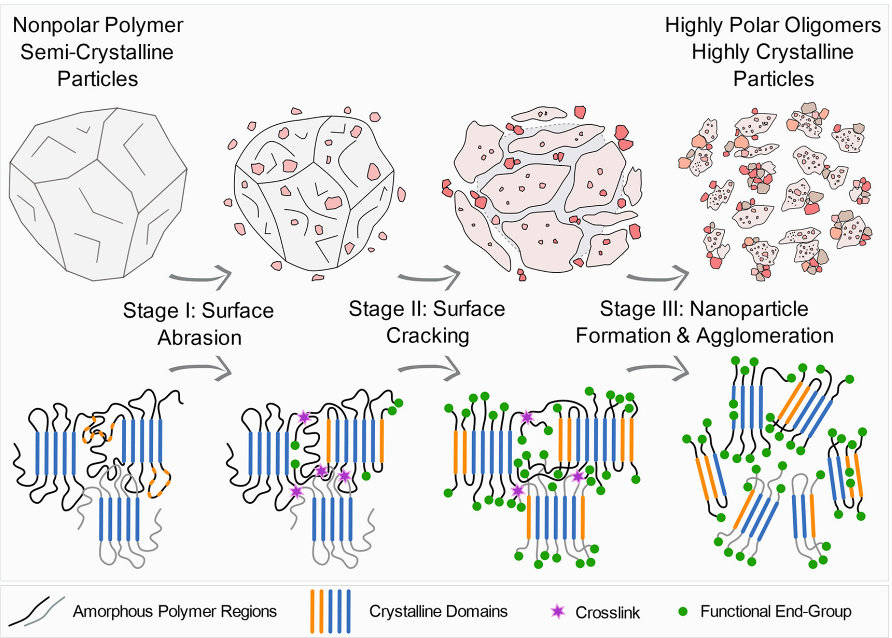

Fig. 7. Three-stage degradation model derived from accelerated, abiotic laboratory weathering of LDPE particles and tensile bars.

SEM images (Fig. 2e–f) clearly show NP particles with sizes in the range of 100 to 300 nm. Compared to the virgin material, the overall particle surface is increased by a factor of ~30 (Table S2). This favors the agglomeration of NP particles on the surface of MP particles (Fig. S3). Consequently, no free NP particles could be identified in our experiments. While agglomeration of NP particles was predicted in literature (Andrady, 2011; Jakubowicz et al., 2021), we deliver experimental evidence. Agglomeration becomes increasingly important with decreasing particle size, particularly when entering the micro- and nanoscale. We are confident that these observations are also applicable for weathering under environmental conditions. Due to a large excess of organic and inorganic colloidal particles in the natural environment, the polar MP and NP particles will attach to their surfaces (Lu et al., 2021).

The toxicity of nanoparticles is a general concern (Hewitt et al., 2020) which has been recently discussed also for micro- and nanoplastic (Liu et al., 2021). The negative effects of MP and NP particles become more prominent with decreasing size, enabling increased incorporation into tissue and cells. We found highly stable particle aggregates, and no free NP particles could be detected. Our finding is of relevance, as the formation of larger aggregates will reduce direct uptake into tissue and cells. On the other hand, aggregates of natural organic and inorganic colloidal matter with NP particles will be unavoidably ingested by organisms and ultimately enter the food chain. Our results show that oxygen-containing functional groups, including peroxides, are formed upon weathering of MP. In particular, peroxides are suspected to be cytotoxic (Chance et al., 1979). Highly weathered NP particles thus pose a potential threat to our ecosystem.

CRediT authorship contribution statement

T.M. and N.M. performed accelerated weathering of particles and tensile bars, tensile testing, particle size analysis, GPC, and DSC measurements. A.M. performed solid-state NMR spectroscopic measurements, MC simulations, and powder XRD measurements, while M.K. and E.M.H. performed WAXS measurements. U.M. performed SEM-EDS measurements and W.K. ^{1}H HT liquid NMR spectroscopy. T.M., N.M., and A.M. wrote the first draft of the manuscript, H.R., V.A., P.S., and J.S. supported the discussion and finalization of the manuscript. All authors read and approved the final version of the manuscript.

Declaration of competing interest

The authors declare that they have no known competing financial interests or personal relationships that could have appeared to influence the work reported in this paper.

Acknowledgements

The authors would like to thank Lisa Weber and Martina Fried for particle preparation, Sebastian Gröschel for injection molding, and Martina Heider and Annika Pfaffenberger for SEM micrographs. We further acknoledge access to various NMR spectrometers of the Northern Bavarian NMR centre (NBNC).

Availability of data and materials

All data needed to evaluate the conclusions in the paper are present in the paper and/or the Supplementary materials.

Funding

This project was funded by the Deutsche Forschungsgemeinschaft (DFG, German Research Foundation) - Project Number 391977956 - SFB 1357, subproject C01. M.K. and E.M.H. gratefully acknowledge funding by the Bavarian State Ministry of Science and the Arts—Collaborative Research Network “Solar Technologies Go Hybrid”.

Appendix A. Supplementary data

Supplementary data to this article can be found online at https://doi.org/10.1016/j.scitotenv.2022.154035.

References

Andrady, A.L., 2011. Microplastics in the marine environment. Mar. Pollut. Bull. 62 (8), 1596–1605.

Assink, R.A., Celina, M., Gillen, K.T., Clough, R.L., Alam, T.M., 2001. Morphology changes during radiation-thermal degradation of polyethylene and an EPDM copolymer by 13C NMR spectroscopy. Polym. Degrad. Stab. 73 (2), 355–362.

Audouin, L., Langlois, V., Verdu, J., de Bruijn, J.C.M., 1994. Role of oxygen diffusion in polymer ageing: kinetic and mechanical aspects. J. Mater. Sci. 29 (3), 569–583.

Biale, G., La Nasa, J., Mattonai, M., Corti, A., Vinciguerra, V., Castelvetro, V., et al., 2021. A systematic study on the degradation products generated from artificially aged microplastics. Polymers 13 (12), 1997.

Bishop, G., Styles, D., Lens, P.N.L., 2020. Recycling of european plastic is a pathway for plastic debris in the ocean. Environ. Int. 142, 105893.

Canopoli, L., Coulon, F., Wagland, S.T., 2020. Degradation of excavated polyethylene and polypropylene waste from landfill. Sci. Total Environ. 698, 134125.

Celina, M.C., 2013. Review of polymer oxidation and its relationship with materials performance and lifetime prediction. Polym. Degrad. Stab. 98 (12), 2419–2429.

Chabira, S.F., Sebaa, M., G'sell, C., 2008. Influence of climatic ageing on the mechanical properties and the microstructure of low-density polyethylene films. J. Appl. Polym. Sci. 110 (4), 2516–2524.

Chance, B., Sies, H., Boveris, A., 1979. Hydroperoxide metabolism in mammalian organs. Physiol. Rev. 59 (3), 527–605.

Da Costa, J.P., Nunes, A.R., Santos, P.S.M., Girao, A.V., Duarte, A.C., Rocha-Santos, T., 2018. Degradation of polyethylene microplastics in seawater: insights into the environmental degradation of polymers. J. Environ. Sci. Health A 53 (9), 866–875.

Dole, M., 1979. Cross-linking and crystallinity in irradiated polyethylene. Polym.-Plast. Technol. Eng. 13 (1), 41–64.

Dong, M., Zhang, Q., Xing, X., Chen, W., She, Z., Luo, Z., 2020. Raman spectra and surface changes of microplastics weathered under natural environments. Sci. Total Environ. 739, 139990.

Ehrenstein, G., 1999. Polymer-Werkstoffe: Struktur-Eigenschaften-Anwendung.

Engler, R.E., 2012. The complex interaction between marine debris and toxic chemicals in the ocean. Environ. Sci. Technol. 46 (22), 12302–12315.

Fairbrother, A., Hsueh, H.-C., Kim, J.H., Jacobs, D., Perry, L., Goodwin, D., et al., 2019. Temperature and light intensity effects on photodegradation of high-density polyethylene. Polym. Degrad. Stab. 165, 153–160.

Feldman, D., 2002. Polymer weathering: photo-oxidation. J. Polym. Environ. 10 (4), 163–173.

Fernández-González, V., Andrade-Garda, J.M., López-Mahía, P., Muniategui-Lorenzo, S., 2021. Impact of weathering on the chemical identification of microplastics from usual packaging polymers in the marine environment. Anal. Chim. Acta 1142, 179–188.

Fotopoulou, K.N., Karapanagioti, H.K. (Eds.), 2017. Hazardous Chemicals Associated With Plastics in the Marine Environment: Degradation of Various Plastics in the Environment. Springer, Cham.

Garvey, C.J., Impéror-Clerc, M., Rouzière, S., Gouadec, G., Boyron, O., Rowenczyk, L., et al., 2020. Molecular-scale understanding of the embrittlement in Polyethylene Ocean debris. Environ. Sci. Technol. 54 (18), 11173–11181.

Gewert, B., Plassmann, M., Sandblom, O., MacLeod, M., 2018. Identification of chain scission products released to water by plastic exposed to ultraviolet light. Environ. Sci. Technol. Lett. 5 (5), 272–276.

Geyer, R., Jambeck, J.R., Law, K.L., 2017. Production, use, and fate of all plastics ever made. Sci. Adv. 3 (7), e1700782.

Ghatge, S., Yang, Y., Ahn, J.-H., Hur, H.-G., 2020. Biodegradation of polyethylene: a brief review. Appl. Biol. Chem. 63 (1), 27.

Grause, G., Chien, M.-F., Inoue, C., 2020. Changes during the weathering of polyolefins. Polym. Degrad. Stabil. 109364.

Han, J., Gee, R.H., Boyd, R.H., 1994. Glass transition temperatures of polymers from molecular dynamics simulations. Macromolecules 27 (26), 7781–7784.

Hartmann, N.B., Hüffer, T., Thompson, R.C., Hassellöv, M., Verschoor, A., Daugaard, A.E., et al., 2019. Are we speaking the same language? Recommendations for a definition and categorization framework for plastic debris. Environ. Sci. Technol. 53 (3), 1039–1047. https://doi.org/10.1021/acs.est.8b05297.

Hewitt, R.E., Chappell, H.F., Powell, J.J., 2020. Small and dangerous? Potential toxicity mechanisms of common exposure particles and nanoparticles. Curr. Opin. Toxicol. 19, 93–98.

Hu, L., Chernick, M., Hinton, D.E., Shi, H., 2018. Microplastics in small waterbodies and tadpoles from Yangtze River Delta, China. Environ. Sci. Technol. 52 (15), 8885–8893.

Jakubowicz, I., Enebro, J., Yarahmadi, N., 2021. Challenges in the search for nanoplastics in the environment—a critical review from the polymer science perspective. Polym. Test. 93, 106953.

Jeon, J.-M., Park, S.-J., Choi, T.-R., Park, J.-H., Yang, Y.-H., Yoon, J.-J., 2021. Biodegradation of polyethylene and polypropylene by Lysinibacillus species JJY0216 isolated from soil grove. Polym. Degrad. Stab. 191, 109662.

Johnson, R.L., Schmidt-Rohr, K., 2014. Quantitative solid-state 13C NMR with signal enhancement by multiple cross polarization. J. Magn. Reson. 239, 44–49.

Julienne, F., Delorme, N., Lagarde, F., 2019. From macroplastics to microplastics: role of water in the fragmentation of polyethylene. Chemosphere 236, 124409.

Kang, C., Huh, J., Tran, Q.H., Kwak, K., Wang, J., 2018. Evaluation of self-healing performance of PE and PVA concrete using flexural test. Adv. Mater. Sci. Eng. 6386280.

Laermanns, H., Lehmann, M., Klee, M., Löder, M.G.J., Gekle, S., Bogner, C., 2021. Tracing the horizontal transport of microplastics on rough surfaces. Microplastics Nanoplastics 1 (1), 1–12.

Lechner, M.D., Nordmeier, E.H., Schmitt, B.J., Hahn, K.-H., Lennartz, C., Heering, R., 2014. Das Makromolekül als Festkörper und als Schmelze. Makromolekulare Chemie. Springer, pp. 429–641.

Lehmann, M., Oehlschlägel, L.M., Häusl, F.P., Held, A., Gekle, S., 2021. Ejection of marine microplastics by raindrops: a computational and experimental study. Microplastics Nanoplastics 1 (1), 1–19.

Liu, K., Wu, T., Wang, X., Song, Z., Zong, C., Wei, N., et al., 2019. Consistent transport of terrestrial microplastics to the ocean through atmosphere. Environ. Sci. Technol. 53 (18), 10612–10619.

Liu, P., Shi, Y., Wu, X., Wang, H., Huang, H., Guo, X., et al., 2021. Review of the artificially-accelerated aging technology and ecological risk of microplastics. Sci. Total Environ. 144969.

Lu, T., Gilfedder, B.S., Peng, H., Peiffer, S., Papastavrou, G., Ottermann, K., et al., 2021. Relevance of iron oxyhydroxide and pore water chemistry on the mobility of nanoplastic particles in water-saturated porous media environments. Water Air Soil Pollut. 232 (5), 168.

LyondellBasell, 2021. Technical Data Sheet Lupolen 1800P: Low Density Polyethylene. https://productsafety.lyondellbasell.com/DirectRequest?ResponseTypeGuid=f1e32c20-d810-4db0-b25e-8e23a59f3733&ProductGuid=28be098e-bb34-4bb8-a683-894ea1c1751e.

Maria, R., Rode, K., Brüll, R., Dorbath, F., Baudrit, B., Bastian, M., et al., 2011. Monitoring the influence of different weathering conditions on polyethylene pipes by IR-microscopy. Polym. Degrad. Stab. 96 (10), 1901–1910.

Martínez-Romo, A., González-Mota, R., Soto-Bernal, J.J., Rosales-Candelas, I., Garcia-Guinea, J., 2015. Investigating the degradability of HDPE, LDPE, PE-BIO, and PE-OXO films under UV-B radiation. J. Spectrosc. 586514.

Meides, N., Menzel, T., Poetzschner, B., MGJ, Löder, Mansfeld, U., Strohriegl, P., et al., 2021. Reconstructing the environmental degradation of polystyrene by accelerated weathering. Environ. Sci. Technol. 55 (12), 7930–7938. https://doi.org/10.1021/acs.est.0c07718.

Morét-Ferguson, S., Law, K.L., Proskurowski, G., Murphy, E.K., Peacock, E.E., Reddy, C.M., 2010. The size, mass, and composition of plastic debris in the western North Atlantic Ocean. Mar. Pollut. Bull. 60 (10), 1873–1878.

Mowery, D.M., Assink, R.A., Derzon, D.K., Klamo, S.B., Clough, R.L., Bernstein, R., 2005. Solid-state 13C NMR investigation of the oxidative degradation of selectively labeled polypropylene by thermal aging and γ-irradiation. Macromolecules 38 (12), 5035–5046.

Mowery, D.M., Clough, R.L., Assink, R.A., 2007. Identification of oxidation products in selectively labeled polypropylene with solid-state 13C NMR techniques. Macromolecules 40 (10), 3615–3623.

Nava, V., Frezzotti, M.L., Leoni, B., 2021. Raman spectroscopy for the analysis of microplastics in aquatic systems. Appl. Spectrosc. 75 (11), 1341–1357.

Ojeda, T., Freitas, A., Birck, K., Dalmolin, E., Jacques, R., Bento, F., et al., 2011. Degradability of linear polyolefins under natural weathering. Polym. Degrad. Stab. 96 (4), 703–707.

Pasch, H., 2001. Recent developments in polyolefin characterization. Macromol. Symp. 165 (1), 91–98.

Petersen, F., Hubbart, J.A., 2021. The occurrence and transport of microplastics: the state of the science. Sci. Total Environ. 758, 143936.

Roy, P.K., Surekha, P., Rajagopal, C., Chatterjee, S.N., Choudhary, V., 2007. Studies on the photo-oxidative degradation of LDPE films in the presence of oxidised polyethylene. Polym. Degrad. Stab. 92 (6), 1151–1160.

Sander, M., 2019. Biodegradation of polymeric mulch films in agricultural soils: concepts, knowledge gaps, and future research directions. Environ. Sci. Technol. 53 (5), 2304–2315.

Scherrer, P., 1912. Bestimmung der inneren Struktur und der Größe von Kolloidteilchen mittels Röntgenstrahlen. Kolloidchemie. Springer, Ein Lehrbuch, pp. 387–409.

Shyichuk, A.V., White, J.R., 2000. Analysis of chain-scission and crosslinking rates in the photo-oxidation of polystyrene. J. Appl. Polym. Sci. 77 (13).

Suhrhoff, T.J., Scholz-Böttcher, B.M., 2016. Qualitative impact of salinity, UV radiation and turbulence on leaching of organic plastic additives from four common plastics—a lab experiment. Mar. Pollut. Bull. 102 (1), 84–94.

Suresh, B., Maruthamuthu, S., Kannan, M., Chandramohan, A., 2011. Mechanical and surface properties of low-density polyethylene film modified by photo-oxidation. Polym. J. 43 (4), 398–406.

Vicentini, D.S., Nogueira, D.J., Melegari, S.P., Arl, M., Köerich, J.S., Cruz, L., et al., 2019. Toxicological evaluation and quantification of ingested metal-Core nanoplastic by Daphnia magna through fluorescence and inductively coupled plasma-mass spectrometric methods. Environ. Toxicol. Chem. 38 (10), 2101–2110.

White, J.R. (Ed.), 2007. Polymer Weathering: Mechanisms of Degradation and Failure.

Wilber, R.J., 1987. Plastic in the North Atlantic. Oceanus 30 (3), 61–68.

Wool, R.P., 2008. Self-healing materials: a review. Soft Matter 4 (3), 400–418.

Wright, S.L., Ulke, J., Font, A., Chan, K., Kelly, F.J., 2020. Atmospheric microplastic deposition in an urban environment and an evaluation of transport. Environ. Int. 136, 105411.

Xu, C., Zhang, B., Gu, C., Shen, C., Yin, S., Aamir, M., et al., 2020. Are we underestimating the sources of microplastic pollution in terrestrial environment? J. Hazard. Mater. 123228.

Zhou, Q., Zhang, H., Fu, C., Zhou, Y., Dai, Z., Li, Y., et al., 2018. The distribution and morphology of microplastics in coastal soils adjacent to the Bohai Sea and the Yellow Sea. Geoderma 322, 201–208.

This article was published in Science of the Total Environment 2022, 826, 154035.

Supplementary material: `https://doi.org/10.1016/j.scitotenv.2022.154035`

8.2.1 Supplementary Material: Degradation of Low-Density Polyethylene to Nanoplastic Particles by Accelerated Weathering.

Supplementary Information

Degradation of Low-Density Polyethylene to Nanoplastic Particles by Accelerated Weathering

Teresa Menzel[1,†], Nora Meides[2,†], Anika Mauel[3,†], Ulrich Mansfeld[4], Winfried Kretschmer[5], Meike Kuhn[6], Eva M. Herzig[6], Volker Altstädt[1], Peter Strohriegl[2], Jürgen Senker[3,*], Holger Ruckdäschel[1,*]

[1] Department of Polymer Engineering, University of Bayreuth, Universitätsstraße 30, 95447 Bayreuth, Germany

[2] Department of Macromolecular Chemistry I, University of Bayreuth, Universitätsstraße 30, 95447 Bayreuth, Germany

[3] Department of Inorganic Chemistry III, University of Bayreuth, Universitätsstraße 30, 95447 Bayreuth, Germany

[4] Bavarian Polymer Institute, University of Bayreuth, Universitätsstraße 30, 95447 Bayreuth, Germany

[5] Department of Inorganic Chemistry II, University of Bayreuth, Universitätsstraße 30, 95447 Bayreuth, Germany

[6] Dynamics and Structure Formation, Institute of Physics, University of Bayreuth, Universitätsstraße 30, 95447 Bayreuth, Germany

† These authors contributed equally to this work

* Corresponding authors: holger.ruckdaeschel@uni-bayreuth.de, juergen.senker@uni-bayreuth.de

List of Figures

Figure S1 – Q-SUN daylight-Q filter compared to direct sunlight. Modified from Q-Lab Corporation, 2014, Technical Bulletin LX-5060, A Choice of Filters for Q-Sun Xenon Test Chambers.

Figure S2 – Global horizontal irradiation for Europe and for Germany in kWh/m^2 for 2019. Source: SOLARGIS.

Figure S3 – SEM images of LDPE particles after 2000 h of exposure, visualizing agglomerates of particles.

Figure S4 – a) Normalized intensity of the 110 reflex of a PE tensile bar weathered for 2000 h plotted for different scattering directions (Ψ). The X-ray beam, with approx. 900 µm diameter, was shifted to five different overlapping positions (1 to 5) as shown in b).

Figure S5 – XRD measurements of a) particles and b) tensile bar surfaces. Upon ageing the amorphous halo decreases indicating an increase of crystallinity.

Figure S6 – a) M_w over M_n of the MC simulation (black dots) compared to the measured values (red squares) for particles. The Đ of the measured MWDs could be reproduced when P_{cl} was first set to 42 % and then reduced to 36.5 % and 20 %, respectively, and b) comparison of particle end group and crosslink proportions obtained by NMR spectroscopy and MC simulations.

Figure S7 – ^{13}C CP MAS NMR spectrum of the initial PE particles between 0-50 ppm. The differences between the backbone resonances of the crystalline (dark grey) and amorphous (light grey) phase become visible. The weaker signals are attributed to the microstructure of PE. Signals at 40 ppm, 36 ppm and 29 ppm correspond to the methine carbons with attached branches C_{br} (yellow) and α (orange) and β (red) carbon atoms neighboring C_{br} in the chain, respectively. The signals at 16 ppm, 13 ppm and 10 ppm correspond to methyl end groups (turquoise) and methyl groups on isolated ethyl branches (light and dark green). The two signals at 25 ppm (pink) and 22 ppm (dark blue) are attributed to the carbon atoms next to the chain ends (Chabira et al., 2008; Chabira et al., 2012).

Figure S8 – Mechanism for the formation of crosslinks, hydroperoxides, ketones, alcohols, aldehydes, olefins, and carboxylic acids during the photooxidation of polyethylene.

Figure S9 – ^{1}H HT NMR spectra of PE bars for different exposure times and sample depths. The spectra are normalized to the integral of the backbone signal (integral between 0 and 1.6 ppm). Individual spectra are shifted horizontally for better overview.

Figure S10 – ATR-FTIR spectra of tensile bar surfaces for different exposure times: a) Overview of all vibrational bands. The polymer CH_2 units were identified by prominent asymmetric (~2915 cm^{-1}) and symmetric (~2848 cm^{-1}) stretching vibrations (ν(CH_2)). The bending (1472 cm^{-1} and 1463 cm^{-1}) and rocking (730 cm^{-1} and 719 cm^{-1}) methylene resonances (δ(CH_2)) of the crystalline fractions occur as doublets and overlap with broad bands at 1467 cm^{-1} and 723 cm^{-1} typical for the amorphous fractions, respectively (Hagemann et al., 1989; Zerbi et al., 1989).Upon weathering vibrational bands for carboxylic acids (I,ν(C=O): ~1714 cm^{-1}), vinylidenes (II+III, ν(C-H): 3100 cm^{-1} - 3000 cm^{-1} (shoulder)) as well as peroxides and alcohols (IV, ν(O-H): 3450 cm^{-1} (broad)) emerge as result of photooxidation. Additionally, broad vibrational bands around 1170 cm^{-1}, typical for oxidation products such as alcohols, carbonyl compounds, esters, ethers, or ketals/acetals, are observed (Da Costa et al., 2018). b) Enlarged sections of the FTIR spectra (Enlargement factors 15(left) and 2.3(right)) simplify the observation of vibrational bands corresponding to photooxidation products. Spectra are normalized to the peak height of the asymmetric stretching vibration (ν(CH_2)) and shifted horizontally for better overview.

List of Tables

Table S1 – Calculation of total irradiance in the Q-SUN Xe-3 chamber.

Table S2 – Average particle size, particle volume, secondary microplastic particle (SMP) quantity, surface area, total surface area (quantity*surface) for LDPE particles at different exposure times from 0 to 3200 h. SMP quantity was calculated by comparison of the volumes from the 0 h mother particle and the daughter particles.

Table S3 – Crystallinity determined via DSC and ^{13}C CP MAS NMR spectroscopy for particles and tensile bar surfaces at different exposure times from 0 to 3200 h.

Table S4 – Correction factors for the crystalline and amorphous resonances derived from quantitative ^{13C} one-pulse NMR spectra of the 1600 h exposed particle and tensile bar surface sample.

Table S5 – Reflex positions and FWHMs of the 110 and 200 reflexes in the exposed particle samples with corresponding calculated crystalline domain sizes.

Table S6 – Reflex positions and FWHMs of the 110 and 200 reflexes in the exposed tensile bar surface samples with corresponding calculated crystalline domain sizes.

Table S7 – Number-averaged (M_n), weight-averaged (M_w) molecular weights in g/mol and dispersity (Đ) values for particles and tensile bar surfaces at different exposure times.

Table S8 – Correction factors for particles and tensile bar surfaces. Used to calibrate the defect intensities in the CP spectra (Meides et al., 2021).Table S8

Material and Methods

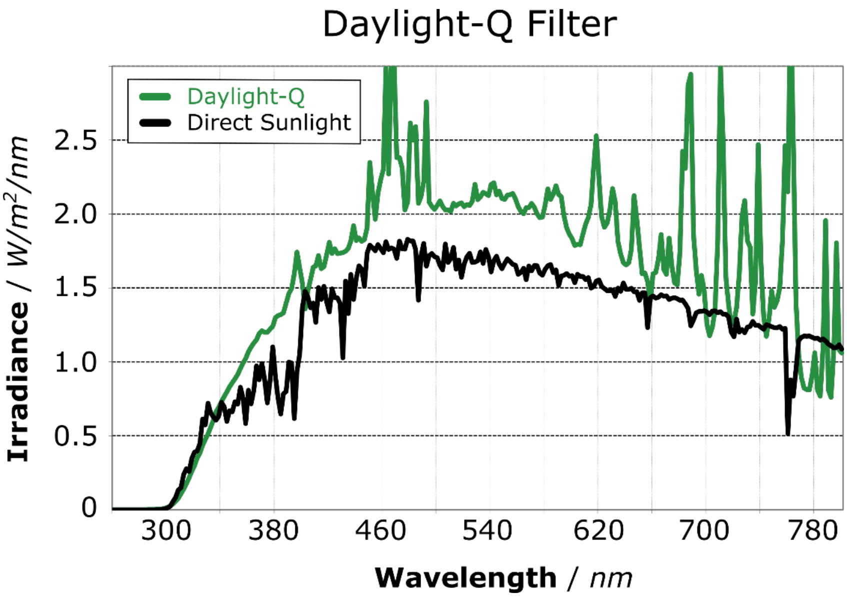

Figure S1 – Q-SUN daylight-Q filter compared to direct sunlight. Modified from Q-Lab Corporation, 2014, Technical Bulletin LX-5060, A Choice of Filters for Q-Sun Xenon Test Chambers.

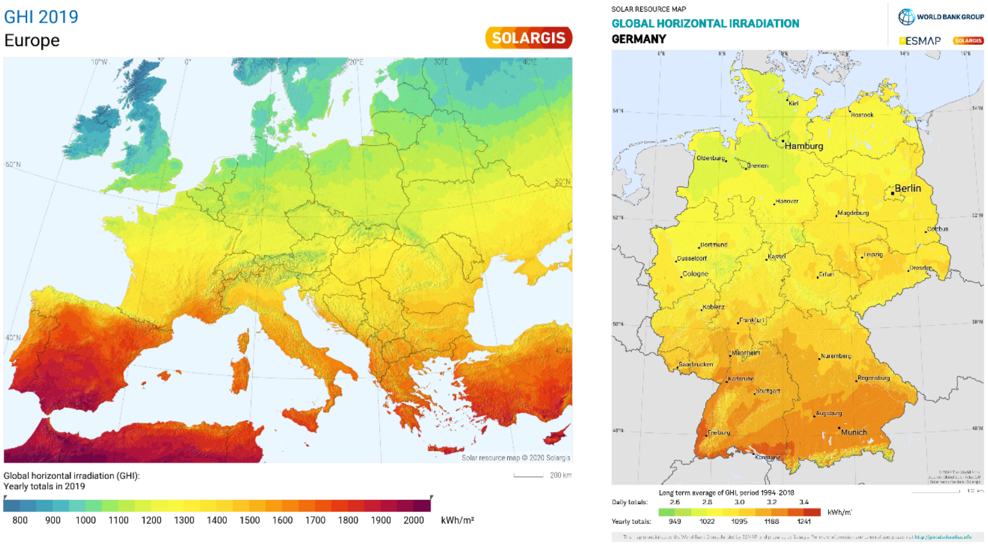

Figure S2 – Global horizontal irradiation for Europe and for Germany in kWh/m² for 2019. Source: SOLARGIS.

Table S1 – Calculation of total irradiance in the Q-SUN Xe-3 chamber.

Calculation of total irradiance in Q-SUN Xe-3 chamber		
Calculation factor*[1]	9.9	-
Lamp settings	60	W/m^2
Total irradiance in Q-SUN Xe-3 chamber	594	W/m^2
Acceleration factor of Q-SUN Xe-3 chamber compared to Central Europe		
Solar irradiance per year*[2]	1000	kWh/m^2
Hours per year	8765	h
Solar irradiance	114	W/m^2
Acceleration factor of Q-SUN Xe-3 chamber*[3]	5.21	-

*[1] *calculation factor extracted from Q-Sun Irradiance Conversion Sheet provided by Q-Lab Germany*

*[2] *value was derived from Figure S2 for the longitude of Central Europe*

*[3] *this value was calculated by division of the total irradiance in the Q-Sun Xe-3 chamber (594 W/m^2) by the solar irradiance determined for Central Europe (114 W/m^2)*

Results

Particle Size Analysis

*Table S2 – Average particle size, particle volume, secondary microplastic particle (SMP) quantity, surface area, total surface area (quantity*surface) for LDPE particles at different exposure times from 0 to 3200 h. SMP quantity was calculated by comparison of the volumes from the 0 h mother particle and the daughter particles.*

LDPE Lupolen 1800p Particles					
Exposure Time	*Average Particle Size*	*Particle Volume*	*SMP Quantity*	*Surface Area*	*Total Surface Area (Quantity*Surface)*
hours	*µm*	*µm^3*	*counts*	*µm^2*	*µm^2*
0	192.2	3717567	-	116053	-
24	187.6	-	-	-	-
50	191.3	-	-	-	-
100	190.5	-	-	-	-
200	189.8	-	-	-	-
400	186.6	-	-	-	-
600	154.0	-	-	-	-
800	97.8	-	-	-	-
1200	33.3	19247	193	3473	-
1600	16.2	2222	1673	824	-
2000	11.2	742	5013	396	1986233
2400	9.6	459	8100	288	-
2800	7.7	234	15859	184	-
3200	7.8	265	14024	200	2798670

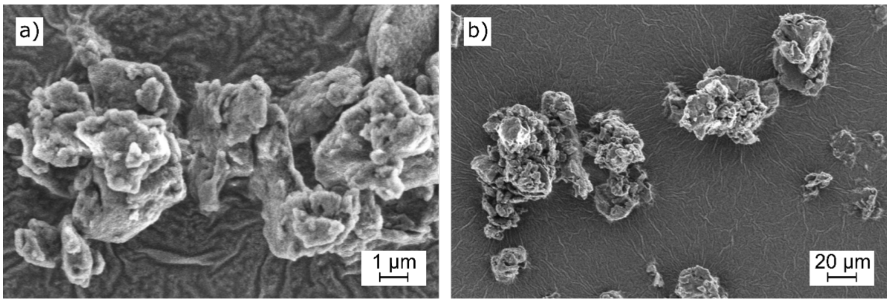

Figure S3 – SEM images of LDPE particles after 2000 h of exposure, visualizing agglomerates of particles.

Polymer Crystallite Orientation

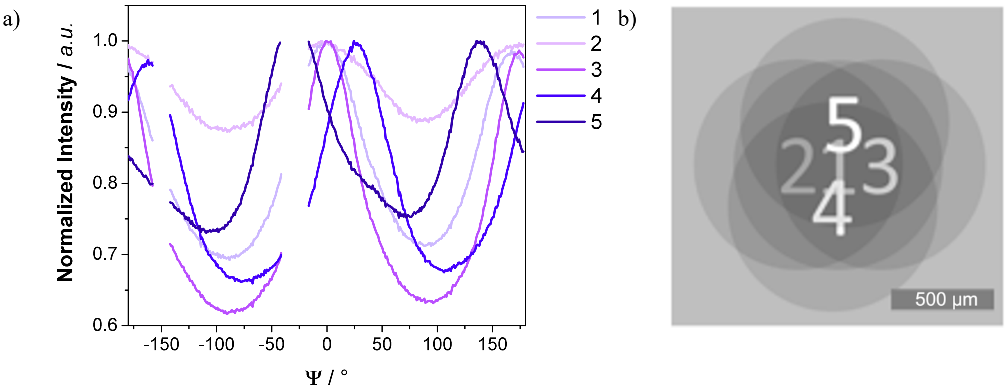

Figure S4 – a) Normalized intensity of the 110 reflex of a PE tensile bar weathered for 2000 h plotted for different scattering directions (Ψ). The X-ray beam, with approx. 900 µm diameter, was shifted to five different overlapping positions (1 to 5) as shown in b).

The crystallite orientation in the 2000 h tensile bar surfaces were examined with WAXS measurements at different overlapping positions. The 2D data show clear changes in orientation of the 110 reflex of the PE crystal structure depending on the measured position. Figure S4a shows how this orientation varies on a length scale of hundred microns, indicating that aligned domains are present on a similar length scale. Looking at the directional distribution of the five measured positions (Figure S4b) the data show that along one measurement direction (2,1,3) the orientation is very similar, while this is not the case for the direction of perpendicularly positioned measurements (4,5). The SEM images of tensile bar surfaces show microcracks on this length scale. The combination of these two observations suggests that the polymer crystallites are oriented in a certain direction and that the direction of the microcracks is correlated with this orientation.

Degree of Crystallinity

Table S3 – Crystallinity determined via DSC and ^{13}C CP MAS NMR spectroscopy for particles and tensile bar surfaces at different exposure times from 0 to 3200 h.

LDPE Lupolen 1800p				
	Crystallinity Particles		**Crystallinity Surfaces**	
Exposure Time	**DSC**	**NMR***	**DSC**	**NMR***
hours	*%*	*%*	*%*	*%*
0	41	40	25	30
24	41	-	-	-
50	40	-	-	-
100	41	-	-	-
200	40	-	30	43
400	44	42	30	43
600	48	48	-	-
800	49	48	34	41
1200	51	52	-	-
1600	54	57	-	42
2000	53	60	39	45
2400	61	65	-	-
2800	60	67	-	-
3200	63	68	42	49

** NMR spectroscopic CP data calibrated with fully relaxed one-pulse experiments for the 1600 h sample.*

To determine the degree of crystallinity the amorphous and crystalline resonances in the ^{13}C CP MAS NMR spectra were deconvoluted with Lorentzian lines. While the intensity was allowed to vary independently, the chemical shift difference was fixed to 2.3 ppm, to improve deconvolution of the overlapping resonances. Regardless of the irradiation doses, Assink *et al.* (Assink et al., 2001) observed constant linewidths of the crystalline resonances that can be explained by the defined long-range order in the crystalline phase. Thus, the linewidth of the crystalline resonance was kept constant, while the width of the amorphous phase could vary independently. As the CP spectra are not quantitative in terms of intensity ratios, they were calibrated with quantitative ^{13}C one-pulse NMR spectra of the 1600 h weathered samples.

Table S4 – Correction factors for the crystalline and amorphous resonances derived from quantitative ^{13}C one-pulse NMR spectra of the 1600 h exposed particle and tensile bar surface sample.

Correction factor	**Crystalline resonance**	**Amorphous resonance**
Particles	1.425	0.718
Surfaces	1.190	0.842

Calculation of Crystalline Domain Size

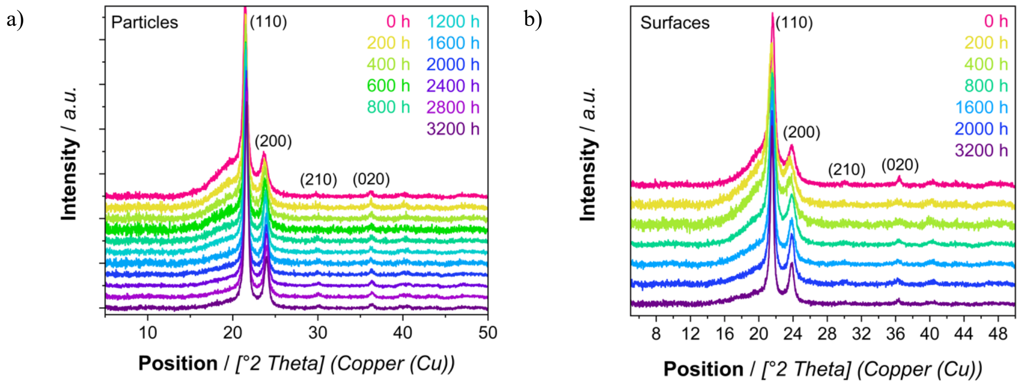

Figure S5 – XRD measurements of a) particles and b) tensile bar surfaces. Upon ageing the amorphous halo decreases indicating an increase of crystallinity.

The diffractograms were deconvoluted with pseudo-Voigt profiles using MatLab R2019b. The obtained reflex positions and FWHMs of the 110 and 200 reflexes for particles and tensile bar surfaces were used to estimate crystalline domain sizes by applying the Scherrer Formula (K~1) (Scherrer, 1912).

Table S5 – Reflex positions and FWHMs of the 110 and 200 reflexes in the exposed particle samples with corresponding calculated crystalline domain sizes.

Particles	**110**			**200**			**Average**
Exposure Time	**Reflex Position**	**FWHM**	**Crystalline Domain Size**	**Reflex Position**	**FWHM**	**Crystalline Domain Size**	**Crystalline Domain Size**
hours	*°2 Theta*	*°2 Theta*	*nm*	*°2 Theta*	*°2 Theta*	*nm*	*nm*
0	21.46	0.531	16.9	23.71	0.916	9.84	13.4
400	21.50	0.450	18.0	23.78	0.808	11.2	14.6
600	21.50	0.462	19.5	23.80	0.753	12.0	15.7
800	21.51	0.449	20.0	23.80	0.700	12.9	16.4
1200	21.53	0.414	21.7	23.84	0.647	13.9	17.8
1600	21.51	0.389	23.1	23.84	0.570	15.8	19.5
2000	21.56	0.389	23.1	23.89	0.575	15.7	19.4
2400	21.59	0.405	22.2	23.94	0.561	16.1	19.2
2800	21.62	0.438	20.5	23.96	0.576	15.7	18.1
3200	21.62	0.451	19.9	23.96	0.589	15.3	17.6

Table S6 – Reflex positions and FWHMs of the 110 and 200 reflexes in the exposed tensile bar surface samples with corresponding calculated crystalline domain sizes.

Surfaces	**110**			**200**			**Average**
Exposure Time	**Reflex Position**	**FWHM**	**Crystalline Domain Size**	**Reflex Position**	**FWHM**	**Crystalline Domain Size**	**Crystalline Domain Size**
hours	*°2 Theta*	*°2 Theta*	*nm*	*°2 Theta*	*°2 Theta*	*nm*	*nm*
200	21.47	0.833	10.8	23.73	1.15	7.83	9.30
400	21.45	0.829	10.8	23.71	1.08	8.36	9.60
800	21.59	0.731	12.3	23.86	1.06	8.54	10.4
1400	21.54	0.551	16.3	23.83	0.786	11.5	13.9
1600	21.55	0.563	15.9	23.83	0.815	11.1	13.5
2000	21.55	0.530	17.0	23.85	0.725	12.4	14.7
3200	21.54	0.424	21.2	23.83	0.642	14.1	17.6

Molecular Weight Distribution – GPC Data

Table S7 – Number-averaged (M_n), weight-averaged (M_w) molecular weights in g/mol and dispersity (Đ) values for particles and tensile bar surfaces at different exposure times.

LDPE Lupolen 1800p (M_n = 36600 g/mol, M_w = 368100 g/mol, Đ = 10.0)						
	Particles			**Tensile Bar Surfaces**		
Exposure Time	**M_n**	**M_w**	**Đ**	**M_n**	**M_w**	**Đ**
hours	*g/mol*	*g/mol*		*g/mol*	*g/mol*	
0	31400	273400	8.7	29600	249200	8.4
24	29700	246900	8.3	-	-	-
50	24500	301200	12.3	-	-	-
100	24700	310900	12.6	-	-	-
200	**15800**	**247700**	**15.6**	**24900**	**442300**	**17.7**
400	**7300**	**58900**	**8.0**	**20800**	**285700**	**13.7**
600	4300	23100	5.5	-	-	-
800	**3500**	**13800**	**4.0**	**9200**	**97300**	**10.6**
1200	2400	7900	3.3	-	-	-
1600	2000	5900	3.0	-	-	-
2000	**1500**	**4800**	**3.1**	**5800**	**65400**	**11.2**
2400	1300	3900	3.0	-	-	-
2800	1100	3600	3.2	-	-	-
3200	**1100**	**3100**	**2.9**	**3700**	**23900**	**6.4**
3200 (1-2 mm)	**-**	**-**	**-**	16500	695300	42.0
3200 (2-3 mm)	**-**	**-**	**-**	14100	442000	31.4

Molecular Weight Distribution – Monte Carlo Simulations

For the MC simulations MatLab R2019b was used. The experimental MWD of reference PE particles served as starting point and was modelled with 30000 initial polymer chains. These chains are represented by their molecular weight and consequently their number of repeating units (RUs, M = 28.05 g/mol). For each time step, either one chain was subjected to chain scission or two chains were crosslinked. The occurring processes were randomly chosen under consideration of an adjustable crosslinking probability (P_{cl}) and chain scission probability ($P_{cs} = 1 - P_{cl}$). During crosslinking two randomly selected chains were combined by addition of their RUs, while in case of chain scissions a randomly selected polymer chain was cut between two randomly chosen repeating units, resulting in two polymer chains with reduced molecular weight. Chains shorter than 4 RUs were excluded from scission. This process was iterated until the simulated MWD was comparable to the experimental one after 3200 h. The crosslink density corresponds to the total number of performed crosslinks, divided by the total number of RUs. The proportion of new end groups is given by the doubled number of chain scissions, divided by the total number of RUs (Meides et al., 2021). The code is available upon request.

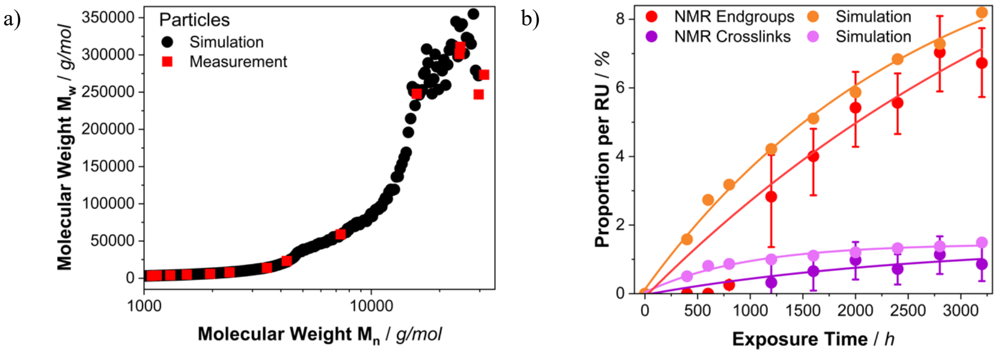

Figure S6 – a) M_w over M_n of the MC simulation (black dots) compared to the measured values (red squares) for particles. The Đ of the measured MWDs could be reproduced when P_{cl} was first set to 42 % and then reduced to 36.5 % and 20 %, respectively, and b) comparison of particle end group and crosslink proportions obtained by NMR spectroscopy and MC simulations.

Solid-State ^{13}C NMR spectroscopy

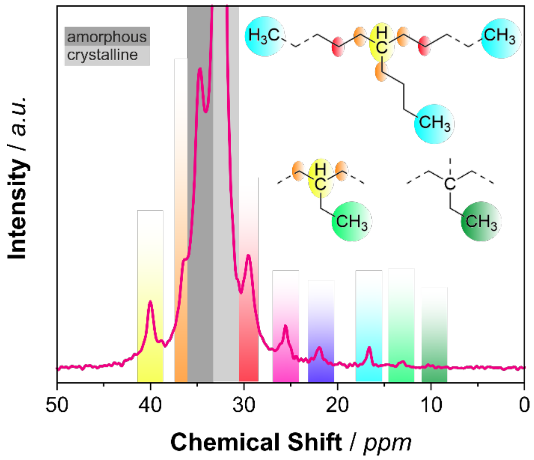

Figure S7 – ^{13}C CP MAS NMR spectrum of the initial PE particles between 0-50 ppm. The differences between the backbone resonances of the crystalline (dark grey) and amorphous (light grey) phases become visible. The weaker signals are attributed to the microstructure of PE. Signals at 40 ppm, 36 ppm and 29 ppm correspond to the methine carbons with attached branches C_{br} (yellow) and α (orange) and β (red) carbon atoms neighboring C_{br} in the chain, respectively. The signals at 16 ppm, 13 ppm and 10 ppm correspond to methyl end groups (turquoise) and methyl groups on isolated ethyl branches (light and dark green). The two signals at 25 ppm (pink) and 22 ppm (dark blue) are attributed to the carbon atoms next to the chain ends (Chabira et al., 2008; Chabira et al., 2012).

Table S8 – Correction factors for particles and tensile bar surfaces. Used to calibrate the defect intensities in the CP spectra (Meides et al., 2021).

Functional Group	**Particles**	**Surfaces**
	c_i 3200 h	**c_i 3200 h**
Carboxylic acid	1.00	1.06
Vinylidene C^1 (141 ppm)	0.46	0.46
Vinylidene C^2 (117 ppm)	0.52	0.58
Peroxide + Alcohol	0.94	0.91

Solid-State ^{13}C NMR spectroscopy: Calculation of defect proportions

$$\rho_{ru} = [1 - (2 \cdot I_{COOH}) - (2 \cdot 0.5 \cdot (I_{olefin1} + I_{olefin2})) - (2 \cdot I_{POOH+OH})] / 2 \qquad \text{(Eq. 1)}$$

with:	ρ_{ru}	proportion of ethylene RUs relative to the proportion of defects
	I_{COOH}	relative intensity of the carboxylic acid resonance
	$I_{olefin1}$	relative intensity of the olefin resonance at 141 ppm
	$I_{olefin2}$	relative intensity of the olefin resonance at 117 ppm
	$I_{POOH+OH}$	relative intensity of the hydroperoxide resonance superimposed with the relative intensity of the alcohol resonance.

Since the ratio of the different groups is I_{COOH} : $0.5(I_{olefin1}+I_{olefin2})$: $I_{POOH+OH}$: ρ_{ru}, the absolute proportions of the carboxy groups (ap_{COOH}), vinylidene groups (ap_{olefin}) and peroxy groups and hydroxy groups ($ap_{POOH+OH}$) can be calculated once ρ_{ru} is known:

$$ap_{COOH} = I_{COOH} / (p_{ru} + I_{COOH} + 0.5 \cdot (I_{olefin1} + I_{olefin\,2}) + I_{POOH+OH}) \qquad \text{(Eq. 2)}$$

$$ap_{olefin} = 0.5 \cdot (I_{olefin1} + I_{olefin2}) / (p_{ru} + I_{COOH} + 0.5 \cdot (I_{olefin1} + I_{olefin\,2}) + I_{POOH+OH}) \qquad \text{(Eq. 3)}$$

$$ap_{POOH+OH} = I_{POOH+OH} / (p_{ru} + I_{COOH} + 0.5 \cdot (I_{olefin1} + I_{olefin\,2}) + I_{POOH+OH}) \qquad \text{(Eq. 4)}$$

Solid-State ^{13}C NMR spectroscopy: Calculation of end group and crosslink densities

From the NMR results the proportion of new end groups (EG_N) can be calculated:

$$EG_N = ap_{COOH} + ap_{olefin} \qquad \text{(Eq. 5)}$$

The combination of NMR and GPC data allows for the calculation of the minimal average number of crosslinks per macromolecule (cl) (Meides et al., 2021):

$$cl = \frac{M_{GPC} - M_{NMR}}{M_{NMR}} \qquad \text{(Eq. 6)}$$

with:	M_{GPC}	average M_n at given weathering time derived from GPC experiments	
	M_{GPC0}	average M_n prior to weathering derived from GPC experiments	
	M_{NMR}	$= \frac{2 \cdot M_{ru}}{EG_A}$	(Eq. 7)
	M_{ru}	molar mass of repeating unit (M_{ru} = 28.05 g/mol for LDPE)	
	EG_A	proportion of all end groups $= EG_N + EG_0$	(Eq. 8)
	EG_0	proportion of end groups at the beginning $= 2 \cdot \frac{M_{ru}}{M_{GPC0}}$	(Eq. 9)

Degradation Mechanism

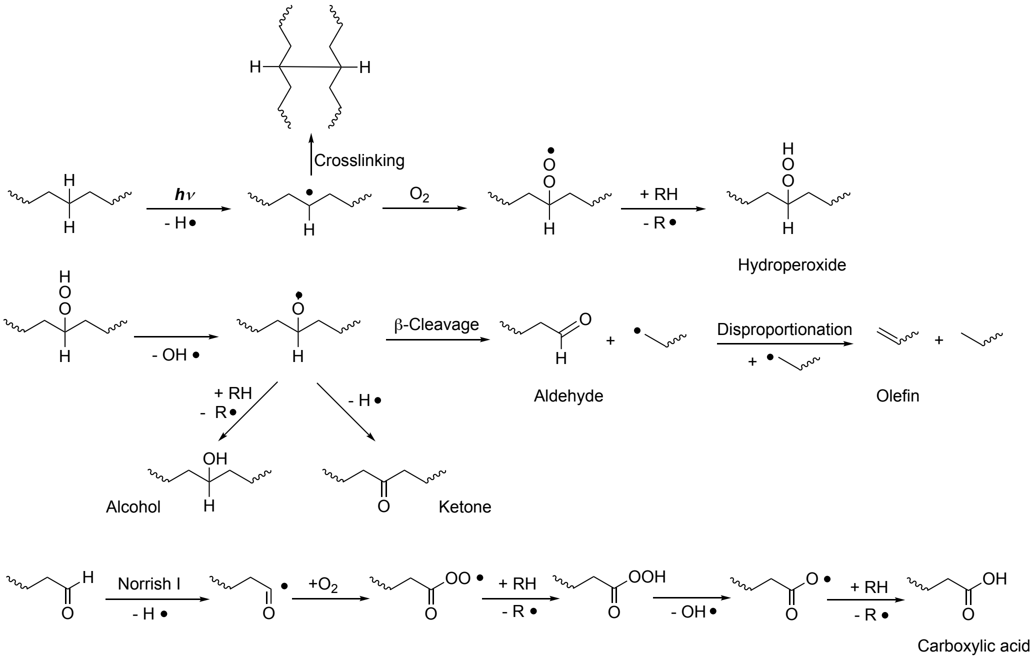

Figure S8 – Mechanism for the formation of crosslinks, hydroperoxides, ketones, alcohols, aldehydes, olefins, and carboxylic acids during the photooxidation of polyethylene.

Liquid state ^{1}H HT NMR spectroscopy

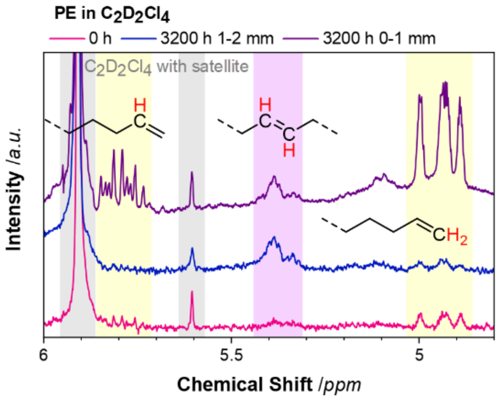

Figure S9 – ^{1}H HT NMR spectra of PE bars for different exposure times and sample depths. The spectra are normalized to the integral of the backbone signal (integral between 0 and 1.6 ppm). Individual spectra are shifted horizontally for better overview.

ATR-FTIR spectroscopy

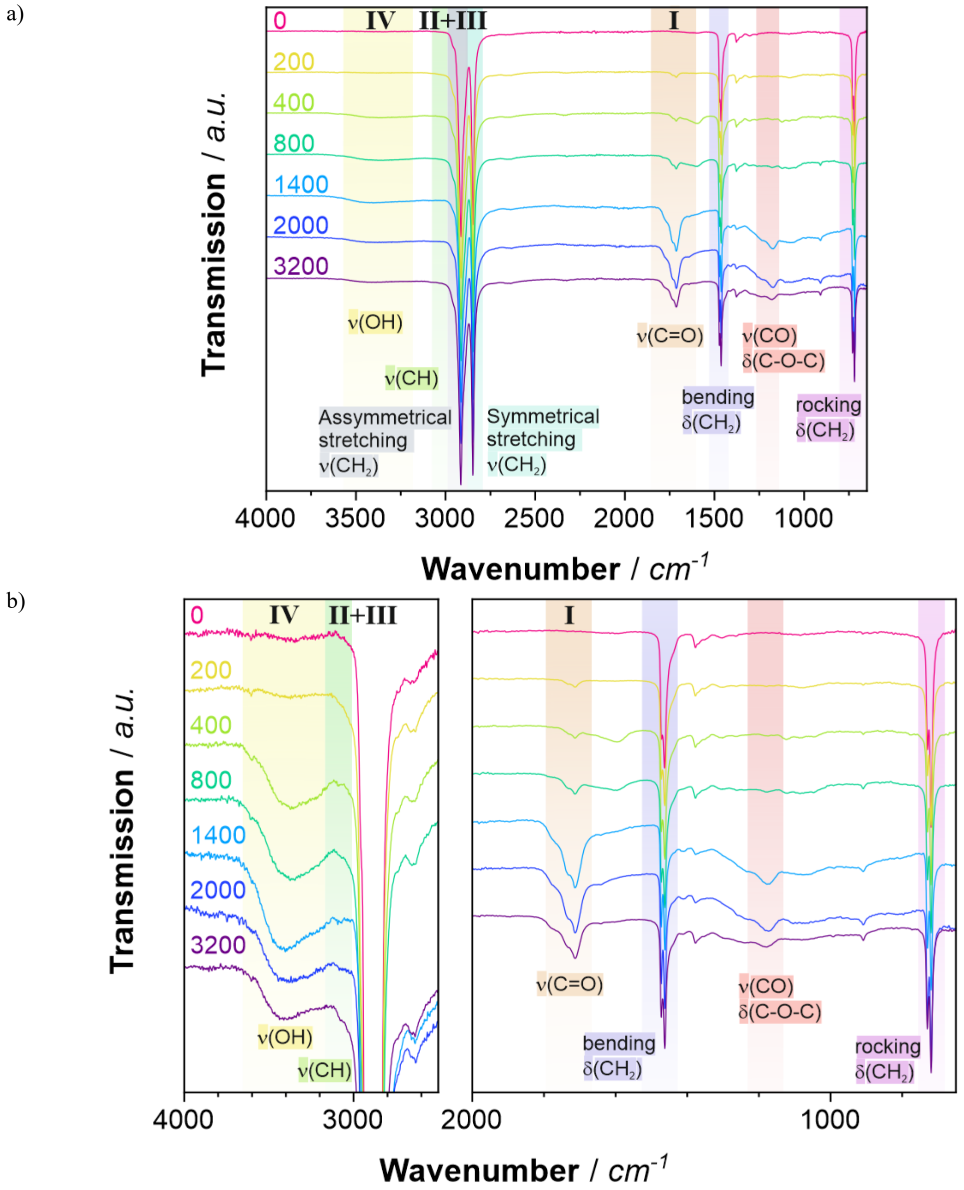

Figure S10 – ATR-FTIR spectra of tensile bar surfaces for different exposure times: a) Overview of all vibrational bands. The polymer CH_2 units were identified by prominent asymmetric (~2915 cm^{-1}) and symmetric (~2848 cm^{-1}) stretching vibrations ($\nu(CH_2)$). The bending (1472 cm^{-1} and 1463 cm^{-1}) and rocking (730 cm^{-1} and 719 cm^{-1}) methylene resonances ($\delta(CH_2)$) of the crystalline fractions occur as doublets and overlap with broad bands at 1467 cm^{-1} and 723 cm^{-1} typical for the amorphous fractions, respectively (Hagemann et al., 1989; Zerbi et al., 1989).Upon weathering vibrational bands for carboxylic acids (I,$\nu(C=O)$: ~1714 cm^{-1}), vinylidenes (II+III, $\nu(C\text{-}H)$: 3100 cm^{-1} - 3000 cm^{-1} (shoulder)) as well as peroxides and alcohols (IV, $\nu(O\text{-}H)$: 3450 cm^{-1} (broad)) emerge as result of photooxidation. Additionally, broad vibrational bands around 1170 cm^{-1}, typical for oxidation products such as alcohols, carbonyl compounds, esters, ethers, or ketals/acetals, are observed (Da Costa et al., 2018). b) Enlarged sections of the FTIR spectra (Enlargement factors 13 (left) and 1.5 (right)) simplify the observation of vibrational bands corresponding to photooxidation products. Spectra are normalized to the peak height of the asymmetric stretching vibration ($\nu(CH_2)$) and shifted horizontally for better overview.

Supplementary References

Assink RA, Celina M, Gillen KT, Clough RL, Alam TM. Morphology changes during radiation-thermal degradation of polyethylene and an EPDM copolymer by 13C NMR spectroscopy. Polymer degradation and stability 2001;73(2):355–62.

Chabira SF, Sebaa M, G'sell C. Influence of climatic ageing on the mechanical properties and the microstructure of low-density polyethylene films. Journal of applied polymer science 2008;110(4):2516–24.

Chabira SF, Sebaa M, G'sell C. Oxidation and crosslinking processes during thermal aging of low-density polyethylene films. Journal of applied polymer science 2012;124(6):5200–8.

Da Costa JP, Nunes AR, Santos PSM, Girao AV, Duarte AC, Rocha-Santos T. Degradation of polyethylene microplastics in seawater: Insights into the environmental degradation of polymers. Journal of Environmental Science and Health, Part A 2018;53(9):866–75.

Hagemann H, Snyder RG, Peacock AJ, Mandelkern L. Quantitative infrared methods for the measurement of crystallinity and its temperature dependence: polyethylene. Macromolecules 1989;22(9):3600–6.

Meides N, Menzel T, Poetzschner B, Löder MGJ, Mansfeld U, Strohriegl P et al. Reconstructing the Environmental Degradation of Polystyrene by Accelerated Weathering. Environmental Science & Technology 55 2021(12):7930–8. 10.1021/acs.est.0c07718.

Scherrer P. Bestimmung der inneren Struktur und der Größe von Kolloidteilchen mittels Röntgenstrahlen. In: Kolloidchemie, Ein Lehrbuch: Springer; 1912. p. 387–409.

Zerbi G, Gallino G, Del Fanti N, Baini L. Structural depth profiling in polyethylene films by multiple internal reflection infra-red spectroscopy. Polymer 1989;30(12):2324–7.

8.3 Quantifying the fragmentation of polypropylene upon exposure to accelerated weathering.

Meides *et al. Microplastics and Nanoplastics* (2022) 2:23
https://doi.org/10.1186/s43591-022-00042-2

Microplastics and
Nanoplastics

RESEARCH **Open Access**

Quantifying the fragmentation of polypropylene upon exposure to accelerated weathering

Nora Meides[1†], Anika Mauel[2†], Teresa Menzel[3], Volker Altstädt[3], Holger Ruckdäschel[3], Jürgen Senker[2] and Peter Strohriegl[1*]

Abstract

Polymers are omnipresent in our everyday lives. For specific applications, their properties can be extensively modified by various types of additives, e.g., processing stabilizers, antioxidants, UV-stabilizers, flame retardants, and plasticizers. While several additives are nowadays considered to be toxic or persistent in the environment, quantitative data characterizing plastic fragmentation and microplastic formation have not yet been discussed in detail. Here, we present a long-term, laboratory-controlled accelerated weathering study on polypropylene (PP) particles with and without processing stabilizers. We were able to identify the stabilizers as Irgafos® 168, and Irganox® 1010. For both PP sample sets, we monitored the degradation using a combination of various analytical methods, such as gel permeation chromatography, particle size distributions, scanning electron microscopy, solid-state ^{13}C magic-angle spinning NMR and liquid-state ^{1}H, ^{13}C, ^{31}P NMR spectroscopy, differential scanning calorimetry and matrix-assisted laser desorption ionization time of flight mass spectrometry. The stabilizers prevent degradation by simulated solar radiation for about 350 h. Then, degradation sets in rapidly, leading to an exponential decrease in molecular weight and particle size, accompanied by an increase in crystallinity and the formation of oxygen-containing functional groups. After 3200 h, representing approximately 2 years of outdoor weathering, both PP samples exhibit comparable characteristics and sizes, regardless if a stabilizer was initially present. During degradation, an extremely large number of 100,000 daughter particles (4 µm) are formed and released from one MP particle of 192 µm diameter. Their physical properties and chemical composition have largely changed, resulting in a very low molecular weight and a hydrophilic character. These particles no longer resemble pristine PP. We thus expect them to be more prone to biodegradation compared to the starting material.

Keywords: Degradation, Microplastic, Nanoplastic particles, Photooxidation, Additives, Secondary daughter MP particle production

Introduction

Plastics are nowadays inevitably a part of our everyday life. They are cheap, lightweight, and durable, and their properties can be easily adapted, leading to a wide range of applications. In 2019, the global plastic production reached a total of 368 million tons, still increasing year by year [1]. The largest end-use market in Europe, with a contribution of 40%, is the packaging industry, where polypropylene (PP) is one of the dominating polymer types [1]. Materials made of PP are often single-use items

---

[†] Nora Meides and Anika Mauel contributed equally to this work and share first authorship.

*Correspondence: peter.strohriegl@uni-bayreuth.de

[1] Department of Macromolecular Chemistry I, University of Bayreuth, Universitätsstraße 30, 95447 Bayreuth, Germany
Full list of author information is available at the end of the article

for wrappers, food packaging, containers and bottle caps. This leads to the generation of large amounts of PP waste, often exported to developing countries with poor waste management strategies [2, 3]. Ultimately, a large amount of the exported waste is expected to end up in environmental compartments, where abiotic and biotic degradation mechanisms lead to fragmentation and break-down [2, 4, 5]. As a consequence, microplastic (MP) is formed, often defined as plastic fragments of all polymer types and shapes with the largest dimension ranging from 1 µm to 1000 µm [6]. In recent years, MP has become a great concern and is seen as an emerging ecological risk [7–10].

Not only are large quantities of secondary MP formed from degradation and fragmentation, their chemical structure is also modified throughout the ageing process. The initially non-polar polymer chains turn gradually into increasingly polar oligomers [5, 11, 12]. As a consequence of pronounced oxidation, aged MP particles become hydrophilic, enhancing biofilm formation [13, 14] as well as the uptake by organisms [15, 16]. Recent studies have addressed the toxicity of small polymer MP particles [17] and negative effects on organisms [18, 19].

Toxicity may not only originate from the polymer itself or from changes in the chemical composition during weathering but can also result from leaching and degradation of low molar mass compounds present in almost all polymers. Plastics for everyday products are optimized to maintain their properties for a specific period of time. For this purpose, a variety of additives are used to stabilize the polymers a) during processing and b) during their service life. With regard to their application, different classes of additives are distinguished such as processing aids, antioxidants, thermo- and UV-stabilizers, flame retardants and plasticizers [20]. Some low molar mass compounds frequently present in consumer products and plastic packaging, are now considered environmentally harmful or even toxic, such as phthalates, bisphenol A, biocides, certain flame retardants, and highly fluorinated substances [21]. Consumer goods and packaging products are very complex materials containing a variety of substances [22]. This complexity is maintained or even increases once polymer materials of any origin are released into natural compartments. The incorporated stabilizers and their degradation products can leach from the plastics, posing an environmental concern [20].

In recent years, multiple studies have addressed the environmental weathering of PP, polystyrene (PS), and polyethylene (PE), reporting changes in chemical composition, a decrease in molecular weight due to chain-scission and the formation of degradation products such as peroxides, alcohols, and carboxylic acids [23–29]. These changes are induced by photooxidation and typically accompanied by a modification of the physical properties, leading to embrittlement and fragmentation [5, 7, 30–32]. In natural compartments, physical stress factors such as mechanical impacts will additionally enhance fragmentation and break-down, leading to MP formation [33].

Photooxidation of polymers and the influence of polymer additives on polymer break-down has been thoroughly investigated for the past decades [34–36]. While the underlying mechanisms of photooxidative degradation are well understood, much less is known about the role of stabilizers and their degradation products [20]. Quantitative data regarding fragmentation rates as well as secondary MP particle production and release remain scarce [32, 37–40], and are lacking for stabilized polymer systems. Furthermore, numeric data for time scales in which the stabilizers avoid degradation, and the effect of the stabilizers on the fragmentation of macroplastic has only gained little attention up to date.

To bridge this knowledge gap, we combined laboratory weathering with extensive analytical investigations and calculation of fragmentation rates for a commercially available stabilized PP. In order to monitor the influence of stabilizers on the polymer degradation, with special focus on the fragmentation into smaller particles, the stabilizers were removed from a second PP batch by Soxhlet extraction and identified. A multitude of analytical methods, such as gel permeation chromatography (GPC), light scattering for particle size distributions, scanning electron microscopy (SEM), and differential scanning calorimetry (DSC) were combined to trace the degradation and fragmentation of stabilized, and non-stabilized PP as a function of exposure time.

Additionally, solid-state ^{13}C magic-angle spinning (MAS) NMR spectroscopy was performed for identification and quantification of photooxidative defects accumulating with proceeding degradation. As previously reported [5, 41] quantification is enabled by a multiple cross polarization (multiCP) pulse sequence [42, 43]. Although solid-state NMR spectroscopy has rarely been considered for investigation of degradation products, it serves as a complementary method to other commonly used techniques, such as Fourier transform infrared (FTIR) or Raman spectroscopy, and pyrolysis–gas chromatography-mass spectrometry (Py-GC–MS) [23, 24, 28, 29, 44–46]. NMR spectroscopy provides volume-averaged results and can give information on the dynamics of the system, e.g., details on the distribution and variations of crystalline and amorphous regions. It is a non-destructive method however, it does require relatively large amounts of sample material, which can pose a problem for environmental samples.

The data presented in this study deliver a profound understanding of fragmentation rates resulting from photooxidative degradation, also considering the influence of stabilizers. The derived numbers give an approximation for how many micro- and nanoplastic particles can potentially be released, when PP is exposed to solar radiation and mechanical stress in an aqueous environmental setting. Experimentally determined numerical fragmentation rates have not yet been reported in the literature. Thus, this study fills a knowledge gap and delivers important information concerning micro- and nanoplastic formation.

Experimental

Material and methods

Polypropylene (PP, Moplen HP526J) in pellet form was provided by LyondellBasell Industries (Basell Polyolefine GmbH, Wesseling, Germany). As stated in the data sheet, this PP grade is supplemented with a standard processing stabilizer. Particles were produced from PP pellets by cryo-milling with an ultra centrifugal Mill ZM-200 (Retsch GmbH, Haan, Germany). Particles were then separated into several fractions using an Alpine air jet sieve E200 LS (Hosokawa Alpine AG, Augsburg, Germany). For the experiments from this study, the fractions < 125 µm and 125–200 µm were used. Reference compounds Irgafos® 168 (Tris(2,4-di-tert-butylphenyl)phosphate), and Irganox® 1010 (Pentaerythritol tetrakis(3-(3,5-di-tert-butyl-4-hydroxyphenyl)propionate)) were purchased from BASF (Ludwigshafen, Germany). 500 mg Irganox® 1010 was dissolved in 100 ml tetrahydrofuran (THF) and placed into the Q-Sun Xe-3 for 100 h. THF was then evaporated to dryness and the compound, further referred to as Irganox® $1010_{\text{weathered}}$, was analyzed via MALDI-TOF MS.

Soxhlet extraction

A Soxhlet extraction was performed on a PP fraction < 125 µm in size. 24 g PP particles were placed into a glass thimble onto a cellulose filter and covered with glass wool. Extraction was performed in a Soxhlet apparatus with 700 ml of boiling THF for 14 days. Particles were filtered off and dried under vacuum (40 °C) and subsequently weathered according to the procedure described below. The extraction solvent was evaporated, and the residue was dissolved in hexane and ethyl acetate (19:1) and passed over a silica column. The products were investigated via MALDI-TOF MS.

Matrix assisted laser desorption ionization-time of flight mass spectrometry (MALDI-TOF MS)

The residue of the stabilizer extraction, as well as Irganox® $1010_{\text{weathered}}$, were analyzed via MALDI-TOF MS using the solvent-based dried droplet sample preparation procedure. Sample and matrix (DHB – 2,5-dihydroxybenzoic acid) were dissolved in THF with a concentration of 10 mg/ml, mixed with a ratio of 5:20 and a thin layer applied onto the target plate. Mass spectra were acquired with a Bruker autoflex® maX TOF/TOF (Bruker Daltonics GmbH & Co. KG, Bremen, Germany) in positive ion reflector mode between 200–2000 Da. The instrumental settings were optimized for best resolution and highest intensity. In total, 5000 shots were taken randomly across the dried-droplet sample spot. The obtained spectra were processed with the flexAnalysis software.

Accelerated weathering

Both stabilized and unstabilized particle fractions were weighed to 20 g each and transferred into quartz glass beakers filled with 600 ml deionized water and covered with quartz glass lids. Stirring of the water-particle mixture was enabled using magnetic stirrers and PTFE-covered stirring devices. This setup was placed into a Q-SUN XE-3 test chamber (Q-LAB Corporation, Westlake, OH, USA) and irradiated for a total of 3200 h. The test chamber is equipped with three xenon lamps, operating at 60 W/m^2 each (at 300–400 nm), which corresponds to a total irradiance of 594 W/m^2 (300–800 nm) and a five-fold acceleration compared to mid-European conditions (Fig. S1, Tab. S1). This acceleration resembles approximately two years of outdoor weathering in central Europe. Further, Daylight-Q filter systems, cutting off radiation with wavelengths < 295 nm, were installed. This assures an irradiation spectrum very similar to the spectrum of natural sunlight (Fig. S2). Additional settings were relative humidity at 50% and chamber temperature at 38 °C.

At each sampling time (24, 50, 100, 200, 400, 600, 800, 1200, 1600, 2000, 2400, 2800 and 3200 h), 1–2 g of sample material were drawn from the water-sample mixture, filtered, and dried under vacuum at 40 °C. Samples were stored in a dark and dry place until further analysis.

High temperature gel permeation chromatography (HT-GPC)

Molecular weight distributions (MWD) as well as M_n, M_w, and Đ values were measured via GPC using an Agilent (Polymer Laboratories Ltd.) PL-GPC 220 high-temperature chromatographic unit. This set is equipped with RI and PD detectors as well as three linear mixed bed and guard columns (Olexis). Analysis was performed at 150 °C (Pasch, 2001) using 1,2,4-trichlorobenzene (TCB) as the mobile phase. All samples were prepared by dissolving 2–3 mg of PP particles (0.1 wt.-%) in 1.5 ml of the mobile phase solvent (TBC) in an external oven at 150 °C upon continuously stirring. The solutions were run without filtration. The determined molecular weights were referenced to linear HDPE standards ($M_w = 142{,}000 - 701{,}000$ g/mol, K = 40,600, and Alpha = 0.725) and were corrected with K and Alpha values for i-PP (K = 19,000 and Alpha = 0.725).

Scanning electron microscopy (SEM)

Field-emission scanning electron microscopy (FESEM) was performed on particles with a Zeiss ULTRA PLUS (Carl Zeiss Microscopy GmbH, Jena, Germany) at an acceleration voltage of 3 kV and a FEI Quanta 250 (Field Electron and Ion Company, Thermo Fisher Scientific, Hillsboro, USA) high resolution field emission gun (FEG) scanning electron microscope at 10 kV, operating at low vacuum. Particles were coated with a thin layer of platinum by a Cressington 208 HR sputter coater prior to investigation.

Particle size analysis

Particle size distributions and the average particle size were determined with a Microtrac FlowSync Particle Size Analyzer (Microtrac Retsch GmbH, Haan, Germany) having a lower detection limit of 10 nm. Measurements were performed in deionized water with 2–5 mg of particles. 2 ml of 5 wt.-% $Na_4P_2O_7$, and a few drops of a 2 wt.-% $C_{20}H_{37}NaO_7S$ (dioctyl sulfosuccinate sodium salt) detergent were added and 60 s of ultrasound at 40 kHz were applied to avoid aggregation. Average values from three measurements were calculated by the Microtrac software.

Differential scanning calorimetry (DSC)

DSC measurements were performed on 8–10 mg sample material using a Mettler Toledo DSC 3+ (Mettler-Toledo GmbH, Gießen, Germany). The samples were heated with 10 K per minute under N_2-atmosphere from 25–200 °C and cooled to 25 °C. An isothermal stage of 5 min was applied between the heating and the cooling cycle. The degree of crystallinity χc in the first heating cycle was determined using $\Delta H_m{}^0 = 207.1$ J/g for a hypothetically 100% crystalline PP [29]. Determination of χ_c and T_m was performed using the STARe software.

NMR spectroscopy

Liquid-state ^1H, ^{13}C and ^{31}P NMR spectroscopic experiments were recorded on a Bruker Avance-III HD spectrometer with 5 mm CryoProbe™ Prodigy BBO 500 S2 head operating at a B_0 field of 11.7 T (^1H: $\upsilon_0 = 500.1$ MHz, ^{13}C: $\upsilon_0 = 125.8$ MHz, ^{31}P: $\upsilon_0 = 242.9$ MHz). Deuterated chloroform ($CDCl_3$) was used as solvent. Via the residual solvent resonance all ^1H and ^{13}C spectra were referenced to tetrametylsilane. For the ^{31}P spectra, triphenylphosphine oxide was used as secondary standard.

Solid-state ^{13}C MAS NMR spectroscopic experiments were recorded on a Bruker Avance-III HD spectrometer operating at a B_0 field of 9.4 T (^1H: $\upsilon_0 = 400.1$ MHz, ^{13}C: $\upsilon_0 = 100.6$ MHz) using a 3.2 mm triple resonance probe (Bruker) with zirconia rotors (approx. 25 mg sample). A spinning frequency of 20 kHz was applied which is sufficiently fast to avoid the occurrence of spinning sidebands as the chemical shift anisotropies (20–40 ppm) of aliphatic carbons are averaged [47]. ^{13}C CP experiments were performed for a series of PP samples with different weathering times. The contact time was set to 2.0 ms, and the same Hartmann-Hahn conditions as for the multiCP experiments were used. MultiCP measurements [43] were conducted for the longest weathered sample. The parameters for the multi-pulse CP measurements [42] were optimized for the PP samples. Seven CP blocks with a contact time of 400 µs (υ_{nut} (^{13}C) = 47 kHz, 39 kHz ≤ υ_{nut} (^1H) ≤ 55 kHz), separated by a time t_z of 3 s, were applied. At the end and the beginning of each CP block $(90°)_{-x}$ pulses with pulse lengths of 2.5 µs (^1H) and 3.8 µs (^{13}C) were used. Proton decoupling was applied during acquisition using the spinal-64 sequence at a B_1 field of 70 kHz.

For defect quantification, all spectra were deconvoluted with pseudo-Voigt profiles using the SOLA program included in TopSpin 3.2 (Bruker). To account for the small defect proportions, a serial refinement procedure was applied. For the two spectra with longest weathering times and thus highest defect proportions, simultaneous, free refinements with one set of isotropic chemical shift, line broadening and Gauss/Lorentz ratio, for each defect resonance, were performed. The corresponding intensities were refined separately. For shorter weathering times, the obtained fitting parameters were applied in subsequent refinements, and only the intensity was varied. This reduces the degrees of freedom sufficiently, allowing to derive meaningful intensities for spectra with lower signal-to-noise ratios. In contrast, for the more intense backbone signals, a free refinement of all parameters was possible. All refinement parameters are given in Table S5.

Results and discussion

We performed accelerated weathering laboratory experiments under abiotic conditions, using particles of a standard PP grade. To elucidate the influence of stabilizers on the degradation, we used one batch with and one batch without stabilizers.

Using MALDI-TOF MS and ^1H, ^{13}C and ^{31}P liquid-state NMR spectroscopy, the Soxhlet extracted additives were analyzed and two stabilizers could be identified.

The MS spectra are shown in Figures S3A and S4A + B. Three peaks at m/z 663.2, m/z 685.2 and m/z 701.2 are dominant in Figure S3A. They match values for tris(2,4-di-tert-butylphenyl)phosphate, the oxidized species of the well-known stabilizer Irgafos® 168 [48, 49]. Tris(2,4-di-tert-butylphenyl)phosphite (Irgafos® 168) itself could not be detected. These findings were validated by the obtained NMR spectra (Fig. S5A-C) exhibiting the typical resonances for tris(2,4-di-tert-butylphenyl)phosphate. In particular, the ^{31}P NMR spectrum (Fig. S5C) shows a single resonance at -19.9 ppm, demonstrating, that only the phosphate is present. Additionally, Irganox® 1010 could be identified as a second stabilizer by analysis of Irganox® 1010 reference material, treated with simulated solar radiation in THF for 100 h (Irganox® 1010$_{\text{weathered}}$). The dominant peaks observed in the MALDI spectra of the extracted stabilizer (Fig. S4A) and in Irganox® 1010$_{\text{weathered}}$ (Fig. S4B) are almost identical and represent fragments of the original Irganox® 1010 molecule (Fig. S4C). These observations could be confirmed by ^{1}H and ^{13}C liquid-state NMR spectra (Fig. S5D-E).

Since Irgafos® 168 and Irganox® 1010 are processing stabilizers, their main purpose is to assure stability of the respective polymer during melt processing, e.g. extrusion [48]. Temperature, shear strain, or other critical factors may lead to chemical degradation, reducing the molecular weight, and resulting in a decrease of the mechanical strength. To assure stability throughout melt processing, stabilizers, such as radical scavengers and hydroperoxide decomposers, are often added. Irgafos® 168 is a hydrolytically stable phosphite processing stabilizer acting as a secondary antioxidant [50]. It is often used in combination with the primary antioxidant Irganox® 1010, a sterically hindered phenol. By deactivation of peroxy radicals and hydroperoxides, formed during autoxidation, degradation of the polymer is prevented. The most important reactions during the decomposition of PP are shown in Figure S6 [49, 51]. The mechanism is very similar for both, thermal and photochemical decomposition. The major difference is, that the energy to create free radicals by a homolytic cleavage of C-H bonds comes from heating, in the case of thermal oxidation, and from high energy photons of the sunlight, in the case of photooxidation. In natural environments, photooxidation is the dominating mechanism to induce degradation. Following the initial formation of radicals, a multitude of reactions proceed via hydroperoxides, and peroxide and alkoxy radicals, leading to chain-scission and crosslinking (Fig. S6, top scheme). The chain-scissions are accompanied by the formation of oxygen-containing functional groups like alcohols, ketones and carboxylic acids. The stabilizer combination is able to prevent decomposition by reacting with all reactive intermediates marked in red in Figure S6 (top scheme). Thereby, the stabilizer combination, which is usually added in quantities of ~ 0.1 to 0.2 wt.% [51], retards degradation up to the point where it is completely consumed. Afterwards, degradation sets in.

To study the degradation of PP, particles were irradiated with simulated solar radiation, while being stirred in water and thus subjected to additional mechanical stress. Degradation of both sample sets, with a special view on the influence of the stabilizers, was monitored over a total experimental duration resembling approximately two years of outdoor weathering under mid-European conditions.

Particle size

Values for the average particle size are displayed in Figure 1 (Tab. S2) and particle size distributions in Figure S7. To ensure efficient extraction of the additives, a smaller particle fraction was chosen for unstabilized PP (Ø = 119 µm) compared to the stabilized particle

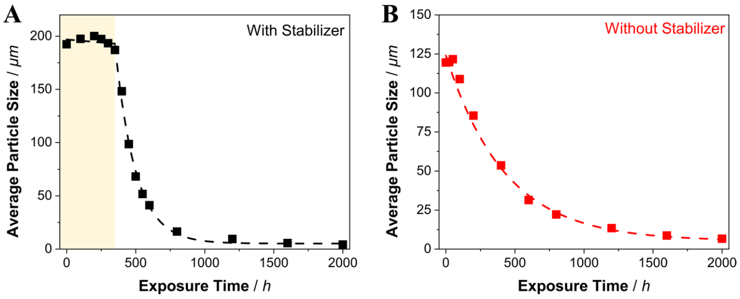

Fig. 1 Average particle size for **A** PP particles with stabilizer and **B** PP particles without stabilizer. The induction phase, characterized by the presence of Irgafos® 168 and Irganox® 1010, is highlighted in yellow. Degradation proceeds in an exponential manner with τ = 149 h for PP with and τ = 427 h for PP without stabilizer (∝ exp(− t/τ))

fraction (Ø = 192 μm). The average size of the particles with stabilizer in Figure 1A remains constant up to 350 h, then rapidly decreases in an exponential manner. We attribute the linear trend between 0–350 h to the influence of the stabilizer, since it is absent for PP without additives (Fig. 1B). We refer to this phase as the induction phase, highlighted in yellow in Fig. 1. The exponential fit from 350 h onwards, reveals a lifetime τ of 149 h, in which the particles have reached half of the original size. PP particles without stabilizer (B) start to decrease already from 50 h onwards, but decay slower, with τ = 427 h. After 800 h, both samples reach the same particle size of ~ 20 μm, which slowly decreases further to ~ 5 μm in the remaining 2400 h of experiment duration (Tab. S2). During weathering the particle size distribution broadens, as can be seen in Figure S7. Further details on the particle size at long irradiation times will be discussed in the upcoming sections.

Molecular weight distributions

Molecular weight distributions (MWD) for both sample sets were obtained by HT GPC (Tab. S3, Fig. S8). Initially, MWDs from both experiments are broad (Fig. 2A, 2B) with dispersity (Đ) values of > 7, typical for commercial PP. Throughout the exposure to simulated solar radiation, PP particles are highly affected by photooxidation, radical formation and chain scission. The M_n decreases from $M_{n,0}$ = 68,000 g/mol down to $M_{n,3200}$ ~ 1000 g/mol within 3200 h (Tab. S3). Major differences between the stabilized and non-stabilized PP are evident within the first 300 h of weathering. The PP sample with stabilizer shows a uniform MWD (Fig. 2A) with curves from 0–250 h overlapping. The M_n-values (Fig. 2C) decrease very slowly in a linear trend until 300 h, then evolve in an exponential manner, revealing rapid decrease of the polymer chain length. This linear trend represents the induction phase, which was also observed within the particle size data (Fig. 1). The PP sample without stabilizer shows an immediate shift of the MWD to lower values and a reduction of M_n, starting with the first sample drawn after 24 h (Fig. 2B, 2D, S8).

Within both, the particle size measurements (Fig. 1A) and the MWD (Fig. 2A), PP with stabilizer shows only little effects from weathering with steady values in particle size and only slow decrease in molecular weight M_n in the beginning. This is due to the deactivation of reactive intermediates from autoxidation by Irgafos® 168 and Irganox® 1010. Once degradation starts, it proceeds rapidly and in an exponential manner, catching up with the non-stabilized PP within few sampling times. M_n values are similar (~ 2000 g/mol) for both PP samples after 800 h of weathering (Tab. S3). Fragmentation however proceeds far faster for the stabilized PP from 350 h onwards, than what is observed for the non-stabilized PP, which

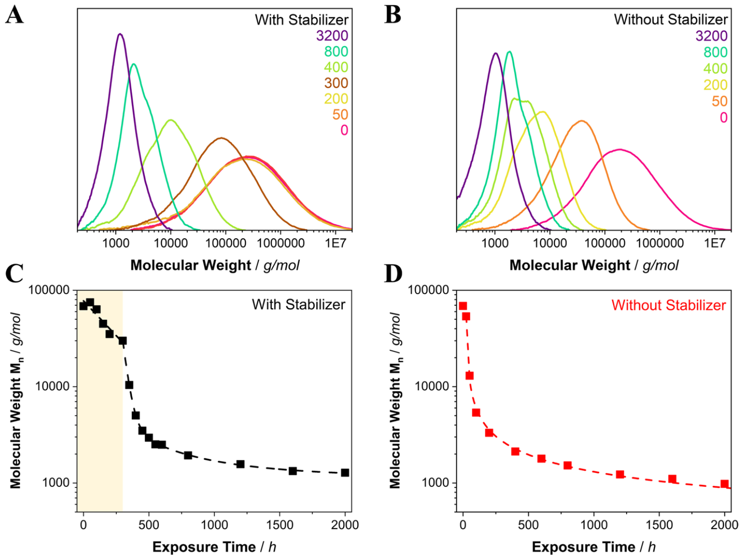

Fig. 2 Molecular weight distributions for **A** PP with additive and **B** PP without additive for chosen exposure time intervals. **C** M_n as a function of exposure time for PP with and **D** without stabilizer. The induction phase is highlighted in yellow

degrades from 50 h on. This is a striking observation. The only difference between the two PP samples is the presence of stabilizers and predominantly their degradation products in the stabilized PP sample, in the time interval where particle size decreases in an exponential manner. Both, stabilizers and degradation products are absent in the non-stabilized PP sample. We speculate that the presence of the degradation products may be responsible for the faster fragmentation, and thus the lower value of τ determined for the exponential decay of the stabilized sample. After 3200 h, the average particle size, as well was the final MW, are almost equivalent for samples with and without stabilizer.

Crystallinity and melting temperature

The thermal characteristics of PP with and without stabilizer were investigated via DSC and are shown in Fig. 3 (Fig. S9). The melting temperature T_m and degree of crystallinity χc for the reference sample were determined to $T_{m,0}=165$ °C; $χc_{,0}=\sim50\%$ (Tab. S4). Heating curves for both PP experiment series, displayed in Fig. 3A, show similarities for PP with stabilizer (solid lines) at 0 and 200 h, while PP without stabilizer (dashed lines) shifts to lower values. The influence of the stabilizer within the first 350 h becomes evident when looking at T_m (Fig. 3B, 3D) and trends for the degree of crystallinity χc (Fig. 3C, 3E) for both PP experiments. No change in T_m can be detected within the induction phase of stabilized PP, highlighted in yellow (Fig. 3B, 3C). The start of degradation is marked in green, with a prominent drop in T_m by ~ 6 °C. The decrease in T_m can be explained by increasing crystal defects occurring as a consequence of degradation [29]. As degradation continues (grey), T_m decreases further from 156 °C to 120 °C (Tab. S4). This is accompanied by a broadening of the melting peak (Fig. 3A), and an increase in the melting enthalpy $ΔH_m$. From integration of the melting peak, χc was determined, and a similar trend is observed (Fig. 3C): no change in χc within the induction phase, followed by a rapid increase by 17%, marking the beginning of degradation. For PP without stabilizer, the induction phase is absent, and degradation is initiated directly. T_m decreases by 13 °C with a linear trend from 0–200 h and χc increases by 17%. The long-term degradation proceeds similar for both PP experiments.

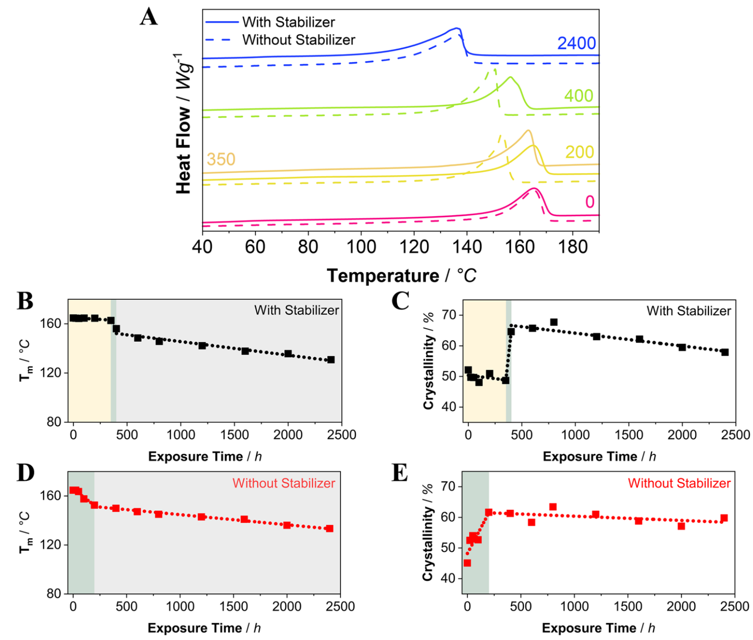

Fig. 3 **A** Melting curves of PP with (solid) and without stabilizer (dashed) for 0, 200, 350, 400 and 2000 h of weathering. Individual curves are shifted vertically for better comparability. **B** T_m in °C and **C** crystallinity in % as a function of exposure time from 0 to 2400 h for PP with stabilizer. **D** T_m and **E** crystallinity for PP without stabilizer. The induction phase is highlighted in yellow. Green marks the start of degradation while grey indicates on-going degradation with minor changes of T_m and crystallinity

The ^{13}C CP MAS NMR spectra for both sets of weathering experiments (with and without stabilizer combination) show the typical resonances for the amorphous and crystalline regions of PP [52] (Fig. S10, S11). The intensity of the crystalline region increases fast up to 200 h. For longer weathering times, the lineshape does not change significantly anymore. For stabilized PP, a similar trend is observed, which is delayed by roughly 200 h, marking the induction period where the stabilizers are consumed. These trends are in line with the conclusions drawn from the DSC measurements. For longer weathering times, the spectral overlap is, however, too strong to allow for quantitative analysis of the spectral intensities, and thus for calculation of the degree of crystallinity.

The thermal and NMR characteristics for both PP experiments correlate well with the observation previously made for MW and MWD (Fig. 2). For semi-crystalline polymers, chain-scission takes place mainly in the amorphous regions. The disassembled polymer chains then rearrange due to the high mobility of the chains within the temperature range of our experiments, which is well above the glass-transition temperature of PP. The chains rearrange in a preferably ordered way, which leads to an increase in crystallinity [53]. These chain dynamics also influence the particle fragmentation and hinder crack-formation. In early weathering stages (0–350 h, Fig. 1A) the particle size thus remains constant, while molecular weight values already indicate a slow decrease in chain length from chain-scission (Fig. 2C). At late stages of degradation, the crystallinity for both PP samples slowly decreases again (Fig. 3C, 3E). We explain this saturation effect by an increasing amount of polar polymer defects [29] hindering the alignment of the residual short polymer chains. Our observations match previous studies, investigating the environmental degradation of PP, where an increase in crystallinity is reported [54, 55] along with a decrease in the MW [55].

Development of chemical functional groups

To trace the continuous degradation by quantifying chain-scissions and formation of chemical functional groups, ^{13}C CP MAS NMR spectra were recorded for both sets of weathering experiments (Fig. 4A, 4B). Compared to the reference material, additional peaks develop,

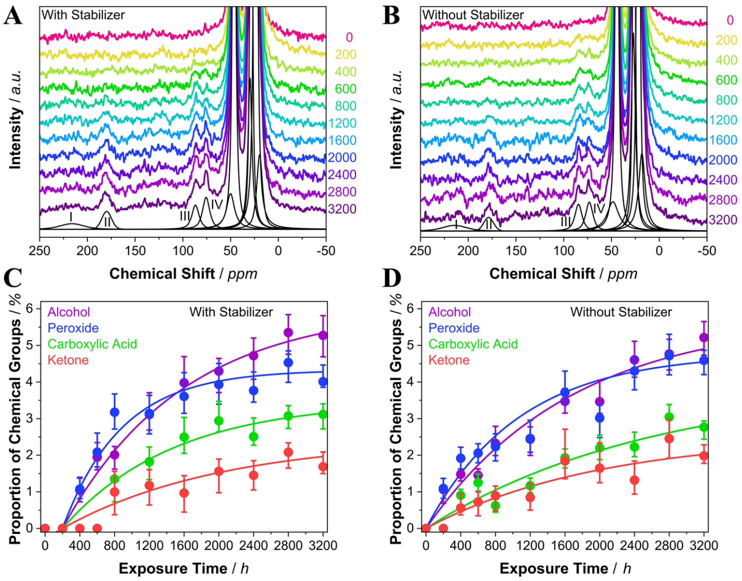

Fig. 4. ^{13}C CP MAS NMR spectra of **A** PP with stabilizer and **B** without stabilizer for different weathering times. Upon irradiation, the generation of new signals assigned as signals I (ketone), II (carboxylic acid), III (peroxide) and IV (alcohol) is observed [56, 57]. No refinement of vinylidenes was performed between 100–150 ppm, since the resonances of the decomposition products of Irgafos® 168 superimpose with the vinylidene resonances. The spectra are normalized to the intensity of the methyl sidechain carbon signal (at approx. 24 ppm). Individual spectra are shifted vertically for better comparability. Exemplarily, the individual fits for the peaks in the spectrum of the 3200 h weathered particles are shown as black lines; Derived proportions (SI Eq. 2 - Eq. 6) of alcohols, peroxides, carboxylic acids and ketones, as functions of the exposure time, for PP particles **C** with and **D** without stabilizer. Trend curves with exponential build-up and an induction period (PP with stabilizer) are included as guide for the eye

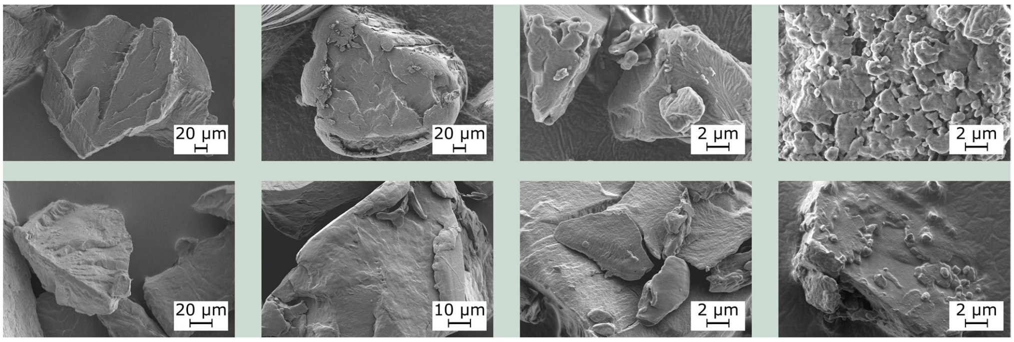

Fig. 5 **A**-**D** SEM images of PP with stabilizer and **E**-**H** without stabilizer. **A**&**E** Virgin particles, reference material, **B**&**F** smoothed particles after 200 h, **C**&**G** particle fragments after 800 h and **D**&**H** particle surfaces after 2000 h. Smaller particles in the nanometer-range are visible on the surfaces

gaining intensity with increasing exposure time. These peaks could be assigned to the degradation products of PP depicted in Figure S6, as ketones (215 ppm), carboxylic acids (179 ppm), peroxides (85 ppm) and alcohols (74 ppm) [56, 57]. Due to the low intensity in the spectral range typical for ketones, end-chain and in-chain ketones [56] are handled as one broad resonance (Fig. S12). Further details on the refinement procedure are given in the section "Experimental". Quantification was achieved by calibrating the CP spectra to a quantitative multi CP experiment, as previously described [43]. The proportions of the chemical groups are displayed in Fig. 4C and 4D. The defect resonances of the stabilized PP (Fig. 4C) remain below the detection limit during the first 200 h of exposure, which is in accordance with the presence of the induction phase. Between 200 and 800 h, a rapid increase for the proportions of all defects occurs. For longer exposure times, a turnover to an attenuated increase was observed. In the case of non-stabilized PP (Fig. 4D), photooxidation sets in with the start of the weathering experiments. Nevertheless, also for this sample a turnover to a smaller photooxidation rate was found with an onset of 400 h exposure time. In both cases, the highest proportions of the polar defects were observed for peroxide and alcohol groups, followed by carboxylic acids. Ketone defects play only a minor role and were observable only for larger weathering times. We attribute the high peroxide and alcohol proportions to the large number of tertiary C-atoms, forming stable radicals and subsequently peroxides and alcohols [27].

Particle surface and degradation characteristics

The changes in particle size and shape during the degradation of PP have been visualized by SEM. A selection of images from experiments with and without stabilizers are displayed in Fig. 5. More images are given in Figures S13 and S14. Aside from the difference in particle size between both fractions, surface characteristics for both particle fractions are very similar (Fig. 5, S13, and S14). The reference sample before irradiation consists of particles with rough shapes and harsh edges, resulting from cryo-grinding (Fig. 5A, 5E). Within the first stage of weathering, particle edges start to smoothen and are rounded off (Fig. 5B, 5F). With continuous exposure to simulated solar radiation and mechanical stress, particles start to disintegrate to average particle sizes < 10 µm for both experiments (Tab. S2). Dominant crack patterns are absent upon break-down, which can be attributed to the high flexibility of PP at ambient temperature, resulting in self-healing by surface rearrangement of the polymer chains [58]. This is in accordance with the interpretation of the thermal characteristics determined from DSC (Fig. 3C, 3E) and NMR spectroscopy (Fig. S11).

Recently, we developed a three-stage degradation model for semi-crystalline, non-stabilized polymers, using unstabilized LDPE as exemplary material [41]. Stage I represents surface abrasion, characterized by a roughly constant particle size, accompanied by a rounding of the particle surface. In stage II fragmentation starts, particle size decreases, the molecular weight is reduced and first chemical functional groups can be identified. The final stage III represents the formation of a large number of small microplastic and nanoplastic (NP) particles. They likely agglomerate, as a result of their high surface-to-volume ratios and an increasingly polar surface, resulting from the large number of oxygen-containing functional groups.

Our three-stage model is also applicable to PP without stabilizer. However, the transition from stage I to stage II is very short, which is evident in the particle size and

MW measurements (Fig. 1B, Fig. 2D). This behavior is related to the chemical structure of PP. Every second carbon in the PP backbone is a tertiary C-atom, making PP very susceptible to photooxidation. The single H-atoms of tertiary C-atoms are prone to abstraction, leading to the formation of a large number of stable radicals [27], which is also evident in the proportion of chemical groups developing (high proportion of peroxides and alcohols, Fig. 4C, 4D). Once degradation is initiated, it proceeds in an autocatalytic manner [59]. Consequently, solar radiation leads to a rapid polymer break-down in the absence of a stabilizer.

Fragmentation sets in together with a loss of MW (stage II), leading to embrittlement. This results in particle break-up and the formation of large quantities of secondary daughter MP particles and a rapid decrease in particle size (Fig. 1B). Due to surface-healing by rearrangement of the polymer chains above T_g [58], no microcracks could be observed. With further weathering, decreasing particle size and accumulation of degradation products, the particle properties change. Stage III is initiated with the average particle size having decreased 10 times. A multitude of daughter particles are formed from disintegration, reaching sizes < 10 µm, and even ranging down to the nanometer scale (Fig. 5D, 5H). They contain a high content of oxidation products and are highly polar. Due to their large surface-to-volume-ratio and polarity, MP and NP particles have a strong tendency to agglomerate (Fig. 5D, 5H) and almost no free NP particles with sizes < 1 m could be observed in our particle size measurements (Fig. S7).

In PP with stabilizer, particle size and MW are not affected up to 300 h of weathering. Surface abrasion however is clearly traceable in the SEM images, where rough edges disappear from being rounded off (Fig. 5B). The induction period observed here is relatively short. We expect a much longer stability if an efficient UV-stabilizer, e.g., a Hindered Amine Light Stabilizer (HALS), is added to the polymer, which is usually the case in polymers for outdoor use. Once the stabilizer combination is consumed, degradation sets in rapidly, leading to an exponential decrease in molecular weight and particle size, and a high fragmentation rate, accompanied by an increase in crystallinity and the formation of functional groups resulting from degradation. Comparing stage III for both experiments, the influence of the stabilizer becomes negligible. While it suppresses degradation for the first 300 h, polymer break-down is accelerated from 400–600 h.

The fragmentation rate of PP is extraordinarily high, and even faster for the stabilized, than for the non-stabilized fraction. This is a striking observation, indicating that the stabilizers and their degradation products accelerate fragmentation, even though they assure some stability in early stages of exposure. From one mother particle (~ 190 µm) 100,000 daughter particles are created and released within ~ 2 years (3200 h accelerated weathering). Within the last stage however, the daughter particles from both experiments have almost the same size (~ 5 µm), low MW ($M_n = 1000$ g/mol), a crystallinity (χ_c) of 50–60%, and a similar proportion of functional groups (Fig. 1-4).

The small size of MP enables an easy distribution throughout multiple environmental compartments, ingestion by aquatic organisms and accumulation through the food chain [60]. A recent study has demonstrated, that secondary PP MP particles, especially with sizes < 20 µm are cytotoxic to human cells [17]. In addition to their small size, sharp edges from fragmentation [61], the degree of weathering, and accumulation of oxygen-containing functional groups [62], as well as the leaching of additives [63] may further enhance the cytotoxicity to living organisms. This highlights not only the necessity to evaluate the effects of relevant, weathered samples in future studies, but also the urge for a further evaluation of the environmental behavior and the ecological risks MP and NP particles may bear.

Conclusion

We conclude, that the stabilizer combination present in our PP sample prevents degradation for a time frame of 300–350 h, while the non-stabilized PP starts to degrade immediately. The stability period of 350 h is very short and can be explained by the fact that the PP used in this study contains only a small amount of additives preventing thermal and photochemical oxidation.

The fragmentation rate of PP is particularly high. Comparing the time constants of particle disintegration, we estimate that PP degrades ~ 6 times faster than PS [5], and ~ 4 times faster than LDPE [41]. The average particle size of the reference (~ 190 µm) decreases down to 4 µm after 3200 h of irradiation with simulated solar radiation, which is comparable to ~ 2 years of outdoor weathering in Central Europe (Tab. S1). From one PP mother particle, 100,000 daughter particles are formed, and released into the environment. This value is extraordinarily high, and highlights the immense secondary PP MP-pollution from inadequate waste disposal.

The degradation of polymers under environmental conditions is a complex process, whereas laboratory experiments, like the ones presented here, can be run with reduced complexity. In our case, the simultaneous influence of solar radiation, and mechanical stress was investigated. From such experiments, a large number of samples can be collected after freely selectable time intervals, thus aged MP particles become available in sufficient amounts for detailed analysis. This allows investigations with a multitude of analytical methods, including e.g., solid-state NMR spectroscopy. Despite the reduced number of experimental parameters, we believe that the major conclusions from laboratory weathering can be transferred to environmental conditions. In this context, our experiment resembles the degradation of PP on the surface of a river or the sea, neglecting the influence of biofilms. The experimental setup, with a permanent exposure of the MP to simulated solar radiation, in combination with mechanical stress induced by stirring, provides optimum conditions for the degradation of MP. In natural environments, additional parameters control the time scales, in which degradation occurs. Exemplarily, biofilm formation may serve as a shield, and thus may lower light exposure. If biofilm formation leads to an increase of the particle density, it may even sink to the ground, where the absence of sunlight combined with a very small amount of oxygen leads to an increase of the MP-lifetime by several orders of magnitude.

It is essential to consider, that the chemical structure of the small daughter MP particles, obtained at the end of our artificial ageing experiment, is very different from the starting material. The highly weathered and fragmented secondary daughter MP particles consist of hydrocarbon chains with a molecular weight of 1000 g/mol, and a large number of oxygen-containing functional groups, e.g., carboxylic acids. Their physical properties and chemical composition have largely changed, no longer resembling pristine PP. We expect, that these particles could be much more prone to biodegradation compared to the hydrophobic, high molecular weight starting material. This question should be addressed in future studies.

Abbreviations

PP: Polypropylene; MP : Microplastic; PS: Polystyrene; PE: Polyethylene; HT-GPC: High temperature gel permeation chromatography; SEM: Scanning electron microscopy; DSC: Differential scanning calorimetry; MAS-NMR spectroscopy: Magic angle spinning nuclear magnetic resonance spectroscopy; FTIR spectroscopy: Fourier-transform infrared spectroscopy; Py-GC-MS: Pyrolysis gas chromatography mass spectrometry; MALDI-TOF MS: Matrix assisted laser desorption ionization-time of flight mass spectrometry; DHB: 2,5-Dihydroxybenzoic acid; THF: Tetrahydrofuran; PTFE: Polytetrafluorethylene; MW: Molecular weight; MWD: Molecular weight distribution; M_n: Number-averaged molecular weight; M_w: Weight-averaged molecular weight; Đ: Dispersity; TCB: 1,2,4-Trichlorobenzene; HDPE: High density polyethylene; FESEM: Field-emission scanning electron microscopy; $CDCl_3$: Deuterated chloroform; HALS: Hindered amine light stabilizer.

Supplementary Information

The online version contains supplementary material available at https://doi.org/10.1186/s43591-022-00042-2.

Additional file 1: Figure S1. Global horizontal irradiation for Europe and for Germany in kWh/m^2 for 2019. Source: SOLARGIS. **Figure S2**. Q-SUN daylight-Q filter compared to direct sunlight. Modified from Q-Lab Corporation, 2014, Technical Bulletin LX-5060, A Choice of Filters for Q-Sun Xenon Test Chambers. **Figure S3.** (A) MALDI spectrum of the first processing stabilizer in PP HP526 J. The three prominent peaks could be assigned to the oxidized species of Irgafos® 168 (Schwarzinger et al., 2012). (B) Chemical structure of Irgafos® 168 (Tris(2,4-di-tert-butylphenyl) phosphite) and (C)Tris(2,4-di-tert-butylphenyl)phosphate) together with m/z values from the literature. **Figure S4.** (A) MALDI-TOF MS spectrum of the second processing stabilizer in PP HP526 J. The prominent peaks are identical to those arising from Irganox® 1010 reference material, treated with simulated solar radiation in THF for 100 h in (B).The structure of Irganox® 1010 is given in (C). **Figure S5.** Comparison of ^{1}H (A), ^{13}C (B), and ^{31}P (C) NMR spectra of the first extracted additive, tris(2,4-di-tert-butylphenyl)-phosphate and Irgafos® 168 as well as ^{1}H (D), ^{13}C (E) spectra of the second extracted additive, Irganox® 1010 and Irganox® 1010 reference material, treated with simulated solar radiation in THF for 100 h. The ^{1}H and ^{13}C spectra were normalised to the proton and carbon resonances of tert-butyl groups and the ^{31}P spectra to the highest peak. **Figure S6.** Above: Scheme for the photooxidative degradation of PP explaining the formation of hydroperoxides, alcohols, ketones, olefins and carboxylic acids. Below: Reactions of the radical scavenger Irgafos® 168 with reactive hydroperoxides and peroxy- and alkoxy radicals. The reactive intermediates marked in red (above) are deactivated by the phosphite Irgafos® 168 which itself is oxidized to the phosphate [51]. **Figure S7.** Average particle size distributions for (A) PP with stabilizer and (B) PP particles without stabilizer. **Figure S8.** Molecular weight distributions in g/mol of (A) PP with stabilizer and (B) PP without stabilizer for exposure time intervals from 0 h to 3200 h. **Figure S9.** DSC measurements. Heat flow in W/g vs. temperature in °C for (A) PP particles with stabilizer and (B) PP particles without stabilizer. **Figure S10.** ^{13}C CP MAS NMR spectrum of the PP particles with stabilizer prior to weathering with signal assignment. In the enlarged PP spectra (blue and orange rectangle) the differences of the resonances of the amorphous (signal a1 and b1) and crystalline (signal a2 and b2) phase become visible [52]. **Figure S11.** ^{13}C CP MAS NMR spectra of the PP particles with (A) and without (B) stabilizer for 0, 400 and 3200 h weathering time. Upon irradiation, a shift of signal intensity fromthe amorphous phase resonances (30 ppm, 48 ppm) to the crystalline phase resonances (28 ppm, 46 ppm) is observed [52]. The spectra are normalised to the integral of the backbone signal (35-20 ppm and 55-35 ppm). **Figure S12.** ^{13}C CP MAS NMR spectra of the PP particles with stabilizer for 0, 2800 and 3200 h weathering time. The spectra are normalised to the intensity of the methyl side chain carbon signal (at approx. 24 ppm). Individual spectra are shifted vertically for better comparability. Additionally, the baselines (green), individual refinements for the peaks (black) and the cumulative lineshape (orange) are shown in the spectra. No refinement of vinylidenes was performed between 100 – 150 ppm since the resonances of the decomposition products of Irgafos® 168 superimpose with the vinylidene resonances. **Figure S13.** SEM images of PP with stabilizer after irradiation for different time intervals. **Figure S14.** SEM images of PP without stabilizer after irradiation for different time intervals. **Table S1.** Calculation of total irradiance in the Q-SUN Xe-3 chamber. **Table S2.** Average particle sizes in µm for PP samples with and without stabilizer at exposure times from 0 h to 3200 h.Values display the average of three measurements. **Table S3.** Number-average (M_n), weight-average (M_w), peak (M_p) molecular weights in g/mol, and dispersity (Đ) values for PP samples with and without stabilizer for different exposure times. **Table S4.** Crystallinity and melting temperature measurements for PP with stabilizer and PP without stabilizer. **Table S5.** Refinement parameters for the ^{13}C CP NMR spectra of weathered PP samples with and without stabilizer. Refinements were carried out with pseudo-Voigt lineshapes (Eq. 1) where δ_{iso} is the isotropic chemical shift, LB the line broadening, x the Gauss/Lorentz ratio and I the relative intensity. The latter is given in percent as fraction of the total spectral intensity. Refinement parameters marked in grey were obtained by simultaneous free refinements of defect peaks in the two spectra with longest weathering times and were kept constant in the subsequent refinements. **Table S6.** Correction factors for PP with and without stabilizer determined with quantitative multi-CP spectra of the respective 3200 h weathered sample. Used to calibrate the defect intensities in the CP spectra [5].

Acknowledgements
The authors would like to thank Lisa Weber, Martina Fried and Dr. Daniel Wagner for particle preparation, Dr. Winfried Kretschmer for HT GPC analysis, Martina Heider and Dr. Ulrich Mansfeld for SEM measurements, and Dr. Francesco Rodella, Irene Bauer, Sandra Opel and Jutta Failner for help and advice concerning Soxhlet extraction and stabilizer processing.

Authors' contributions

N.M. performed accelerated weathering of particles, particle size analysis, GPC, and DSC measurements. A.M. performed solid-state and liquid-state NMR spectroscopic measurements. N.M. and A.M. wrote the first draft of the manuscript, T.M., H.R., V.A., P.S., and J.S. supported the discussion and finalization of the manuscript. All authors read and approved the final version of the manuscript.

Funding
Open Access funding enabled and organized by Projekt DEAL. This project was funded by the Deutsche Forschungsgemeinschaft (DFG, German Research Foundation)—Project Number 391977956—SFB 1357, subproject C01.

Availability of data and materials

All data needed to evaluate the conclusions in the paper are present in the paper and/or in the Supplementary Material.

Declarations

Ethics approval and consent to participate

Not applicable.

Consent for publication

Not applicable.

Competing interests

The authors declare to have no competing financial or personal interests.

Author details
[1]Department of Macromolecular Chemistry I, University of Bayreuth, Universitätsstraße 30, 95447 Bayreuth, Germany. [2]Department of Inorganic Chemistry III and Northern Bavarian NMR Centre, University of Bayreuth, Universitätsstraße 30, 95447 Bayreuth, Germany. [3]Department of Polymer Engineering, University of Bayreuth, Universitätsstraße 30, 95447 Bayreuth, Germany.

Received: 1 July 2022 Accepted: 7 September 2022

References

1. PlasticsEurope. Plastics - The Facts 2020: An analysis of European plastics production, demand and waste data; 2020.
2. Bishop G, Styles D, Lens PNL. Recycling of European plastic is a pathway for plastic debris in the ocean. Environ Int. 2020;142: 105893.
3. Chen HL, Nath TK, Chong S, Foo V, Gibbins C, Lechner AM. The plastic waste problem in Malaysia: management, recycling and disposal of local and global plastic waste. SN Applied Sciences. 2021;3(4):1–15.
4. Andrady AL. Microplastics in the marine environment. Mar Pollut Bull. 2011;62(8):1596–605.
5. Meides N, Menzel T, Poetzschner B, Löder MGJ, Mansfeld U, Strohriegl P, et al. Reconstructing the Environmental Degradation of Polystyrene by Accelerated Weathering. Environ Sci Technol. 2021;55(12):7930–8.
6. Hartmann NB, Hüffer T, Thompson RC, Hassellöv M, Verschoor A, Daugaard AE, et al. Are we speaking the same language? Recommendations for a definition and categorization framework for plastic debris. Environ Sci Technol. 2019;53(3):1039–47.
7. Andrady AL. The plastic in microplastics: A review. Mar Pollut Bull. 2017;119(1):12–22.
8. Wu X, Liu P, Shi H, Wang H, Huang H, Shi Y, et al. Photo aging and fragmentation of polypropylene food packaging materials in artificial seawater. Water Research. 2021;188:116456.
9. Duan J, Bolan N, Li Y, Ding S, Atugoda T, Vithanage M, et al. Weathering of microplastics and interaction with other coexisting constituents in terrestrial and aquatic environments. Water Research. 2021;196:117011.
10. Kumar M, Xiong X, He M, Tsang DCW, Gupta J, Khan E, et al. Microplastics as pollutants in agricultural soils. Environ Pollut. 2020;265(Pt A): 114980.
11. Gewert B, Plassmann MM, MacLeod M. Pathways for degradation of plastic polymers floating in the marine environment. Environ Sci Process Impacts. 2015;17(9):1513–21.
12. Zweifel H. Principles of oxidative degradation. In: Stabilization of Polymeric Materials. Springer; 1998. p. 1–40.
13. Kirstein IV, Kirmizi S, Wichels A, Garin-Fernandez A, Erler R, Löder M et al. Dangerous hitchhikers? Evidence for potentially pathogenic Vibrio spp. on microplastic particles. Marine Environmental Research 2016; 120:1–8. Available from: URL: https://www.sciencedirect.com/science/article/pii/S014111361630112X.
14. Zettler ER, Mincer TJ, Amaral-Zettler LA. Life in the "Plastisphere": Microbial Communities on Plastic Marine Debris. Environ Sci Technol. 2013;47(13):7137–46.
15. Imhof HK, Ivleva NP, Schmid J, Niessner R, Laforsch C. Contamination of beach sediments of a subalpine lake with microplastic particles. Curr Biol. 2013;23(19):R867–8.
16. Imhof HK, Rusek J, Thiel M, Wolinska J, Laforsch C. Do microplastic particles affect Daphnia magna at the morphological, life history and molecular level? PLoS ONE. 2017;12(11): e0187590.
17. Hwang J, Choi D, Han S, Choi J, Hong J. An assessment of the toxicity of polypropylene microplastics in human derived cells. Sci Total Environ. 2019;684:657–69.
18. Engler RE. The Complex Interaction between Marine Debris and Toxic Chemicals in the Ocean. Environ Sci Technol. 2012;46(22):12302–15.
19. Avio CG, Gorbi S, Regoli F. Plastics and microplastics in the oceans: From emerging pollutants to emerged threat. Mar Environ Res. 2017;128:2–11.
20. Barrick A, Champeau O, Chatel A, Manier N, Northcott G, Tremblay LA. Plastic additives: challenges in ecotox hazard assessment. PeerJ. 2021;9: e11300.
21. OECD. Considerations and criteria for sustainable plastics from a chemicals perspective (Background Paper 1).: OECD Global Forum on Environment: Plastics in a Circular Economy Designing Sustainable Plastics from a Chemicals Perspective. [OECD Environment, Health and Safety Publications, Series on Risk Managemenet]. No. 53; 2018. Available from: URL: https://www.oecd.org/chemicalsafety/risk-management/considerations-and-criteria-for-sustainable-plastics-from-a-chemicals-perspective.pdf.
22. Blázquez-Blázquez E, Cerrada ML, Benavente R, Pérez E. Identification of Additives in Polypropylene and Their Degradation under Solar Exposure Studied by Gas Chromatography-Mass Spectrometry. ACS Omega. 2020;5(16):9055–63.
23. Biale G, La Nasa J, Mattonai M, Corti A, Vinciguerra V, Castelvetro V, et al. A systematic study on the degradation products generated from artificially aged microplastics. Polymers. 2021;13(12):1997.
24. Garvey CJ, Impéror-Clerc M, Rouzière S, Gouadec G, Boyron O, Rowenczyk L, et al. Molecular-Scale Understanding of the Embrittlement in Polyethylene Ocean Debris. Environ Sci Technol. 2020;54(18):11173–81.
25. Shi Y, Qin J, Tao Y, Jie G, Wang J. Natural weathering severity of typical coastal environment on polystyrene: Experiment and modeling. Polym Testing. 2019;76:138–45.
26. Gewert B, Plassmann M, Sandblom O, MacLeod M. Identification of chain scission products released to water by plastic exposed to ultraviolet light. Environ Sci Technol Lett. 2018;5(5):272–6.

27. Grause G, Chien M-F, Inoue C. Changes during the weathering of polyolefins. Polymer degradation and stability 2020:109364.
28. Da Costa JP, Nunes AR, Santos PSM, Girao AV, Duarte AC, Rocha-Santos T. Degradation of polyethylene microplastics in seawater: Insights into the environmental degradation of polymers. Journal of Environmental Science and Health, Part A. 2018;53(9):866–75.
29. Ojeda T, Freitas A, Birck K, Dalmolin E, Jacques R, Bento F, et al. Degradability of linear polyolefins under natural weathering. Polym Degrad Stab. 2011;96(4):703–7.
30. Khelassi A, Belhaneche-Bensemra N. Investigation of pro-oxidant agents' effects on the ageing of polypropylene bags. Int J Environ Stud. 2020;77(2):264–74.
31. Brandon J, Goldstein M, Ohman MD. Long-term aging and degradation of microplastic particles: Comparing in situ oceanic and experimental weathering patterns. Mar Pollut Bull. 2016;110(1):299–308.
32. Andrady AL, Koongolla B. Degradation and Fragmentation of Microplastics. In: Plastics and the Ocean. John Wiley & Sons, Ltd; 2022. p. 227–68.
33. Efimova I, Bagaeva M, Bagaev A, Kileso A, Chubarenko IP. Secondary Microplastics Generation in the Sea Swash Zone With Coarse Bottom Sediments: Laboratory Experiments. Front Mar Sci. 2018;5:313.
34. Al-Malaika S. Oxidative degradation and stabilisation of polymers. Int Mater Rev. 2003;48(3):165–85.
35. Carlsson DJ, Wiles DM. The Photooxidative Degradation of Polypropylene. Part I. Photooxidation and Photoinitiation Processes. Journal of Macromolecular Science, Part C: Polymer Reviews 1976; 14(1):65–106.
36. Allen NS, Chirinos-Padron A, Henman TJ. Photoinitiated oxidation of polypropylene: a review. Prog Org Coat. 1985;13(2):97–122.
37. Kalogerakis N, Karkanorachaki K, Kalogerakis GC, Triantafyllidi EI, Gotsis AD, Partsinevelos P et al. Microplastics Generation: Onset of Fragmentation of Polyethylene Films in Marine Environment Mesocosms. Frontiers in Marine Science 2017; 4. Available from: URL: https://www.frontiersin.org/article/https://doi.org/10.3389/fmars.2017.00084.
38. Julienne F, Delorme N, Lagarde F. From macroplastics to microplastics: Role of water in the fragmentation of polyethylene. Chemosphere. 2019;236: 124409.
39. Mattsson K, Björkroth F, Karlsson T, Hassellöv M. Nanofragmentation of Expanded Polystyrene Under Simulated Environmental Weathering (Thermooxidative Degradation and Hydrodynamic Turbulence). Front Mar Sci. 2021;7:1252.
40. Born MP, Brüll C. From model to nature - A review on the transferability of marine (micro-) plastic fragmentation studies. Sci Total Environ. 2022;811: 151389.
41. Menzel T, Meides N, Mauel A, Mansfeld U, Kretschmer W, Kuhn M, et al. Degradation of low-density polyethylene to nanoplastic particles by accelerated weathering. Sci Total Environ. 2022;826:154035.
42. Johnson RL, Schmidt-Rohr K. Quantitative solid-state 13C NMR with signal enhancement by multiple cross polarization. J Magn Reson. 2014;239:44–9.
43. Mauel A, Pötzschner B, Meides N, Siegel R, Strohriegl P, Senker J. Quantification of photooxidative defects in weathered microplastics using 13 C multiCP NMR spectroscopy. RSC Adv. 2022;12(18):10875–85.
44. Canopoli L, Coulon F, Wagland ST. Degradation of excavated polyethylene and polypropylene waste from landfill. Sci Total Environ. 2020;698: 134125.
45. Dong M, Zhang Q, Xing X, Chen W, She Z, Luo Z. Raman spectra and surface changes of microplastics weathered under natural environments. Sci Total Environ. 2020;739: 139990.
46. Fernández-González V, Andrade-Garda JM, López-Mahía P, Muniategui-Lorenzo S. Impact of weathering on the chemical identification of microplastics from usual packaging polymers in the marine environment. Anal Chim Acta. 2021;1142:179–88.
47. Veeman WS. Carbon-13 chemical shift anisotropy. Prog Nucl Magn Reson Spectrosc. 1984;16:193–235.
48. Schwarzinger C, Gabriel S, Beißmann S, Buchberger W. Quantitative Analysis of Polymer Additives with MALDI-TOF MS Using an Internal Standard Approach. J Am Soc Mass Spectrom. 2012;23(6):1120–5.
49. Fouyer K, Lavastre O, Rondeau D. Direct monitoring of the role played by a stabilizer in a solid sample of polymer using direct analysis in real time mass spectrometry: the case of Irgafos 168 in polyethylene. Anal Chem. 2012;84(20):8642–9.
50. BASF. Safety Data Sheet Irgafos 168 FF; 2017 [cited 2017 Aug 2]. Available from: URL: https://basf.available-equipment.com/ProductDocument.aspx?ID=195&type=11.
51. Maier R-D, Schiller M. Handbuch Kunststoff Additive. Carl Hanser Verlag GmbH Co KG; 2016.
52. Hronský V, Koval'aková M, Vrábel P, Uhrínová M, Olčák D. Estimation of the Degree of Crystallinity of Partially Crystalline Polypropylenes Using 13 C NMR. Acta Physica Polonica, A 2014; 125(6).
53. Ehrenstein G. Polymer-Werkstoffe: Struktur-Eigenschaften-Anwendung; 1999.
54. Li J, Yang R, Yu J, Liu Y. Natural photo-aging degradation of polypropylene nanocomposites. Polym Degrad Stab. 2008;93(1):84–9.
55. Craig IH, White JR, Kin PC. Crystallization and chemi-crystallization of recycled photo-degraded polypropylene. Polymer. 2005;46(2):505–12.
56. Mowery DM, Assink RA, Derzon DK, Klamo SB, Clough RL, Bernstein R. Solid-state 13C NMR investigation of the oxidative degradation of selectively labeled polypropylene by thermal aging and γ-irradiation. Macromolecules. 2005;38(12):5035–46.
57. Mowery DM, Clough RL, Assink RA. Identification of oxidation products in selectively labeled polypropylene with solid-state 13C NMR techniques. Macromolecules. 2007;40(10):3615–23.
58. Wool RP. Self-healing materials: a review. Soft Matter. 2008;4(3):400–18.
59. Rajakumar K, Sarasvathy V, Thamarai Chelvan A, Chitra R, Vijayakumar CT. Natural Weathering Studies of Polypropylene. J Polym Environ. 2009;17(3):191.
60. Xu C, Zhang B, Gu C, Shen C, Yin S, Aamir M et al. Are we underestimating the sources of microplastic pollution in terrestrial environment? Journal of Hazardous Materials 2020:123228.
61. Völkl M, Jérôme V, Weig A, Jasinski J, Meides N, Strohriegl P, et al. Pristine and artificially-aged polystyrene microplastic particles differ in regard to cellular response. J Hazard Mater. 2022;435: 128955.
62. Yu X, Lang M, Huang D, Yang C, Ouyang Z, Guo X. Photo-transformation of microplastics and its toxicity to Caco-2 cells. Sci Total Environ. 2022;806:150954.
63. Bridson JH, Gaugler EC, Smith DA, Northcott GL, Gaw S. Leaching and extraction of additives from plastic pollution to inform environmental risk: A multidisciplinary review of analytical approaches. Journal of Hazardous Materials 2021; 414:125571. Available from: https://www.sciencedirect.com/science/article/pii/S0304389421005343.

This article was published in the Journal Microplastics & Nanoplastics 2022, 2:23.

Supplementary material: `https://doi.org/10.1186/s43591-022-00042-2`

8.3.1 Supplementary Material: Quantifying the fragmentation of polypropylene upon exposure to accelerated weathering.

Quantifying the fragmentation of polypropylene upon exposure to accelerated weathering

Nora Meides,[1,†] Anika Mauel,[2,†] Teresa Menzel,[3] Volker Altstaedt,[3] Holger Ruckdäschel,[3] Jürgen Senker,[2] Peter Strohriegl[1,*]

[1] Department of Macromolecular Chemistry I, University of Bayreuth, Universitätsstraße 30, 95447 Bayreuth, Germany

[2] Department of Inorganic Chemistry III and Northern Bavarian NMR Centre, University of Bayreuth, Universitätsstraße 30, 95447 Bayreuth, Germany

[3] Department of Polymer Engineering, University of Bayreuth, Universitätsstraße 30, 95447 Bayreuth, Germany

†These authors contributed equally to this work and share first authorship

*Corresponding author: peter.strohriegl@uni-bayreuth.de

List of Figures

Figure S1. *Global horizontal irradiation for Europe and for Germany in kWh/m2 for 2019. Source: SOLARGIS.*

Figure S2. *Q-SUN daylight-Q filter compared to direct sunlight. Modified from Q-Lab Corporation, 2014, Technical Bulletin LX-5060, A Choice of Filters for Q-Sun Xenon Test Chambers.*

Figure S3. (A) *MALDI spectrum of the first processing stabilizer in PP HP526 J. The three prominent peaks could be assigned to the oxidized species of Irgafos® 168 (Schwarzinger et al., 2012).* ***(B)*** *Chemical structure of Irgafos® 168 (Tris(2,4-di-tert-butylphenyl)phosphite)* ***and (****C) Tris(2,4-di-tert-butylphenyl)phosphate) together with m/z values from the literature.*

Figure S4. (A) *MALDI-TOF-MS spectrum of the second processing stabilizer in PP HP526 J. The prominent peaks are identical to those arising from Irganox® 1010 reference material, treated with simulated solar radiation in THF for 100 h in* ***(B)****. The structure of Irganox® 1010 is given in* ***(C)****.*

Figure S5. *Comparison of* ^{1H} ***(A)****,* ^{13C} ***(B)****, and* ^{31P} ***(C)*** *NMR spectra of the first extracted additive, tris(2,4-di-tert-butylphenyl)-phosphate and Irgafos® 168 as well as* ^{1H} ***(D)****,* ^{13C} ***(E)*** *spectra of the second extracted additive, Irganox® 1010 and Irganox® 1010 reference material, treated with simulated solar radiation in THF for 100 h. The* ^{1H} *and* ^{13C} *spectra were normalised to the proton and carbon resonances of tert-butyl groups and the* ^{31P} *spectra to the highest peak.*

Figure S6. *Above: Scheme for the photooxidative degradation of PP explaining the formation of hydroperoxides, alcohols, ketones, olefins and carboxylic acids. Below: Reactions of the radical scavenger Irgafos® 168 with reactive hydroperoxides and peroxy- and alkoxy radicals. The reactive intermediates marked in red (above) are deactivated by the phosphite Irgafos® 168 which itself is oxidized to the phosphate (Maier and Schiller, 2016).*

Figure S7. *Average particle size distributions for* ***(A)*** *PP with stabilizer and* ***(B)*** *PP particles without stabilizer.*

Figure S8. *Molecular weight distributions in g/mol of* ***(A)*** *PP with stabilizer and* ***(B)*** *PP without stabilizer for exposure time intervals from 0 h to 3200 h.*

Figure S9. *DSC measurements. Heat flow in W/g vs. temperature in °C for* ***(A)*** *PP particles with stabilizer and* ***(B)*** *PP particles without stabilizer.*

Figure S10. ^{13C} *CP MAS NMR spectrum of the PP particles with stabilizer prior to weathering with signal assignment. In the enlarged PP spectra (blue and orange rectangle) the differences of the resonances of the amorphous (signal a1 and b1) and crystalline (signal a2 and b2) phase become visible (Hronský et al., 2014).*

Figure S11. ^{13C} *CP MAS NMR spectra of the PP particles with* ***(A)*** *and without* ***(B)*** *stabilizer for 0, 400 and 3200 h weathering time. Upon irradiation, a shift of signal intensity from the amorphous phase resonances (30 ppm, 48 ppm) to the crystalline phase resonances (28 ppm, 46 ppm) is observed (Hronský et al., 2014). The spectra are normalised to the integral of the backbone signal (35-20 ppm and 55-35 ppm).*

Figure S12. ^{13C} *CP MAS NMR spectra of the PP particles with stabilizer for 0, 2800 and 3200 h weathering time. The spectra are normalised to the intensity of the methyl sidechain carbon signal (at approx. 24 ppm). Individual spectra are shifted vertically for better comparability. Additionally, the baselines (green), individual refinements for the peaks (black) and the cumulative lineshape (orange) are shown in the spectra. No refinement of vinylidenes was performed between 100 – 150 ppm since the resonances of the decomposition products of Irgafos® 168 superimpose with the vinylidene resonances.*

$$f(\delta) = I \cdot \left[(1-x)\frac{2\,LB}{4\pi\cdot(\delta-\delta_{iso})^2+\pi\cdot LB^2} + x \cdot \frac{\sqrt{4\ln(2)}}{\sqrt{\pi}\,LB} \cdot e^{-\frac{4\ln(2)}{LB^2}(\delta-\delta_{iso})^2}\right] \qquad \text{(Eq. 1)}$$

Figure S13. *SEM images of PP with stabilizer after irradiation for different time intervals.*

Figure S14. *SEM images of PP without stabilizer after irradiation for different time intervals.*

List of Tables

Table S1. *Calculation of total irradiance in the Q-SUN Xe-3 chamber.*

Table S2. *Average particle sizes in µm for PP samples with and without stabilizer at exposure times from 0 h to 3200 h. Values display the average of three measurements.*

Table S3. *Number-average (Mn), weight-average (Mw), peak (Mp) molecular weights in g/mol, and dispersity (Đ) values for PP samples with and without stabilizer for different exposure times.*

Table S4. *Crystallinity and melting temperature measurements for PP with stabilizer and PP without stabilizer.*

Table S5. *Refinement parameters for the* ^{13C} *CP NMR spectra of weathered PP samples with and without stabilizer. Refinements were carried out with pseudo-Voigt lineshapes (Eq. 1) where δiso is the isotropic chemical shift, LB the line broadening, x the Gauss/Lorentz ratio and I the relative intensity. The latter is given in percent as fraction of the total spectral intensity. Refinement parameters marked in grey were obtained by simultaneous free refinements of defect peaks in the two spectra with longest weathering times and were kept constant in the subsequent refinements.*

Table S6. *Correction factors for PP with and without stabilizer determined with quantitative multi-CP spectra of the respective 3200 h weathered sample. Used to calibrate the defect intensities in the CP spectra (Meides et al., 2021).*

Experimental Section

Materials and Methods

Accelerated Weathering

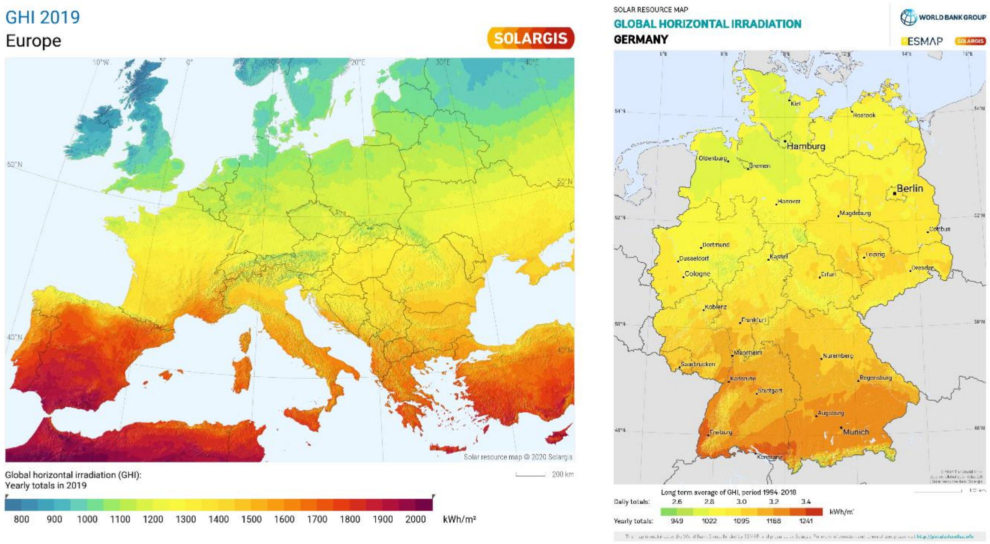

Figure S1. *Global horizontal irradiation for Europe and for Germany in kWh/m^2 for 2019. Source: SOLARGIS.*

Table S1. *Calculation of total irradiance in the Q-SUN Xe-3 chamber.*

Calculation of total irradiance in Q-SUN Xe-3 chamber		
Lamp settings*[1]	60	W/m^2
Calculation factor*[2]	9.9	
Total irradiance in Q-SUN Xe-3 chamber	594	W/m^2
Acceleration factor of Q-SUN Xe-3 chamber compared to Central Europe		
Solar irradiance per year*[3]	1000	kWh/m^2
Hours per year	8765	h
Solar irradiance	114	W/m^2
Acceleration factor of Q-SUN Xe-3 chamber*[4]	5.21	-

*[1] *measured in the wavelength interval from 300 to 400 nm*

*[2] *calculation factor converting the irradiance from 300 to 400 nm to the whole emission range of the Xenon lamp (300 – 800 nm). Extracted from Q-Sun Irradiance Conversion Sheet provided by Q-Lab Germany*

*[3] *value was derived from Figure S1 for the longitude of Central Europe*

*[4] *this value was calculated by division of the total irradiance in the Q-Sun Xe-3 chamber (594 W/m^2) by the solar irradiance determined for Central Europe (114 W/m^2)*

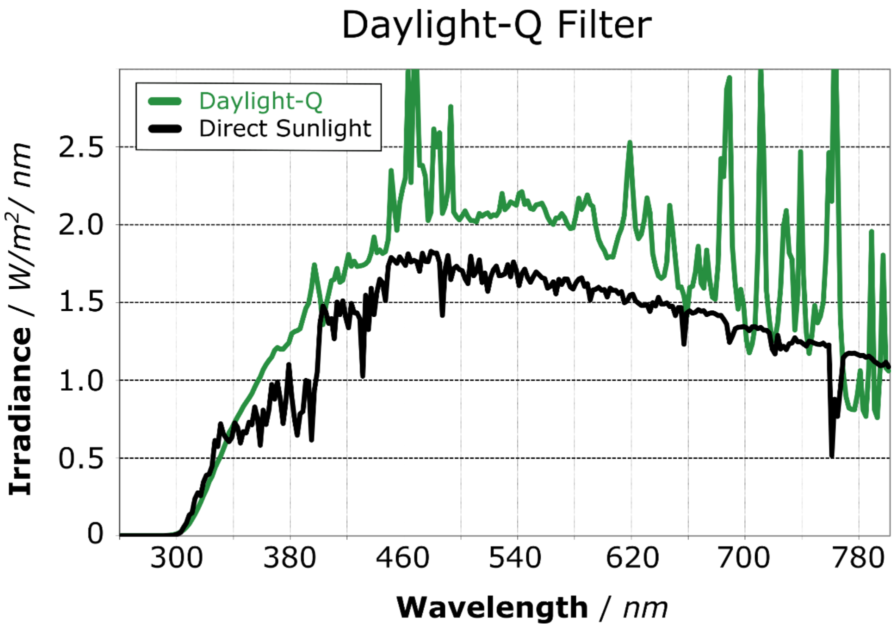

Figure S*2. Q-SUN daylight-Q filter compared to direct sunlight. Modified from Q-Lab Corporation, 2014, Technical Bulletin LX-5060, A Choice of Filters for Q-Sun Xenon Test Chambers.*

Results

Identification of the Processing Stabilizer via MALDI-TOF Mass Spectrometry

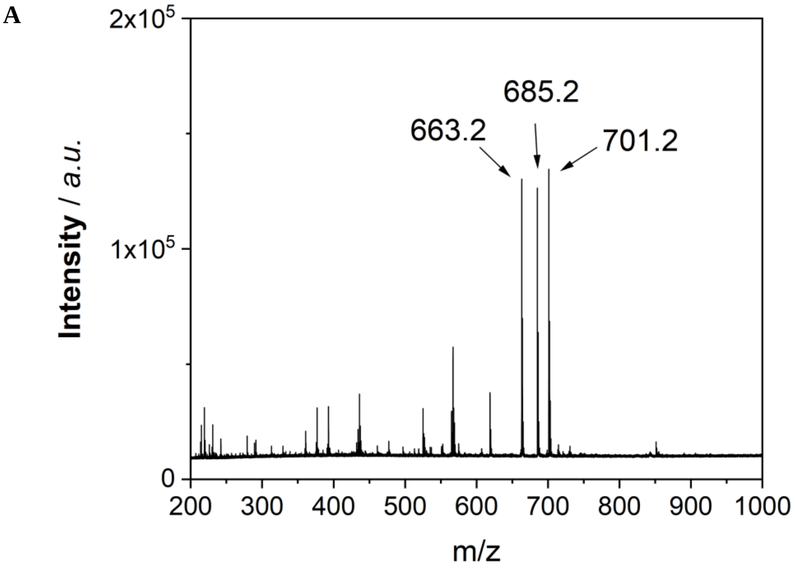

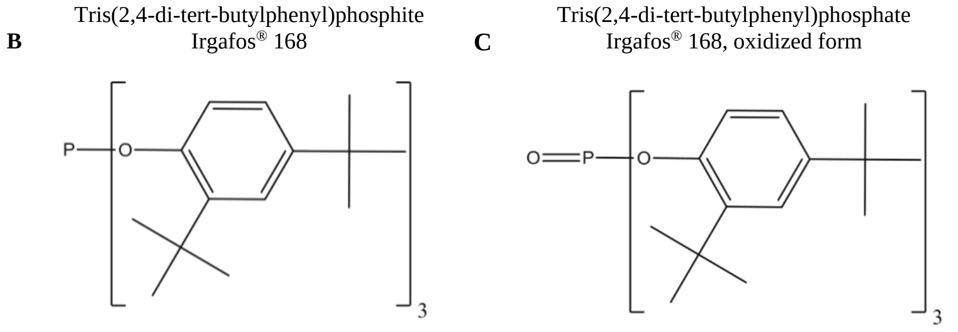

$C_{42}H_{64}O_3P$

$C_{42}H_{64}O_4P$

m/z = 647.5 [M+H]$^+$ (Fouyer et al., 2012; Schwarzinger et al., 2012)

m/z = 663.5 [M+H]$^+$ (Fouyer et al., 2012; Schwarzinger et al., 2012)

m/z = 685.4 [M+Na]$^+$ (Schwarzinger et al., 2012)

m/z = 701.4 [M+K]$^+$ (Schwarzinger et al., 2012)

***Figure S3. (A)** MALDI spectrum of the first processing stabilizer in PP HP526 J. The three prominent peaks could be assigned to the oxidized species of Irgafos® 168 (Schwarzinger et al., 2012). **(B)** Chemical structure of Irgafos® 168 (Tris(2,4-di-tert-butylphenyl)phosphite) and **(C)** Tris(2,4-di-tert-butylphenyl)phosphate) together with m/z values from the literature.*

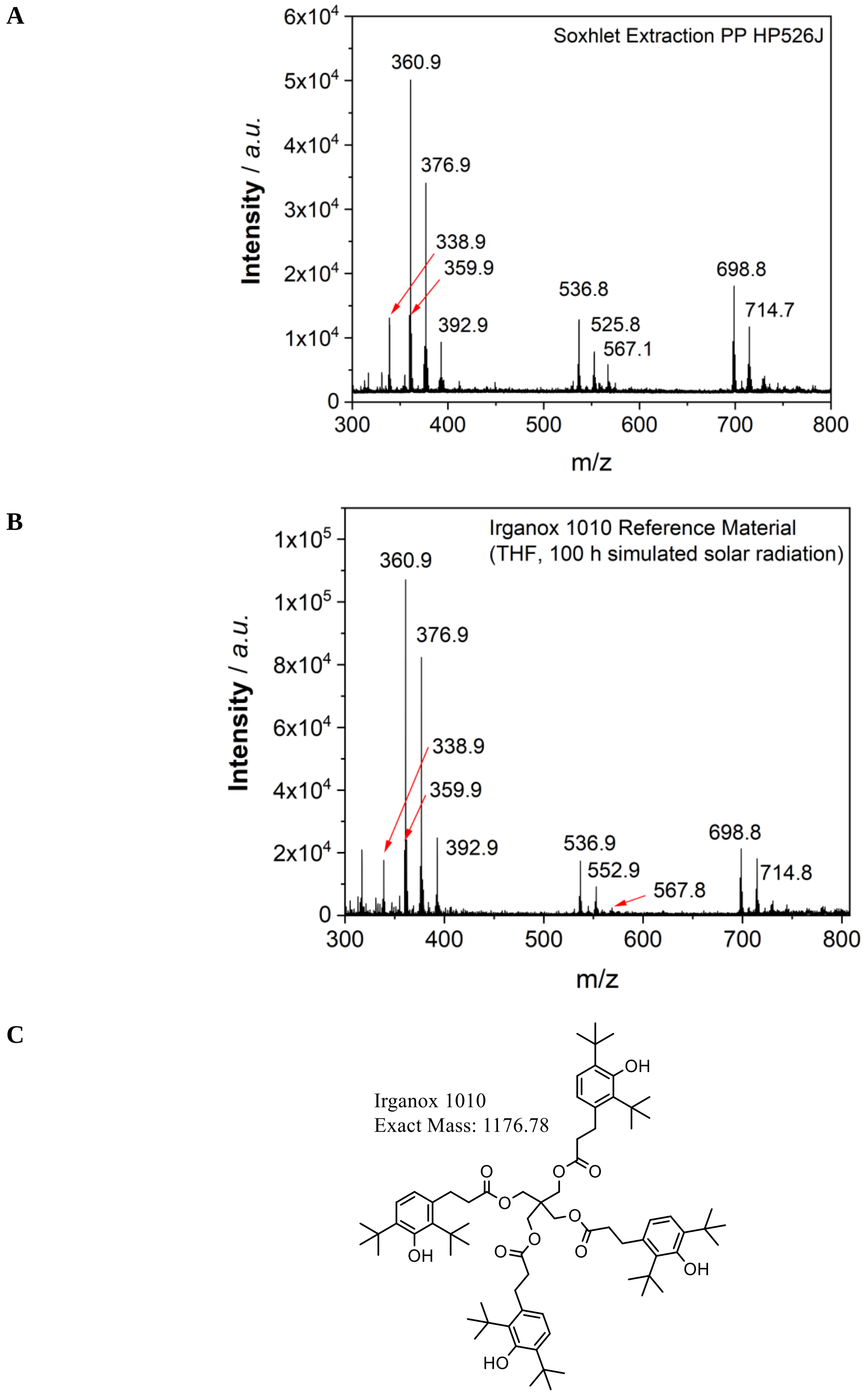

Figure S4. ***(A)*** *MALDI-TOF-MS spectrum of the second processing stabilizer in PP HP526 J. The prominent peaks are identical to those arising from Irganox® 1010 reference material, treated with simulated solar radiation in THF for 100 h in* ***(B)****. The structure of Irganox® 1010 is given in* ***(C)****.*

Identification of the processing stabilizers via ^{1}H, ^{13}C and ^{31}P liquid-state NMR spectroscopy

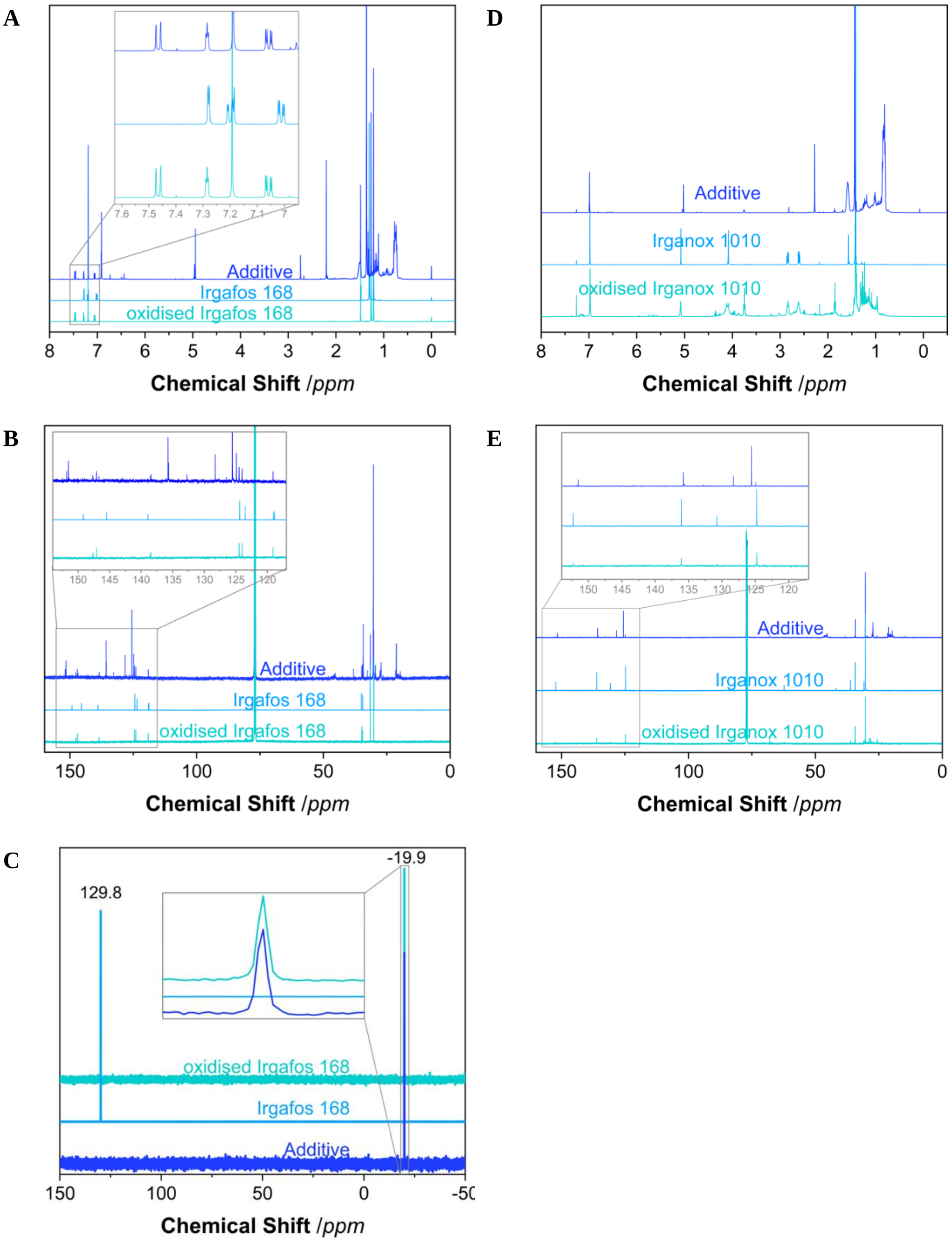

Figure S5. *Comparison of ^{1}H **(A)**, ^{13}C **(B)**, and ^{31}P **(C)** NMR spectra of the first extracted additive, tris(2,4-di-tert-butylphenyl)-phosphate and Irgafos® 168 as well as ^{1}H **(D)**, ^{13}C **(E)** spectra of the second extracted additive, Irganox® 1010 and Irganox® 1010 reference material, treated with simulated solar radiation in THF for 100 h. The ^{1}H and ^{13}C spectra were normalised to the proton and carbon resonances of tert-butyl groups and the ^{31}P spectra to the highest peak.*

Degradation Mechanisms

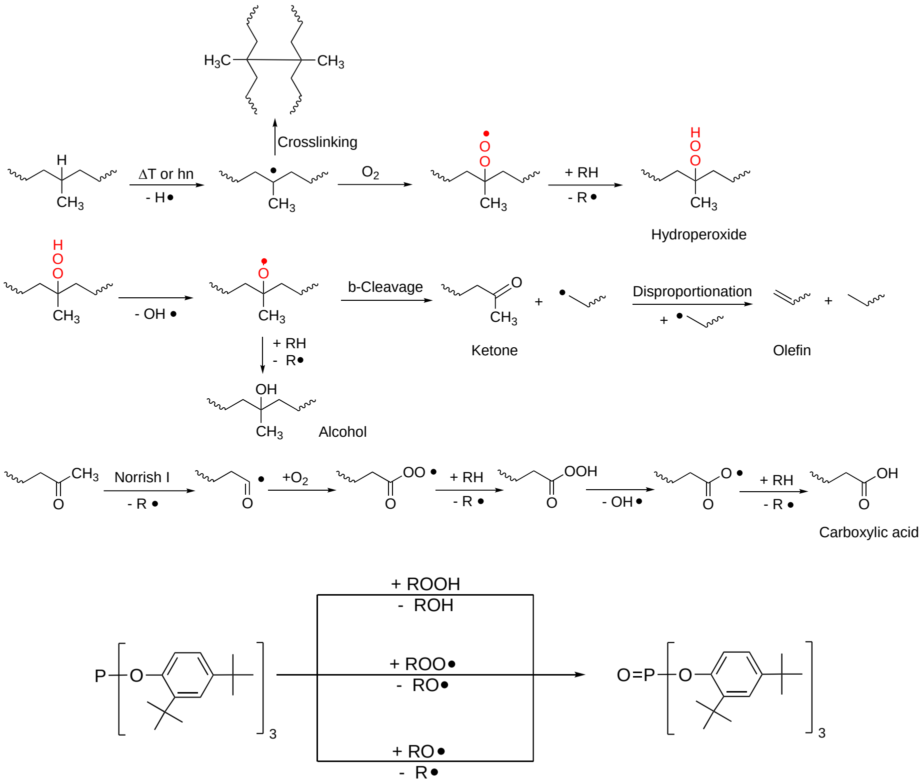

Figure S6. Above: Scheme for the photooxidative degradation of PP explaining the formation of hydroperoxides, alcohols, ketones, olefins and carboxylic acids. Below: Reactions of the radical scavenger Irgafos® 168 with reactive hydroperoxides and peroxy- and alkoxy radicals. The reactive intermediates marked in red (above) are deactivated by the phosphite Irgafos® 168 which itself is oxidized to the phosphate (Maier and Schiller, 2016).

Average Particle Size and Particle Size Distributions

Table S2. *Average particle sizes in µm for PP samples with and without stabilizer at exposure times from 0 h to 3200 h. Values display the average of three measurements.*

	With Stabilizer						**Without Stabilizer**
Exposure Time	**Average Particle Size**	**σ***	*Particle Volume*	*DMP Quantity*	*Surface Area*	*Total Surface Area (Quantity*Surface)*	**Average Particle Size**
hours	*µm*	*µm*	*μm^3*	*counts*	*μm^2*	*μm^2*	*µm*
0	192.4	3.2	3705973		115812		119.4
24	197.0	1.9					119.7
50	189.9	3.1					121.6
100	197.5	3.6					108.8
150	199.7						-
200	200.1	3.1					85.4
250	197.4						-
300	193.4						-
350	187.0						-
400	148.1	0.8					53.6
450	98.5						-
500	68.2						-
550	51.8						-
600	41.3	0.9					31.4
800	16.5	0.04					22.2
1200	9.4	0.04					13.4
1600	5.6	0.01					8.6
2000	4.2	0.02					6.6
2400	4.1	0.04					5.8
2800	4.2	0.14					4.9
3200	4.1	0.21	36	102696	53	10^9	5.1

*****σ is defined as the standard deviation of three independent measurements, from which the average particle size was calculated

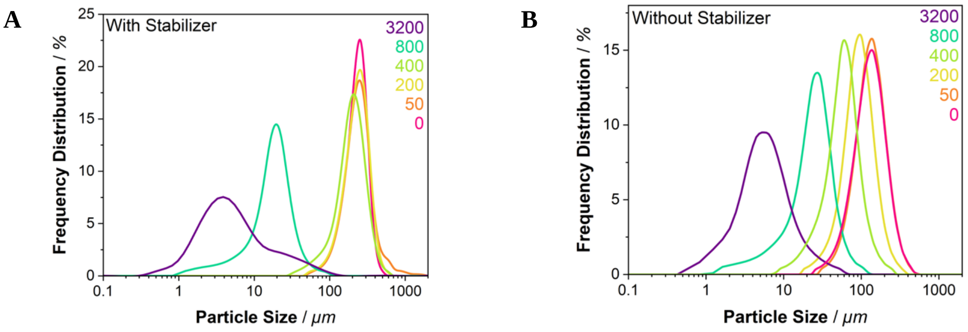

Figure S7. *Average particle size distributions for **(A)** PP with stabilizer and **(B)** PP particles without stabilizer.*

Molecular Weight Data

Table S3. *Number-average (M_n), weight-average (M_w), peak (M_p) molecular weights in g/mol, and dispersity (Đ) values for PP samples with and without stabilizer for different exposure times.*

	PP with stabilizer				**PP without stabilizer**			
Exposure Time	**M_n**	**M_w**	**M_p**	**Đ**	**M_n**	**M_w**	**M_p**	**Đ**
hours	*g/mol*	*g/mol*	*g/mol*		*g/mol*	*g/mol*	*g/mol*	
0	68300	795800	342000	11.7	68800	532000	256700	7.7
24	-	-	-	-	53500	293700	174000	5.5
50	75000	739700	328200	9.9	13000	47700	41300	3.7
100	63400	698600	296200	11.0	5400	17200	13700	3.2
150	44900	731200	328200	16.3	-	-	-	-
200	35100	669100	296200	19.1	3300	8800	7500	2.7
250	64600	661800	296200	10.2	-	-	-	-
300	30000	162700	93900	5.4	-	-	-	-
350	10400	40300	31500	3.9	-	-	-	-
400	5000	16100	10900	3.2	2100	4500	4000	2.1
450	3500	9300	7600	2.7	-	-	-	-
500	3000	6500	4100	2.2	-	-	-	-
550	2500	5000	3800	2.0	-	-	-	-
600	2400	4400	3700	1.9	1800	3400	2000	1.9
800	1900	3500	2200	1.8	1500	2700	1900	1.8
1200	1600	2600	1900	1.7	1200	2000	1600	1.7
1600	1300	2200	1700	1.6	1100	1700	1500	1.6
2000	1300	1900	1600	1.5	1000	1500	1300	1.6
2400	1100	1700	1500	1.6	800	1400	1200	1.7
2800	900	1600	1300	1.7	800	1200	1200	1.7
3200	1000	1500	1300	1.6	700	1200	1000	1.7

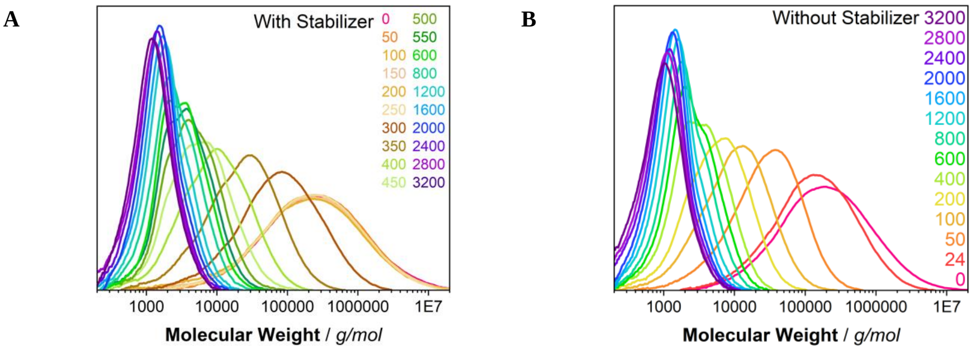

Figure S8. *Molecular weight distributions in g/mol of* ***(A)*** *PP with stabilizer and* ***(B)*** *PP without stabilizer for exposure time intervals from 0 h to 3200 h.*

Crystallinity and Melting Temperature

__Table S4.__ Crystallinity and melting temperature measurements for PP with stabilizer and PP without stabilizer.

	PP with stabilizer		**PP without Stabilizer**	
Exposure Time	**Crystallinity χ_c**	**Melting Temp. T_m**	**Crystallinity χ_c**	**Melting Temp. T_m**
hours	*%*	*°C*	*%*	*°C*
0	52.1	164.8	45.1	164.7
24	49.7	164.6	52.5	164.8
50	49.6	164.4	54.0	163.6
100	48.0	164.7	52.7	157.7
200	51.0	164.6	61.6	152.6
350	48.7	162.4	-	-
400	64.6	156.1	61.3	150.0
600	65.7	148.5	58.4	147.2
800	67.7	145.8	63.4	145.0
1200	63.0	142.2	61.0	143.0
1600	62.2	137.8	58.8	141.0
2000	59.50	135.8	57.1	136.1
2400	57.9	130.9	59.8	133.4
2800	48.0	122.9	57.8	131.2
3200	51.3	119.5	63.0	125.3

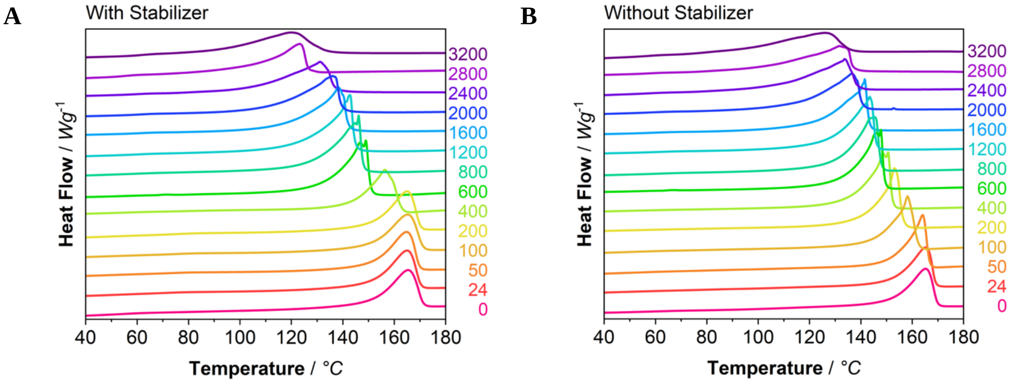

__Figure S9.__ DSC measurements. Heat flow in W/g vs. temperature in °C for __(A)__ PP particles with stabilizer and __(B)__ PP particles without stabilizer.

Evaluation of Crystallinity via ^{13}C CP MAS NMR Spectroscopy

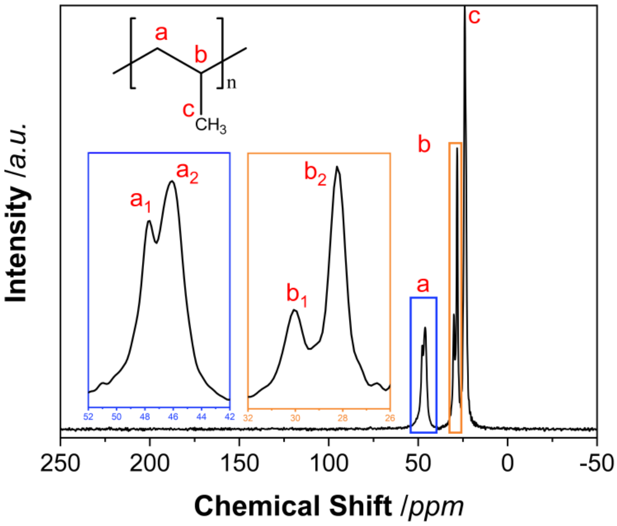

Figure S10. *^{13}C CP MAS NMR spectrum of the PP particles with stabilizer prior to weathering with signal assignment. In the enlarged PP spectra (blue and orange rectangle) the differences of the resonances of the amorphous (signal a1 and b1) and crystalline (signal a2 and b2) phase become visible (Hronský et al., 2014).*

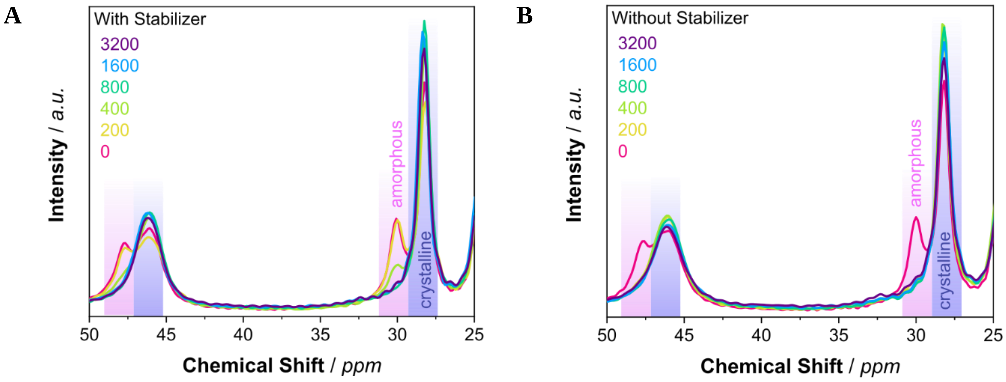

Figure S11. *^{13}C CP MAS NMR spectra of the PP particles with **(A)** and without **(B)** stabilizer for 0, 400 and 3200 h weathering time. Upon irradiation, a shift of signal intensity from the amorphous phase resonances (30 ppm, 48 ppm) to the crystalline phase resonances (28 ppm, 46 ppm) is observed (Hronský et al., 2014). The spectra are normalised to the integral of the backbone signal (35-20 ppm and 55-35 ppm).*

Calculation of Defect Proportions via ^{13}C CP MAS NMR Spectroscopy

Table S5. *Refinement parameters for the ^{13}C CP NMR spectra of weathered PP samples with and without stabilizer. Refinements were carried out with pseudo-Voigt lineshapes (Eq. 1) where δ_{iso} is the isotropic chemical shift, LB the line broadening, x the Gauss/Lorentz ratio and I the relative intensity. The latter is given in percent as fraction of the total spectral intensity. Refinement parameters marked in grey were obtained by simultaneous free refinements of defect peaks in the two spectra with longest weathering times and were kept constant in the subsequent refinements.*

$$f(\delta) = I \cdot \left[(1-x)\frac{2\,LB}{4\pi\cdot(\delta-\delta_{iso})^2+\pi\cdot LB^2} + x\cdot\frac{\sqrt{4\ln(2)}}{\sqrt{\pi}\,LB}\cdot e^{-\frac{4\ln(2)}{LB^2}(\delta-\delta_{iso})^2}\right] \qquad \text{(Eq. 1)}$$

Spectrum	Peak Assignment	δ_{iso} [ppm]	LB [ppm]	x	Intensity [%]
PP with stabilizer 3200 h	Ketone	216	29.8	0.5	1.1
	Carboxylic acid	179.8	11.9	0.9	1.3
	Peroxide	86.8	8.8	0.2	1.6
	Alcohol	75.6	8.8	0.2	2.2
	CH_2	46.4	2.6	0.0	17.8
		50.1	10.0	0.0	3.0
	CH	28.5	1.5	0.0	19.2
		29.7	4.9	0.0	6.2
	CH_3	23.9	2.3	0.3	41.6
		19.6	7.2	0.2	4.1
PP with stabilizer 2800 h	Ketone	216	29.8	0.5	1.4
	Carboxylic acid	179.8	11.9	0.9	1.2
	Peroxide	86.8	8.8	0.2	2.0
	Alcohol	75.6	8.8	0.2	2.2
	CH_2	46.5	2.6	0.0	18.6
		50.6	11.6	0.0	4.0
	CH	28.6	1.5	0.0	19.8
		29.9	5.3	0.0	7.8
	CH_3	24.1	2.3	0.4	41.3
		19.4	5.8	1.0	1.6
PP with stabilizer 2400 h	Ketone	216	29.8	0.5	1.0
	Carboxylic acid	179.8	11.9	0.9	1.0
	Peroxide	86.8	8.8	0.2	1.7
	Alcohol	75.6	8.8	0.2	2.0
	CH_2	46.5	2.6	0.0	18.4
		51.0	11.4	0.0	3.7
	CH	28.5	1.5	0.0	21.9
		30.1	5.9	0.0	5.3
	CH_3	24.1	2.3	0.4	41.0
		20.7	7.1	0.5	4.2
PP with stabilizer 2000 h	Ketone	216	29.8	0.5	1.1
	Carboxylic acid	179.8	11.9	0.9	1.2
	Peroxide	86.8	8.8	0.2	1.7
	Alcohol	75.6	8.8	0.2	1.8
	CH_2	46.5	2.6	0.0	19.1
		50.4	11.3	0.0	3.5
	CH	28.5	1.5	0.0	20.9
		29.9	5.4	0.0	6.8
	CH_3	24.0	2.3	0.4	42.3
		19.4	5.7	1.0	1.5

Spectrum	Peak Assignment	δ_{iso} [ppm]	LB [ppm]	x	Intensity [%]
PP with stabilizer 1600 h	Ketone	216	29.8	0.5	0.7
	Carboxylic acid	179.8	11.9	0.9	1.0
	Peroxide	86.8	8.8	0.2	1.6
	Alcohol	75.6	8.8	0.2	1.7
	CH_2	46.5	2.5	0.0	18.8
		50.4	10.8	0.0	4.0
	CH	28.5	1.6	0.0	24.1
		31.5	4.8	0.0	3.4
	CH_3	24.0	2.3	0.4	42.2
		20.5	7.5	0.9	2.5
PP with stabilizer 1200 h	Ketone	216	29.8	0.5	0.8
	Carboxylic acid	179.8	11.9	0.9	0.7
	Peroxide	86.8	8.8	0.2	1.4
	Alcohol	75.6	8.8	0.2	1.3
	CH_2	46.3	2.6	0.0	20.6
		50.9	9.8	0.0	3.1
	CH	28.4	1.4	0.0	20.2
		29.4	4.0	0.0	6.6
	CH_3	24.0	2.2	0.3	44.6
		18.1	5.9	1.0	0.6
PP with stabilizer 800 h	Ketone	216	29.8	0.5	0.7
	Carboxylic acid	179.8	11.9	0.9	0.5
	Peroxide	86.8	8.8	0.2	1.4
	Alcohol	75.6	8.8	0.2	0.8
	CH_2	46.3	2.5	0.0	19.2
		50.6	10.3	0.0	3.3
	CH	28.4	1.5	0.0	22.8
		30.3	5.3	0.0	4.1
	CH_3	23.9	2.3	0.3	45.0
		19.7	7.1	0.4	2.1
PP with stabilizer 600 h	Ketone	216	29.8	0.5	0.0
	Carboxylic acid	179.8	11.9	0.9	0.0
	Peroxide	86.8	8.8	0.2	0.9
	Alcohol	75.6	8.8	0.2	0.8
	CH_2	46.2	2.8	0.4	16.0
		48.0	8.7	0.0	8.6
	CH	28.3	1.5	0.0	21.6
		29.5	5.7	0.8	7.0
	CH_3	23.8	2.3	0.4	43.5
		19.1	6.0	1.0	1.4
PP with stabilizer 400 h	Ketone	216	29.8	0.5	0.0
	Carboxylic acid	179.8	11.9	0.9	0.0
	Peroxide	86.8	8.8	0.2	0.5
	Alcohol	75.6	8.8	0.2	0.4
	CH_2	46.4	2.6	0.0	18.9
		48.5	3.7	0.0	3.3
	CH	28.4	1.5	0.0	20.3
		29.8	4.2	1.0	5.6
	CH_3	23.9	2.2	0.4	45.7
		21.4	7.8	0.0	5.2

Spectrum	Peak Assignment	δ_{iso} [ppm]	LB [ppm]	x	Intensity [%]
PP with stabilizer 200 h	Ketone	216	29.8	0.5	0.0
	Carboxylic acid	179.8	11.9	0.9	0.0
	Peroxide	86.8	8.8	0.2	0.0
	Alcohol	75.6	8.8	0.2	0.0
	CH_2	44.1	2.8	0.0	14.6
		45.9	2.5	0.0	8.1
	CH	26.4	1.6	0.0	18.4
		28.2	1.9	0.0	9.9
	CH_3	22.0	2.1	0.3	41.8
		19.8	8.5	0.0	7.2
PP with stabilizer 0 h	Ketone	216	29.8	0.5	0.0
	Carboxylic acid	179.8	11.9	0.9	0.0
	Peroxide	86.8	8.8	0.2	0.0
	Alcohol	75.6	8.8	0.2	0.0
	CH_2	46.3	2.5	0.6	9.9
		47.9	3.7	0.0	14.3
	CH	28.4	1.5	0.0	18.2
		30.3	1.9	0.0	9.9
	CH_3	24.0	2.1	0.2	44.5
		24.4	1.1	0.2	3.2
PP without stabilizer 3200 h	Ketone	214	29.8	0.5	1.3
	Carboxylic acid	178.7	11.9	0.9	1.1
	Peroxide	84.6	8.8	0.2	2.0
	Alcohol	74.0	8.8	0.2	2.2
	CH_2	44.4	3.1	0.0	18.1
		48.5	14.4	0.0	4.0
	CH	26.5	1.6	0.0	18.0
		27.1	5.2	0.0	9.7
	CH_3	22.0	2.3	0.4	35.4
		18.1	8.2	0.0	6.0
PP without stabilizer 2800 h	Ketone	214	29.8	0.5	1.6
	Carboxylic acid	178.7	11.9	0.9	1.2
	Peroxide	84.6	8.8	0.2	2.1
	Alcohol	74.0	8.8	0.2	2.0
	CH_2	44.4	3.1	0.0	18.6
		49.6	12.4	0.0	3.1
	CH	26.5	1.6	0.0	19.8
		27.2	5.6	0.0	8.4
	CH_3	21.9	2.3	0.5	33.8
		19.0	7.5	0.0	7.7
PP without stabilizer 2400 h	Ketone	214	29.8	0.5	0.9
	Carboxylic acid	178.7	11.9	0.9	0.9
	Peroxide	84.6	8.8	0.2	1.9
	Alcohol	74.0	8.8	0.2	2.0
	CH_2	44.4	3.1	0.0	18.9
		49.8	15.3	0.0	4.2
	CH	26.5	1.5	0.0	18.7
		27.1	4.9	0.0	9.2
	CH_3	22.0	2.3	0.4	36.7
		18.1	7.2	0.0	5.2

Spectrum	Peak Assignment	δ_{iso} [ppm]	LB [ppm]	x	Intensity [%]
PP without stabilizer 2000 h	Ketone	214	29.8	0.5	1.1
	Carboxylic acid	178.7	11.9	0.9	0.9
	Peroxide	84.6	8.8	0.2	1.4
	Alcohol	74.0	8.8	0.2	1.5
	CH_2	44.3	3.0	0.1	18.1
		48.0	6.7	0.0	1.9
	CH	26.4	1.6	0.2	19.9
		27.7	4.3	0.0	4.2
	CH_3	22.0	2.3	0.3	37.9
		20.0	11.9	0.0	12.4
PP without stabilizer 1600 h	Ketone	214	29.8	0.5	1.2
	Carboxylic acid	178.7	11.9	0.9	0.8
	Peroxide	84.6	8.8	0.2	1.7
	Alcohol	74.0	8.8	0.2	1.5
	CH_2	44.3	3.0	0.2	17.0
		47.2	9.9	0.0	4.0
	CH	26.4	1.6	0.2	19.5
		27.3	6.1	0.7	5.0
	CH_3	21.9	2.3	0.4	35.2
		20.2	9.6	0.0	13.3
PP without stabilizer 1200 h	Ketone	214	29.8	0.5	0.6
	Carboxylic acid	178.7	11.9	0.9	0.5
	Peroxide	84.6	8.8	0.2	1.1
	Alcohol	74.0	8.8	0.2	1.1
	CH_2	44.2	3.0	0.0	19.9
		49.1	6.1	0.0	0.7
	CH	26.5	1.6	0.0	23.4
		28.1	5.8	1.0	2.2
	CH_3	11.7	18.9	0.4	2.1
		-16.8	53.8	0.1	1.9
		21.9	2.3	0.4	38.3
		19.3	6.6	0.0	7.6
PP without stabilizer 800 h	Ketone	214	29.8	0.5	0.6
	Carboxylic acid	178.7	11.9	0.9	0.2
	Peroxide	84.6	8.8	0.2	1.0
	Alcohol	74.0	8.8	0.2	1.0
	CH_2	44.3	3.0	0.2	18.5
		48.0	6.7	0.0	2.6
	CH	26.5	1.7	0.0	24.9
		29.5	3.6	1.0	1.1
	CH_3	-7.6	49.1	0.4	2.1
		21.9	2.3	0.4	38.2
		19.4	9.2	0.0	9.3

Spectrum	Peak Assignment	δ_{iso} [ppm]	LB [ppm]	x	Intensity [%]
PP without stabilizer 600 h	Ketone	214	29.8	0.5	0.5
	Carboxylic acid	178.7	11.9	0.9	0.5
	Peroxide	84.6	8.8	0.2	0.9
	Alcohol	74.0	8.8	0.2	0.6
	CH$_2$	44.4	3.0	0.1	20.0
		48.8	4.1	0.3	1.1
	CH	26.5	1.7	0.5	19.2
		28.0	4.4	0.9	4.3
	CH$_3$	0.5	49.5	1.0	2.5
		22.1	2.4	0.3	42.1
		19.3	9.7	0.0	7.9
PP without stabilizer 400 h	Ketone	214	29.8	0.5	0.4
	Carboxylic acid	178.7	11.9	0.9	0.4
	Peroxide	84.6	8.8	0.2	0.9
	Alcohol	74.0	8.8	0.2	0.6
	CH$_2$	44.4	2.9	0.2	19.5
		48.5	6.9	0.0	2.8
	CH	26.5	1.6	0.4	20.1
		27.4	6.2	1.0	5.4
	CH$_3$	1.2	50.7	0.0	1.7
		22.1	2.3	0.3	41.5
		19.2	9.6	0.0	6.2
PP without stabilizer 200 h	Ketone	214	29.8	0.5	0.4
	Carboxylic acid	178.7	11.9	0.9	0.3
	Peroxide	84.6	8.8	0.2	0.8
	Alcohol	74.0	8.8	0.2	0.6
	CH$_2$	44.4	2.9	0.3	18.6
		47.9	5.4	0.0	3.1
	CH	26.5	1.7	0.2	23.6
		29.0	3.9	1.0	1.9
	CH$_3$	-0.7	38.8	0.8	1.3
		22.1	2.3	0.3	42.3
		19.9	9.6	0.0	6.5
PP without stabilizer 0 h	Ketone	214	29.8	0.5	0.0
	Carboxylic acid	178.7	11.9	0.9	0.0
	Peroxide	84.6	8.8	0.2	0.0
	Alcohol	74.0	8.8	0.2	0.0
	CH$_2$	44.1	2.6	0.5	10.4
		46.0	3.0	0.0	13.0
	CH	26.4	1.6	0.2	17.4
		28.3	1.9	0.0	10.1
	CH$_3$	-0.7	49.5	0.2	2.5
		22.1	2.0	0.3	38.7
		21.4	5.5	0.0	7.9

Table S6. *Correction factors for PP with and without stabilizer determined with quantitative multi-CP spectra of the respective 3200 h weathered sample. Used to calibrate the defect intensities in the CP spectra (Meides et al., 2021).*

Functional Group	**PP with stabilizer**	**PP without stabilizer**
	c_i 3200 h	**c_i 3200 h**
Ketone	0.49	0.50
Carboxylic acid	0.85	0.84
Peroxide	0.76	0.74
Alcohol	0.80	0.77

$\rho_{ru} = [1 - (3 \cdot I_{ketone}) - (2 \cdot I_{COOH}) - (3 \cdot I_{POOH}) - (3 \cdot I_{OH})] / 3$ (Eq. 2)

with:	ρ_{ru}	proportion of propylene RUs relative to the proportion of defects
	I_{ketone}	relative intensity of the ketone resonance
	I_{COOH}	relative intensity of the carboxylic acid resonance
	I_{POOH}	relative intensity of the peroxide resonance
	I_{OH}	relative intensity of the alcohol resonance.

Since the ratio of the different groups is $I_{ketone} : I_{COOH} : I_{POOH} : I_{OH} : p_{ru}$, the absolute proportions of the carbonyl groups (ap_{ketone}), carboxy groups (ap_{COOH}), peroxy groups (ap_{POOH}) and hydroxy groups (ap_{POH}) can be calculated once ρ_{ru} is known:

$ap_{ketone} = I_{ketone} /(p_{ru} + I_{ketone} + I_{COOH} + I_{POOH} + I_{OH})$ (Eq. 3)

$ap_{COOH} = I_{COOH} /(p_{ru} + I_{ketone} + I_{COOH} + I_{POOH} + I_{OH})$ (Eq. 4)

$ap_{POOH} = I_{POOH} /(p_{ru} + I_{ketone} + I_{COOH} + I_{POOH} + I_{OH})$ (Eq. 5)

$ap_{OH} = I_{OH} /(p_{ru} + I_{ketone} + I_{COOH} + I_{POOH} + I_{OH})$ (Eq. 6)

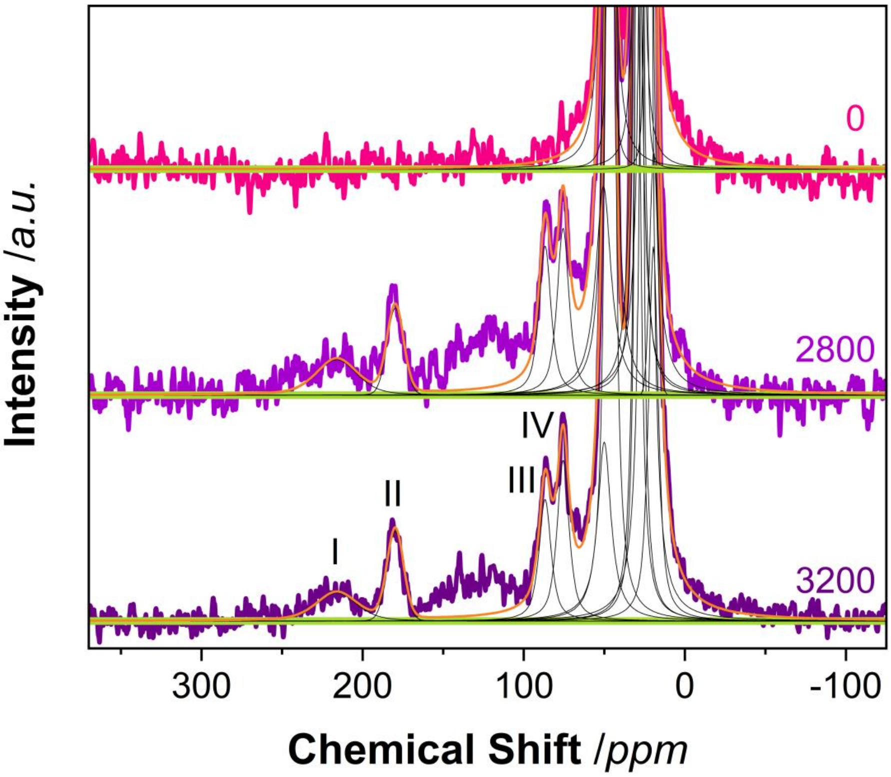

__Figure S12.__ ^{13}C CP MAS NMR spectra of the PP particles with stabilizer for 0, 2800 and 3200 h weathering time. The spectra are normalised to the intensity of the methyl sidechain carbon signal (at approx. 24 ppm). Individual spectra are shifted vertically for better comparability. Additionally, the baselines (green), individual refinements for the peaks (black) and the cumulative lineshape (orange) are shown in the spectra. No refinement of vinylidenes was performed between 100 – 150 ppm since the resonances of the decomposition products of Irgafos® 168 superimpose with the vinylidene resonances.

SEM Images

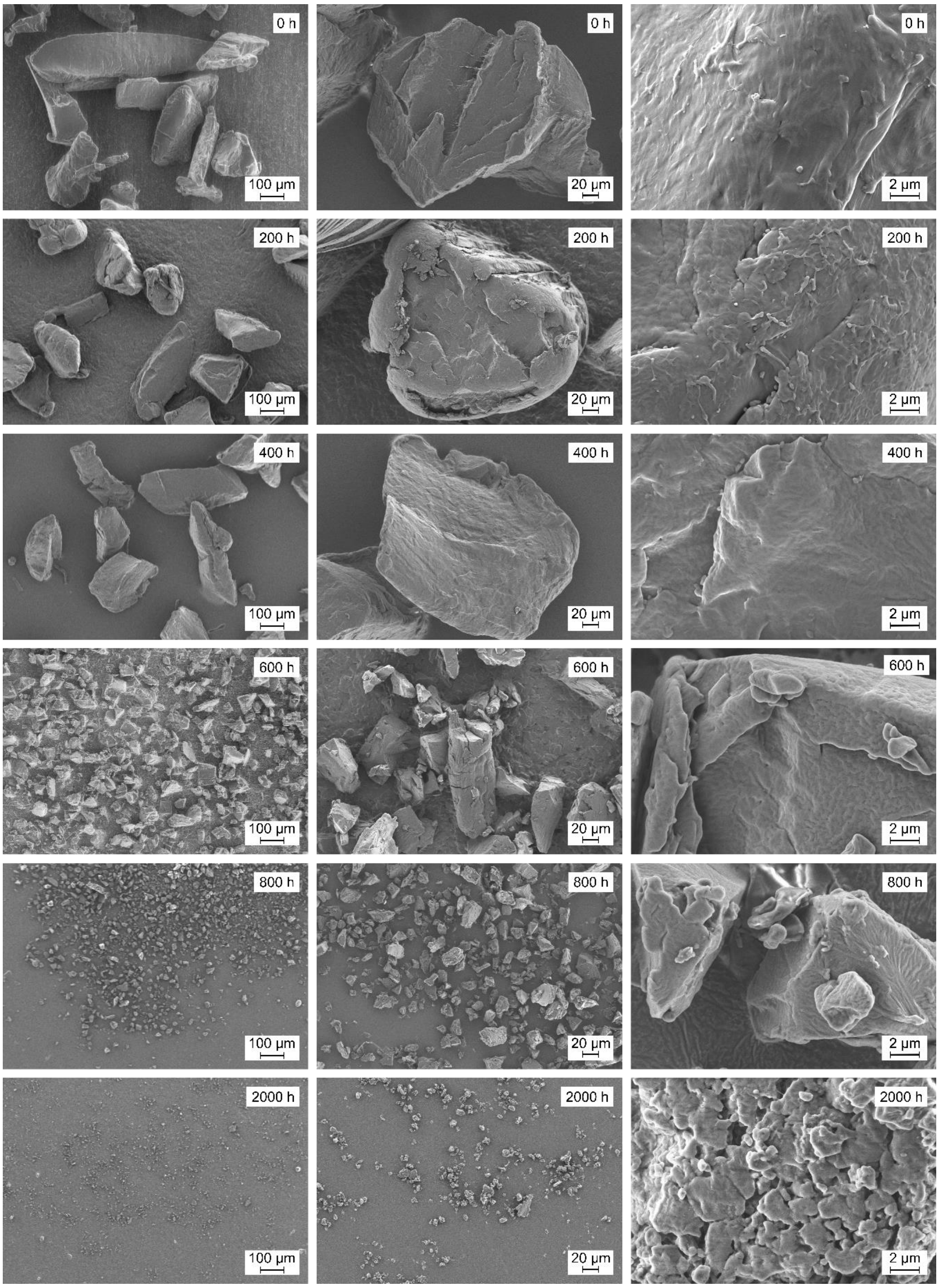

Figure S13. *SEM images of PP with stabilizer after irradiation for different time intervals.*

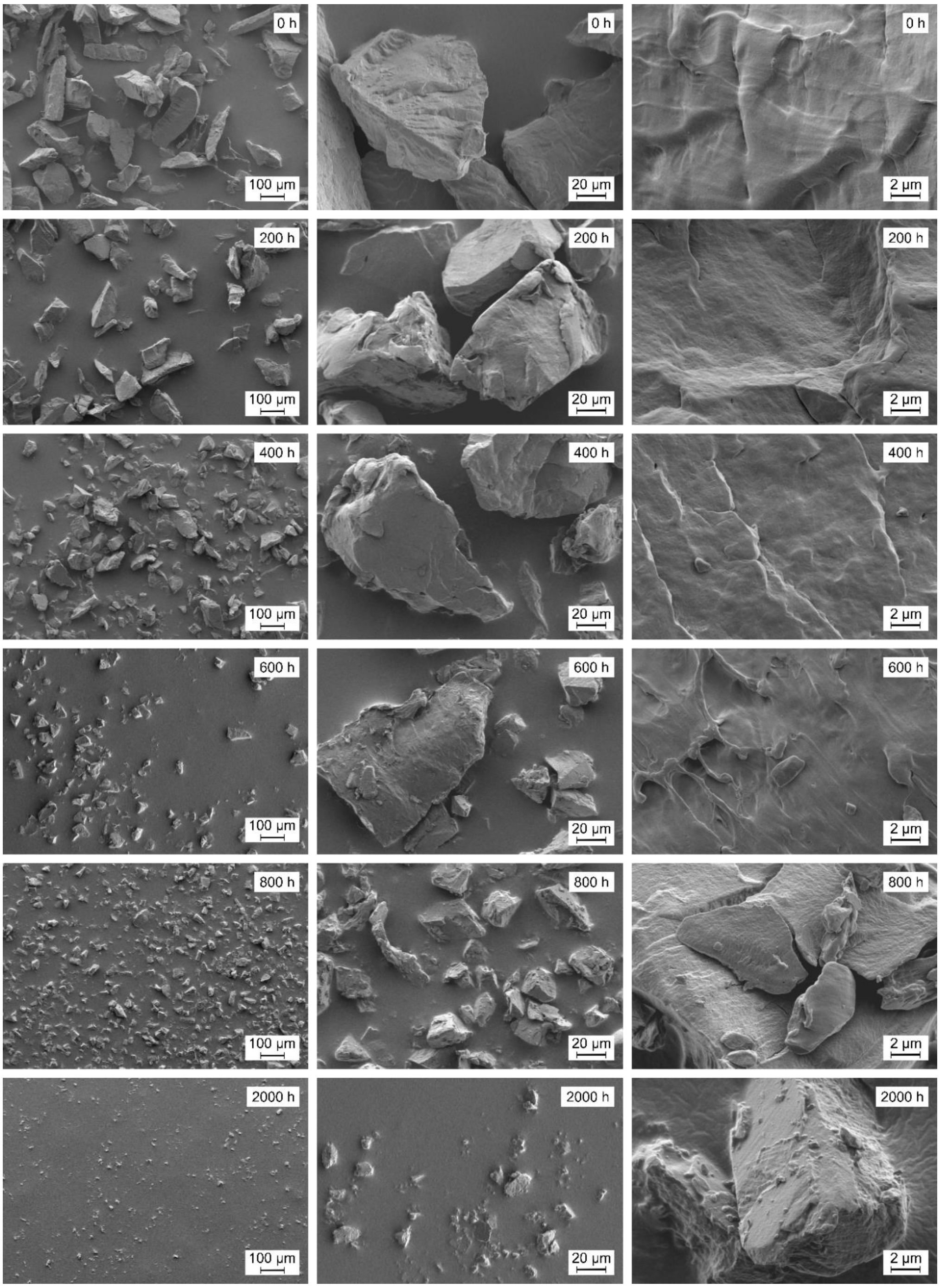

Figure S14. *SEM images of PP without stabilizer after irradiation for different time intervals.*

Supplementary References

Fouyer K, Lavastre O, Rondeau D. Direct monitoring of the role played by a stabilizer in a solid sample of polymer using direct analysis in real time mass spectrometry: the case of Irgafos 168 in polyethylene. Analytical chemistry 2012;84(20):8642–9.

Hronský V, Koval'aková M, Vrábel P, Uhrínová M, Olčák D. Estimation of the Degree of Crystallinity of Partially Crystalline Polypropylenes Using 13 C NMR. Acta Physica Polonica, A 2014;125(6).

Maier R-D, Schiller M. Handbuch Kunststoff Additive: Carl Hanser Verlag GmbH Co KG; 2016.

Meides N, Menzel T, Poetzschner B, Löder MGJ, Mansfeld U, Strohriegl P et al. Reconstructing the Environmental Degradation of Polystyrene by Accelerated Weathering. Environmental Science & Technology 55 2021(12):7930–8. 10.1021/acs.est.0c07718.

Schwarzinger C, Gabriel S, Beißmann S, Buchberger W. Quantitative Analysis of Polymer Additives with MALDI-TOF MS Using an Internal Standard Approach. Journal of the American Society for Mass Spectrometry 2012;23(6):1120–5.

8.4 Environmental degradation of polystyrene, polyethylene, and polypropylene - a comparison of natural and accelerated weathering.

Environmental degradation of polystyrene, polyethylene, and polypropylene - a comparison of natural and accelerated weathering

Nora Meides,[1] Anika Mauel,[2] Teresa Menzel,[3] Wolfgang Babel,[4] Jürgen Senker,[2] Volker Altstädt,[3] Holger Ruckdäschel,[3] Peter Strohriegl[1,*]

[1] Department of Macromolecular Chemistry I, University of Bayreuth, Universitätsstraße 30, 95447 Bayreuth, Germany

[2] Department of Inorganic Chemistry III, University of Bayreuth, Universitätsstraße 30, 95447 Bayreuth, Germany

[3] Department of Polymer Engineering, University of Bayreuth, Universitätsstraße 30, 95447 Bayreuth, Germany

[4] Micrometeorology Group, University of Bayreuth, Universitätsstraße 30, 95447 Bayreuth, Germany

* Corresponding author: peter.strohriegl@uni-bayreuth.de

Abstract

Secondary microplastics (MP) have to date been verified in every environmental compartment of the earth. In order to understand the time scales and degradation rates of the formation of MP from macroplastic particles under exposure to environmental stress factors, accelerated, abiotic laboratory weathering has gained significant attention in polymer degradation research. The constant irradiation and controlled parameters enable the detailed investigation in a reasonable time frame. However, direct evaluation of the applicability to an outdoor setting is rarely performed. To test the transferability of accelerated weathering in an industrially available weathering chamber to outdoor weathering, we performed a direct comparison study using polystyrene (PS), polypropylene (PP), and polyethylene (LDPE) particles. Accelerated weathering was performed over a total experimental duration of 3200 h. Outdoor weathering for a supposedly corresponding 1.5 years. Both experiments were continuously sampled, and degradation investigated via gel permeation chromatography, particle size analysis, differential scanning calorimetry, SEM imaging, and ^{13}C NMR spectroscopy. Our results show that the degrading mechanisms are the same, comparing accelerated to outdoor weathering. The time scales however, are strongly influenced by individual parameters, especially the temperature.

Keywords:

Degradation, microplastic, fragmentation, photooxidation, accelerated weathering

Introduction

Plastic pollution in natural compartments all over our planet has become a topic of global concern. A major contribution to this issue is mismanaged plastic waste, either discarded directly into nature, or disposed in dumps, or open, uncontrolled landfills (Jambeck et al., 2015). The European population contributes indirectly to this issue. 8 % of the post-consumer plastic waste collected in Europe in 2020 was exported from the European Union to other countries for recycling (Statista, 2021). A recent study by Bishop et al., 2020) has investigated the fate of exported plastic waste, with a special focus on polyethylene (PE), one of the most commonly used type of plastic. The authors conclude, that 31 % of PE waste exported for recycling, is not actually recycled, but either incinerated or disposed in open landfills. Nevertheless, this proportion remains classified as *recycled* and is filed as such within the statistics. Open landfills greatly contribute to the distribution of plastic waste (Brooks et al., 2018). Wind and animals have direct access to these sites, enabling an easy distribution to environmental compartments, such as the oceans (Andrady, 2017; Eerkes-Medrano et al., 2015). Bishop et al., 2020 ultimately modelled, that approximately 3 % of all exported PE waste, amounting to 83,000 tons, ends up in the oceans.

Upon exposure in the environment, multiple stress factors will affect the chemical and physical composition of plastic materials (Gewert et al., 2015). UV-radiation in particular, will lead to radical formation, chain scission, and cross-linking, reducing the molecular weight, which further enhances embrittlement (Dobkowski, 1995; Fayolle et al., 2008). Chemical degradation is directly linked to a modification in the physical properties, and on-going exposure leads to fragmentation, and ultimately the formation of secondary microplastic (MP) particles (Andrady, 2017; Fairbrother et al., 2019; Gewert et al., 2015; Zweifel, 1998).

The majority of MP in the environment is secondary MP, resulting from degradation and fragmentation processes, as a consequence of weathering (Andrady and Koongolla, 2022). While precise definitions of the size range of MP particles have been a matter of debate in recent years (Frias and Nash, 2019; Hartmann et al., 2019), within this study, we adapted the nomenclature suggested by Hartmann et al., 2019, defining MP to a size range between 1 - 1000 µm. In order to understand how MP are formed and degrade under natural influence, it is crucial to mimic these processes, either in an environmental setting, or in a laboratory-controlled weathering chamber. Accelerated weathering chambers are frequently used in testing the lifetime of plastic parts in industry and have also become a useful tool in microplastic research (e.g., Atlas Suntest, Q-Lab weathering chambers). These chambers can mimic natural sunlight almost perfectly and enable the imitation of natural weathering in an accelerated, yet very controlled manner.

Previous studies have addressed the direct comparison of outdoor to accelerated weathering, however there are only few studies, and the results are diverse. Gijsman et al., 1996 exposed PE films to accelerated and outdoor weathering in the Netherlands, and conclude, that weathering takes place only during the spring and summer. They argue that the acceleration factor depends on the parameter measured and propose different mechanisms between accelerated and outdoor weathering. Further exposure sites of studies focusing exclusively on outdoor weathering were Florida (Hill et al., 2021), Florida and France (Moreira et al., 2021), or China (Lv et al., 2015). Other studies perform both types of weathering with a focus on additive testing (Al-Salem, 2009), or service life prediction (Qin et al., 2021). Understanding polymer degradation processes and the correlation to MP formation is not addressed in these studies. Additionally, due to variations in composition, shape and thickness, comparison studies should be performed for every material.

In our recent publications (Meides et al., 2021; Meides et al., 2022; Menzel et al., 2022), we thoroughly investigated the degradation and fragmentation rates for three commodity polymers (PS, LDPE, and PP) using accelerated-laboratory weathering (Q-Sun Xe-3 weathering chamber) for ~ 4 months (3200 h). With this study we want to verify, that the mechanisms are comparable from the laboratory to the outdoor setting. We want to check if our conclusions drawn from accelerated weathering are applicable to natural weathering. To do so, we performed outdoor weathering as well as accelerated laboratory weathering on three different polymers, PS, PP, and LDPE. We used the same basic experimental setup for both settings; however, temperature, and solar irradiance were certainly different in the outdoor setup. In order to compare both experiments, we used the data from the meteorological station located in the botanical garden at the University of Bayreuth, which is positioned only ~ 100 meters from our experiment. Outdoor degradation was monitored over a total exposure time of 1.5 years, from July 2020 to January 2022. We compared both sets of data for all three polymers using a multitude of analytical tools, such as gel permeation chromatography, particle size analysis, differential scanning calorimetry, SEM imaging, and ^{13}C NMR spectroscopy.

Results and discussion

Surface characteristics

SEM images of PS particle surfaces from outdoor weathering experiments are displayed in Figure 1a-c. Within the first stage of weathering, the particles are rounded off, revealing smoother surfaces. Crack patterns become visible within individual particles after 10 months of exposure (Figure 1b). These patterns indicate weakness in the structure and represent potential breaking points with further irradiation and mechanical influence. This is supported by the image of PS particles after 12 months of outdoor weathering (Figure 1c). The large starting particles break up and secondary daughter particles with smaller sizes are formed. These particles have different sizes and shapes, down to < 1 µm (Figure 1c).

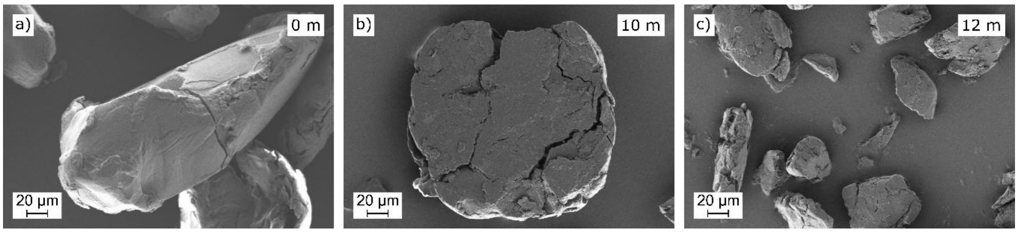

Figure 1 – Surface characteristics of PS particles from outdoor weathering a) of a reference particle, b) after 10 months and c) after 12 months.

Similar observations can be made from SEM images of PP particles and LDPE particles (Figure S1). However, while the particles become smaller with increasing weathering, harsh fractures remain largely absent. More dominant surface characteristics are flakes which seem to be peeling off and small particles attached to the surface of larger ones (Figure S1e+l). LDPE particles reveal hardly any changes after 10 and even 12 months (Figure S1e+f). A closer view to the particle surface after 10 months reveals many < 1 µm particles, potentially down to the nanometer-scale for PP (Figure S1o). After 12 months of outdoor exposure, PP particles are extremely small compared to the other two polymers (Figure S1m).

Average particle size

Quantitative particle size measurements allowed for the determination of the average particle sizes (Figure 2, Table S1) as well as particle size distributions (Figure S2) at each exposure time. The data are plotted with each month of sampling (between July 2020 to January 2022) at the bottom of the x-axis, as well as the exposure time in days at the top. Seasonal changes are highlighted in yellow for summer and blue for winter.

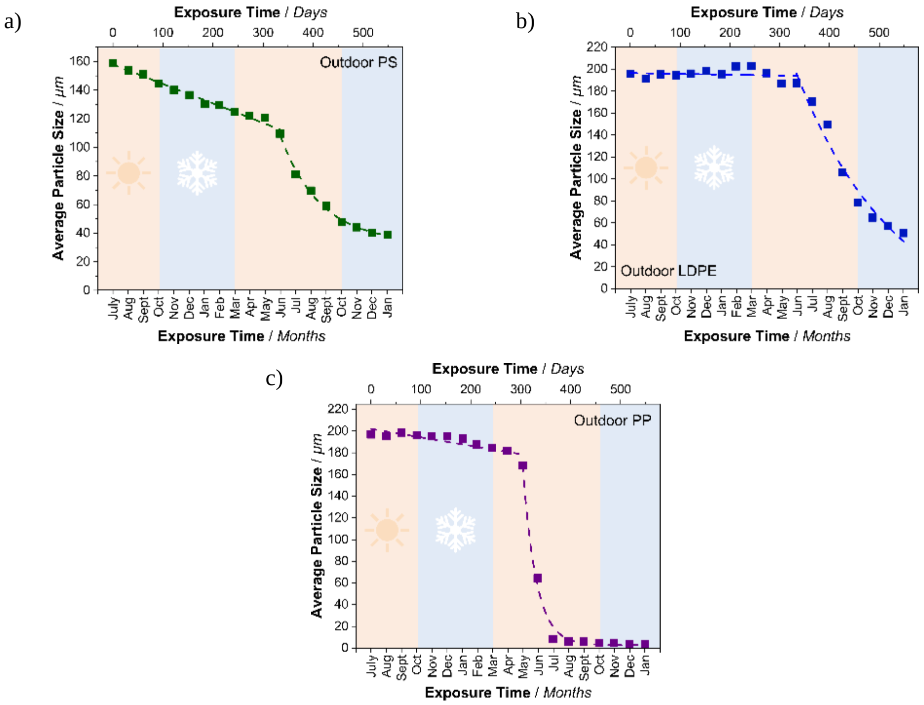

Figure 2 – Average particle size as a function of exposure time in months (x-axis, bottom) and in days (x-axis, top) for a) PS particles in green, b) LDPE particles in blue and c) PP particles in purple. Summer months are highlighted in orange, winter months are highlighted in blue.

All three polymer systems show similar trends: within the first few months of weathering, the particle size evolves in a linear trend. While PS and PP slowly decrease up to 10-11 months of outdoor weathering, LDPE particles remain largely unchanged within this time frame, showing only minor fluctuations (198 ± 4 µm, Table S1). After 11-12 months, the linear trend turns into an exponential decay of the particle size for all three polymers, which is differently pronounced for each system. PS degrades in a rather slow manner (Figure 2a), showing a more rapid decrease in the following summer months (May-Oct), with a particle size changing from 121 to 48 µm. In the subsequent winter months, the particle size decreases only down to 38 µm with $\tau = 80$ days (Table S1). LDPE shows the slowest fragmentation character (Figure 2b), with a time constant $\tau = 199$ days for the exponential decay. Here too, the summer months show a faster size decrease (May-Oct, 187-78 µm), whereas the winter months show a slower size reduction (Oct-Jan, 78-51 µm). The turning point of linear to exponential is the same for all three systems and occurs within the summer months of May to July. PP however reveals a sharp turning point from linear to exponential (Figure 2c), with a pronounced reduction of the particle size from 168 µm down to 5 µm (May-Oct). In the final months the size remains between 5 to 4 µm, the time constant of the exponential decay being $\tau = 27$ days.

Development of molecular weight

Investigations of the molecular weight (MW) and molecular weight distributions (MWD) were performed using gel permeation chromatography. Data for number-average (M_n) and weight-average (M_w) as well as the peak molecular weight (M_p) and dispersity Đ values are given in Table S2-4, the MWD in Figure S3. The M_n is plotted in dependence of the exposure time in months (x-bottom) and days (x-top) in Figure 3.

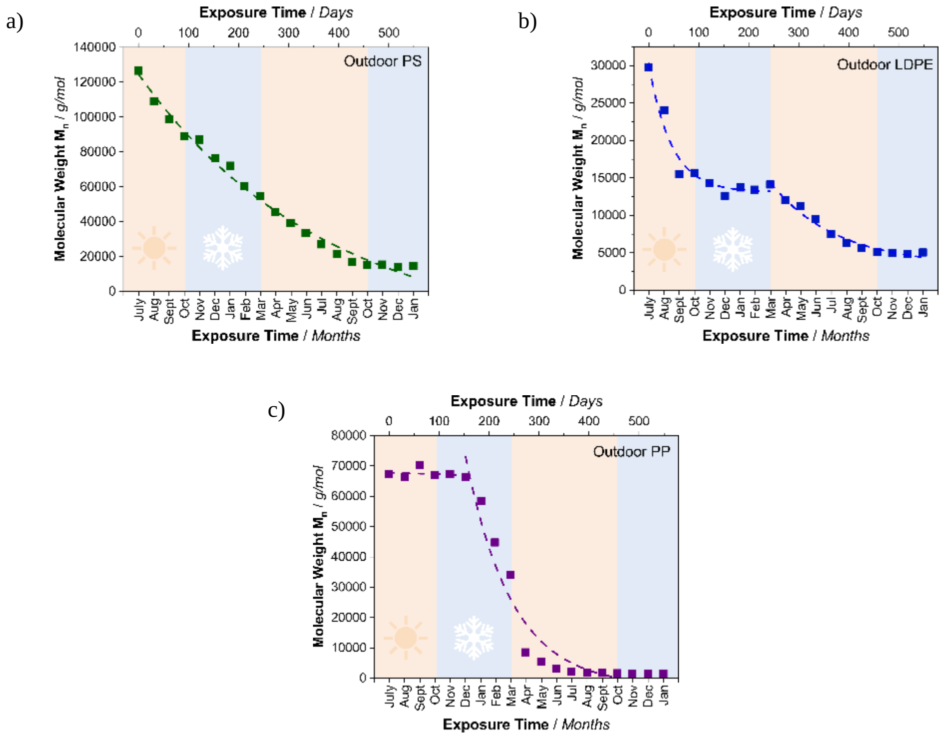

Figure 3 – Development of molecular weight (M_n) as a function of exposure time in months (x-axis, bottom) and in days (x-axis, top) for a) PS particles in green, b) LDPE particles in blue, and c) PP particles in purple. Summer months are highlighted in orange, winter months are highlighted in blue.

The trends for the development of the M_n are unique for all three polymers. A linear trend is clearly visible within PP (Figure 3c), whereas PS and LDPE (Figure 3a+b) immediately reveal a reduction of the M_n in the first months from July to October, which is more pronounced for LDPE (30-16 kg/mol) than it is for PS (127-90 kg/mol, Table S2). Further, PS shows a roughly linear decrease over the entire duration of the experiment, with a slight plateau at the end. This may correlate to the winter time with lower UV activity. The final M_n of PS has reached 15 kg/mol (Table S2). LDPE seems to show distinct seasonal dependence. M_n decreases exponentially during the first 8 months (July-March), with a slight plateau during the winter time. During the summer months the M_n decrease seems to be speeding up again, until reaching a further plateau from October to January (Figure 3b). After 18 months, the M_n of LDPE has decreased down to 5000 g/mol. PP shows a different behavior: from July to December no reduction of the MW can be observed, resulting in a linear plateau of ~ 66-70 kg/mol (Figure 3c). Then, the M_n decreases rapidly with a reduction from 66 kg/mol to 9 kg/mol (Dec-Apr). After 1.5 years, the M_n has reached 1600 g/mol.

Identification of polymer defects

Photooxidation was monitored via solid-state ^{13}C NMR spectroscopic experiments (Figure 4). The prominent peaks observed in the spectra of all three polymers can be assigned to the carbons of the repeating units unaffected by weathering. For PS (Figure 4a) the resonances between 35-55 ppm correspond to the aliphatic backbone while the resonances at 128 ppm and 145 ppm correspond to the CH units and the ipso carbon of the phenyl ring. In the PP spectra (Figure 4c), the dominant peaks at 44, 27 and 22 ppm can be assigned to the CH_2, CH and CH_3 groups, respectively (Hronský et al., 2014). For LDPE (Figure 4b), the peaks at 35 and 33 ppm are attributed to crystalline and amorphous CH_2 units in the aliphatic backbone (Assink et al., 2000), whereas additional weaker signals between 50-0 ppm correspond to the microstructure within the chain architecture of LDPE (Chabira et al., 2008). Upon outdoor exposure, new peaks emerge within the spectra of all three polymers. Previously, these could be assigned to polymer defects such as ketones (~ 205 ppm), carboxylic acids (~ 175 ppm), vinylidenes (~ 141 and ~ 117 ppm), peroxides (~ 83 ppm) and alcohols (~ 74 ppm) (Mauel et al., 2022; Meides et al., 2021; Meides et al., 2022; Menzel et al., 2022; Mowery et al., 2005; Mowery et al., 2007). Here, in the outdoor weathered PS, PP and PE samples, carboxylic acids, peroxides and alcohols were detected. Additionally, vinylidene polymer defects emerged in the LDPE samples. Ketone defects are still below the detection limit after 1.5 years of outdoor weathering.

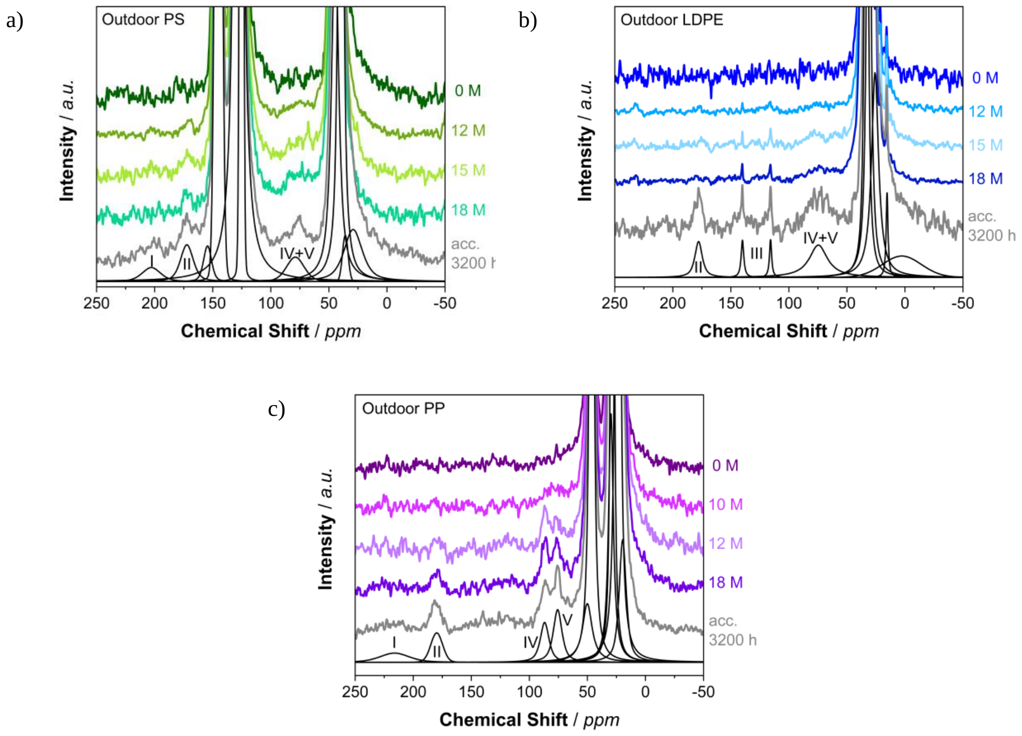

Figure 4 – Solid-state ^{13}C NMR spectra of a) PS, b) LDPE and c) PP for exposure times of 0, 10, 12, 15, and 18 months compared to the spectra of the respective polymers after 3200 h of accelerated weathering. With increasing exposure time, new peaks arise within the spectra, which can be attributed to defect types such as ketones (I), carboxylic acids (II), vinylidenes (III), peroxides (IV), and alcohols (V). The spectra are either normalized to the intensity of the aliphatic backbone (PS and LDPE) or to the intensity of the methyl side chain carbon signal (PP). Individual spectra are shifted vertically for better comparability. Exemplarily, the individual fits for the peaks in the spectra of the 3200 h weathered particles are shown as black lines.

Development of thermal characteristics for semi-crystalline PP and LDPE

Thermal characteristics of both semi-crystalline polymers (LDPE and PP) were investigated via differential scanning calorimetry (Figure 5, Table S5, Figure S4). The melting curves are given in Figure 5a, and Figure 5b. For LDPE, the melting curves in Figure 5a remain around the same T_m (106-108 °C) during the entire experimental duration, however the shape of the peak shows some changes with increasing weathering. In the curve of the reference sample, a small shoulder is visible at lower temperatures, between 50-70 °C. This shoulder indicates smaller crystallites with lower T_m. With increasing weathering, the shoulder slowly shifts to higher values, indicated by the black arrow in Figure 5a. Ultimately, this shoulder merges into the main melting peak, indicating growth of the smaller crystallites to larger ones with increasing outdoor exposure. This observation matches the development of crystallinity χc (Figure 5c), which increases in a linear manner over the exposure time frame of 1.5 years (36 – 53 %). For PP in b), the melting curves remain very similar within the first months (July-April), with a consistent melting temperature T_m of 164 °C (Table S5). The crystallinity shows a minor increase during this time frame, from 41 % to 52 %. From May on, the melting peak shifts to lower values, resulting in a lowering of T_m from 164 to 139 °C until the end of the experiment. The development of the crystallinity for PP is slightly more complex (Figure 5d). After the linear increase until May (52 %) a rapid increase in crystallinity by ~ 15 % was recorded from May to June (66 %), followed by an almost immediate decrease from July to September (66 % to 48 %) and a further decline down to 44 % at the end of the experiment.

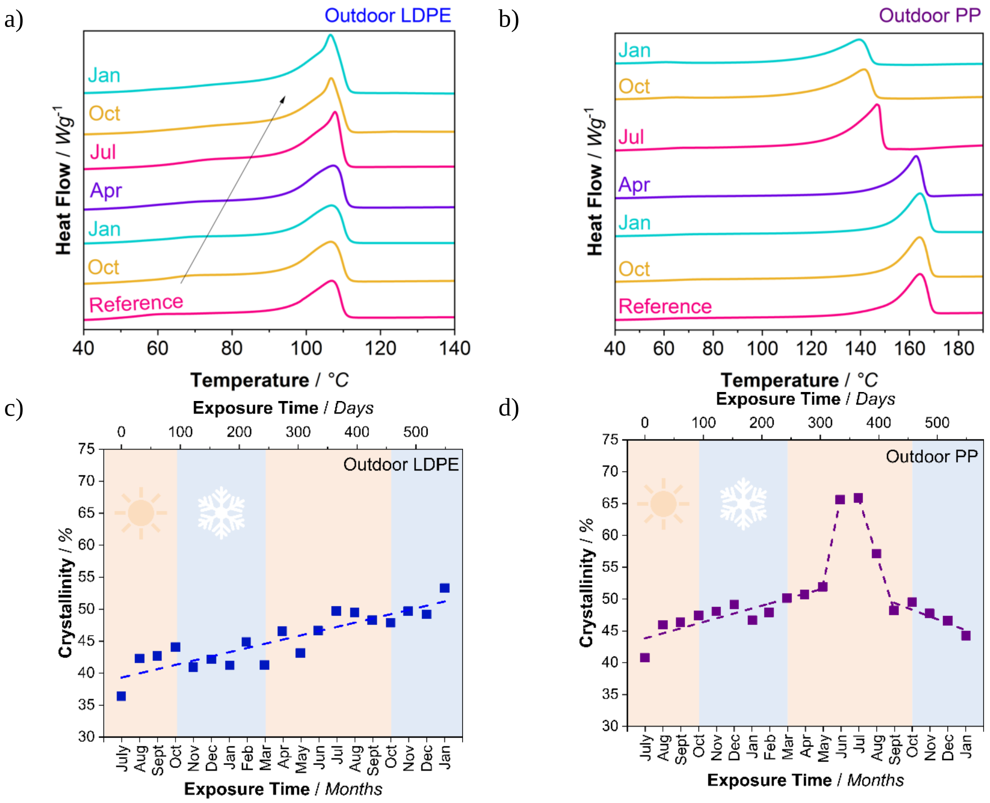

Figure 5 – Thermal characteristics for semi crystalline LDPE and PP. Heat flow vs. temperature in °C for chosen samples of a) LDPE and b) PP. Development of crystallinity χc as a function of exposure time for c) LDPE and d) PP.

Discussion

Correlation of the chain defects and thermal characteristics to the particle fragmentation

Comparing the data for the chain defects (MWD and M_n), the thermal properties (T_m and χc), to the particle fragmentation (particle size in µm) we can correlate the characteristics of each of the curves plotted in Figure 2, Figure 3, and Figure 5.

For PS, the turning point of fragmentation is from May-June, where the particle size decrease shifts from a linear to an exponential decrease (Figure 2a). This timing overlaps with the development of the molecular weight, which decreases in a linear manner, without showing distinct characteristics, but reaches a value below the critical MW (M_c) at the same time, as particles start to break up (Figure 3a). The M_c of PS is around 34 kg/mol (Dobkowski, 1995), which is reached between May (39 kg/mol) and June (33 kg/mol) in our study. Below M_c, the polymer chains are becoming too short for sufficient entanglement, enhancing embrittlement and break up. Chain scission is a result of photoinitiated degradation and subsequent radical reactions of polymers exposed to solar radiation at the presence of oxygen (Gewert et al., 2015). For PS particles, degradation and fragmentation can be correlated very well.

For LDPE particles, the particle size remains unchanged for almost one year, whereas the M_n continuously decreases and the crystallinity steadily increases (Figure 2b, Figure 3b, Figure 5c). As observed for PS, the initiation of fragmentation of LDPE coincides with the surpassing of M_c (M_w = ~ 70 kg/mol, Fayolle et al., 2007) in June ($M_{w\ (June)}$ = 60 kg/mol). From this point on, the particle size rapidly degrades, accompanied by a further decrease in molecular weight and an on-going increase in crystallinity. As previously mentioned, the MW of LDPE seems to be very dependent on the temperature. We attribute these observations to the temperature of our experiment, which is, on average, above the glass-transition temperature (T_g) of LDPE, which is < 0 °C (Han et al., 1994).

Above T_g, the molecular structure exhibits macromolecular mobility, facilitating chain movement and the reactions of macroradicals. Rearrangements of the chains thus lead to a 'healing' of potential crack-patterns (Bracco et al., 2018; Wool, 2008). Degradation primarily affects the amorphous domains (Hiejima et al., 2018), thus amorphous chains are cleaved and then rearrange in a preferably ordered manner, leading to an increase of crystallinity. With the tie-molecules declining, embrittlement and fragmentation are provoked. While for amorphous polymers, embrittlement is directly correlated to the critical MW (M_c), for semi-crystalline polymers, the lamellar thickness plays the more prominent role (Fayolle et al., 2008).

In the trends of PP, the molecular weight (Figure 2c) remains unchanged in the first months until the trend shifts from linear to exponential during winter. We attribute the initial stability within the MW (and the particle size) to the presence of stabilizers, as indicated by the manufacturer (LyondellBasell, 2021), and experimentally and analytically verified in a previous study (Meides et al., 2022). Once the stabilizers are consumed, degradation sets in rapidly, leading to an exponential decrease of the MW, despite the lower solar irradiance during winter. Meanwhile, the particle size is consistent for another few months until May (Figure 3c). At this state, the M_n is as low as 5000 g/mol and sunshine duration and radiation are higher (Figure 8). The degree of crystallinity slowly increases in the first 10 months until May (Figure 5b+d), indicating that the molecular chains rearrange while preserving the particle size and shape. Similarly, SEM images do not show any distinct signs of fragmentation, such as deep cracks (Figure S1e+l), unlike what was observed for PS. Here too, connections can be drawn to the T_g of PP (< 0 °C, Gitsas and Floudas, 2008). Once the MW has reached M_c ($M_{c\ (PP)}$ = < 7000 g/mol, Wool, 2008), no sufficient entanglement can be ensured, resulting in fragmentation and break-up ($M_{n\ (May)}$ = 5000 g/mol). As soon as fragmentation is initiated, the crystallinity shows a rapid increase (May-July). However, once the amorphous chains have been largely consumed, the crystalline domains and tie-molecules are also affected by degradation. This leads to a decrease in crystallinity and an even more pronounced break-up resulting from the reduction of tie-molecules (Grause et al., 2020). This effect is intensified between July and September. From this point on, the crystallinity decreases.

While we assume, that the influence of the stabilizer on the fragmentation of PP may be substantial (Meides et al., 2022), the LDPE system represents a polyolefin system without the external influence of stabilizers on degradation, and reflects the strong dependence of degradation on the temperature (e.g., Figure 3b). This matches a previous study by Fairbrother et al., 2019, who also report a strong temperature dependence on chemical changes during photodegradation of PE.

Correlation to accelerated, laboratory-controlled weathering – Particle characteristics

Comparing the surface characteristics of PS from outdoor weathering (Figure 1a-c) directly to the observations made in accelerated weathering (Figure 6, and Meides et al., 2021), the development of the particle characteristics is very comparable. Within the first stage of weathering, we observed smoothening of sharp edges and a rounding of the particles (Figure 6b). This first stage (stage I) of surface abrasion indicates, that UV irradiation affects the particles only from the surface. Within the first stage, only a thin layer is affected, leading to minor embrittlement, the peeling off of smaller flakes, and a rounding off from mechanical impact. Changes in molecular weight and particle size are small (linear trends, comp. Meides et al., 2021). With prolonged weathering, and UV irradiation reaching deeper layers, a further decrease in molecular weight (below M_c) leads to embrittlement, which ultimately triggers fragmentation in stage II. The particles break apart, forming a large number of secondary daughter particles.

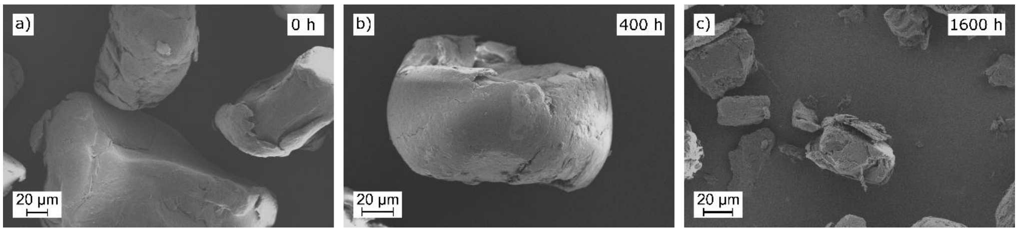

Figure 6 – Surface characteristics of PS particles from accelerated weathering a) of reference material, b) of a particle after 400 h and c) of particles after 1600 h (Meides et al., 2021).

The same observations apply to the semi-crystalline systems LDPE and PP. The developed model from accelerated weathering is also applicable to the results from outdoor weathering. For LDPE and PP, no dominant cracks are observable (Figure S1d-b), but rather larger flakes peeling off of the outer surface layer (surface cracking) which lead to disintegration of the individual particles.

Correlation to accelerated, laboratory-controlled weathering – Particle size, molecular weight and thermal characteristics

In order to compare the data from natural exposure to the data from accelerated weathering, the acceleration factor of 5.2, as calculated from the global irradiation for Central Europe (Figure S5, Table S6 and Meides et al., 2021), was used. The data from the Q-Lab chamber was decelerated with this factor and thus the *"actual"* exposure, under natural weathering conditions, was calculated. 2400 h of accelerated weathering should correspond to 1.5 years of outdoor weathering or 520 days, according to our calculations previously made (Figures S5, Table S6). The data trends correlate well, but the time scales show some deviations. Thus, we performed an adjustment of the acceleration factor for each polymer and plot, in order to draw conclusions on the actual acceleration of our weathering chamber.

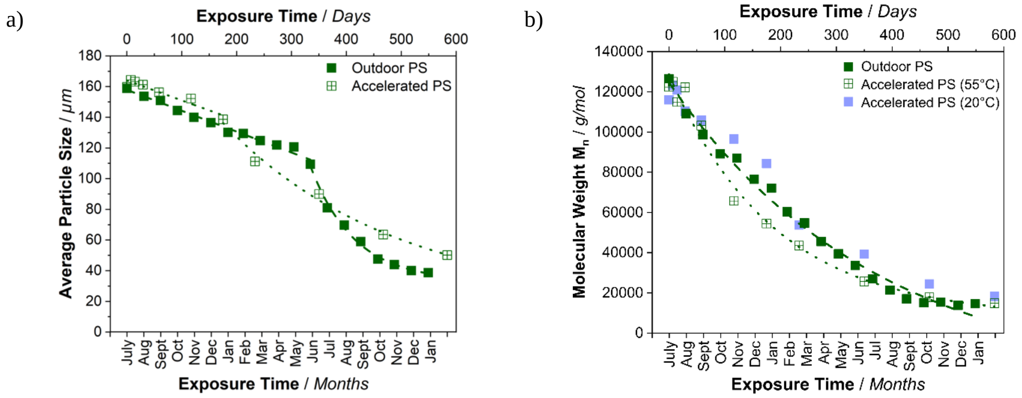

Figure 7 – a) Average particle size for outdoor PS (solid symbols) and accelerated PS (open symbols). b) Molecular weight M_n for outdoor PS and accelerated PS at 55 °C and at 20 °C. Both sets of data from accelerated weathering were decelerated by a factor of 7 relative to the outdoor setting, corresponding to a total of 583 days.

For PS, the outdoor data and the accelerated data (decelerated by a factor of 7) are given in Figure 7a for the particle size and Figure 7b for M_n. Using a deceleration of 7, both data sets overlap almost perfectly, especially the M_n. PS thus seems to show only a minor dependence on temperature and UV-intensity fluctuations of the seasons. We ascribe this to the high T_g of PS, which is at > 100 °C (Andrady, 2017). During the outdoor and the accelerated experiments, we are far below the T_g at all times, thus the molecular chains of PS are stiff, hampering molecular movement and rapid reactions (Shrivastava, 2018). Nevertheless, higher temperatures will still have a small effect on the reaction rate, especially given the large temperature deviation between the simulation chamber (55 °C) and winter temperatures (0 to – 20 °C, Figure 8b). This explains the discrepancy from a factor 5, which was calculated exclusively using the solar irradiance. The factor 7 considers all other influences, especially the temperature. An irradiation experiment within the same accelerated weathering chamber, but cooled to 20 °C with a cryostat, was run to investigate the actual T-dependence of PS photooxidative degradation (Table S7). The data reveals a slowing down of degradation during the first stage of weathering (0-600 h), on a long-term view however, the effect of a cooler temperature is negligible (Figure 7b). The extension of the linear first stage of weathering is more pronounced in Figure S7. Apart from the minor discrepancies, the evolution of chain defects for PS from all three experiments (outdoor, and accelerated at 55 °C, and 20 °C) overlap almost perfectly (Figure 7b).

For amorphous PS, the dominating degradation mechanism is the irradiation intensity, while other parameters, such as temperature, play only a secondary role. The dependence on certain parameters however, depends on the polymer type and varies between different polymer systems. For polyolefins (LDPE and PP), temperature plays a dominant role and thus has a stronger influence on the degradation rates.

For polyolefins in general, degradation is slightly more complex. Because they do not contain any chromophoric groups within their structure, they do not absorb UV irradiation, and are thus expected to be immune towards photo-initiated degradation. Nevertheless, they do degrade due to the presence of smaller impurities or structural abnormalities (Gewert et al., 2015). LDPE data from both sets show a decrease in molecular weight from the first sample on, accompanied by an increase in crystallinity. Because both experiments are constantly above their T_g, the molecular chains are mobile and inhibit fragmentation for a specific amount of time. With deceleration factors between 10-13, the data from both experiments can be correlated nicely.

For PP, we observe some stability during the first few months of outdoor exposure. The same characteristics are also observed within the data sets from accelerated, laboratory weathering, which we could attribute to the presence of the stabilizers Irgafos® 168 and Irganox® 1010, which inhibit degradation for a certain amount of time (Meides et al., 2022). As soon as degradation sets in, a rapid exponential decrease is observed in the particle size, and the molecular weight, accompanied by a drastic increase in crystallinity. With a deceleration factor of 13 for the development of the particle size and 19 for the molecular weight, not only the trends, but also the data correlate nicely (Figure S6). We attribute the higher deviation to the previously calculated acceleration factor of 5 (Table S6) to the strong temperature dependence of LDPE and PP on degradation.

The observations made for the development of chemical defects as a consequence of photooxidation in an outdoor setting, correlate well to the data obtained from laboratory-accelerated weathering. For PS, during accelerated weathering we were able to identify ketones, carboxylic acids, peroxides and alcohols (Mauel et al., 2022; Meides et al., 2021), for PP we observed ketones, carboxylic acids, peroxides and alcohols (Meides et al., 2022), and for LDPE carboxylic acids, vinylidenes as well as peroxides and alcohols (Menzel et al., 2022). The same functional groups could be observed after outdoor exposure, indicating that the mechanisms are equivalent. Only ketone defects are still below the detection limit after 1.5 years of outdoor weathering.

Weather data from the Botanical Garden, University of Bayreuth

In order to evaluate the influence of the different weathering parameters, which ultimately influence the degradation in an outdoor setting, we acquired weather data from the weather station located in the botanical garden at the University of Bayreuth. Values for the global irradiation in kWh/m^2 and the mean temperature in °C are given in Figure 8a and b. In addition, the consistent values from the accelerated weathering chamber are plotted in the same graphs. The global radiation is seasonally dependent, being highest in summer and lowest in winter. This also applies to the temperature. Not only is it coupled to the total sunshine duration (Figure S8a-b), which is lower in winter in the northern hemisphere, but also dependent on weather in general. On cloudy days, the irradiation is low, which will have an influence on the initiation reaction, requiring the energy of photons in the UV-A range (Singh and Sharma, 2008).

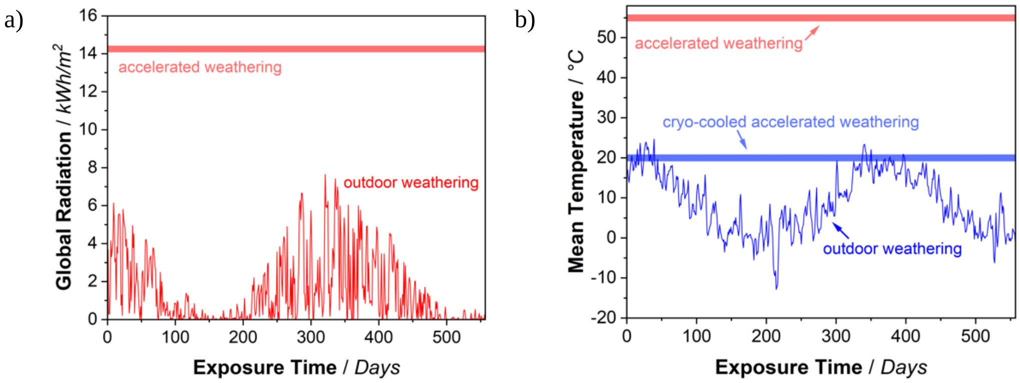

Figure 8 – Weather data from the Botanical Garden, University of Bayreuth. In a) the global radiation in kWh/m² is plotted with the average daily irradiation within the chamber (5-fold accelerated, as calculated using the global irradiation of Germany). In b) mean temperature values in °C are given for each day of exposure, along with the consistent chamber temperature from accelerated weathering (55 °C) and cryo-cooled accelerated weathering (20 °C).

Surprisingly, visible effects of the seasonal fluctuations in solar irradiance and temperature on the degradation of the three investigated polymers, are only clearly traceable within the degradation of LDPE (M_n in Figure 3b). For the other polymers, degradation proceeds in a continuous, but slower manner, with comparable trends to accelerated weathering.

Conclusion

We exposed particles from standard polymer grades of PS, PP, and LDPE to accelerated-controlled laboratory weathering in a Q-Sun Xe-3 test chamber for 3200 h, and performed similar experiments using the same polymer grades simultaneously in an outdoor setting for 1.5 years (567 days). According to our calculations, 3200 h of accelerated weathering correspond to 1.5 years of outdoor weathering (Central Europe).

Comparing outdoor weathering to accelerated weathering, the trends we observe for the evolution of the particle size, the molecular weight, as well as the trends for crystallinity and the development of functional groups, as a consequence of degradation, are very similar for both experimental setups. This observation applies to all three polymer systems: amorphous PS, and semi-crystalline PP and LDPE. We conclude from this, that the mechanisms of degradation are equivalent. This could be supported by solid-state ^{13}C NMR measurements, where ketones, carboxylic acids, peroxides, vinylidenes, and alcohols could be identified.

The most prominent difference between both setups are the time scales, which are not as comparable as the trends. Degradation proceeds slower for all three experiments from outdoor weathering, compared to laboratory weathering. The results clarify, that photooxidative degradation does not only depend on the irradiation intensity, and individual degradation parameters play a paramount role, here the temperature. The amorphous PS chains are immobile at our experimental temperatures, while LDPE and PP reveal a high chain mobility in the amorphous domains. The reaction rate of the propagation reactions is highly dependent on the individual polymer characteristics (e.g., amorphous or crystalline, T_g). The polymer characteristics are thus directly linked to the degradation rate.

Our study emphasizes that accelerated weathering is a very powerful and useful tool to study the environmental degradation of different polymer systems, and enables the simulation of degradation in reasonable time scales. For

PS, considering only the irradiation intensity gives a satisfactory fit for both data sets. For polyolefins (LDPE and PP) the situation is more complex, as also temperature plays an important role for the degradation rate. Generally, the degradation mechanisms are the same, as demonstrated by the identification of the same degradation products in accelerated and outdoor weathering.

Experimental

Materials

Commercially available polymer grades were purchased for the experiments in this study. PS (Styrolution PS 158N) pellets were manufactured by INEOS Styrolution Group (Frankfurt am Main, Germany), PP (Moplen HP526J) as well as LDPE (Lupolen 1800p) in pellet form was provided by LyondellBasell Industries (Basell Polyolefine GmbH, Wesseling, Germany). PS 158N is a standard PS type and contains no additives besides 600 ppm of zinc stearate, according to the manufacturer. LDPE is claimed to be free of additives, PP contains standard processing stabilizers which could recently be identified as Irgafos® 168 and Irganox® 1010 (Meides et al., 2022). All particles were produced by grinding of pellets via cryo-milling, using an ultra centrifugal Mill ZM-200 (Retsch GmbH, Haan, Germany). Particles were then separated into several fractions using an Alpine air jet sieve E200 LS (Hosokawa Alpine AG, Augsburg, Germany). For all experiments, the fraction between 125-200 µm was used.

Methods

Outdoor Weathering

For exposure to outdoor conditions, 20 g of each polymer powder was weighed into quartz glass beakers, 600 ml of deionized water added to the particles and the beaker was covered with a quartz glass lid. Stirring of the particle-water mixture was performed using magnetic stirring plates and PTFE-covered stirring devices, operating at 80 rounds per minute. All three beakers and stirring plates were placed on the roof outside of the Department of Macromolecular Chemistry I, building NWII on the university campus of the University of Bayreuth. All three experiments were continuously kept outside during the entire time frame between July 14th 2020 and January 21st 2022. The weathering conditions were continuously monitored by the weather station located in the ecological botanical gardens at the University of Bayreuth, which is located approximately 500 meters from our experimental setup. Temperature in °C, global irradiance in kWh/m^2, and total hours of sunlight were recorded and for each day an average value determined. These daily averages are plotted in Figure 8 and S8.

Samples were taken on a monthly basis, where 1-2 g of particles were extracted from the particle-water mixture, filtered with a suction filter and dried at 40 °C under vacuum. Samples where then stored in a dark and dry place until further processing and analysis.

Accelerated Weathering

The data, materials, methods and the weathering protocols for accelerated weathering was previously published. The PS data is published in Meides et al., 2021, the LDPE data in Menzel et al., 2022, and the PP data in Meides et al., 2022. The same polymer grades, particle production, size range and quantities were used, as described above for the outdoor weathering experiments. The weathering setting is described in the upcoming paragraph.

Cryo-cooled Accelerated Weathering

For the cryo-cooled experimental setup, double-wall beakers were purchased from proQuarz (proQuarz GmbH, Mainz, Germany) and connected to a Julabo F32 cryostat (Julabo Labortechnik GmbH, Seelbach, Germany) set to 20 °C. Circulation of 20 °C-water at all times allowed for a sample temperature of ~ 20 °C as well. This setup was placed into a Q-SUN XE-3 test chamber (Q-LAB Corporation, Westlake, OH, USA) and exposed to simulated solar radiation for 3200 h. This chamber is equipped with three xenon lamps, operating at 60 W/m^2 each (at 300-400 nm), and Daylight-Q filter systems. This assures an irradiation spectrum very similar to the spectrum of natural sunlight, and corresponds to a total irradiance of 594 W/m^2 (300-800 nm) and a ~5-fold acceleration compared to Mid-European Conditions (Figure S5, Table S6). Additional settings were relative humidity at 50 % and chamber temperature at 38 °C.

At each sampling time (24, 50, 100, 200, 400, 600, 800, 1200, 1600, 2000, 2400, 2800 and 3200 h), 1-2 g of sample material was taken from the water-sample mixture, filtered and dried as described above.

Particle Size Analysis

Particle size distributions and the average particle size were determined with a Microtrac FlowSync Particle Size Analyzer (Microtrac Retsch GmbH, Haan, Germany) having a lower detection limit of 10 nm. Measurements were performed in deionized water with 2-5 mg of particles. 2 ml of 5 wt.-% $Na_4P_2O_7$, and a few drops of a 2 wt.-% detergent were added. For PS, Tween®20 was used, for PP and LDPE, dioctyl sulfosuccinate sodium salt detergent was added. Then, 60 seconds of ultrasound at 40 kHz were applied to avoid aggregation. Average values from three measurements were calculated by the Microtrac Software.

Gel Permeation Chromatography, GPC (PS)

Measurements of the MWD, M_n, M_w, and Đ values were performed via GPC using a Waters gel permeation chromatography set equipped with a 515 HPLC Pump, 2707 Autosampler, 2414 Refractive Index Detector and 2998 Photodiode Array Detector (Waters GmbH, Eschborn, Germany). The column set consisted in a guard column (ResiPore Guard, 5 x 0.75 cm, particle size 3 µm) and two separation columns (ResiPore Guard, 30 x 0.75 cm, particle size 3 µm). Tetrahydrofuran (THF) was used as the mobile phase and calibration was performed using narrow distributed PS standards. A sample volume of 100 µl (1 mg/ml) was measured with a flow rate of 0.5 ml/min at ca. 30 °C. 1,2-dichlorobenzene was used as internal standard.

High Temperature GPC (PP, LDPE)

MWD of semi-crystalline polymers (PP, LDPE) were measured using an Agilent (Polymer Laboratories Ltd.) PL-GPC 220 high-temperature chromatographic unit. This set is equipped with RI and PD detectors as well as three linear mixed bed and guard columns (Olexis). Analysis was performed at 150 °C (Pasch, 2001) using 1,2,4-trichlorobenzene (TCB) as the mobile phase. All samples were prepared by dissolving 2-3 mg of PP particles (0.1 wt.-%) in 1.5 ml of the mobile phase solvent (TBC) in an external oven at 150 °C upon continuously stirring. The solutions were run without filtration. The determined molecular weights were referenced to linear HDPE standards (M_w = 142,000 – 701,000 g/mol, K = 40,600, and Alpha = 0.725) and were corrected with K and Alpha values for i-PP (K = 19,000 and Alpha = 0.725).

Differential Scanning Calorimetry (DSC)

DSC measurements were performed on 8-10 mg sample material using a Mettler Toledo DSC 3+ (Mettler-Toledo GmbH, Gießen, Germany). The samples were heated with 10 K per minute under N_2-atmosphere from 25-200 °C and cooled to 25 °C. An isothermal stage of 5 min was applied between the heating and the cooling cycle. The degree of crystallinity χ_c in the first heating cycle was determined using ΔH_m^0= 207.1 J/g for a hypothetically 100 % crystalline PP, and ΔH_m^0= 293.7 J/g for LDPE (Ojeda et al., 2011). Determination of χ_c and T_m was performed using the STARe software.

Scanning Electron Microscopy (SEM)

Field-emission scanning electron microscopy (FESEM) was performed on particles with a Zeiss ULTRA PLUS (Carl Zeiss Microscopy GmbH, Jena, Germany) at an acceleration voltage of 3 kV and a FEI Quanta 250 (Field Electron and Ion Company, Thermo Fisher Scientific, Hillsboro, USA) high resolution field emission gun (FEG) scanning electron microscope at 10 kV, operating at low vacuum. Particles were coated with a thin layer of platinum by a Cressington 208 HR sputter coater prior to investigation.

NMR Spectroscopy

All ^{13}C CP MAS NMR spectroscopic experiments were acquired with a Bruker Avance-III HD spectrometer operating at a B_0 field of 9.4 T. The ^{13}C (ν_0 = 100.6 MHz) MAS NMR spectra were obtained with a ramped ^{1}H-^{13}C CP experiment using a commercial 3.2 mm triple resonance probe (Bruker). The spectra were recorded with a spinning frequency of 20 kHz and a contact time of 2.0 ms. The corresponding nutation frequency υ_{nut} for the ^{13}C channel was set to 50 kHz while for the ^{1}H channel the nutation frequency was varied linearly from 26 kHz to 53 kHz. During acquisition, proton broadband decoupling with a spinal-64 sequence (υ_{nut} (^{1}H) = 70 kHz) was applied. All ^{13}C NMR spectra were referenced to tetramethylsilane (TMS) using the secondary standard adamantane. The spectra were deconvoluted with the simulation package SOLA included in Topspin 3.6. To obtain quantitative spectral intensities, we used a multi-pulse CP sequence. For this sequence, several CP blocks ((PS: contact time 250 µs (7 loops), PP: contact time 400 µs (6 loops), PE: contact time 500 µs (6 loops)) are applied, separated by a time t_z of 3 s to allow for the proton spins to relax. The (90°)-x pulses at the end and the beginning of each CP block were set to 2.5 µs (^{1}H) and 3.8 µs (^{13}C).

Authors' contributions

N.M. performed outdoor weathering of all three particle experiments, accelerated, the cryo-cooled weathering experiment, particle size analysis, GPC, and DSC measurements. A.M. performed solid-state NMR spectroscopic measurements. W.B. provided the data from the weather station of the botanical garden UBT. N.M. wrote the first draft of the manuscript, A.M., T.M., H.R., V.A., P.S. and J.S. supported the discussion and finalization of the manuscript. All authors read and approved the final version of the manuscript.

Acknowledgements

The authors would like to thank Lisa Weber and Martina Fried for particle preparation, Dr. Winfried Kretschmer for HT GPC analysis, Martina Heider and Ulrich Mansfeld for SEM measurements, and Alexander Kern for help with the setup.

References

Al-Salem SM. Influence of natural and accelerated weathering on various formulations of linear low density polyethylene (LLDPE) films. Materials & Design 2009;30(5):1729–36.

Andrady AL. The plastic in microplastics: A review. Marine pollution bulletin 2017;119(1):12–22.

Andrady AL, Koongolla B. Degradation and Fragmentation of Microplastics. In: Plastics and the Ocean: John Wiley & Sons, Ltd; 2022. p. 227–268.

Assink RA, Celina M, Dunbar TD, Alam TM, Clough RL, Gillen KT. Analysis of hydroperoxides in solid polyethylene by MAS 13C NMR and EPR. Macromolecules 2000;33(11):4023–9.

Bishop G, Styles D, Lens PNL. Recycling of European plastic is a pathway for plastic debris in the ocean. Environment International 2020;142:105893.

Bracco P, Costa L, Luda MP, Billingham N. A review of experimental studies of the role of free-radicals in polyethylene oxidation. Polymer degradation and stability 2018;155:67–83.

Brooks AL, Wang S, Jambeck JR. The Chinese import ban and its impact on global plastic waste trade. Science advances 2018;4(6):eaat0131.

Chabira SF, Sebaa M, G'sell C. Influence of climatic ageing on the mechanical properties and the microstructure of low-density polyethylene films. Journal of applied polymer science 2008;110(4):2516–24.

Dobkowski Z. Determination of critical molecular weight for entangled macromolecules using the tensile strength data. Rheola Acta 1995;34(6):578–85.

Eerkes-Medrano D, Thompson RC, Aldridge DC. Microplastics in freshwater systems: a review of the emerging threats, identification of knowledge gaps and prioritisation of research needs. Water Research 2015;75:63–82.

Fairbrother A, Hsueh H-C, Kim JH, Jacobs D, Perry L, Goodwin D et al. Temperature and light intensity effects on photodegradation of high-density polyethylene. Polymer degradation and stability 2019;165:153–60.

Fayolle B, Colin X, Audouin L, Verdu J. Mechanism of degradation induced embrittlement in polyethylene. Polymer degradation and stability 2007;92(2):231–8.

Fayolle B, Richaud E, Colin X, Verdu J. Review: degradation-induced embrittlement in semi-crystalline polymers having their amorphous phase in rubbery state. J Mater Sci 2008;43(22):6999–7012. https://link.springer.com/article/10.1007/s10853-008-3005-3.

Frias J, Nash R. Microplastics: Finding a consensus on the definition. Marine pollution bulletin 2019;138:145–7.

Gewert B, Plassmann MM, MacLeod M. Pathways for degradation of plastic polymers floating in the marine environment. Environmental science: processes & impacts 2015;17(9):1513–21.

Gijsman P, Hennekens J, Janssen K. Comparison of UV Degradation of Polyethylene in Accelerated Test and Sunlight. In: Advances in Chemistry. Washington, DC: American Chemical Society; 1996. p. 621–636.

Gitsas A, Floudas G. Pressure Dependence of the Glass Transition in Atactic and Isotactic Polypropylene. Macromolecules 2008;41(23):9423–9.

Grause G, Chien M-F, Inoue C. Changes during the weathering of polyolefins. Polymer degradation and stability 2020:109364.

Han J, Gee RH, Boyd RH. Glass transition temperatures of polymers from molecular dynamics simulations. Macromolecules 1994;27(26):7781–4.

Hartmann NB, Hüffer T, Thompson RC, Hassellöv M, Verschoor A, Daugaard AE et al. Are we speaking the same language? Recommendations for a definition and categorization framework for plastic debris. Environmental Science & Technology 2019;53(3):1039–47. 10.1021/acs.est.8b05297.

Hiejima Y, Kida T, Takeda K, Igarashi T, Nitta K. Microscopic structural changes during photodegradation of low-density polyethylene detected by Raman spectroscopy. Polymer degradation and stability 2018;150:67–72.

Hill G, Moreira C, Huynh F, Trufasila A, Ly F, Lloyd R et al. Correlation of a Temperate UV-Weathering Cycle to Outdoor Exposure for the Determination of the Environmental Instability of Polyethylene Films Using HT-GPC Analysis. Polymers 2021;13(4):591. https://www.mdpi.com/1000422.

Hronský V, Koval'aková M, Vrábel P, Uhrínová M, Olčák D. Estimation of the Degree of Crystallinity of Partially Crystalline Polypropylenes Using 13 C NMR. Acta Physica Polonica, A 2014;125(6).

Jambeck JR, Geyer R, Wilcox C, Siegler TR, Perryman M, Andrady A et al. Marine pollution. Plastic waste inputs from land into the ocean. Science 2015;347(6223):768–71.

Lv Y, Huang Y, Yang J, Kong M, Yang H, Zhao J et al. Outdoor and accelerated laboratory weathering of polypropylene: A comparison and correlation study. Polymer degradation and stability 2015;112:145–59.

LyondellBasell. Technical Data Sheet Lupolen 1800P: Low Density Polyethylene, 2021. https://productsafety.lyondellbasell.com/DirectRequest?ResponseTypeGuid=f1e32c20-d810-4db0-b25e-8e23a59f3733&ProductGuid=28be098e-bb34-4bb8-a683-894ea1c1751e.

Mauel A, Pötzschner B, Meides N, Siegel R, Strohriegl P, Senker J. Quantification of photooxidative defects in weathered microplastics using 13 C multiCP NMR spectroscopy. RSC Adv. 2022;12(18):10875–85. https://pubs.rsc.org/en/content/articlehtml/2022/ra/d2ra00470d.

Meides N, Mauel A, Menzel T, Altstädt V, Ruckdäschel H, Senker J et al. Quantifying the fragmentation of polypropylene upon exposure to accelerated weathering. Microplastics and Nanoplastics 2022;2(1):23.

Meides N, Menzel T, Poetzschner B, Löder MGJ, Mansfeld U, Strohriegl P et al. Reconstructing the Environmental Degradation of Polystyrene by Accelerated Weathering. Environmental Science & Technology 55 2021(12):7930–8. 10.1021/acs.est.0c07718.

Menzel T, Meides N, Mauel A, Mansfeld U, Kretschmer W, Kuhn M et al. Degradation of low-density polyethylene to nanoplastic particles by accelerated weathering. Science of the Total Environment 2022(826):154035. https://www.sciencedirect.com/science/article/pii/S0048969722011275.

Moreira C, Lloyd R, Hill G, Huynh F, Trufasila A, Ly F et al. Temperate UV-Accelerated Weathering Cycle Combined with HT-GPC Analysis and Drop Point Testing for Determining the Environmental Instability of Polyethylene Films. Polymers 2021;13(14).

Mowery DM, Assink RA, Derzon DK, Klamo SB, Clough RL, Bernstein R. Solid-state 13C NMR investigation of the oxidative degradation of selectively labeled polypropylene by thermal aging and γ-irradiation. Macromolecules 2005;38(12):5035–46.

Mowery DM, Clough RL, Assink RA. Identification of oxidation products in selectively labeled polypropylene with solid-state 13C NMR techniques. Macromolecules 2007;40(10):3615–23.

Ojeda T, Freitas A, Birck K, Dalmolin E, Jacques R, Bento F et al. Degradability of linear polyolefins under natural weathering. Polymer degradation and stability 2011;96(4):703–7.

Pasch H. Recent developments in polyolefin characterization. Macromol. Symp. 2001;165(1):91–8.

Qin J, Jiang J, Tao Y, Zhao S, Zeng W, Shi Y et al. Sunlight tracking and concentrating accelerated weathering test applied in weatherability evaluation and service life prediction of polymeric materials: A review. Polymer Testing 2021;93:106940.

Shrivastava A, editor. Introduction to Plastics Technology. Saint Louis: William Andrew; 2018.

Singh B, Sharma N. Mechanistic implications of plastic degradation. Polymer degradation and stability 2008;93(3):561–84.

Statista. Industries & Markets, Plastic waste in Europe: Statista Dossier on plastic waste in Europe, 2021. https://www.statista.com/study/56285/plastic-waste-in-europe/.

Wool RP. Self-healing materials: a review. Soft Matter 2008;4(3):400–18.

Zweifel H. Principles of oxidative degradation. In: Stabilization of Polymeric Materials: Springer; 1998. p. 1–40.

8.4.1 Supplementary Material: Environmental degradation of polystyrene, polyethylene, and polypropylene - a comparison of natural and accelerated weathering.

Environmental degradation of polystyrene, polyethylene, and polypropylene - a comparison of natural and accelerated weathering

Nora Meides,[1] Anika Mauel,[2] Teresa Menzel,[3] Wolfgang Babel,[4] Jürgen Senker,[2] Volker Altstaedt,[3] Holger Ruckdäschel,[3] Peter Strohriegl[1,*]

[1] Department of Macromolecular Chemistry I, University of Bayreuth, Universitätsstraße 30, 95447 Bayreuth, Germany

[2] Department of Inorganic Chemistry III, University of Bayreuth, Universitätsstraße 30, 95447 Bayreuth, Germany

[3] Department of Polymer Engineering, University of Bayreuth, Universitätsstraße 30, 95447 Bayreuth, Germany

[4] Micrometeorology Group, University of Bayreuth, Universitätsstraße 30, 95447 Bayreuth, Germany

* Corresponding author: peter.strohriegl@uni-bayreuth.de

List of Figures

List of Tables

Results

Surface Characteristics

Polystyrene

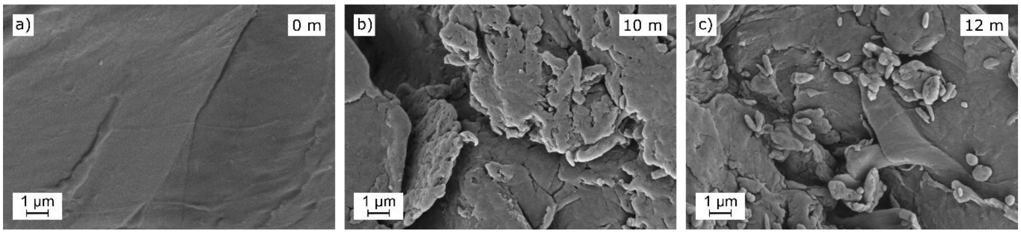

LD-Polyethylene

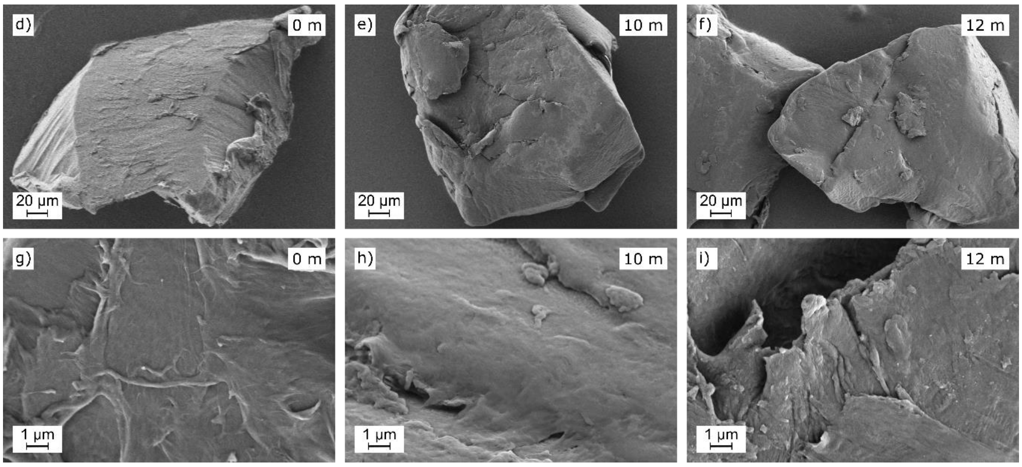

Polypropylene

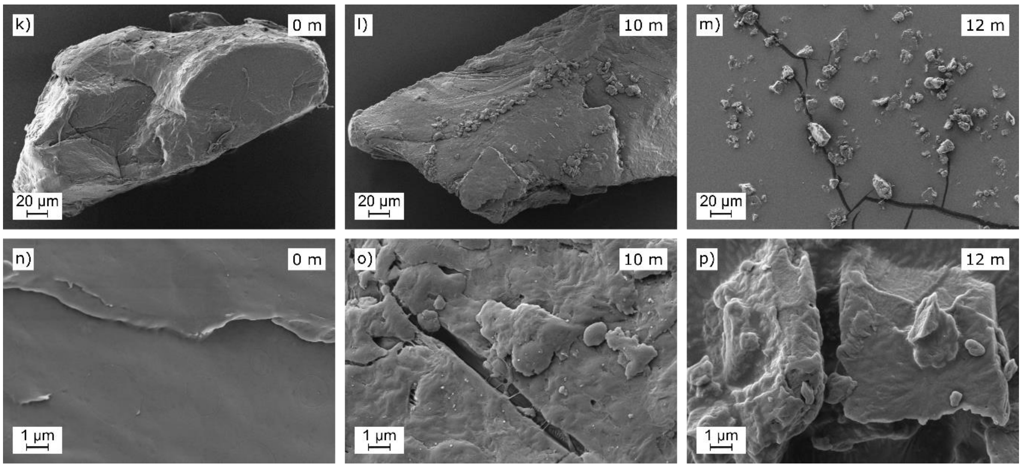

*Figure **S1.** SEM images of PS (a-c), LDPE (d-i) and of PP (k-p) at different magnifications.*

Average Particle Size and Particle Size Distributions

*Table **S1.** Average particle size values for each exposure time in months and days for polystyrene (green), low-density polyethylene (blue), and polypropylene (purple).*

Exposure Time			**Average Particle Size**		
Month	**Months**	**Days**	**Polystyrene**	**LD-Polyethylene**	**Polypropylene**
			µm	*µm*	*µm*
July	0	0	158.9	195.7	196.9
Aug	1	31	153.7	191.2	195.5
Sept	2	61	151.0	195.1	198.5
Oct	3	92	144.4	194.3	196.0
Nov	4	122	140.0	195.9	195.1
Dec	5	153	136.5	198.3	195.2
Jan	6	184	130.2	195.2	193.0
Feb	7	212	129.5	202.4	187.7
Mar	8	243	124.8	202.7	184.7
Apr	9	273	122.0	196.2	181.9
May	10	304	120.7	187.0	168.1
Jun	11	334	109.4	187.2	64.4
Jul	12	365	81.0	170.2	8.4
Aug	13	396	69.7	149.4	6.1
Sept	14	426	59.0	105.8	6.0
Oct	15	457	47.6	78.2	4.5
Nov	16	487	44.0	64.7	4.9
Dec	17	518	40.1	57.2	3.9
Jan	18	549	38.7	50.6	3.7

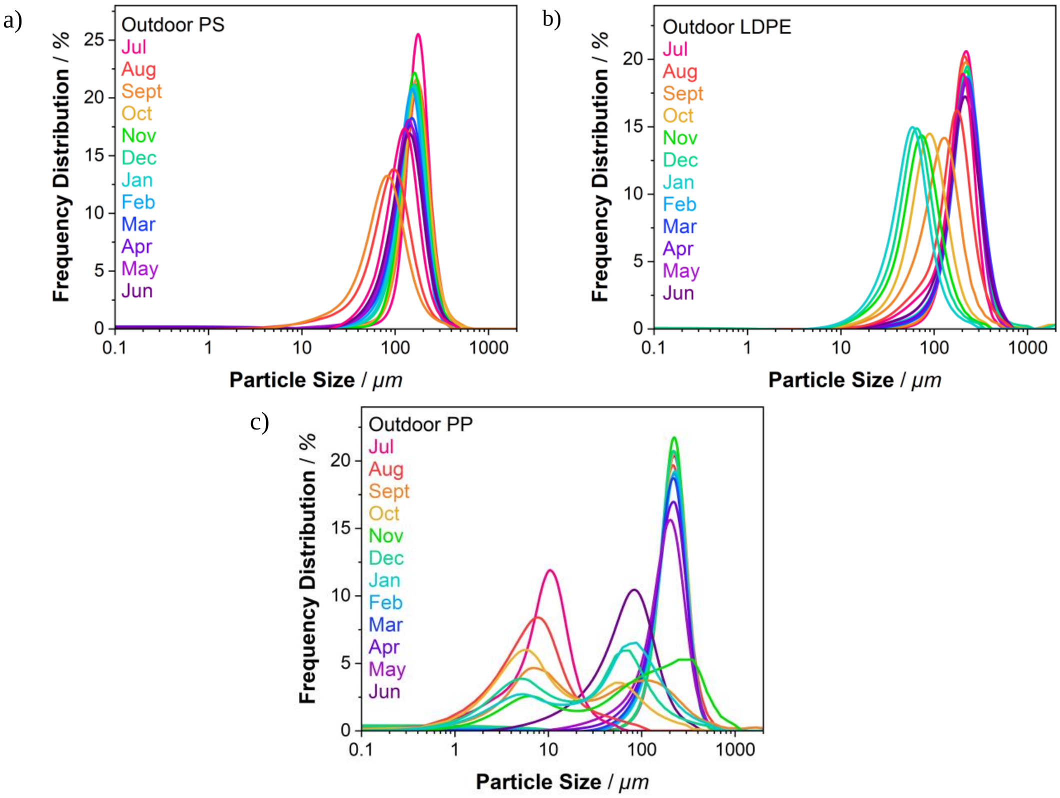

Figure ***S2.*** *Particle size distributions for a) outdoor PS, b) outdoor LDPE and c) outdoor PP. The bimodal distribution in c) is due to agglomeration effects as a consequence of very small particle sizes and their large surface-to-volume ratio.*

Molecular Weight Data

Table ***S2.*** *Number-average (M_n), weight-average (M_w), and peak (M_p) molecular weights in g/mol, and dispersity (Đ) values for PS.*

Polystyrene						
Exposure Time			**M_n**	**M_w**	**M_p**	**Đ**
Month	**Months**	**Days**	*g/mol*	*g/mol*	*g/mol*	
July	0	0	126500	263600	224600	2.1
Aug	1	31	109200	253300	201900	2.3
Sept	2	61	98700	241300	189000	2.4
Oct	3	92	89200	231900	176300	2.6
Nov	4	122	87000	229300	166600	2.6
Dec	5	153	76500	228000	167800	3.0
Jan	6	184	72100	211200	149100	2.9
Feb	7	212	60400	190600	137100	3.2
Mar	8	243	54800	186500	131800	3.4
Apr	9	273	45600	181200	122800	4.0
May	10	304	39400	165400	107600	4.2
Jun	11	334	33700	144300	88600	4.3
Jul	12	365	27000	120900	73500	4.5
Aug	13	396	21400	101400	61600	4.8
Sept	14	426	17000	90400	53400	5.3
Oct	15	457	15100	77200	46200	5.1
Nov	16	487	15400	87800	51300	5.7
Dec	17	518	13900	84300	48800	6.1
Jan	18	549	14700	82600	48300	5.6

Table ***S3.*** *Number-average (M_n), weight-average (M_w), and peak (M_p) molecular weights in g/mol, and dispersity (Đ) values for LDPE.*

Low-density Polyethylene						
Exposure Time			**M_n**	**M_w**	**M_p**	**Đ**
Month	**Months**	**Days**	*g/mol*	*g/mol*	*g/mol*	
July	0	0	29700	362100	131600	12.2
Aug	1	31	24000	203400	79400	8.5
Sept	2	61	15500	138700	56700	8.9
Oct	3	92	15700	167600	58800	10.7
Nov	4	122	14300	158400	54600	11.1
Dec	5	153	12600	159400	53600	12.0
Jan	6	184	13700	143500	52700	10.5
Feb	7	212	13400	124600	51700	9.3
Mar	8	243	14100	126500	49900	9.0
Apr	9	273	12000	120900	44700	10.1
May	10	304	11200	82600	23800	7.4
Jun	11	334	9500	56700	19200	6.0
Jul	12	365	7500	44200	16500	6.0
Aug	13	396	6300	31300	16300	5.0
Sept	14	426	5600	25000	14100	4.5
Oct	15	457	5100	21900	13200	4.3
Nov	16	487	5000	20300	13600	4.1
Dec	17	518	4900	21700	13000	4.5
Jan	18	549	5000	22900	13800	4.5

*Table **S4.** Number-average (M_n), weight-average (M_w), and peak (M_p) molecular weights in g/mol, and dispersity (Đ) values for PP.*

Polypropylene						
Exposure Time			**M_n**	**M_w**	**M_p**	**Đ**
Month	**Months**	**Days**	*g/mol*	*g/mol*	*g/mol*	
July	0	0	67300	818400	315000	12.2
Aug	1	31	66400	729500	296200	11.0
Sept	2	61	70300	744300	315000	10.6
Oct	3	92	66900	685500	273100	10.2
Nov	4	122	67300	657800	302400	9.8
Dec	5	153	66300	537000	284400	8.1
Jan	6	184	58400	445500	246900	7.6
Feb	7	212	44800	312200	186900	7.0
Mar	8	243	34100	197800	122200	5.8
Apr	9	273	8600	39900	36100	4.7
May	10	304	5400	19400	12400	3.6
Jun	11	334	3100	7400	4300	2.4
Jul	12	365	2200	4000	3500	1.9
Aug	13	396	1900	3100	2000	1.6
Sept	14	426	1700	2800	1900	1.6
Oct	15	457	1700	2600	1900	1.6
Nov	16	487	1600	2600	1900	1.6
Dec	17	518	1500	2500	1900	1.7
Jan	18	549	1600	2700	1900	1.7

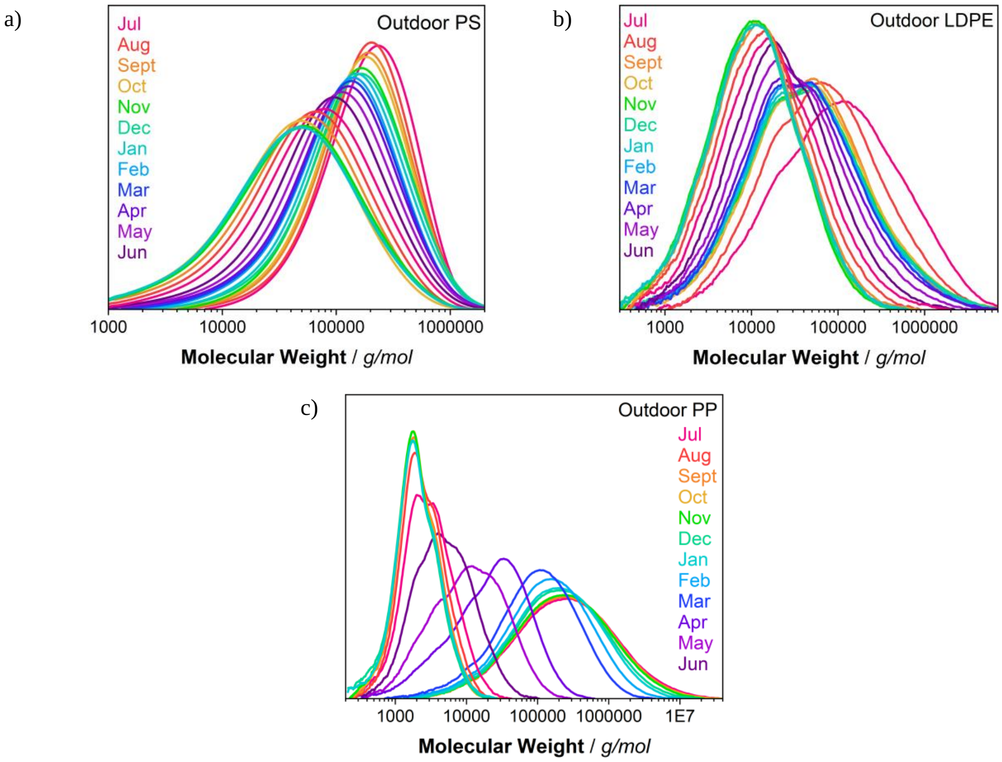

*Figure **S3.** Molecular weight distributions for the different months of exposure from a) outdoor PS, b) outdoor LDPE and c) outdoor PP.*

Thermal Characteristics

Table ***S5.*** *Thermal characteristics (crystallinity χc in % and melting temperature T_m in °C) determined for LDPE and PP via DSC measurements.*

			low-density Polyethylene		Polypropylene	
Exposure Time			Crystallinity χc	Melting Temp. T_m	Crystallinity χc	Melting Temp. T_m
Month	**Months**	**Days**	*%*	*°C*	*%*	*°C*
July	0	0	36	107	41	164
Aug	1	31	42	107	46	164
Sept	2	61	43	107	46	164
Oct	3	92	44	107	47	164
Nov	4	122	41	107	48	164
Dec	5	153	42	107	49	164
Jan	6	184	41	107	47	164
Feb	7	212	45	107	48	164
Mar	8	243	41	107	50	164
Apr	9	273	47	107	51	163
May	10	304	43	108	52	158
Jun	11	334	47	108	66	150
Jul	12	365	50	108	66	147
Aug	13	396	50	107	57	144
Sept	14	426	48	107	48	144
Oct	15	457	48	107	50	142
Nov	16	487	50	106	48	140
Dec	17	518	49	107	47	139
Jan	18	549	53	107	44	139

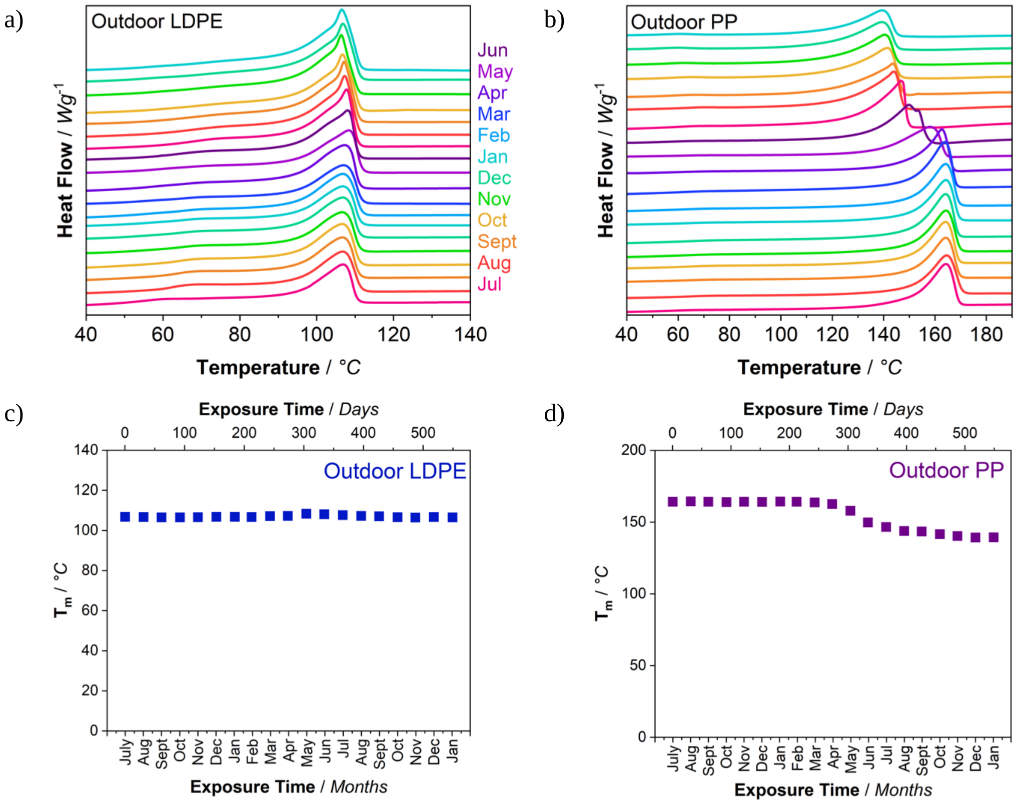

*Figure **S4**. Heat flow in W/g vs. temperature in °C from all months of exposure for a) outdoor LDPE and b) outdoor PP. T_m in °C for all months of exposure for c) outdoor LDPE and d) outdoor PP.*

Calculation of Acceleration factor

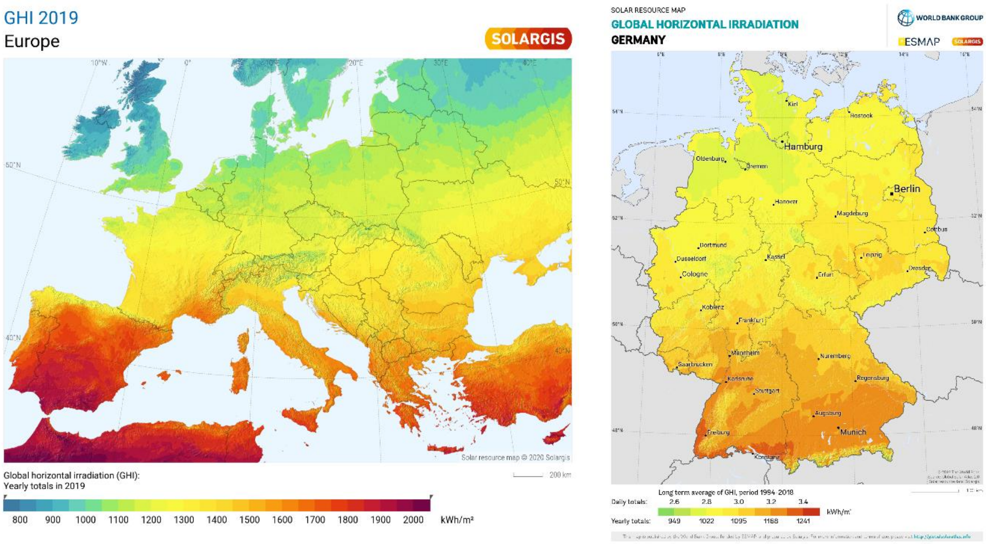

*Figure **S5.** Global horizontal irradiation for Europe and for Germany in kWh/m^2 for 2019. Source: SOLARGIS.*

*Table **S6**. Calculation of total irradiance in the Q-SUN Xe-3 chamber.*

Calculation of total irradiance in Q-SUN Xe-3 chamber		
Lamp settings*[1]	60	W/m^2
Calculation factor*[2]	9.9	
Total irradiance in Q-SUN Xe-3 chamber	594	W/m^2
Acceleration factor of Q-SUN Xe-3 chamber compared to Central Europe		
Solar irradiance per year*[3]	1000	kWh/m^2
Hours per year	8765	h
Solar irradiance	114	W/m^2
Acceleration factor of Q-SUN Xe-3 chamber*[4]	5.2	-

*[1] *measured in the wavelength interval from 300 to 400 nm*

*[2] *calculation factor converting the irradiance from 300 to 400 nm to the whole emission range of the Xenon lamp (300 – 800 nm). Extracted from Q-Sun Irradiance Conversion Sheet provided by Q-Lab Germany*

*[3] *value was derived from Figure S1 for the longitude of Central Europe*

*[4] *this value was calculated by division of the total irradiance in the Q-Sun Xe-3 chamber (594 W/m^2) by the solar irradiance determined for Central Europe (114 W/m^2)*

Correlating particle size, molecular weight and thermal characteristics to accelerated-laboratory weathering

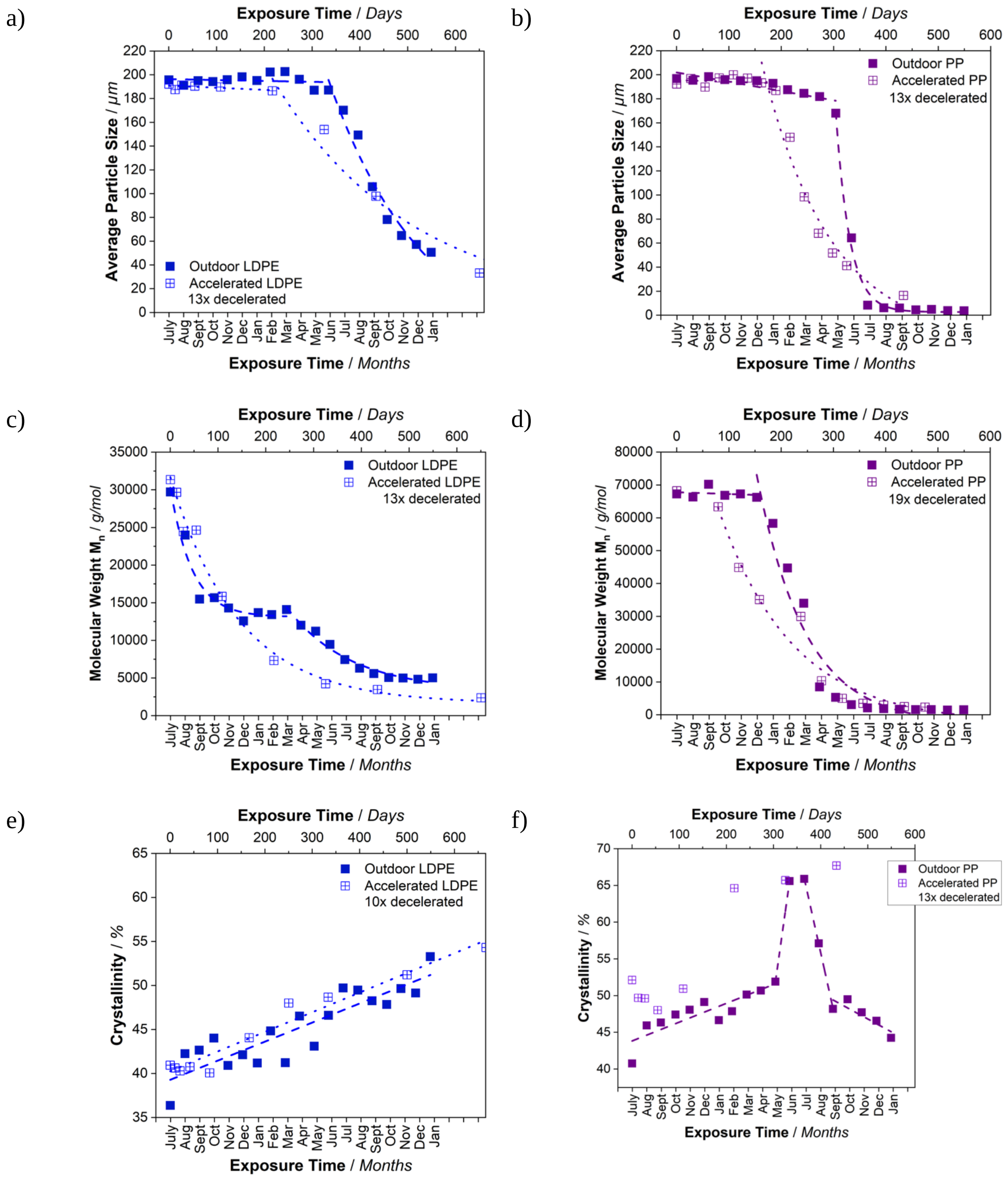

*Figure **S6.** a)-b) Average particle size, b)-c) molecular weight M_n, and e)-f) degree of crystallinity for outdoor and accelerated LDPE and PP. Outdoor data: solid symbols, accelerated data: open symbols. Both sets of data from accelerated weathering were decelerated relative to the outdoor setting, by a factor given within each graphic.*

Comparison of temperature-dependence of the degradation of PS

*Table **S7.** Molecular weight M_n in g/mol for PS from accelerated weathering, exposed at 20 °C and at 55 °C. The exposure time was decelerated by a factor of 7.*

Exposure Time		**PS at 20 °C**	**PS at 55 °C**
actual	**decelerated**	**M_n**	**M_n**
hours	*days*	*g/mol*	*g/mol*
0	0	116100	122400
24	7	123300	125100
50	15	120900	115000
100	29	110300	122300
200	58	105800	103300
400	117	96600	65800
600	175	84400	54500
800	233	53800	43500
1200	350	39400	25700
1600	467	24500	17800
2000	583	18300	14800
2400	700	14200	8700
2800	817	11000	7900
3200	933		5500

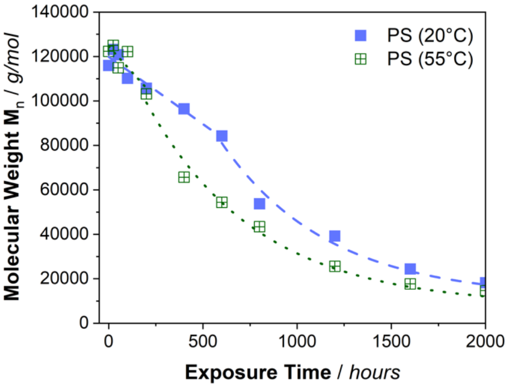

*Figure **S7**. Molecular weight (M_n) in g/mol for accelerated PS at 55 °C (green) and 20 °C (blue). For PS at 20 °C, the linear first stage of weathering is longer (0-600 h) than for the experiment at 55 °C (0-200 h). The long-term trends however evolve in the same manner. After 2000 h of exposure, the M_n is within the same range for both sample sets.*

Documentation of weather parameters from July 2020 – January 2022

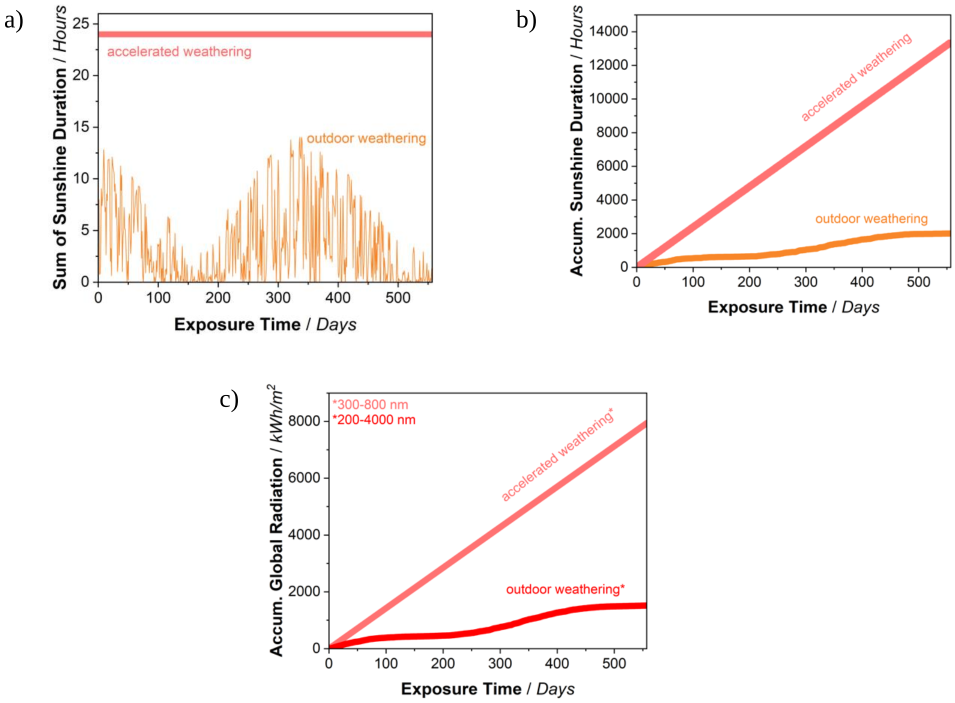

*Figure **S8.** Additional weather data from the Botanical Garden at the University of Bayreuth. a) Sum of the sunshine duration in hours as a function of exposure time in days, b) accumulated sunshine duration in hours and c) accumulated global irradiation in kWh/m^2 for accelerated-controlled laboratory weathering and outdoor weathering.*

8.5 Quantification of photooxidative defects in weathered microplastics using ^{13}C multiCP NMR spectroscopy.

RSC Advances

ROYAL SOCIETY OF CHEMISTRY

PAPER

Check for updates

Cite this: *RSC Adv.*, 2022, **12**, 10875

Quantification of photooxidative defects in weathered microplastics using ^{13}C multiCP NMR spectroscopy†

Anika Mauel, ‡[a] Björn Pötzschner,‡[a] Nora Meides,[b] Renée Siegel, [a]
Peter Strohriegl*[b] and Jürgen Senker *[a]

Received 22nd January 2022
Accepted 29th March 2022

DOI: 10.1039/d2ra00470d

rsc.li/rsc-advances

Weathering of microplastics made of commodity plastics like polystyrene, polypropylene and polyethylene introduces polar polymer defects as a result of photooxidation and mechanical stress. Thus, hydrophobic microplastic particles gradually become hydrophilic, consisting of polar oligomers with a significant amount of oxygen-bearing functional groups. This turnover continuously changes interactions between microplastics and natural colloidal matter. To be able to develop a better understanding of this complex weathering process, quantification of the corresponding defect proportions is a first and essential step. Using polystyrene, ^{13}C enriched at the α position to 23%, we demonstrate that ^{13}C cross polarisation (CP) NMR spectroscopy allows for probing the typical alcohol, peroxo, keto and carboxyl defects. Even the discrimination between in- and end-chain ketones, carboxylic acids and esters as well as ketal functions was possible. Combined with multiCP excitation, defect proportions could be determined with excellent accuracy down to 0.1%. For materials with ^{13}C in natural abundance, this accounts for a detection limit of roughly 1%. The best trade-off between measurement time and accuracy for the quantification of the defect intensities for multiCP excitation was obtained for CP block lengths shorter than 250 μs and total build-up times longer than 2 ms. Further measurement time reduction is possible by using multiCP excitation to calibrate intensities obtained from series of ^{13}C CP MAS NMR spectra. As photooxidation is an important degradation mechanism for microplastics in the environment, we expect these parameters to be transferable for probing defect proportions of weathered microplastics in general.

Introduction

Like for no other material class, polymer materials feature a uniquely broad range of applications due to their low production costs and favourable, easily adjustable properties. Meanwhile, plastic production reaches more than 350 million tons per year,[1] with more than half of this amount belonging to commodity plastics like polypropylene (PP), polyethylene (PE) and polystyrene (PS) for single-use applications.[1–4] Insufficient waste management causes large quantities of plastic materials to be released into the environment.[5] Once in the environment, plastic is expected to persist for ages due to its inherently high durability and chemical inertness. It accumulates and is intensely discussed to pose substantial risks for whole ecosystems.[6–9] In particular, small particles with dimensions in the micrometre regime are likely to be ingested by sea- and wildlife, inevitably entering the global food chain.[10,11] Such particles were defined as microplastic (MP), if their dimensions are smaller than 1 mm.[12] MP particles were found in substantial amounts in aquatic and terrestrial environmental compartments.[13,14]

Degradation of plastics in natural environments plays an important role in understanding the interaction of MP particles with their abiotic and biotic surroundings.[12,15,16] Starting from hydrophobic materials, the combination of fragmentation and photooxidation creates substantial numbers of chain scissions, polar defects and crosslinks.[17–19] Weathering gradually changes MP polymer chains to highly polar, heavily branched, medium-sized oligomers.[17] Polar and charged groups expressed on particle surfaces favour particle cell interactions and cellular responses,[20] as well as the formation of an ecocorona by adsorption of natural inorganic and organic colloidal particles[21,22] or by deposition of biofilms due to microbe activity.[23,24] This in turn enhances the uptake by microorganisms.[25,26] Considering that, *e.g.*, weathered PS MP particles accumulate hazardous peroxo groups with proportions of several per cent,[17] the uptake of weathered MP is likely to have negative effects on

---

[a] *Department of Inorganic Chemistry III, University of Bayreuth, Universitätsstraße 30, 95447 Bayreuth, Germany. E-mail: Juergen.senker@uni-bayreuth.de*

[b] *Department of Macromolecular Chemistry I, University of Bayreuth, Universitätsstraße 30, 95447 Bayreuth, Germany. E-mail: Peter.strohriegl@uni-bayreuth.de*

† Electronic supplementary information (ESI) available. See DOI: 10.1039/d2ra00470d

‡ These authors contributed equally to this work.

the organisms.[26,27] Additionally, the small particle sizes enable fast transport and thus a global distribution.[22,28–30]

The underlying degradation mechanisms of commodity plastics are meanwhile well understood.[2,3,17–19,31–33] PE, PP and PS consist of an aliphatic backbone and aliphatic or aromatic side chains. Light- and stress-induced radical formation in the presence of oxygen leads to (photo)oxidation, subsequent chain scissions and crosslinking (Fig. S4†).[18,34–36] As a consequence, a broad variety of functional groups is formed, with the most frequent ones being alcohols, peroxo units, aldehydes, keto groups, carboxy functions and vinyl units.[17,18,37–41] The individual defect proportions depend on several factors like chemical composition, solar and stress intensity, oxygen fugacity, salinity, temperature fluctuation and more. As the defect types vary in polarity and the ability to form charges as a function of the pH, a prediction of MP physicochemical properties and subsequent model building is not possible without quantifying the defect proportions.[17]

Typical defect proportions are on the order of a few per cent, which makes their quantification challenging.[17,18] In the past, mostly Fourier Transform Infrared (FTIR), Raman (Ra) and Nuclear Magnetic Resonance (NMR) spectroscopy were used for this purpose.[3,17,20,36,42,43] FTIR and Raman spectroscopy are very sensitive and are able to probe defect proportions down to a few per mill, if optimal conditions are reached.[3,41] Nevertheless, the detection limit for Ra spectroscopy is influenced by fluorescence.[41] FTIR spectroscopy is often used in a semiquantitative fashion by reporting a carbonyl index, which estimates the integral proportion of carbonyl-containing functional groups. Several methods are established to determine the carbonyl index, each leading to a range of possible values.[44] Especially, when the attenuated total reflection (ATR) technique is used, the results become surface dependent and require concentration-dependent calibration.[3,41] *E.g.*, for weathered LDPE particles, significantly higher carboxyl proportions were detected with FTIR spectroscopy compared to ^{13}C MAS NMR spectroscopy, which was attributed to a preferential accumulation of carboxyl groups close to the surfaces.[45] NMR spectroscopy is an element sensitive bulk method and can be used in a quantitative fashion.[46] If the samples are soluble, ^{1}H liquid-state NMR spectroscopy provides sufficient sensitivity.[42] Nevertheless, an unambiguous assignment is challenging, as most photooxidation defects consist of quaternary carbon atoms.[20,47] Using ^{13}C as probe instead, provides a better resolution, however, reduces the sensitivity and often requires labelling. Additionally, signal intensities are influenced by cross relaxation, as the decoupling times, during which the proton bath is saturated, are on the order of the spin–lattice relaxation times.[34,37,40,48] They are also influenced by anisotropic spin–spin relaxation, due to the medium slow polymer dynamics.

Polymer defects were also probed using high-resolution ^{13}C solid-state NMR spectroscopy.[38,39,49–51] As cross relaxation between ^{1}H and ^{13}C is inefficient for the typically short free induction decay (FID) times, single-pulse (SP) excitation promises sufficient resolution and quantitative intensities.[38,39,50] Slow spin–lattice relaxation, however, leads to extremely long measurement times. Most studies thus rely on ^{13}C labelling for probing the weak defect signals. Alternatively, ^{1}H–^{13}C cross polarisation (CP) was applied to enhance sensitivity and reduce measurement times.[48,49] As CP excitation is not quantitative, this approach requires calibration.[48,49] As an alternative to the insensitive but quantitative SP excitation, recently, the multiCP technique was successfully invoked.[17] MultiCP relies on a series of short, successive CP bursts separated by a short waiting period, where the polarisation is stored.[52] In this way, $T_{1\rho}$ effects are minimized, allowing the signal intensity of carbon species with small build-up rates to develop properly. ^{1}H–^{13}C multiCP NMR spectra are, therefore, expected to obtain a quantitative character, if the total polarization transfer times are long enough, and were used for a broad variety of materials covering porous, organic and hybrid materials as well as polymers.[17,53–58] In particular, for chemical units with small effective heteronuclear dipole sums caused by low proton densities in their vicinity[17,53,56,57] and fast molecular dynamics,[52,54] significant improvements with deviations from the quantitative intensities below 10% could be reached.[57]

The quantitative determination of proportions, as low as the ones observed for photooxidative defects, is even more challenging with ^{13}C MAS NMR spectroscopy. Although recently, multiCP excitation was applied to determine quantitative ^{13}C MAS NMR spectra of weathered PS, the low sensitivity coming along with natural abundance prevented to optimise the experimental conditions for the defect resonances themselves.[17] However, previous studies suggest that this is crucial.[51–57] Depending on the material properties, the number of CP blocks and the block length needed to be varied between 3 to 10 and 15 µs to 1 ms. Therefore, we performed a case study, evaluating the performance of multiCP for the defect quantification of weathered PS MP particles. These were prepared from partially ^{13}C enriched PS (PS-^{13}C) by accelerated weathering. The obtained results provide guidelines for the optimal setup of multiCP experiments in order to excite the markedly different defects introduced upon weathering. As the defect types are similar for most commodity plastics like PE and PP, our results impact on the quantification of polymer defects for a major part of weathered MP in the environment.

Experimental

Polystyrene: synthesis

PS-^{13}C was synthesised by radical polymerisation (Fig. S1†) of 80% styrene (Sigma Aldrich, Missouri, United States of America) and 20% styrene-α-^{13}C (99% ^{13}C enriched in α position, Sigma Aldrich). While the stabiliser 4-*tert*-butylcatachol was removed *via* an Alox column from styrene, styrene-α-^{13}C was used without further purification, thus containing small amounts of 4-*tert*-butylcatechol as stabiliser. The radical initiator azobisisobutyronitrile (AIBN) was freshly recrystallized prior to use. 4.4 ml styrene (38 mmol, 0.80 eq.), 1.1 ml styrene-α-^{13}C (9.5 mmol, 0.20 eq.) and 68 mg AIBN (0.48 mmol, 0.010 eq.) were mixed in a Schlenk flask under dry argon (Ar 5.0, Riessner-Gase, Germany) atmosphere and were degassed applying three freeze–pump–thaw cycles. The reaction mixture was heated to 60 °C and stirred overnight for 20 h. The solid product was dissolved in 45 ml toluene at 80 °C. Subsequently, the dissolved polymer was precipitated in 1 l methanol, filtered off and dried in a drying chamber at 40 °C under vacuum. 4.5 g (91% yield) PS-^{13}C was obtained with an enrichment degree of 23% at the α-carbon as determined by quantitative ^{13}C MAS NMR spectroscopic experiments. It was ground using an Ultra Centrifugal Mill ZM 200 (Retsch GmbH, Haan, Germany) and sieved with an Alpine Air Jet Sieve E200 LS (Hosokawa Alpine AG, Augsburg, Germany) resulting in 125–200 μm sized particles.

Accelerated weathering

The accelerated weathering experiments were carried out under controlled laboratory conditions in a test chamber Q-SUN XE-3 (Q-LAB Corporation, Westlake, OH, USA) according to a protocol developed previously.[17] The weathering chamber is equipped with three xenon arc lamps and a Daylight-Q filter system. The latter filters radiation with wavelengths smaller than 295 nm. The emitted radiation is thus similar to natural sunlight (comparison of the emission spectrum to sunlight is given in Fig. S2†). The irradiance was set to 60 W m^{-2} at 300–400 nm, corresponding to 594 W m^{-2} total irradiance (for calculation of the irradiance refer to Table S2†), and the relative humidity was adjusted to 50%. The chamber-irradiance is five-fold enhanced in comparison to the average mid-European irradiation of 114 W m^{-2} (Fig. S3 and Table S2†). 2 g of PS-^{13}C particles were weighed into a quartz glass beaker and covered with a quartz-glass lid to enable light penetration from all sides. The particles were constantly stirred in 200 ml deionized water (55 °C) using a PTFE-coated magnetic stirrer at 150 rpm. Particle samples with a weight of 0.3 g each were taken for analysis after 0 h, 200 h, 600 h, 1400 h, 1900 h, 2400 h from the MP-water-dispersion, filtered with a suction filter, and dried at 40 °C in a vacuum oven.

Solid-state NMR spectroscopy

Table 1 Conducted multiCP ^{13}C MAS NMR spectroscopic experiments for pristine and two weathered samples of PS-^{13}C

Weathering time	Number of blocks, n	Block length, $\tau_{\mathrm{multiCP}}^{\mathrm{block}}$	Total pol. time, $\tau_{\mathrm{CP}}^{\mathrm{tot}}$	Waiting time, t_z
0 h	12	250 μs	3000 μs	3 s
2400 h	20	150 μs	3000 μs	2 s
	13	150 μs	1950 μs	2 s
	13	150 μs	1950 μs	3 s
	20	150 μs	3000 μs	3 s
	12	250 μs	3000 μs	3 s
	6	500 μs	3000 μs	3 s
	3	1000 μs	3000 μs	3 s
	8	250 μs	2000 μs	3 s
1900 h	8	250 μs	2000 μs	3 s

^{13}C MAS NMR spectra were acquired with a Bruker Avance-III HD spectrometer operating at a B_0 field of 9.4 T corresponding to Larmor frequencies ν_0 of 400.01 MHz and 100.62 MHz for ^{1}H and ^{13}C, respectively. Samples were spun in a commercial 3.2 mm triple resonance probe. The ^{13}C NMR spectra were referenced with respect to tetramethylsilane (TMS) using the secondary standard adamantane. Cross polarisation (CP) experiments were carried out with a ramped ^{1}H–^{13}C CP sequence at a spinning frequency of 20 kHz, a recycle delay of 3 s and a contact time of 2.0 ms, except for the contact time dependent measurements, where the contact time was varied from 100 μs to 15 ms. The corresponding nutation frequency υ_{nut} for the ^{13}C channel was set to 50 kHz. The power for the shaped pulse (linear ramp from 50% to 100%) on the ^{1}H channel was adjusted to maximal polarisation transfer. ^{1}H–^{13}C multi-pulse CP experiments were recorded with a sequence (Fig. S5†) published in ref. 51 for PS-^{13}C weathered for 1900 h and 2400 h, respectively. While contact times and number of blocks were varied, the Hartman–Hahn conditions and the recycle delay were adopted from the ^{1}H–^{13}C CP NMR experiments and for t_z 2 s and 3 s were used, respectively. A list of the performed experiments is given in Table 1. The $(90°)_{-x}$ pulses at the end and the beginning of each CP block were set to 2.5 μs (^{1}H) and 3.8 μs (^{13}C). During acquisition, proton broadband decoupling was applied with a spinal-64 sequence (υ_{nut} (^{1}H) = 70 kHz). The spectra were deconvoluted using pseudo-Voigt profiles within the simulation package SOLA included in TopSpin 3.2 (Bruker).

Results and discussion

Recently, we proposed a strategy for the quantification of defect proportions based on ^{13}C multiCP NMR spectroscopy.[17] However, due to the extremely long measurement times of several days for one sample, a thorough quality assessment of the applied strategy could not be carried out, in particular not for the weak signals of the polymer defects themselves. By preparing the model system PS-^{13}C (partially enriched with ^{13}C at the α carbon) we could reduce the measurement time by a factor of ≈400 corresponding to the enhancement of NMR active ^{13}C nuclei. Since the majority of photooxidative defects are introduced at the α position (Fig. S4†),[17,18,37,38,47] we achieve a markedly higher sensitivity for probing the defects. This allows for a systematic exploration of the parameter space of the multiCP experiment, in order to determine the accuracy and reliability of the derived defect proportions.

Synthesis and qualitative analysis of weathered PS-^{13}C

PS-^{13}C was synthesized by radical polymerization using a mix of styrene-α-^{13}C (99% enriched), non-enriched styrene, in a proportion of one to four, and a radical initiator. The resulting PS-^{13}C exhibits a number average molecular weight M_{n} of 51 500 g mol^{-1}, a weight average molecular weight M_{w} of 194 500 g mol^{-1} and a dispersity $Đ$ of 3.78. A quantitative ^{13}C multiCP NMR spectrum (Fig. 1 inset) of the pristine material shows the typical peaks for the ipso carbon at 149 ppm, the aromatic CH groups at 130 ppm and the aliphatic backbone consisting of CH$_2$ and CH units at about 43 ppm with intensity ratios of 1 : 5.1 : 22.4. The resonances of the aliphatic groups are strongly superimposed due to the high signal intensity of the partially ^{13}C enriched CH groups. Similar intensity ratios

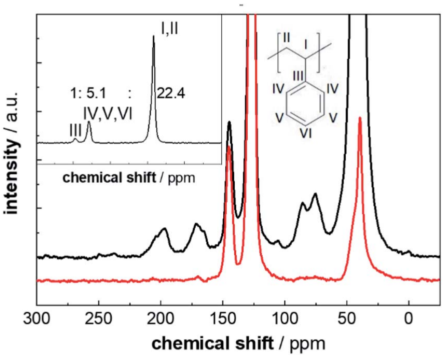

Fig. 1 Comparison of ^{13}C CP MAS NMR spectra of PS-^{13}C (black) and PS in natural abundance (red) of the particle samples weathered for 2400 h. Both spectra are normalized to the intensity of the ipso carbon resonance at 149 ppm and were shifted horizontally for a better overview (full-scale spectra are given in Fig. S6†). Inset: ^{13}C multiCP MAS spectrum of pristine PS-^{13}C. The relative intensities for the resonances of the ipso carbon(III), the aromatic carbons (IV, V and VI) and the aliphatic carbons (I (enriched), II) were determined by deconvolution.

were obtained for ^{13}C multiCP NMR spectra of different weathering times (Fig. 2 and Table S5†). This ratio corresponds to approximately 23% ^{13}C enrichment for the aliphatic CH carbons (ESI chapter S2†). PS-^{13}C particles were weathered following the same protocol as previously used.[17] Fig. 1 shows the intensity improvement for the defect signals due to ^{13}C labelling compared to the non-enriched sample. Both samples were weathered for 2400 h and the CP spectra were adjusted to one day measurement time and are normalised to the intensity of the ipso carbon. Within the obtained accuracy for weathered PS in natural abundance the intensity gain for PS-^{13}C matches the expectation due to the isotope enrichment, demonstrating that the defects are indeed introduced mostly at the α position (Fig. S4†). For dark control experiments (same experimental setup, but without irradiation) carried out on commercial PS with ^{13}C in natural abundance, no degradation takes place, which is demonstrated by the unchanged particle sizes and molecular weight distributions as function of the exposure time.[17] This proves that irradiation is crucial to introduce oxidation defects for the chosen controlled weathering conditions.

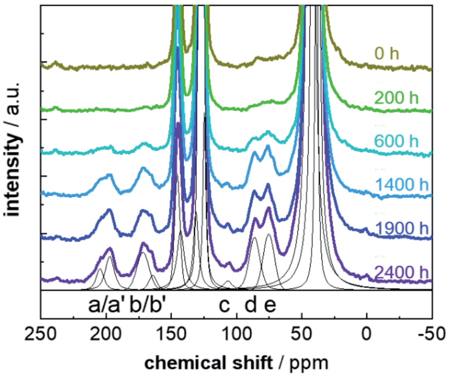

Fig. 2 ^{13}C CP MAS NMR spectra of PS-^{13}C for weathering times between 0 h and 2400 h. The functional groups are marked; (a) in-chain and (a') end-chain ketones, (b) carboxylic acids and (b') esters, (c) ketals, (d) peroxides and (e) alcohols. The spectra for the individual weathering times are normalized and horizontally shifted for a better overview. An exemplary fit of the different peaks of the spectra with pseudo-Voigt functions is shown in black for a weathering time of 2400 h.

^{13}C CP MAS NMR spectra acquired for a set of PS-^{13}C samples after various weathering times are shown in Fig. 2. The improved S/N ratios allow for a more detailed signal assignment due to a better resolution and the possibility to apply spectral editing by contact-time dependent CP measurements. Even for short weathering times, the seven typical resonances (a–e) of the emerging defects were observed. Surprisingly, also for the pristine PS-^{13}C resonances characteristic for alcohol and peroxide units (region around 70–90 ppm) were found. This suggests that already the processing, *e.g.* the grinding, of the samples introduces some defects, due to the emergence of radicals in the presence of strong mechanical forces,[59] as PS-^{13}C is free of any additives.

Contact-time dependent measurements (Fig. 3a) reveal pronounced differences for the build-up behaviour. We use a classic I–S model for the CP build-up[60] for the refinement. It reads as

$$I = \frac{I_0}{\left(1-\frac{T_{\mathrm{IS}}}{T_{1\rho}^{1\mathrm{H}}}\right)} \times \left(\exp\left(-\frac{t}{T_{1\rho}^{1\mathrm{H}}}\right) - \exp\left(-\frac{t}{T_{\mathrm{IS}}}\right)\right) \qquad (1)$$

with T_{IS} being the CP build-up time, $T_{1\rho}^{1\mathrm{H}}$ representing the spin–lattice relaxation time within the rotating frame of the ^{1}H bath, and I_0 being the maximum intensity. This equation holds in the limit of abundant protons (I) and $T_{\mathrm{IS}}/T_{1\rho}^{13\mathrm{C}} \approx 0$, ($T_{1\rho}^{13\mathrm{C}}$ being the spin–lattice relaxation time in the rotating frame of the non-abundant (S) carbons), which is usually fulfilled for polymers.[49,59] We expect $T_{1\rho}$ in the rotating frame to be proportional to the corresponding T_1 values in the laboratory frame. With $T_1(^1\mathrm{H}) = 1.55$ s and $T_1(^{13}\mathrm{C}) \geq 60$ s the corresponding $T_{1\rho}^{13\mathrm{C}}$ values would be on the order of 100 ms ($T_{1\rho}^{13\mathrm{C}} \geq 60$ s/1.55 s $\times$ $T_{1\rho}^{1\mathrm{H}}$) based on the $T_{1\rho}^{1\mathrm{H}}$ values obtained from the refinement (Table S3†).

The build-up time constant T_{IS} varies between 90 μs and 1700 μs (Fig. 3b and Table S3†) and the relaxation time constants of ^{1}H within the rotating frame $T_{1\rho}^{1\mathrm{H}}$ differ between 1800 μs and 3900 μs (Table S3†). The T_{IS} values for the joint refinement of the CH$_2$ and CH units of the aliphatic backbone and aromatic CH's are smaller than 100 μs and thus within the expected range.[59] T_{IS} decreases with the number of protons in the vicinity of a carbon atom, and is particularly small if the protons are covalently attached to carbon atoms. The other eight resonances have longer or much longer built-up times

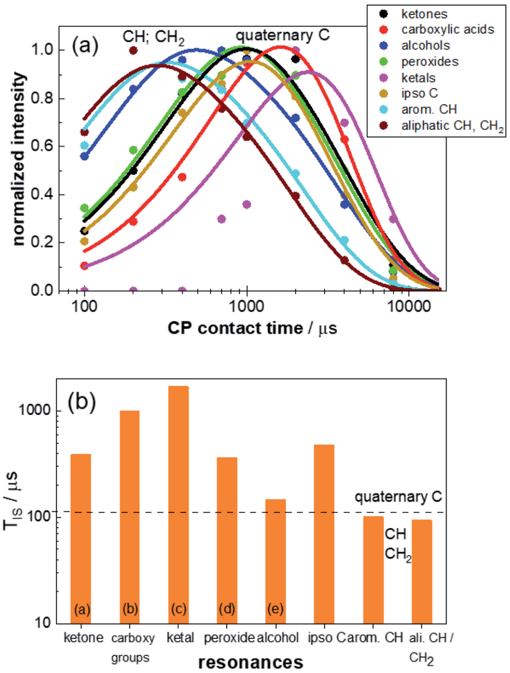

Fig. 3 (a) Contact-time dependent intensities of the characteristic resonances for weathered PS-^{13}C. The intensities were derived by deconvolution of the ^{13}C CP NMR spectra acquired with contact times between 100 μs and 15 ms. The build-up curve for each defect signal (circles) was normalized to the maximum intensity and refined using eqn (1) (solid lines). The determined values for $T_{\rm IS}$ and $T_{1\rho}^{1\rm H}$ are given in Table S3.† (b) CP build-up time $T_{\rm IS}$ derived from the contact-time dependent build-up curves obtained from the refinements of the CP spectra for the different resonances: (from left to right: ketone groups (a), carboxy groups and esters (b), ketals (c), peroxide groups (d), alcohols (e), ipso carbon, aromatic CH carbons, aliphatic CH and CH$_2$ carbons). The shoulders in resonance (a) and (b) were evaluated together with the main peaks of resonance (a) and (b), respectively, since for short CP build-up times shoulder and main peak could not be resolved and the shape of the resonances for longer build-up times does not change for different build up times (Fig. S7†). Due to the heavily superimposed resonances for the aliphatic CH and CH$_2$ groups, these two signals were also treated with one build-up curve. Typical $T_{\rm IS}$ ranges for quaternary carbons and CH$_n$ groups are marked by dashed lines.

ranging from 150 μs for the alcohol resonance to 1700 μs for a resonance at 110 ppm. This resonance could not be detected in previous studies carried out on samples without ^{13}C enrichment due to the small proportion of the corresponding defect. The $T_{\rm IS}$ values for these signals agree with the previous assignment to quaternary carbon atoms, not directly bound to a proton.[17,18,37,38]

In this way, we assigned (a) ketones ($\approx$200 ppm), (b) carboxy units (172 ppm), (c) ketals (105 ppm), (d) peroxide groups (85 ppm) and (e) alcohols (76 ppm). Due to the improved S/N ratio, a distinction between the alcohol and the peroxide signals is now possible, proving that both defect types are present in weathered PS, which was an open debate up to now.[17,18,47] Additionally, the signals for ketone and carboxy groups split into two resonances each (Fig. 2, peaks a/a' and b/b' and Fig S7†). For the ketone signal group, the chemical shift difference of 7 ppm is characteristic for the difference between (a) in- and (a') end-chain ketones. Both types of defects occur, with the low field-shifted in-chain ketones (204 ppm) being less frequent than the end-chain ketones (197 ppm). The intensity ratio of both resonances (1.7 ± 0.3) suggests that roughly 40% in-chain ketones are formed. The splitting for the carboxy resonances implies that, although the majority of –CO$_2$R units consist of carboxylic acids (b), also esters (b') are formed. Their intensity ratio of 4 ± 1 shows that approximately 20% ester groups are formed. The resonance at 105 ppm (c) expresses the typical shift range for vinylidene carbon atoms, which might be a result of the disproportionation reaction (Fig. S4†).[18,37] However, the long $T_{\rm IS}$ value of 1.7 ms, contradicts this assignment since it is characteristic for quaternary carbon units. Thus, it is more likely, that this signal is caused by (hemi)ketal formation (Fig. S4†) by a subsequent reaction of the ketones.[61] This also explains why this resonance occurs only in later weathering stages after formation of a substantial amount of ketones.

The occurrence of ester and ketal functionalities, suggests two additional crosslinking mechanisms. While C–C bond formation by pairing two radicals dominates early weathering stages, the formation of esters and ketals will become important for later stages, as they require the presence of carboxylic acids, ketones and alcohols in substantial amounts. This explains the surprisingly high crosslinking rates previously observed for weathered PS.[17]

Quantitative analysis

To be able to derive a better understanding of weathered plastic particles, a reasonably fast and accurate quantitative characterisation of photooxidative defects is essential. We recently proposed a strategy for this purpose.[17] ^{13}C multiCP NMR spectra were recorded for selected, preferably longer weathering times, and ^{13}C CP NMR spectra were acquired for the complete set of weathered samples. The quantitative ^{13}C multiCP NMR spectra provide a correction factor c_i for each resonance, which is calculated as $c_i = I_i^{\rm multiCP}/I_i^{\rm CP}$ after normalising both the ^{13}C CP and multiCP NMR spectra of the calibration sample to the same overall spectral intensity. The intensities of each defect resonance within the ^{13}C CP spectra for sample (a) are then corrected by $I_i^{\rm quant}({\rm a}) = c_i \times I_i^{\rm CP}({\rm a})$. The strategy is time efficient, as multiCP spectra take significantly longer to be recorded with similar S/N ratios. For the present study the measurements are four to five times faster. As long as the materials under investigation are comparable, similar filling factors and measurement parameters for all CP experiments are used, this strategy should be applicable to a broad range of polymers and microplastic samples.

The accuracy of the defect proportions thus crucially depends on how accurate the quantitative relative intensities can be determined for the corresponding resonances within the

^{13}C multiCP spectra. The high sensitivity provided by PS-^{13}C, enables us to explore the parameter space of the multiCP experiment in a systematic fashion, in particular, for the defect signals. Thus, it provides guidelines and trends to improve the accuracy of future experiments on weathered MP. The multiCP NMR sequence (Fig. S5†) used for this work, is adopted from ref. 51. It consists of a series of n short CP blocks. Between the blocks, a z-filter stores the ^{1}H and ^{13}C polarisation along the external magnetic field. It allows decayed ^{1}H polarisation to relax according to T_1^{1H} and flips back the ^{1}H and ^{13}C polarisation into the *xy* plane of the doubly rotating frame before the next CP burst. Thus, already created polarisation does not decay and is added to the one generated within the next block.[51] If the waiting time t_z during the z-filter is much shorter than the spin–lattice relaxation of ^{13}C nuclei and much longer than the one of ^{1}H nuclei ($T_1^{1H} \ll t_z \ll T_1^{13C}$) and the block length of the individual CP blocks does not become too short, the I–S model can be applied and the intensity build-up of a resonance with a nominal intensity of one follows eqn (2):[54]

$$I_i\left(\tau_{CP}^{tot}\right) = I_\infty\left(1-\exp\left(-\frac{\tau_{CP}^{tot}}{T_{IS}}\right)\right) \text{ and } I_\infty = \frac{\exp\left(-\frac{\tau_{CP}^{tot}}{n\times T_{1\rho}^{1H}}\right) - \exp\left(-\frac{\tau_{CP}^{tot}}{n\times T_{IS}}\right)}{\left(1-\frac{T_{IS}}{T_{1\rho}^{1H}}\right)\left(1-\exp\left(-\frac{\tau_{CP}^{tot}}{n\times T_{IS}}\right)\right)} \qquad (2)$$

The individual blocks of multiCP experiments should be much shorter than $T_{1\rho}^{1H}$, to avoid relaxation within the rotating frame. With values between 1.8 ms and 3.9 ms obtained for $T_{1\rho}^{1H}$ (Table S3†), we carried out a set of experiments with block lengths from 1 ms down to 150 μs. According to eqn (2), the total contact time τ_{CP}^{tot} should be on the order of or larger than $3 \times T_{IS}$, which accounts for roughly 95% transfer efficiency. With values for T_{IS} (Table S3†) between 90 μs (CH$_n$ groups) and 1000 μs (carboxy units), we chose to record two series of measurements with τ_{CP}^{tot} either set to 2 ms or 3 ms. Finally, the waiting time t_z during the z-filter should allow for the spin–lattice relaxation of the decayed ^{1}H polarisation and should thus be on the order of $2 \times T_1^{1H}$. However, to avoid significant decay of ^{13}C polarisation, $t_z \ll T_1^{13C}$ also has to be fulfilled. T_1^{1H} was determined to 1.5 s and T_1^{13C} was estimated to be larger than 60 s. Therefore, we explored the influence of t_z by collecting ^{13}C multiCP NMR spectra with t_z being either 2 s or 3 s. Furthermore, three samples with weathering times of 0 h, 1900 h, and 2400 h were probed. The latter two samples were chosen to guarantee meaningful defect proportions. An overview of all multiCP experiments and values for I_∞ for each resonance (eqn (2)) are given in Tables 1 and S4.† With some limitations, I_∞ might be used to correct the intensities obtained from multiCP experiments. Additionally, it allows to estimate whether the chosen block lengths and number of blocks are appropriate to avoid heavy losses due to $T_{1\rho}^{1H}$. To benefit from eqn (2) though, T_{IS} and $T_{1\rho}^{1H}$ need to be determined separately, which might not always be feasible for studies on complex materials like microplastics.

For the chosen block lengths $\tau_{multiCP}^{block}$ and number of blocks n, I_∞ varies between 0.60 and 0.98 (Table S4†) suggesting that significant deviations for the intensities are to be expected, in particular for longer $\tau_{multiCP}^{block}$ and smaller n. This trend (Fig. 4 and Table S5†) is nicely reproduced for the relative intensities for the three main resonances of PS-^{13}C (ipso carbon, aromatic CH and aliphatic CH/CH$_2$). For $\tau_{multiCP}^{block}$ of 500 μs and 1 ms (n adjusted to yield a τ_{CP}^{tot} of 3 ms) the relative intensities of the signals of the aromatic CH groups and the aliphatic CH/CH$_2$ units are significantly smaller than the expected stoichiometric values (1 : 5 : ≈22). The deviation becomes stronger for longer block lengths. For $\tau_{multiCP}^{block} = 1$ ms, the aromatic CH and aliphatic units are underestimated by roughly 20% to 30% (Fig. 4).

This demonstrates that the block lengths need to be kept short enough to avoid polarisation loss due to $T_{1\rho}^{1H}$, in particular, for chemical units with small T_{IS} (*e.g.* CH and CH$_2$) and thus fast build-ups. Consequently, the number of blocks becomes large to adjust the long τ_{CP}^{tot} necessary to accommodate for quaternary carbon atoms with large T_{IS} values (Table S3†). For $\tau_{multiCP}^{block}$ of 250 μs and 150 μs the expected relative intensities were obtained. With respect to a nominal intensity of 1 for $I(C_{ipso})$, $I(CH_{aro})$ scatters between 5.1 and 5.5 and $I(C_{aliphatic})$ lies between 21.1 and 22.6. This implies that convergence is reached and that quantitative intensities and thus proportions can be calculated with an accuracy of roughly 10%, estimated from the variation of the determined relative intensities. As similar relative intensities were also obtained for $\tau_{CP}^{tot} = 2$ ms, the influence of the total contact-time is less severe in the chosen regime. Especially, for the $\tau_{multiCP}^{block} = 150$ us measurements (see Fig. S8†), the spectral shape and thus the relative intensities do

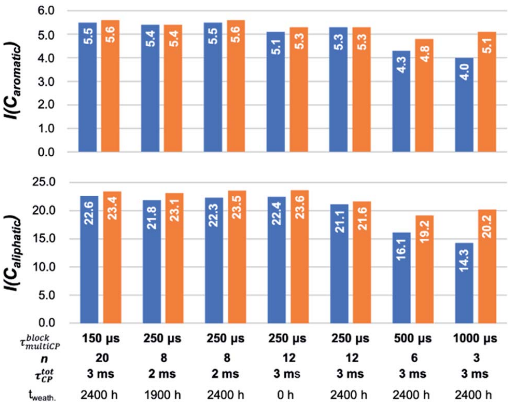

Fig. 4 Comparison of the relative intensities for the aromatic CH units (top) and the aliphatic CH/CH$_2$ groups (bottom) for various multiCP experiments before (blue) and after correcting with I_∞ (orange). All relative intensities are given after normalising the intensity for the ipso carbon to one (Table S5†). For small block length average relative intensities of 1 : 5.4 : 22.0 for $I(C_{ipso})$, $I(CH_{aro})$ and $I(C_{aliphatic})$ were obtained matching the expected stoichiometry and enrichment degree.

not change when reducing $\tau_{\mathrm{CP}}^{\mathrm{tot}}$ from 3 ms (20 blocks) to 2 ms (13 blocks) or when reducing the waiting time t_z to 2 s (Fig. S8†). This indicates that we are already in the limit of sufficient long waiting times t_z and total contact-times $\tau_{\mathrm{CP}}^{\mathrm{tot}}$.

Using I_∞ to correct for lost polarisation during the individual CP blocks allows for compensating the major part of the polarisation losses (Fig. 4). For ^{13}C multiCP experiments with $\tau_{\mathrm{multiCP}}^{\mathrm{block}}$ = 500/1000 μs average relative intensities of 4.9 for $I(\mathrm{CH_{aromatic}})$ and 19.7 for $I(\mathrm{C_{aliphatic}})$ were reached. Although they are close to the plateau values of 5.4 and 22.0 established from the shorter block lengths, the remaining differences are on the order of 10%. They might be caused by deviations from the I–S model due to coherent polarization transfer, which should be strongest for the proton bearing groups. For smaller $\tau_{\mathrm{multiCP}}^{\mathrm{block}}$, I_∞ approaches unity and thus leads to small corrections only. Within the limit of the aimed for accuracy of 10%, I_∞ might then be neglected. This is important, as for many complex materials the determination of T_{IS} and $T_{1\rho}^{1\mathrm{H}}$, needed to calculate I_∞, is challenging and would reduce the applicability of multiCP experiments.

In a second step, the intensities determined from the ^{13}C multiCP NMR spectra were used to calibrate the ^{13}C CP NMR spectra. Calibration factors c_i were derived for every resonance as described above (Fig. 5, blue bars and Table S6†). In particular, for the analysis of the defect resonances, the calibration is advantageous, for two reasons. First, a direct comparison to expected proportions is not feasible since the latter are not known in advance. Second, the defect intensities are weak, on the order of roughly 10% of the total accumulated intensity and their intensity changes are easier recognized in the calibration factors c_i. Due to its very weak intensity, we exclude the ketal resonance at 110 ppm from this analysis. For comparison, the c_i values were also corrected with I_∞ (Fig. 5, orange bars and Table S7†), to test how well the I–S model (eqn (2)) can be used to account for polarisation losses, if the block length $\tau_{\mathrm{multiCP}}^{\mathrm{block}}$ of the CP blocks becomes too long. The general CP conditions were chosen to be the same for both the CP and multiCP experiments. To obtain better S/N ratios though, all CP NMR spectra were obtained with a contact time $\tau_{\mathrm{CP}}^{\mathrm{tot}}$ of 2 ms, due to the markedly higher signal intensity compared to 3 ms. Fig. 6 shows the typical differences between a ^{13}C CP ($\tau_{\mathrm{CP}}^{\mathrm{tot}} = 2\mathrm{ms}$) and a ^{13}C multiCP spectrum ($\tau_{\mathrm{CP}} = 250$ μs with 12 blocks and $\tau_{\mathrm{CP}}^{\mathrm{tot}} = 3$ ms). Interestingly, with these conditions the defect intensities derived from the CP NMR spectra are overestimated compared to the quantitative values obtained from the multiCP experiments. As a consequence, all c_i values for the defects are smaller than one (Fig. 5).

As observed for intensities of the main PS-^{13}C resonances within the ^{13}C multiCP NMR spectra, the c_i values for the defects converge for $\tau_{\mathrm{multiCP}}^{\mathrm{block}}$ smaller than 250 μs to values between 0.6 and 0.7 depending on the defect type. This trend holds for $\tau_{\mathrm{CP}}^{\mathrm{tot}}$ of 2 ms and 3 ms as well as for t_z of 2 s and 3 s equally, demonstrating that both total contact-times and waiting times are long enough, to guarantee a sufficient polarisation build-up for the polymer defects. For $\tau_{\mathrm{multiCP}}^{\mathrm{block}}$ larger than 500, the calibration factors grow and approach one for $\tau_{\mathrm{multiCP}}^{\mathrm{block}} = 1000$ μs. Correcting the ^{13}C multiCP NMR spectra with I_∞ before calibration improves the c_i values for $\tau_{\mathrm{multiCP}}^{\mathrm{block}}$ of 500 μs and 1000 μs markedly. For smaller block lengths the correction is negligible. We attribute the increase in c_i for longer $\tau_{\mathrm{multiCP}}^{\mathrm{block}}$ to polarisation losses for the resonances of the aromatic and aliphatic CH and CH$_2$ units. They exhibit the smallest I_∞ of around 0.6 (Table S4†) and thus should suffer the strongest losses.

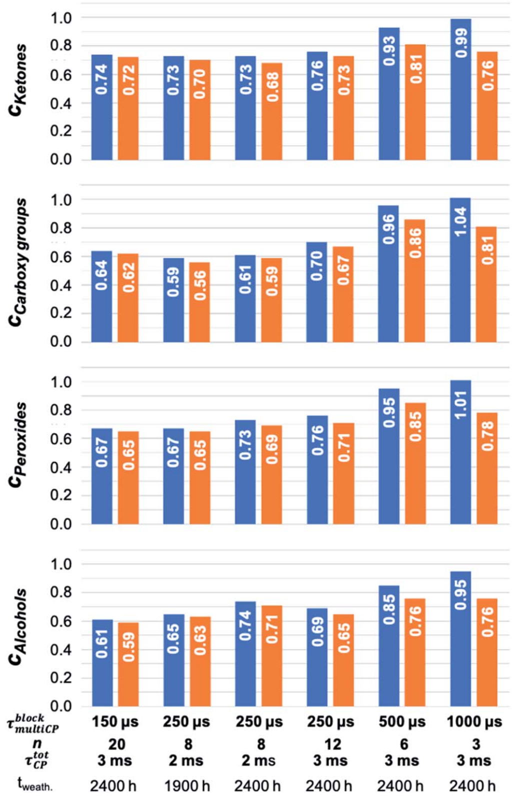

Fig. 5 Comparison of calibration factors c_i (blue) for the major polymer defects. The c_i were derived by dividing the intensities of resonance i, obtained from the ^{13}C multiCP NMR spectrum, by the ones extracted from the ^{13}C CP NMR spectrum. Both NMR spectra are normalised to the same total intensity. Calibration factors c_i which are corrected for polarisation loss due to $T_{1\rho}^{1\mathrm{H}}$ within the CP blocks according to eqn (2) are given in orange.

Underestimating the intensities of the main PS resonances, in turn, leads to an overestimation of the defect intensities and thus an increase for c_i. Nevertheless, the corrected c_i values do not reach the plateau derived from the experimental data for the smaller block length, suggesting that additional polarisation losses due to, *e.g.*, $T_{1\rho}^{13\mathrm{C}}$ and $T_1^{13\mathrm{C}}$ relaxation as well as coherent polarisation transfer, beyond the I–S model, are playing a role. While the calibration factors c_i for the ipso carbon atoms exhibit the same trend as for the defect c_i values, the ones for the aromatic and aliphatic CH and CH$_2$ units are apparently independent of the conditions chosen for the multiCP experiments.

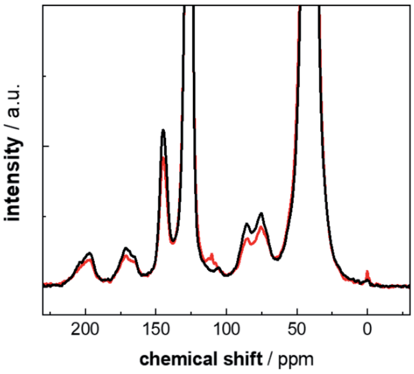

Fig. 6 Comparison of ^{13}C CP ($\tau_{\mathrm{CP}}^{\mathrm{tot}} = 2$ ms; black line) and multiCP ^{13}C ($\tau_{\mathrm{multiCP}}^{\mathrm{block}} = 250$ µs with 12 blocks and $\tau_{\mathrm{CP}}^{\mathrm{tot}} = 3$ ms; red line) MAS NMR spectra for PS-^{13}C weathered for 2400 h. Both spectra are normalized to the same total intensity (full scale spectra are given in Fig. S9†).

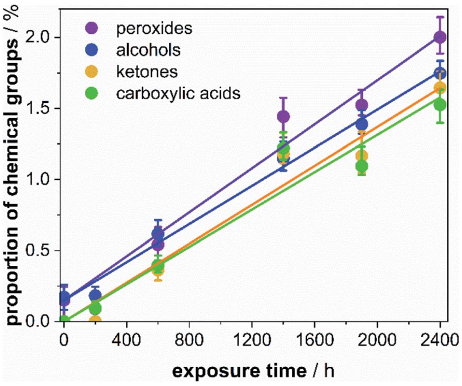

Fig. 7 Proportion of the defect groups with respect to the total number of repeating units of PS-^{13}C in dependence of the weathering time. The defect proportions were refined with a linear function allowing to derive growth rates for carboxylic acids (6.6×10^{-6} h^{-1}), ketones (6.9×10^{-6} h^{-1}), alcohols (6.7×10^{-6} h^{-1}) and peroxide (7.7×10^{-6} h^{-1}) functions. The non-zero interception for the peroxides and alcohols is a consequence of the grinding procedure of the pristine PS-^{13}C.

As they share similar build-up and relaxation behaviour and account for 95% of the total spectral intensity, calibration leads to constant c_i values (Fig. 4).

To show that the optimized experimental conditions for the multiCP experiment ($\tau_{\mathrm{multiCP}}^{\mathrm{block}} = 250$ µs, 12 blocks) are meaningful also for samples in natural abundance we remeasured a sample of commercial PS (weathered for 3200 h) from ref. 17, which was previously obtained with a block length of 500 µs and 6 blocks. The comparison between both spectra is given in Fig. S10.† As expected from Fig. 4, the intensity of the aromatic and aliphatic proton bearing groups is enhanced by roughly 20%. Especially the expected intensity ratios 1 : 5 : 2 of the three main polystyrene resonances (ipso C, aromatic CH's and aliphatic CH/CH$_2$) are correctly reproduced. In consequence, the total defect proportions amounting to 13% are roughly 20% smaller than the previously reported ones (16.5%).[17] This matches the expected trends of the correction factors shown in Fig. 5.

Applying the proposed calibration method, the intensities derived from the ^{13}C CP MAS NMR spectroscopic experiments were calibrated according to the correction factors for $\tau_{\mathrm{multiCP}}^{\mathrm{block}} =$ 150 µs and 20 blocks (Table S6†). From these spectral intensities, the proportion of the respective defects was calculated according to Meides *et al.*,[17] additionally considering the selective ^{13}C enrichment of 23% at the α position of PS (see ESI† for calculations). Within the probed weathering time, the proportions for all defect types grow with a linear trend. Rates between 6.6×10^{-6} h^{-1} and 7.7×10^{-6} h^{-1} were observed, demonstrating that all defect types grow at similar rates. Considering that weathering in our controlled weathering experiment is roughly 5 times faster compared to average central European conditions, the maximum gain of total defect proportions of PS microplastic particles in the environment is extrapolated to roughly 5% per year (Fig. 7). The rates are slightly smaller than observed for commercial non-additivated PS in natural abundance.[17] For shorter weathering times, the improved S/N ratio allows for probing even very small defect proportions down to 0.1%. In this way, we show that the implied induction period for ketone formation[17] was caused by a lack of sensitivity. Here, a continuous increase of the ketone proportions was observed.

Conclusion

For the present study, we synthesised PS-^{13}C – polystyrene partially ^{13}C labelled at the α position – by radical polymerisation with an enrichment degree of ≈23%. Accelerated weathering by exposure to mechanical stress and simulated solar radiation, then allowed to introduce typical photooxidative defects. They increase in a linear trend as function of the weathering time up to individual proportions of 2%. As most defects originate at the α position, PS-^{13}C proved to be a highly sensitive model system for probing defect types and their proportions by combining ^{13}C CP and multiCP MAS NMR spectroscopy. While detection *via* ^{13}C offers the necessary resolution for identifying and distinguishing the defect types, CP excitation promises reasonable measurement times. Calibration with multiCP NMR spectra led to quantitative relative intensities and thus to defect proportions. As the S/N ratio was improved roughly 20 times, we could explore the influence of essential parameters for the multiCP experiment on the intensities of the defects themselves.

In addition to the typical alcohol, peroxo, keto and carboxy functions already described earlier,[17] the higher sensitivity for PS-^{13}C allowed to distinguish between in- and end-chain ketones, carboxylic acids and esters. Even (hemi)ketal functionalities in very low proportions could be identified. The presence of ester and ketal groups suggest that carboxylic acids and ketones react with alcohol units for longer weathering times. They thus introduce two additional crosslinking mechanisms, besides radical pairing and subsequent C–C bond formation. For selected PS-^{13}C samples (0 h, 1900 h and 2400 h weathering times), we characterised ^{1}H and ^{13}C spin–lattice relaxation, which exhibits averaged time constants of 1.5 s (T_1^{1H}) and ≈60 s (T_1^{13C}) in the laboratory frame and of 3 ms ($T_{1\rho}^{1H}$) and ≈100 ms ($T_{1\rho}^{13C}$) in the double rotating frame. The CP build-up time constants T_{IS}, determined *via* contact-time dependent measurements, vary markedly from 90 μs for CH/CH$_2$ units up to 1 ms for carboxy units. Remarkably, although all defect types are quaternary in nature, already their T_{IS} values reach down to 150 μs.

The broad spread for T_{IS} requires a careful setup for the multiCP experiments. We explored the influence of essential parameters, like number of CP blocks, their block length and the waiting time between the successive blocks, to determine ideal conditions and guidelines for samples with ^{13}C in natural abundance, where an adjustment on the defect resonances themselves is not possible. While the effect on the main resonances of PS-^{13}C (C$_{ipso}$, CH$_{aromatic}$ and C$_{aliphatic}$) was best studied on the relative intensities of the ^{13}C multiCP NMR spectra, for the defect resonances *i* the calibration factors $c_i = I_i^{multiCP}/I_i^{CP}$ turned out to be more meaningful. We found convergence for all resonances (both main and defects) for total contact-times (τ_{CP}^{tot}) and waiting times (t_z) longer than 2 ms and 2 s, respectively. This matches previously reported guidelines,[51,54] where $t_z > 2 \times T_1^{1H}$, $t_z < T_1^{13C}$ and $\tau_{CP}^{tot} \approx 3 \times T_{IS}$ should be adjusted. While chemical units with large T_{IS} values turned out to be relative insensitive with respect to the CP block length ($\tau_{multiCP}^{block}$), in particular, the intensities for the aromatic and aliphatic CH and CH$_2$ units showed large deviations from expected relative intensities for longer block lengths. For a block length of 1 ms already a polarisation loss on the order of 20 to 30% occurred. This effect could be avoided for block length smaller than 250 μs and the best conditions were observed for 150 μs. Thus, to reach a total contact-time larger than 2 ms, a minimum of 8 and 13 blocks is required, respectively.

As weathered MP generally contains a broad mix of defects and functional groups, which may cover the whole range between quaternary and primary carbon atoms, multiCP experiments with block lengths shorter than 250 μs and total contact times longer than 2 ms are advisable for future experiments. This opposes, to a certain extent, previous studies on other complex materials,[51–57] where often significantly longer block length were used. The necessary short block lengths, however, increase the measurement time markedly, as the number of repetitions will be large. Collecting ^{13}C multiCP NMR spectra for whole sample series is thus not feasible. We, therefore, suggest to calibrate conventional ^{13}C CP NMR spectra with selectively acquired multiCP experiments. Our results demonstrate that the proposed strategy offers a reasonable fast and accurate way to characterise polymer defects for MP even for ^{13}C in natural abundance and for the low inherent defect proportions. We expect that both the calibration and the obtained parameter range are applicable to other types of commodity plastics and thus will help to overcome the challenge of determining average stoichiometries for weathered MP. In addition, the presented approach will be transferable to a broad range of organic, inorganic and hybrid materials supporting structure determination of complex materials.

Conflicts of interest

There are no conflicts to declare.

Acknowledgements

This project was funded by the Deutsche Forschungsgemeinschaft (DFG, German Research Foundation) – Project Number 391977956 – SFB 1357. Publication was funded by the DFG – 491183248 and the Open Access Publishing Fund of the University of Bayreuth. We acknowledge the Northern Bavarian NMR centre (NBNC) at the University of Bayreuth for access to the solid-state NMR spectrometers.

References

1 PlasticsEurope, *Plastics – the Facts 2019, An analysis of European plastics production, demand and waste data*, https://www.plasticseurope.org/en/resources/publications/1804-plastics-facts-2019.

2 F. Julienne, N. Delorme and F. Lagarde, From macroplastics to microplastics: Role of water in the fragmentation of polyethylene, *Chemosphere*, 2019, **236**, 124409.

3 J. P. Da Costa, A. R. Nunes, P. S. Santos, A. V. Girao, A. C. Duarte and T. Rocha-Santos, Degradation of polyethylene microplastics in seawater: Insights into the environmental degradation of polymers, *J. Environ. Sci. Health, Part A: Toxic/Hazard. Subst. Environ. Eng.*, 2018, **53**(9), 866–875.

4 K. Rajakumar, V. Sarasvathy, A. T. Chelvan, R. Chitra and C. T. Vijayakumar, Natural weathering studies of polypropylene, *J. Polym. Environ.*, 2009, **17**(3), 191–202.

5 R. Geyer, J. R. Jambeck and K. L. Law, Production, use, and fate of all plastics ever made, *Sci. Adv.*, 2017, **3**(7), e1700782.

6 Y. Chae and Y. J. An, Current research trends on plastic pollution and ecological impacts on the soil ecosystem: A review, *Environ. Pollut.*, 2018, **240**, 387–395.

7 A. A. de Souza Machado, W. Kloas, C. Zarfl, S. Hempel and M. C. Rillig, Microplastics as an emerging threat to terrestrial ecosystems, *Global Change Biol.*, 2018, **24**(4), 1405–1416.

8 T. S. Galloway, M. Cole and C. Lewis, Interactions of microplastic debris throughout the marine ecosystem, *Nat. Ecol. Evol.*, 2017, **1**(5), 1–8.

9 K. L. Law, S. E. Morét-Ferguson, D. S. Goodwin, E. R. Zettler, E. DeForce, T. Kukulka and G. Proskurowski, Distribution of surface plastic debris in the eastern Pacific Ocean from an 11-year data set, *Environ. Sci. Technol.*, 2014, **48**(9), 4732–4738.

10 O. Setälä, V. Fleming-Lehtinen and M. Lehtiniemi, Ingestion and transfer of microplastics in the planktonic food web, *Environ. Pollut.*, 2014, **185**, 77–83.

11 E. Huerta Lwanga, J. Mendoza Vega, V. Ku Quej, J. Chi, L. Sanchez del Cid, C. Chi, G. Escalona Segura, H. Gertsen, T. Salánki, M. van der Ploeg, A. A. Koelmans and

V. Geissen, Field evidence for transfer of plastic debris along a terrestrial food chain, *Sci. Rep.*, 2017, **7**(1), 14071.

12 N. B. Hartmann, T. Hüffer, R. C. Thompson, M. Hassellöv, A. Verschoor, A. E. Daugaard, *et al.* Are we speaking the same language? Recommendations for a definition and categorization framework for plastic debris, *Environ. Sci. Technol.*, 2019, **53**(3), 1039–1047.

13 A. L. Andrady, The plastic in microplastics: A review, *Mar. Pollut. Bull.*, 2017, **199**, 12–22.

14 D. Eerkes-Medrano, R. C. Thompson and D. C. Aldridge, Microplastics in freshwater systems: a review of the emerging threats, identification of knowledge gaps and prioritisation of research needs, *Water Res.*, 2015, **75**, 63–82.

15 E. Syranidou, K. Karkanorachaki, F. Amorotti, M. Franchini, E. Repouskou, M. Kaliva, M. Vamvakaki, B. Kolvenbach, F. Fava, P. F.-X. Corvini and N. Kalogerakis, Biodegradation of weathered polystyrene films in seawater microcosms, *Sci. Rep.*, 2017, **7**, 17991.

16 E. Syranidou, K. Karkanorachaki, F. Amorotti, A. Avgeropoulos, B. Kolvenbach, N. Y. Zhou, F. Fava, P. F.-X. Corvini and N. Kalogerakis, Biodegradation of mixture of plastic films by tailored marine consortia, *J. Hazard. Mater.*, 2019, **375**, 33–42.

17 N. Meides, T. Menzel, B. Pötzschner, M. G. J. Löder, U. Mansfeld, P. Strohriegl, V. Altstaedt and J. Senker, Reconstructing the Environmental Degradation of Polystyrene by Accelerated Weathering, *Environ. Sci. Technol.*, 2021, **55**, 7930–7938.

18 B. Gewert, M. M. Plassmann and M. MacLeod, Pathways for Degradation of Plastic Polymers Floating in the Marine Environment, *Environ. Sci.: Processes Impacts*, 2015, **17**, 1513–1521.

19 A. Fairbrother, H. C. Hsueh, J. H. Kim, D. Jacobs, L. Perry, D. Goodwin, C. White, S. Watson and L. P. Sung, Temperature and light intensity effects on photodegradation of high-density polyethylene, *Polym. Degrad. Stab.*, 2019, **165**, 153–160.

20 A. F. R. M. Ramsperger, J. Jasinski, M. Völkl, T. Witzmann, M. Meinhart, V. Jérôme, W. P. Kretschmer, R. Freitag, J. Senker, A. Fery, H. Kress, T. Scheibel and C. Laforsch, Supposedly identical microplastic particles substantially differ in their material properties influencing particle–cell interactions and cellular responses, *J. Hazard. Mater.*, 2022, **425**, 127961.

21 M. Mansor, S. Drabesch, T. Bayer, A. Van Le, A. Chauhan, J. Schmidtmann, S. Peiffer and A. Kappler, Application of Single-Particle ICP-MS to Determine the Mass Distribution and Number Concentrations of Environmental Nanoparticles and Colloids, *Environ. Sci. Technol. Lett.*, 2021, **8**(7), 589–595.

22 T. Lu, B. Gilfedder, H. Peng, S. Peiffer, G. Papastavrou, K. Ottermann and S. Frei, Relevance of Iron Oxyhydroxide and Pore Water Chemistry on the Mobility of Nanoplastic Particles in Water-Saturated Porous Media Environments, *Water, Air, Soil Pollut.*, 2021, **232**(5), 168.

23 E. R. Zettler, T. J. Mincer and L. A. Amaral-Zettler, Life in the "plastisphere": microbial communities on plastic marine debris, *Environ. Sci. Technol.*, 2013, **47**(13), 7137–7146.

24 I. V. Kirstein, S. Kirmizi, A. Wichels, A. Garin-Fernandez, R. Erler, M. Löder and G. Gerdts, Dangerous hitchhikers? Evidence for potentially pathogenic *Vibrio* spp. on microplastic particles, *Mar. Environ. Res.*, 2016, **120**, 1–8.

25 H. K. Imhof, J. Rusek, M. Thiel, J. Wolinska and C. Laforsch, Do microplastic particles affect Daphnia magna at the morphological, life history and molecular level?, *PLoS One*, 2017, **12**(11), e0187590.

26 R. E. Engler, The complex interaction between marine debris and toxic chemicals in the ocean, *Environ. Sci. Technol.*, 2012, **46**(22), 12302–12315.

27 C. G. Avio, S. Gorbi and F. Regoli, Plastics and microplastics in the oceans: from emerging pollutants to emerged threat, *Mar. Environ. Res.*, 2017, **128**, 2–11.

28 M. Lehmann M, L. M. Oehlschlägel, F. P. Häusl, A. Held and S. Gekle, Ejection of marine microplastics by raindrops: a computational and experimental study, *Microplast. Nanoplast.*, 2021, **1**(1), 1–19.

29 K. Liu K, T. Wu, X. Wang, Z. Song, C. Zong, N. Wie and L. Daoji, Consistent Transport of Terrestrial Microplastics to the Ocean through Atmosphere, *Environ. Sci. Technol.*, 2019, **53**(18), 10612–10619.

30 F. Petersen and J. A. Hubbart, The occurrence and transport of microplastics: The state of the science, *Sci. Total Environ.*, 2021, **758**, 143936.

31 T. Ojeda T, A. Freitas, K. Birck, E. Dalmolin, R. Jacques, F. Bento and F. Camargo, Degradability of linear polyolefins under natural weathering, *Polym. Degrad. Stab.*, 2011, **96**(4), 703–707.

32 K. N. Fotopoulou and H. K. Karapanagioti, *Hazardous Chemicals Associated with Plastics in the Marine Environment: Degradation of various plastics in the environment*, Springer, Cham, 2017.

33 F. A. Bottino, A. R. Cinquegrani, G. Di Pasquale, L. Leonardi and A. Pollicino, Chemical modifications, mechanical properties and surface photo-oxidation of films of polystyrene (PS), *Polym. Test.*, 2004, **23**(4), 405–411.

34 F. Horii, Q. Zhu, R. Kitamaru and H. Yamaoka, Carbon-13 NMR study of radiation-induced crosslinking of linear polyethylene, *Macromolecules*, 1990, **23**(4), 977–981.

35 A. V. Shyichuk and J. R. White, Analysis of chain-scission and crosslinking rates in the photo-oxidation of polystyrene, *J. Appl. Polym. Sci.*, 2000, **77**(13), 3015–3023.

36 G. Grause, M.-F. Chien and C. Inoue, Changes during the weathering of polyolefins, *Polym. Degrad. Stab.*, 2020, **181**, 109364.

37 Y. Shi, J. Qin, Y. Tao, G. Jie and J. Wang, Natural weathering severity of typical coastal environment on polystyrene: Experiment and modeling, *Polym. Test.*, 2019, **76**, 138–145.

38 D. Vaillant, J. Lacoste and G. Dauphin, The oxidation mechanism of polypropylene: contribution of ^{13}C-NMR spectroscopy, *Polym. Degrad. Stab.*, 1994, **45**, 355–360.

39 D. M. Mowery, R. A. Assink, D. K. Derzon, S. B. Klamo, R. L. Clough and R. Bernstein, Solid-state ^{13}C NMR

investigation of the oxidative degradation of selectively labeled polypropylene by thermal aging and γ-irradiation, *Macromolecules*, 2005, **38**, 5035–5046.

40 R. A. Assink, M. Celina, T. D. Dunbar, T. M. Alam, R. L. Clough and K. T. Gillen, Analysis of hydroperoxides in solid polyethylene by MAS ^{13}C NMR and EPR, *Macromolecules*, 2000, **33**(11), 4023–4029.

41 S. F. Chabira, M. Sebaa and C. G'sell, Oxidation and crosslinking processes during thermal aging of low-density polyethylene films, *J. Appl. Polym. Sci.*, 2012, **124**, 5200–5208.

42 W. J. Shim, S. H. Hong and S. E. Eo, Identification methods in microplastic analysis: a review, *Anal. Methods*, 2017, **9**, 1384–1391.

43 N. Peez, M.-C. Janiska and W. Imhof, The First Application of Quantitative ^{1}H NMR Spectroscopy as a Simple and Fast Method of Identification and Quantification of Microplastic Particles (PE, PET, and PS), *Anal. Bioanal. Chem.*, 2019, **411**(4), 823–833.

44 J. Almond, P. Sugumaar, M. N. Wenzel, G. Hill and C. Wallis, Determination of the carbonyl index of polyethylene and polypropylene using specified area under band methodology with ATR-FTIR spectroscopy, *e-Polym.*, 2020, **20**, 369–381.

45 T. Menzel, N. Meides, A. Mauel, U. Mansfeld, W. Kretschmer, M. Kuhn, E. M. Herzig, V. Altstädt, P. Strohriegl, J. Senker and H. Ruckdäschel, Degradation of low-density polyethylene to nanoplastic particles by accelerated weathering, *Sci. Total Environ.*, 2022, **826**, 154035.

46 K. Schmidt-Rohr and H. W. Spiess, *Multidimensional Solid-State NMR and Polymers*, Academic Press, San Diego, 1998.

47 M. Ronagh-Baghbani, F. Ziaee, H. Bouhendi and F. Ziaie, Crosslinking investigation of polybutadiene thermal degradation by carbon-13 nuclear magnetic resonance, *Polym. Degrad. Stab.*, 2011, **96**(10), 1805–1811.

48 A. V. Prasad and R. P. Singh, Photooxidative degradation of styrenic polymers: ^{13}C-NMR and morphological changes upon irradiation, *J. Appl. Polym. Sci.*, 1998, **70**(4), 637–645.

49 Y. C. Hsu, R. W. Truss, B. Laycock, M. P. Weir, T. M. Nicholson, C. J. Garvey and P. J. Halley, The effect of comonomer concentration and distribution on the photo-oxidative degradation of linear low-density polyethylene films, *Polymer*, 2017, **119**, 66–75.

50 M. Pop, S. Traian, L. Daraban and R. Fechete, ^{13}C NMR Study of Gamma Irradiated Polystyrene, *Stud. Univ. Babes-Bolyai, Chem.*, 2011, **56**(3), 129–134.

51 Y. Wang, L. Xu, M. Wang, W. Pang and X. Ge, Structural identification of polyacrylonitrile during thermal treatment by selective ^{13}C labeling and solid-state ^{13}C NMR spectroscopy, *Macromolecules*, 2014, **47**(12), 3901–3908.

52 R. L. Johnsen and K. Schmidt-Rohr, Quantitative solid-state ^{13}C NMR with signal enhancement by multiple cross polarization, *J. Magn. Reson.*, 2014, **239**, 44–49.

53 R. Vieira, I. Marin-Montesinos, J. Pereira, R. Fonseca, M. Ilkaeva, M. Sardo and L. Mafra, "Hidden" CO_2 in Amine-Modified Porous Silicas Enables Full Quantitative NMR Identification of Physi- and Chemisorbed CO_2 Species, *J. Phys. Chem. C*, 2021, **125**, 14797–14806.

54 N. J. Brownbill, R. S. Sprick, B. Bonillo, S. Pawsey, F. Aussenac, A. J. Fielding, A. I. Cooper and F. Blanc, Structural Elucidation of Amorphous Photocatalytic Polymers from Dynamic Nuclear Polarization Enhanced Solid State NMR, *Macromolecules*, 2018, **51**, 3088–3096.

55 J. Raya, A. Bianco and J. Hirschinger, Kinetics of ^{1}H–^{13}C multiple-contact cross-polarization as a powerful tool to determine the structure and dynamics of complex materials: application to graphene oxide, *Phys. Chem. Chem. Phys.*, 2020, **22**, 12209–12227.

56 H. Liu, X. Zhou, Q. Chen and S. Zhang, Accurate quantitative and maximum cross polarization *via* multiple ramped contacts, *Chem. Phys. Lett.*, 2017, **679**, 233–236.

57 F. Saïdi, F. Taulelle and C. Martineau, Quantitative ^{13}C Solid-State NMR Spectra by Multiple-Contact Cross-polarization for Drug Delivery: From Active Principles to Excipients and Drug Carriers, *J. Pharm. Sci.*, 2016, **105**, 2397–2401.

58 A. Bertarello, P. Berruyer, U. Skantze, S. Sardana, M. Sardana, C. S. Elmore, M. Schade, E. Chiarparin, S. Schantz and L. Emsley, Quantification of magic angle spinning dynamic nuclear polarization NMR spectra, *J. Magn. Reson.*, 2021, **329**, 107030.

59 H. A. Larsen and H. G. Drickamer, Mechanical degradation and cross linking of polymers by plastic deformation at high pressure, *J. Phys. Chem.*, 1957, **61**(12), 1643–1646.

60 W. Kolodziejski and J. Klinowski, Kinetics of Cross-Polarization in Solid-State NMR: A Guide for Chemists, *Chem. Rev.*, 2002, **102**, 613–628.

61 D. M. Mowery, R. L. Clough and R. A. Assink, Identification of Oxidation Products in Selectively Labeled Polypropylene with Solid-State ^{13}C NMR Techniques, *Macromolecules*, 2007, **40**, 3615–3623.

This article was published in Royal Society of Chemistry Advances 2022, 12, 10875.

Royal Society of Chemistry (2022). *2022 The Author(s). Published by the Royal Society of Chemistry*

Supplementary material: `https://doi.org/10.1039/D2RA00470D`

8.6 Pristine and artificially-aged polystyrene microplastic particles differ in regard to cellular response.

Journal of Hazardous Materials 435 (2022) 128955

Contents lists available at ScienceDirect

Journal of Hazardous Materials

journal homepage: www.elsevier.com/locate/jhazmat

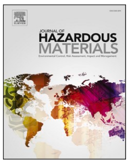

Pristine and artificially-aged polystyrene microplastic particles differ in regard to cellular response

Matthias Völkl[a,1], Valérie Jérôme[a,2], Alfons Weig[b,3], Julia Jasinski[c,4], Nora Meides[d,5], Peter Strohriegl[d,6], Thomas Scheibel[c,7], Ruth Freitag[a,*,8]

[a] *Process Biotechnology, University of Bayreuth, 95447 Bayreuth, Germany*
[b] *Genomics and Bioinformatics, University of Bayreuth, 95447 Bayreuth, Germany*
[c] *Biomaterials, University of Bayreuth, 95447 Bayreuth, Germany*
[d] *Macromolecular Chemistry I, University of Bayreuth, 95447 Bayreuth, Germany*

HIGHLIGHTS

- Biological reaction of macrophages differ between aged and pristine MP.
- Fragmentation and formation of ROS are assumed to contribute a high noxiousness.
- Artificially weathered MP induce higher toxicitiy compared to pristine particles.
- Pristine particles show an higher inflammatory potential.

GRAPHICAL ABSTRACT

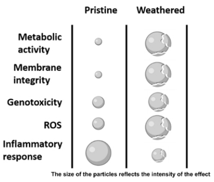

ARTICLE INFO

Editor: Youn-Joo An

Keywords:
Weathered particles
Fragments
Cytotoxicity
Biological effects
Inflammation
Genotoxicity
Transcriptomic
RNA sequencing

ABSTRACT

Microplastic particles (MP), arising from the gradual decomposition of plastics in the environment, have been identified as a global problem. Most investigations of MP cytotoxicity use pristine spherical particles available from commercial sources when evaluating their impact on mammalian cells, while only limited data is available for the more relevant “weathered microplastic”. In this study, we exposed murine macrophages to polystyrene MP either after up to 130 days of accelerated ageing or in pristine condition. Weathered and pristine MP were physicochemically characterized, and their cytotoxicity was investigated using biological assays, transcriptome analysis, and metabolic pathways prediction. Whereas the response to pristine MP is mainly dominated by a TNF-α release, sharp-edged weathered MP induce broader adverse cellular reactions. This study stresses the importance of including more realistic test particles (e.g., weathered particles) in combination with a broad range of biological assays when evaluating the potential risk of microplastic exposure.

---

[*] Correspondence to: Process Biotechnology, University of Bayreuth, 95440 Bayreuth, Germany.
E-mail address: ruth.freitag@uni-bayreuth.de (R. Freitag).

[1] 0000–0002-8750–8733
[2] 0000–0001-6492–2168
[3] 0000–0001-8712–7060
[4] 0000–0003-1093–5857
[5] 0000 0002 2185 4609
[6] 0000–0001-9060–4606
[7] 0000–0002-0457–2423
[8] 0000–0002-6569–9137

https://doi.org/10.1016/j.jhazmat.2022.128955
Received 18 January 2022; Received in revised form 12 April 2022; Accepted 15 April 2022

Reactive oxygen species
Microplastic

1. Introduction

The spread of microplastic is a recognized global problem (Issac and Kandasubramanian, 2021; Conkle et al., 2018; Frei et al., 2019; Weithmann et al., 2018; Amato-Lourenço et al., 2020). Possible accumulation in the food chain and finally the human body seems to be a logical and therefore troubling consequence (Jiang et al., 2020). In recent years, various studies analysed the toxicity of microplastic towards mammalian cells (Liu et al., 2020a, 2020b; Rudolph et al., 2021; Stock et al., 2019; Wu et al., 2019; Liang et al., 2021; Vlacil et al., 2021; Hwang et al., 2020). Most of these studies concluded that microplastic particles (MP) are not as harmful as feared and that they exert effects only at concentrations far above the current environmental ones. However, it has been reported by several groups that environmental concentrations are difficult to measure for MP < 5 µm and could be indeed much higher than assumed (Lindeque et al., 2020). Furthermore, after intake in organisms (e.g., mice, human), MP accumulate over time, are embedded in tissues, and yet persist in the body (Deng et al., 2017; Amato-Lourenço et al., 2021; Ibrahim et al., 2021). In a recent contribution, the concentration of microplastic in human blood was estimated to be 99.4 µg/mL/day (Lee et al., 2021). As recently reviewed, established biological effects of MP on mammalian cells comprise mainly cytotoxicity, oxidative stress, genotoxicity and inflammatory response (Rubio et al., 2020b). In this context, the liver as detoxifying organ seems to be of particular concern in in vivo as well as in cell line-based studies (Zhao et al., 2021a, 2021b; Lu et al., 2018; Li et al., 2021a, 2021b). Even though possible changes on the transcriptional level have been reported (Wu et al., 2020; Jin et al., 2019), only a few studies to date used RNA sequencing for in-depth investigation of the transcriptome of cells challenged with MP.

Moreover, most prior in vitro studies of MP effects on cells used pristine spherical polystyrene (PS) particles due to their defined size and easily accessible surface chemistry (i.e., functionalization) (Rozman and Kalčikova, 2021; Weis and Palmquist, 2021), both of which have been demonstrated to be of high importance for particle-cell interactions (PCI) (Rudolph et al., 2021; Banerjee and Shelver, 2021; Kurtz-Chalot et al., 2017; Ramsperger et al., 2021, 2020). However, such pristine test particles do not necessarily replicate the effect of MP found in the environment (Rubin et al., 2021), since the latter must be expected to become degraded under the influence of mechanical stress as well as photo- and biotic-degradation (Syranidou et al., 2017; Gewert et al., 2015; Meides et al., 2021). This degradative process, commonly referred to as “ageing” or “weathering“, leads to the formation of secondary plastic particles with changed size and surface characteristics (physical and chemical) (Rozman and Kalčikova, 2021; Liu et al., 2021, 2020b).

Laboratory approaches to mimic this degradation process have been suggested and rely on repeated milling (Han et al., 2020) to simulate mechanical abrasion or (accelerated) weathering mostly via photooxidation (Meides et al., 2021). Mechanical stress alone is insufficient to fully simulate the environmental ageing of MP since photodegradation also plays an important role (Liu et al., 2021). Photo-initiated radical reactions with oxygen lead to chain-scission, accompanied by molecular weight decrease and a deterioration of the mechanical properties (Yousif and Haddad, 2013). As a result, oxygen-containing functional groups are formed (e.g., peroxides, -COOH, reactive oxygen species (ROS), ketones) which accumulate at the surface of MP (67–200 µm) along with increasing degradation processes (Meides et al., 2021; Zhu et al., 2019). As recently reported, the oxygen-to-carbon (O/C) ratio of in-house UV-aged 1 µm PS-MP increased by 4.7-fold in comparison to pristine ones (i.e., O/C: 0.031) (Chen et al., 2021). These “weathered” MP are more toxic than pristine ones to a wide range of model organisms (e.g., bacteria, algae, fish) (Huang et al., 2021; Zou et al., 2020; Guimarães et al., 2021; Wang et al., 2020a, 2020b; Zhao et al., 2021b). However, only a few reports are available for mammalian cells. Increased toxicity of photooxidized-particles compared to pristine ones was recently demonstrated using human intestinal epithelial (Caco-2) and lung epithelial (A549) cells (Yu et al., 2021; Zhu et al., 2020). Both reports stressed the fact that there is a correlation between the duration of the light irradiation time and the oxidative potential of the particles, which in turn augments their cytotoxicity. Jeon et al., on the other hand, showed a decreased cytotoxicity for weathered MP compared to milled ones (Jeon et al., 2021). However, none of these works attempted to elucidate the cause of the observed biological effects on a broader basis.

In this work, we analysed the biological effects induced by artificially weathered PS-MP vs. the corresponding pristine ones. The particles (2 µm) were exposed for up to 600 h of controlled accelerated weathering corresponding to 130 days of natural irradiation and their physicochemical properties were characterised. Cellular responses were investigated at the level of metabolic activity, membrane integrity, reactive oxygen species formation, genotoxicity and inflammatory response using the murine liver macrophage cell line ImKC. To better understand the cellular response at the molecular level, we extended our investigation to the analysis of the cellular transcriptome via RNA sequencing. Using extensive data mining, ranging from single genes regulation to pathway analysis, we unravelled the major cytotoxic differences between pristine and weathered MP.

2. Methods

2.1. Materials

If not otherwise indicated, cell culture materials were obtained from Greiner Bio-One (Frickenhausen, Germany) and Thermo Fisher Scientific (Schwerte, Germany). L-glutamine, penicillin, streptomycin, Dulbecco’s Phosphate-Buffered Saline without Ca^{2+} and Mg^{2+} (DPBS), RPMI1640 (Roswell Park Memorial Institute) was obtained from Lonza (Lonza Group Ltd, Basel, Switzerland). Phalloidin-tetramethylrhodamine B isothiocyanate, foetal calf serum (FCS), 4′,6-Diamidino-2-phenylindol (DAPI), 3-(4,5-dimethyl-2-thiazolyl)− 2,5-Diphenyl-2H-tetrazolium bromide (MTT), 2′,7′-dichlorofluorescein diacetate (DCFDA), antimycin A from *Streptomyces sp.* were obtained from Sigma Aldrich (Taufkirchen, Germany). The ELISA Max™ Deluxe Set mouse TNF-α was purchased from Biolegend (San Diego, CA, USA). The CyQuant™ LDH Cytotoxicity Assay Kit was purchased from Invitrogen (Waltham, MA, USA). Low melting agarose was purchased from Carl Roth (Karlsruhe, Germany). The following components were used for RNA extraction, quantification, and library preparation for next-generation sequencing: RNeasy Plus Micro Kit (Qiagen, Hilden, Germany), Precellys kit with 0.5 mm glass beads (VWR, Darmstadt, Germany), NEBNext Ultra II Directional RNA Library Prep Kit, NEBNext Poly(A) mRNA Magnetic Isolation Module, and NEBNext Multiplex Oligos (New England Biolabs, Frankfurt am Main, Germany).

2.2. Particles

Non-functionalized (plain) 2 µm polystyrene particles (non-fluorescent Cat. # 19814–15 and fluorescent Fluoresbrite® YG Microspheres, Cat. # 18338–5, PS-YG, Ex_{Max} 441 nm, Em_{Max} 486 nm, 5.68×10^9 particles/mL, size CV ≤ 5) were purchased from Polyscience (Polyscience Europe GmbH, Eppenheim, Germany). The microplastic particles (MP) solution was delivered as a sterile aqueous suspension at a concentration of 25 mg/mL. According to the supplier, all MP therein are plain particles with a slight residual anionic surface charge from sulphate ester. These MP have been extensively characterized by our group in the past, revealing the presence of 3‰ styrene monomers as well as the absence of surfactant (Ramsperger et al., 2021). The non-fluorescent particles showed no autofluorescence in the ex/em ranges of interest for the intended experiments. The fluorescence measurement of the MP was conducted using flow cytometry at 525 nm (Cytomics FC500, Beckman Coulter, Krefeld, Germany). Data analysis was done using the FlowJo software v 10.5.0 (Tree Star, Stanford University, CA, USA, 2018).

2.3. Accelerated weathering

Accelerated weathering was carried out according to Meides et al. Meides et al. (2021) and is described in detail in the supplementary information. The applied irradiance was calculated to be 594 W/m^2 in total (Fig. S1, Table S1). Compared to the average mid-European irradiation of 114 W/m^2 (Fig. S2), the irradiance in the weathering chamber is thus 5.2-fold enhanced (Table S1). Samples were drawn after 200 (PS$_{43}$), 400 (PS$_{86}$) and 600 h (PS$_{130}$) of incubation in the weathering chamber, translating to approximately 43, 86 and 130 days of weathering in nature. The effective ageing time was calculated according to Eq. (1).

$$\frac{Irradiation\quad time\quad [h] * Acceleration\quad factor}{24} = effective\quad weathering\quad in\quad the\quad environment\quad [days] \tag{1}$$

2.4. Particles preparation

PS$_{\text{pristine}}$ were used as received. Weathered particles (2.5 mg/mL in Milli Q water; 50 mL total volume) were recovered by centrifugation (16,000 *g*, 5 min), washed with 1 mL Milli Q water and incubated overnight in 1 mL of 70 vol% ethanol in sterile Milli Q water. After incubation, particles were collected by centrifugation (16,000 *g* for 5 min), the ethanol solution was discarded and the remaining ethanol was evaporated overnight under sterile conditions. Particles were then resuspended in 1 mL sterile Milli Q water, centrifugated at 16,000 *g* for 5 min, the supernatant was then carefully discarded. Thereafter, the particles were suspended in sterile MilliQ water to reach a final concentration of 25 mg/mL. For experiments, MP were diluted 1/167–1/1667-fold in complete growth medium to reach final concentrations of 150 µg/mL and 15 µg/mL, respectively.

2.5. Particle characterization

The ζ-potential measurements were performed using the LiteSizer 500 (Anton Paar Germany GmbH, Ostfildern-Scharnhausen, Germany) and Omega cuvettes (Anton Paar Germany GmbH, Ostfildern-Scharnhausen, Germany). Briefly, 2.5 µL of the stock solution was directly diluted in 1 mL of a 1 mM aqueous KCl solution or complete growth medium and measured immediately. Measurements with MP incubated in complete growth medium were conducted as follows: 2.5 µL of the stock solution was incubated in 1 mL complete growth medium overnight at 37 °C. Thereafter, the MP were collected using centrifugation (17,000 *g* for 40 min at room temperature (RT)) and resuspended in 1 mL of a 1 mM KCl solution for measurement. Three measurements, with at least 100 runs each, were performed at 21 °C with an adjusted voltage of 200 V. The ζ-potential was calculated using the Helmholtz-Smoluchowski equation (von Smoluchowski, 1906).

For particle imaging, a 0.5 mg/mL aqueous particle solution was put on a silica wafer. The samples were dried overnight and were afterwards sputter coated with platinum. The imaging was performed using SEM (FEI Apreo Volumescope, Thermo Fisher Scientific, magnification: 50,000, 2 kV, Everhart-Thornley detector (ETD)).

2.6. Cell culture

The murine hepatic resident macrophage (Kupffer cells) cell line ImKC was obtained from Merck (SCC119, Merck KGaA, Darmstadt, Germany). This cell line was cultivated in RPMI1640 medium supplemented with 10% (v/v) FCS, 2 mM glutamine and 100 U/mL penicillin/streptomycin (complete growth medium) in a standard cell culture incubator (5% CO$_2$, 95% humidity, 37 °C). Cells were passaged three times a week. Detaching of the cells was performed by incubating the cells in pre-warmed (37 °C) citric saline buffer (135 mM potassium chloride, 15 mM sodium citrate) for 10 min.

2.7. Qualitative analysis of MP uptake

15,000 cells were seeded in each well of an 8-well Ibidi slide (µ-Slide 8 Well, ibiTreat, ibidi GmbH, Gräfelfing, Germany). After 24 h incubation, fluorescent particles were added (150 µg/mL, total cultivation volume: 300 µL). Thereafter, cells were fixed for 15 min at RT with preheated 3.7% (v/v) paraformaldehyde in DPBS. Afterwards, the cells were permeabilized with 0.1% (v/v) TritonX-100 for 10 min at RT. Actin filaments and nuclei were stained with 100 nM rhodamine-phalloidin and 100 nM DAPI, respectively. The samples were analysed using a confocal laser scanning microscope (TCS SP8, 63x oil immersion objective, laser: 408 nm, 488 nm, and 552 nm, Leica Microsystems, Wetzlar, Germany). Z-stacks were taken with a step size of 0.2 – 0.33 µm.

2.8. Quantitative analysis of MP uptake

MP uptake was performed as previously described (Rudolph et al., 2021). Briefly, for quantification of the particle-cell-interaction, 150,000 cells per well were seeded in 12-well culture plates and incubated for 24 h for cell adhesion. Afterwards, 150 µg/mL fluorescent particles (PS$_{\text{pristine}}$, PS$_{\text{aged}}$) were added. After another 24 h of incubation, the cells were collected as described above and analysed using flow cytometry (Cytomics FC500, Beckman Coulter, Krefeld, Germany). Analysis was done using the FlowJo software v 10.5.0 (Tree Star, Stanford University, CA, USA, 2018).

2.9. MTT assay

MTT (3-(4,5-dimethyl-2-thiazolyl)– 2,5-diphenyl-2 H tetrazolium bromide) assay, based on the reduction of tetrazolium salt to formazan, was used to analyse the metabolic activity of the cells. This assay is an established assay for the toxicological assessment of microplastic (Rudolph et al., 2021; Stock et al., 2019; Hesler et al., 2019). Briefly, 10,000 cells/well were seeded in a 96-well plate in a 100 µL complete growth medium. After 24 h incubation in the cell culture incubator, the medium was aspirated, and a freshly prepared particle suspension in the desired concentration was added. In this study, we used 15 and 150 µg/mL MP, both shown to be sublethal as shown in our previous studies for pristine particles (Rudolph et al., 2021; Ramsperger et al., 2021). Cells were then cultivated for another 24 h in the cell culture incubator. Afterwards, the medium was replaced by 50 µL per well freshly prepared MTT reagent (1 mg/mL MTT in MEM without phenol red, sterile-filtrated). Cells were incubated for 2 h, the supernatant was removed, and 100 µL isopropanol was added to dissolve the formazan crystals. The whole plate was shaken for 5 min at 600 rpm. The absorbance was measured at 570 nm (reference wavelength 650 nm) using a Tecan GENios Pro plate reader (Tecan Austria GmbH, Gröding, Austria) and metabolic activity was calculated according to Eq. (2). Cells put through mock treatment (i.e., incubated without MP) were used as a negative control (blank, corresponding to 100% metabolic activity). Cells incubated with 0.3% v/v Triton X-100 were used to prepare the positive control. As part of the experimental setting, we previously examined the influence of MP on the MTT assay readout and showed that, at the used concentration range, MP do not interfere with the absorption measurement (Ramsperger et al., 2021).

$$metabolic \quad activity \quad [\%] = \frac{Abs570_{sample}}{Abs570_{blank}} x \quad 100 \tag{2}$$

where: $Abs_{570\text{-}sample}$ is the mean value of the measured absorption of the test sample; $Abs_{570\text{-}blank}$ is the mean value of the measured absorption of the negative control.

2.10. Reactive oxygen species assay

The intracellular ROS assay is based on the conversion of the non-fluorescent, membrane-permeable dye 2′,7′-dichlorofluorescein diacetate (DCFDA) into the fluorescent 2′, 7′-dichlorofluorescein (DCF) upon oxidation by ROS. 150,000 cells per well in 1 mL complete growth medium were seeded in a 12-well plate. After 24 h of incubation (5% CO_2, 95% humidity, 37 °C), freshly prepared particle suspensions were added at the respective concentration. Cells incubated without MP or in the presence of 50 µM Antimycin A under otherwise identical conditions were used as negative (NC) and positive controls, respectively. After 60 min incubation, 37.5 µM DCFDA was added per well and incubated for another 24 h in the cell culture incubator. Cells were then collected, washed in DPBS and measured using flow cytometry at 525 nm (Cytomics FC500, Beckman Coulter, Krefeld, Germany). ROS amount was calculated according to Eq. (3).

$$ROS \quad amount \quad [\%] = \frac{MFI_{sample}}{MFI_{NC}} x \quad 100 \tag{3}$$

where: MFI_{sample} is the mean fluorescence intensity of the green fluorescence of the test sample; MFI_{NC} is the mean fluorescence intensity of the green fluorescence of the negative control (i.e., cells incubated without MP).

2.11. LDH assay

The lactate dehydrogenase (LDH) assay measures the release of the cytosolic enzyme LDH in the supernatant upon plasma membrane damage. The assay was done according to the manufacturer's instructions. Briefly, 10,000 cells were seeded in 100 µL of complete growth medium in a 96-well plate and incubated for 24 h under cell culture conditions. The medium was then aspirated and a freshly prepared particle suspension was added at the respective concentration. Cells incubated without MP under otherwise identical conditions were used as a negative control to record the spontaneous LDH release. Afterwards, cells were cultivated for another 24 h in the cell culture incubator. To estimate the maximum releasable LDH, 10 µL of the diluted lysis buffer (proprietary composition) was added to cells without MP (45 min incubation). 50 µL of supernatant from each well was transferred to a fresh 96-well plate, then 50 µL of the freshly prepared reaction mixture was added and incubated for another 30 min in the cell culture incubator. Finally, 50 µL of stop solution were added to each well and the absorbance was measured at 490 nm (reference wavelength 680 nm). The cytotoxicity was calculated according to Eq. (4):

$$\% \quad LDH \quad release = \frac{Abs_{sample} - Abs_{spontaneous}}{Abs_{max} - Abs_{spontaneous}} \tag{4}$$

where: Abs_{sample} is the mean value of the measured absorption of the test sample; $Abs_{spontaneous}$ is the mean value of the measured absorption of the negative control; Abs_{max} is the mean value of the measured absorption of the positive control.

2.12. COMET assay

A detailed step-by-step protocol of the COMET assay can be found in the supplementary information. Briefly, 150,000 cells were seeded in a 12-well plate, incubated for 24 h and treated with the respective (15 and 150 µg/mL) particle concentration for another 24 h (5% CO_2, 95% humidity, 37 °C). Cells were then harvested, resuspended in 0.1 mL of a solution of 1% low melting point agarose in DPBS and then transferred onto agarose pre-coated slides. After conducting the lysis and pretreatment, electrophoresis was conducted at 20 V (0.6 V/cm) and 200 mA for 30 min, conditions which had been established as suitable in pre-experiments. DNA on the slides was stained with 2 µg/mL DAPI (1 mL) for 20 min in the dark. Slides were analysed using a fluorescent microscope (BX51, Olympus Life Science Solutions, Hamburg, Germany). Pictures were taken and afterwards analysed with the COMET-SCORE™ software (version 2.0.0.38; http://rexhoover.com).

2.13. ELISA TNF-α

TNF-α was analysed to screen the inflammatory potential of the MP. 10,000 cells/well were seeded in 100 µL of growth medium in a 96-well plate and incubated for 24 h in the cell culture incubator. Afterwards, the particles were added and incubated for another 24 h (5% CO_2, 95% humidity, 37 °C). As a negative control, cells were incubated without MP, while cells in the positive control were stimulated with 2.5 µg lipopolysaccharides (LPS). TNF-α release in the cell culture medium was detected by ELISA according to the manufacturer's instructions.

2.14. RNA sequencing

Samples for the RNA sequencing (RNA seq) were prepared as follows: 300,000 cells/well were seeded in 2 mL of complete growth medium in a 6-well plate and incubated for 24 h (5% CO_2, 95% humidity, 37 °C). The indicated particle concentration was added and incubated for another 24 h (5% CO_2, 95% humidity, 37 °C). Afterwards, the supernatant was discarded, the cells were washed twice with DPBS and 350 µL lysis buffer RLT© was added to each well. The lysate was transferred to an RNAse-free Eppendorf tube and immediately frozen at - 20 °C. Thereafter, the lysate was homogenized with 0.5 mm glass beads (Precellys kit, tube size 2 mL) at the intensity setting 6 for 40 s on a Fast Prep 24 device (MP Biomedicals, Eschwege, Germany). Total RNA was purified from the homogenate using the RNeasy Plus Micro Kit and the RNA quality was analysed using a Fragment Analyzer and the DNF-471 kit (Agilent, Waldbronn, Germany). RNA-Seq libraries were constructed using the NEBNect Ultra II Directional RNA Library Prep kit for Illumina in combination with the NEBNect Poly(A) mRNA Magnetic Isolation Module and NEBNext Multiplex Oligos as described in Section 1 of the instruction manual (New England Biolabs, Frankfurt am Main, Germany). The quality of the obtained cDNA libraries was analysed using a Fragment Analyzer and the DNF-477 kit. The sample libraries were combined in a single library pool and sequenced in 2 × 150 bp mode on a NovaSeq instrument (Genewiz, Leipzig, Germany).

2.15. Statistics

Demultiplexed RNA-Seq data were analysed using the OmicsBox bioinformatics package (ver. 2.0.36; www.biobam.com/omicsbox), which included all of the following tools: Reads were pre-processed by Trimmomatic to remove remnants of Illumina TruSeg3 adapters and reads with Q score below 25 were filtered out. The selected reads were mapped to the mouse reference genome (genome assembly GRCm39, www.ensembl.org) by STAR, and gene-specific quantifications of mapped reads were created using HTseq. Pairwise differential expression of the count data was performed by edgeR. Gene Ontology (GO) enrichment analyses were conducted using Fisher's Exact Test and the GRCm39 functional annotation, and the resulting GO terms were filtered by FDR < 0.05. Gene Set Enrichment Analyses (GSEA, implemented in the OmicsBox package) were conducted based on a rank matrix (rank = sign(logFC) * -log10(P-Value)) using gene ontology sets based on the GRCm39 functional annotation as well as the Kyoto Encyclopedia of Genes and Genomes (KEGG). In addition, networks of enriched GO were predicted using ClueGO (Bindea et al., 2009), a Cytoscape plug-in, based most recent ClueGO database releases (May 13, 2021). Enriched pathways of the KEGG database were identified by a mouse-specific KEGG dataset available in Cytoscape-ClueGO. Unless otherwise indicated, default settings of the bioinformatics tools were used to analyse the data.

Statistical analysis was performed using Origin software 2019b (Origin, Northampton, MA, USA). All data were tested for the homogeneity of variances (Levene test). To investigate differences in MP interactions with cells results, a one-way ANOVA with a Tukey post hoc test was used.

3. Results

3.1. Particle characterization

The goal of this study was, to compare the noxic effects of pristine (spherical beads with smooth surface) particles and artificially weathered corresponding ones. It is well-recognized in the microplastics research field that surface property and size of the particles both influence their uptake rate and noxious effects. In this context, it was important to cut down the number of parameters changed and hence to choose an ageing stage that leads to changes in surface properties while preserving the size of the particles as much as possible. Therefore, we prepared the weathered particles using the same weathering chamber and procedure used in the past (Meides et al., 2021) but restricted the irradiation time to 200, 400, and 600 h, where the degradation is mainly consisting of surface abrasion, to preserve the particle size (as shown using DLS in the current manuscript, Table 1). Due to the acceleration factor (5.2) of the weathering chamber, these irradiation times approximately correspond to 43 (PS_{43}), 86 (PS_{86}) and 130 days (PS_{130}) of ageing in the environment. Particle characteristics (i.e., size, surface charge and topology) are decisive for the effects of MP on cells (Ramsperger et al., 2021). Here, qualitative scanning electron microscopy (SEM) revealed that prolonged weathering of the particles intensified the degradation effect (Fig. 1).

While there was almost no difference in morphology between $PS_{pristine}$, PS_{43} and PS_{86}, PS_{130} showed a high frequency of cracks and pits in the majority of the MP (75%). The analysis using dynamic light scattering (DLS) confirmed that extending the irradiation time led to a decrease in the average particle size from 1.80 μm to 1.21 μm. In case of fluorescent particles, weathering led to a decrease in the fluorescence by two orders of magnitude (Fig. S3). Compared to $PS_{pristine}$ and PS_{43}, PS_{130} exhibited a broader fluorescence range being in line with DLS and SEM data, since it can be ascribed to the presence of smaller fragments. In all cases, the remaining fluorescence was still high enough to be detectable with the methods used in this study (e.g., confocal microscopy, flow cytometry). ζ-potential measurements were performed to estimate the influence of the weathering on the surface charge of the MP. Small but significant differences in surface charge were identified when KCl was used as an ionic background stabiliser. The charge of PS_{aged} was lower (13% for PS_{43} and PS_{86}, 18% for PS_{130}) compared to that of $PS_{pristine}$. When incubated in a complete cell culture medium containing serum proteins, the charge of the different MP decreased about two-fold while minor, ageing-dependent differences remained (Table 1).

Table 1
Size distribution measured using DLS and ζ-potential for $PS_{prisitne}$ and PS_{aged}.

	MP size (μm)		ζ-potential (mV)	
	KCL	Medium[a]	KCl	Medium[a]
$PS_{pristine}$	1.80 ± 0.03[b]	1.50 ± 0.04[b]	-76.7 ± 0.3[c]	-30.7 ± 0.1[c]
PS_{43}	1.63 ± 0.11	1.88 ± 0.05	-67.1 ± 0.7	-33.9 ± 0.2
PS_{86}	1.50 ± 0.12	1.49 ± 0.10	-67.8 ± 0.4	-29.5 ± 0.1
PS_{130}	1.21 ± 0.04	1.63 ± 0.22	-64.6 ± 1.6	-26.4 ± 0.2

Data represent mean value ± SD, n = 3.
[a] Medium: complete growth medium.
[b] Data from Riedl et al. (2021).
[c] Data from Rudolph et al. (2021).

In addition, the exposition of reactive groups on the surface, usually reported as oxygen-to-carbon (O/C) ratio, should also be considered as it plays an important role in microplastic ageing processes (Wang et al., 2020a, 2020b). In this context, we found an increased O/C ratio for both PS MP and tensile bars exposed to the same weathering method (Meides et al., 2021). Further, these data demonstrated that independently of the geometry and size of the sample the ageing progression underwent a two-stage degradation process. Whereas the first stage (< 800 h of treatment) mainly consists of surface abrasion, the second step (> 800 h of treatment) involves a progressive fragmentation of the samples. Consequently, it can be assumed that this former characterization of the particles is also valid for the, here, used 2 μm particles.

3.2. Qualitative and quantitative particle uptake

In this study, we used murine hepatic stellate macrophages (ImKC), which are, as previously shown by our group (Rudolph et al., 2021), well-suited for the investigation of the potential adverse effects of MP in in vitro assays. We first determined the uptake of PS_{aged} and $PS_{pristine}$ using confocal microscopy using 150 μg/mL fluorescent particles per 15, 000 cells in 300 μL complete growth medium and 24 h incubation. Even though the particle fluorescence for PS_{aged} was reduced (Fig. S3) cellular uptake could be demonstrated (Fig. S4). Using a gating strategy previously developed (Rudolph et al., 2021), quantitative analysis using flow cytometry showed no significant difference in the particle-cell interaction (PCI) for $PS_{pristine}$, PS_{43} and PS_{130} (Fig. S5). When treated with 150 μg/mL MP, only 60% of the cells did show any interaction with the particles (Table S2). The tendency for particle uptake by the cells is therefore similar for weathered and pristine MP.

3.3. Evaluation of cellular toxicity

To gain a deeper understanding of the cellular responses after exposure of cells to PS_{aged} and $PS_{pristine}$, we performed a multiparametric cytotoxicity assessment. Therefore, our study first compared results obtained after MTT or the LDH assay in identically MP-treated cells. The metabolic activity of the cells was measured using the MTT assay. The cells were treated with 15 μg/mL and 150 μg/mL MP and incubated for 24 h, i.e. conditions, which had previously been shown to be non-toxic for $PS_{pristine}$ (Rudolph et al., 2021). A particle concentration in this range has been recently estimated in human blood (Lee et al., 2021). Therefore, the concentrations chosen here can be considered as physiologically relevant.

3.3.1. Cytotoxicity and genotoxicity of PS_{aged} compared to $PS_{pristine}$

While the effect of the $PS_{pristine}$ was again negligible, cells responded differently to the PS_{aged} (Fig. 2A). The metabolic activity significantly dropped for PS_{130} at low (63%) and high concentrations (48%) compared to the control group with no further treatment. PS_{43} and PS_{86}, also caused a reduction in metabolic activity, albeit only when applied at

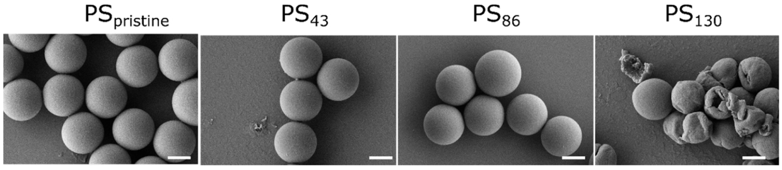

Fig. 1. Representative SEM pictures of $PS_{pristine}$, PS_{43}, PS_{86} and PS_{130}. Shown are SEM pictures of MP at the respective ageing time, scale bars = 1 μm.

high concentrations.

Although the MTT assay is a useful tool for the first evaluation of cytotoxic effects, it may be biased by various biological aspects (Stepanenko and Dmitrenko, 2015). To gather additional information, putative effects of MP on ImKC cells were subsequently studied in more detail, including membrane integrity, genotoxicity, oxidative stress and immune response.

To estimate the degree of cell membrane damage, the lactate dehydrogenase (LDH) release was quantified using control cells to normalize for background LDH release. While no significant effects were detected for $PS_{pristine}$, PS_{43} and PS_{86}, neither for the low nor the high concentration, PS_{130} induced concentration-dependent LDH release and subsequently higher membrane damage (Fig. 2B). In case of genotoxicity, the COMET assay is an established method to detect DNA damages in single cells using denaturing electrophoresis (Ostling and Johanson, 1984). This assay was used to detect possible genotoxicity induced by the MP and included untreated cells and cells incubated with 170 μM H_2O_2 as negative and positive controls, respectively (Fig. 2C, Fig. S6). Cells incubated with $PS_{pristine}$ showed an increased percentage in tail DNA at the highest particle concentration (Median = 21.84% Tail DNA) compared to control cells with no further particle treatment (14.98%), indicating some impact of MP on DNA integrity. Similar effects were detected upon incubation with PS_{43} (18.05%) and PS_{86} (19.55%). The most pronounced DNA damage was observed in the presence of 150 μg/mL PS_{130} (33.69%) with a significantly higher percentage of tail DNA compared to that of untreated and $PS_{pristine}$ treated cells. The high deviation in the respective data sets was probably due to different amounts of taken-up MP resulting in a broad variation in the cellular response.

3.3.2. Evaluation of the reactive oxygen species production

Another influencing factor of the outcome of the previous assays might be an intracellular accumulation of ROS (Valdivia et al., 2015; Haider et al., 2021). In Fig. 2D, the ROS amount was first determined by considering the whole cell population. At low concentrations, none of the treatments showed a statistically significant increase in ROS production in comparison to non-treated cells. However, the amount of ROS significantly increased (1.3-fold) when PS_{86} and PS_{130} were applied at a high concentration. Since ROS were measured using flow cytometry, the amount of ROS can be analysed at the single-cell level and yet correlated with the number of MP interacting with cells, (Fig. S7) (Rudolph et al., 2021). When the subpopulation showing PCI was gated (PCI^+ gate, Fig. S7), the ROS amount increased significantly (1.2-fold for $PS_{pristine}$, 2.0-fold for PS_{43}, 2.7-fold for PS_{86}, 2.7-fold for PS_{130}) compared to cells without MP (PCI^- gate, Fig. S7) corresponding to the ROS intracellular background in the same sample (Fig. 2E).

3.4. Detection of TNF-α as pro-inflammatory response to MP

The inflammatory response in macrophages is usually triggered by the uptake of foreign matter including MP (Merkley et al., 2021) or the secretion of cytokines from other cells (Frostegård et al., 1999). One of the main cytokines in the cell-mediated inflammatory response is the secreted TNF-α cytokine (Coppack, 2001), which we analysed to get a first survey for a pro-inflammatory response (Fig. 3).

While control cells with no further treatment did show an amount of secreted TNF-α (0.35 ng/mL) comparable to that described in literature (Wang et al., 2014), MP treated cells consistently showed an increased level. Surprisingly, the level of secreted TNF-α was the highest for $PS_{pristine}$ exposed cells (a 7.8-fold increase compared to control). With a 7.0-fold and 6.7-fold increase, comparable and slightly lower TNF-α levels were detected for PS_{43} and PS_{86} treated cells, respectively. Exposure to PS_{130} on the other hand, resulted in the lowest, albeit still significant, induction of TNF-α (2.5-fold increase). LPS (2.5 μg/mL) was used as positive control and induced a TNF-α secretion with a 69-fold increase.

3.5. Gene expression and metabolic pathway

We limited the transcriptome analysis to untreated cells and cells challenged with $PS_{pristine}$ as well as PS_{130} at the highest concentration, which induced the most significant effects as shown above. Comparing the transcriptome for differentially-expressed (DE) genes, significant differences could be observed between untreated samples and the samples treated with $PS_{pristine}$ and PS_{130}, respectively. This variation in gene regulation is reflected in the multidimensional scaling (MDS) plot (Fig. 4A). Replicates show a small overall distribution, ensuring a high significance in the subsequent analysis. The unique separation of $PS_{pristine}$ (mainly dim 1) and PS_{130} (mainly dim 2) samples compared to control ones argues for fundamental differences in the transcriptional response to the two types of particles. The number of induced (up) and repressed (down) genes were considerably larger in the $PS_{pristine}$ vs. control pairwise comparison (251 up, 126 down; $\log_2FC > \pm 1$, false discovery rate (FDR) < 0.05) compared to the PS_{130} vs. control comparison (39 up, 15 down; $\log_2FC > \pm 1$, FDR < 0.05), where only 20 induced and eight repressed overlapping genes were seen (Supplementary Data 1). Focussing on the top 10 up- and top 10 downregulated genes for the respective treatment (Table S3 and S4) indicates a partial association with immune response-related processes. In particular, a challenge with $PS_{pristine}$ induced bi-directional regulation (five upregulated, five downregulated), while PS_{130} treatment exclusively led to downregulation (four downregulated genes) of genes.

For a deeper correlation to possible biological effects, gene set enrichment analysis (GSEA) using the gene ontology (GO) annotations of the mouse genome were performed using DE gene rank matrices of $PS_{pristine}$ or PS_{130} treated cell samples vs. control cell samples, respectively. Again, the majority of enriched GO terms elicited by $PS_{pristine}$ or PS_{130} treatments highlight different transcriptional responses towards the two types of MP as shown in a Venn diagram (Fig. 4B). Based on the hierarchical structure of the GO database, the top 50 upregulated and the top 50 downregulated GO terms for $PS_{pristine}$ and PS_{130} (by normalized enrichment score (NES)) were reduced to most specific terms. The 36 remaining GOs were then manually sorted into unifying terms (Table 2). Again, both treatments showed a high difference, with 20 GOs showing a unique response for either $PS_{pristine}$ or PS_{130}. The most affected parental terms were "cellular respiration (eleven annotations)", "immune response (seven annotations)" and "membrane-related (six annotations)".

Furthermore, a cluster analysis of involved upregulated GOs was performed using the Cytoscape plug-in ClueGO. This type of analysis

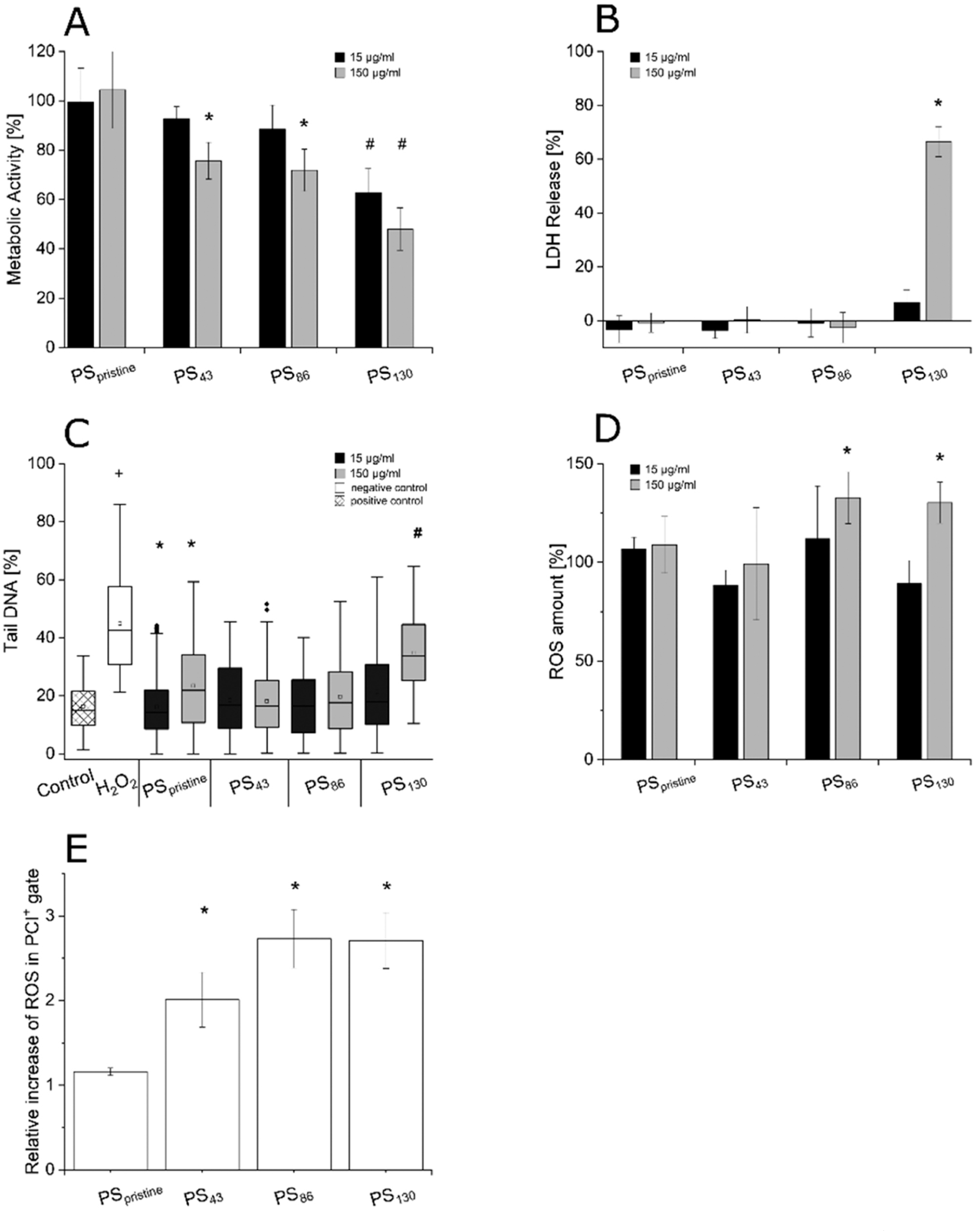

(caption on next page)

Fig. 2. Toxicity evaluation of ImKC cells on different biological levels for $PS_{pristine}$ and PS_{aged}. Black bar bars represent 15 µg/mL, grey bars 150 µg/mL MP treatment. Data represent mean ± SD with at least n = 3 biological replicates if not otherwise noted. Cells without any treatment acted as a negative control. (A) MTT assay was used to determine the cellular metabolic activity. * significantly lower compared to $PS_{pristine}$ within a concentration group, # significantly lower than all previous data points within a concentration group, $p < 0.05$. (B) LDH assay was used to determine the membrane integrity. * significantly higher compared to all other samples, $p < 0.05$. (C) COMET assay was used to estimate the genotoxicity. Pictured is the percentage of Tail DNA for the respectively treated cells. Data are represented with whisker boxplots showing the 25% and 75% quartile with the whiskers representing the maximal and minimal values. Outliers are defined as 1.5 times the value of the 25% and 75% quartile threshold and are represented as diamonds outside the boxplot. The median is indicated as a black line and the mean value as a black square. Control (n = 314), H_2O_2 (n = 59), $PS_{pristine}$ 15 µg/mL (n = 418), $PS_{pristine}$ 150 µg/mL (n = 324), PS_{43} 15 µg/mL (n = 103), PS_{43} 150 µg/mL (n = 107), PS_{86} 15 µg/mL (n = 71), PS_{86} 150 µg/mL (n = 71), PS_{130} 15 µg/mL (n = 72), PS_{130} 150 µg/mL (n = 102). * significantly higher compared to control, # significantly higher within MP-treated groups, + significantly higher than all other groups, $p < 0.05$. (D) Intracellular ROS quantification. Quantity was normalized to a negative control without MP. * significantly higher within concentration and treatment groups, $p < 0.05$. (E) Shown is the fold increase of ROS amount in the subpopulation of cells with PCI (PCI^+ gate, Fig. S7) in comparison to cells without PCI (ROS intracellular background, PCI^- gate, Fig. S7) in the same sample. * significantly higher compared to $PS_{pristine}$, $p < 0.05$.

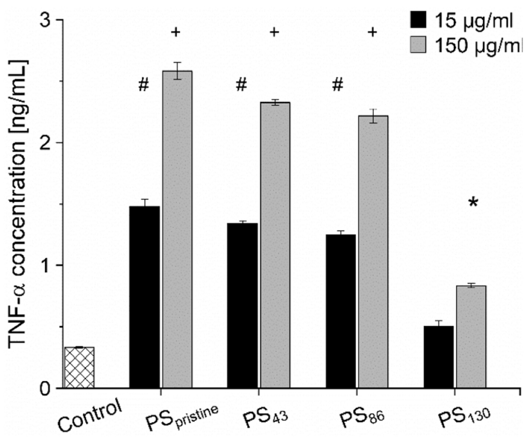

Fig. 3. TNF-α concentration measured in the medium. Black bars represent 15 µg/mL, grey bars 150 µg/mL of MP treatment. Cells without any treatment acted as negative control (control). Data represent mean ± SD, n = 3 biological replicates. * significantly higher compared to control, # significantly higher than PS_{130}, + significantly higher within a treatment group, $p < 0.05$.

confirmed that most of these GOs were specifically clustered for the respective treatment (Fig. S8B). Within these clusters, nine specific groups were highly connected for the respective treatments (Fig. S8A).

Finally, the Kyoto Encyclopedia of Genes and Genomes (KEGG) pathway database (mouse-specific version of ClueGO) was analysed using induced genes to identify enriched KEGG pathways. Using the default pathway selection parameters of ClueGO, 35 KEGG pathways could be identified from 251 $PS_{pristine}$ induced genes. Among the ten most significant (based on FDR) pathways, seven could again be allocated to known inflammation-related pathways (e.g., “cytokine-cytokine receptor, TNF signalling, IL-17 signalling and NF-κB signalling”) (Fig. 5) (Li et al., 2021b, 2019, 2017; Osborn et al., 1989). However, the same default pathway selection parameters did not result in any enriched pathway predictions neither for downregulated genes of $PS_{pristine}$ treatments nor for up- and downregulated genes in PS_{130} experiments. This can most probably be ascribed to the considerably smaller number of identified genes in both cases (Data S1).

4. Discussion

Our investigation of cellular responses (membrane integrity, metabolic activity, genotoxicity, oxidative stress) in the presence of pristine vs. weathered PS-MP revealed that even though both particle types are similarly taken up by the cells, only the long-time weathered MP induced cytotoxic effects in a dose-dependent manner, while pristine and short to middle-time weathered MP tended to induce a pro-inflammatory response in a concentration-dependent manner.

As recently reported, the cytotoxicity of PS MP could also at least partly be related to leachable components (i.e., surfactants used to stabilize sub-micron MP, unreacted monomers due to incomplete purification) (Choi et al., 2020; Campanale et al., 2020). Therefore, we chose for our study conditions that are expected to reduce the influence of leachable components to the minimum (i.e., sub-lethal MP concentrations, extensive washing of PS_{aged}). We have shown in the past that $PS_{pristine}$ does not contain a detectable amount of surfactant, however, a non-negligible amount of residual styrene monomers (3 µg/mL) was found (Ramsperger et al., 2021). Such styrene monomers concentration is in a range (1.04–10.4 µg/mL) reported as non-toxic for the C2C12

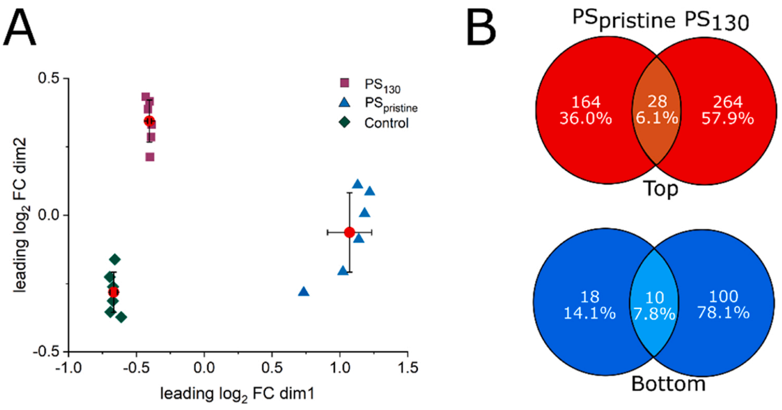

Fig. 4. Different transcriptomic impacts of PS_{130} and $PS_{pristine}$ (A) Multidimensional scaling plot based on the $\log_2$ fold changes (FC) between control, $PS_{pristine}$ and PS_{130} samples. The axes of the MDS plot represent dimensional reductions of genes expression visualizing the variability of the transcriptional changes for a given treatment. (B) Venn diagram comparing the most specific GOs identified by GSEA for $PS_{pristine}$ and PS_{130}, respectively, against the control. Red: upregulated genes; blue: downregulated genes.

Table 2
Direct comparison of all appearing gene ontologies (GOs), reduced to most specific ones for $PS_{pristine}$ and PS_{130} treatment. Grey boxes highlight upregulated GOs.

Parental GO term	Gene Ontology	GO ID [GO-xx]	NES[a]	
			$PS_{pristine}$ vs. Control	PS_{130} vs. Control
Uptake	early endosome	0005769	2.904	
	vacuole organization	0007033	2.714	
	nucleotide transport	0006862	-2.248	
Ribosomes	cytosolic small ribosomal subunit	0022627	-3.388	-3.540
	cytosolic large ribosomal subunit	0022625	-2.963	-3.764
	structural constituent of ribosome	0003735	-2.913	-6.619
Immune response	positive regulation of response to external stimulus	0032103	3.152	
	cellular response to interleukin-1	0071347	2.799	
	regulation of inflammatory response	0050727	-2.482	-2.460
	transforming growth factor-beta binding	0050431	-2.242	
	interleukin-1 production	0032612	-2.238	
	cellular response to interferon-beta	0035458		-3.348
	defence response to virus	0051607		-3.307
Oxygen Level	cellular response to hypoxia	0071456	2.858	2.068
	positive regulation of reactive oxygen species metabolic process	2000379	-2.402	
Cellular Respiration	mitochondrial respiratory chain complex I	0005747	-3.174	-3.658
	proton-transporting V-type ATPase complex	0033176	3.114	2.353
	fatty acid beta-oxidation	0006635	-2.884	-2.107
	mitochondrial respiratory chain complex I assembly	0032981	-2.830	-3.644
	proton-transporting ATPase activity, rotational mechanism	0046961	2.779	2.017
	glycolytic process	0006096	2.660	
	NADH dehydrogenase (ubiquinone) activity	0008137	-2.449	-2.348
	mitochondrial electron transport, NADH to ubiquinone	0006120	-2.240	-2.848
	small GTPase binding	0031267	2.030	3.856
	mitochondrial large ribosomal subunit	0005762		-3.447
	GTPase activator activity	0005096		2.890
Membrane-related	nucleotide transmembrane transporter activity	0015215	-2.366	
	basement membrane	0005604	-2.363	
	cell projection membrane	0031253	2.123	2.788
	apical plasma membrane	0016324	2.095	2.878
	focal adhesion	0005925		3.294
	phosphatidylinositol binding	0035091		2.988
Other	positive regulation of peptidyl-serine phosphorylation	0033138	2.671	
	DNA repair	0006281	-2.230	
	cholesterol biosynthetic process	0006695	2.228	3.123
	ALTERNATE of GO:0140658	0070615		3.054

[a] NES: normalized enrichment score.

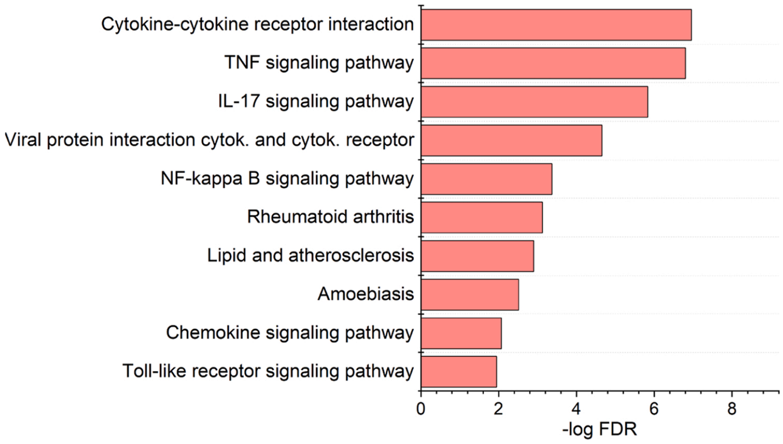

Fig. 5. Pathway analysis by KEGG for the upregulated genes of $PS_{pristine}$ Shown are the ten most significantly upregulated pathways predicted by KEGG analysis with Cytoscape ClueGO.

murine cells (Surinlert et al., 2020). In line with these results, we showed here that $PS_{pristine}$ hardly induced any aberrant cellular responses independently of the used assays. This points out, that even if styrene monomers were still present, they did not influence the cellular response at the MP concentrations tested. Furthermore, extensive washing of PS_{aged} post-weathering make the presence of residual leachable components in the PS_{aged} fraction very unlikely. Hence, the noxic effects of MP reported in this contribution can most probably be ascribed to the PS MP and not to co-contaminants.

Most of these results can be correlated with physicochemical (i.e., decrease of the surface charge) and morphological (i.e., degradation) changes of the PS-MP as introduced during the weathering step. As recently reported by our group, PS-MP degradation can be divided into two main steps (Meides et al., 2021). During step I, photooxidation reactions occur at the surface. As a result, MPs experience chemical chain scission, O_2 /H_2O addition, and formation of reactive oxygen free radicals on the surface (Zhu et al., 2019, 2020). In this context, we previously showed a linear time-dependent formation of functional groups like carboxylic acids, peroxides and ketones for weathered PS particles (150 μm) within the first 1500 h of comparable accelerated weathering (594 W/m^2) (Meides et al., 2021). During step II, the formation of microcracks and particle splintering accelerate the degradation process. In the present study, such major degradation of the MP was only visible for the longest treatment in the weathering chamber (PS_{130}). As a result, PS_{130} exhibited sharp edges, which presumably damaged the plasma membrane, as detected by an increased release of the intracellular enzyme LDH, upon PCI in this case. Membrane damages induced by plastic micro-fragments displaying sharp edges have been reported for human cell lines and primary blood cells (Choi et al., 2020, 2021). In line with this, PS-MP with preserved smooth spherical morphologies did not cause loss of the plasma membrane integrity. In terms of cytotoxicity, distincting between apoptosis and necrosis mechanisms yields important basic information for determining the mode of action of MPs. Our study compared results obtained when using the MTT or the LDH assay in identically MP-treated cells. Considering that MTT and LDH assays are indicators of apoptosis and necrosis, respectively (Hu et al., 2021), this allows us to draw some hypotheses on the mechanism of action of the investigated MP. Whereas $PS_{pristine}$ neither induce apoptosis nor necrosis, the observed cytotoxic effects of PS_{aged} could mainly be attributed to necrosis. However, some apoptotic processes cannot be fully excluded in the latter. The MTT assay was performed at a late time point (e.g., 24 h post-treatment), at which the apoptosis process was assumably already completed. Yet, the observed decrease in metabolic activity could also reflect a post-apoptotic secondary necrosis process (Silva et al., 2010).

Furthermore, we can hypothesize that the physical aspect (i.e., sharpness) of PS-MP affects the cellular uptake mechanisms with spherical particles recruiting the endocytic and phagocytic pathways (Banerjee and Shelver, 2021; Behzadi et al., 2017), whereas irregular-shaped structures use a non-biological pathway (i.e., destabilization of the plasma membrane). Noticeably, macrophage phagocytosis of PS-MP also depends on the protein corona covering the particles, which in turn is influenced by the surface topology (Chen et al., 2020). The membrane damaging effects might also induce organelle dysfunction, which could be partly responsible for the reduced metabolic activity detected after PS_{130} treatment. Recently, Pan et al. showed that pristine PS-MP (5 μm) treatment decreased the mitochondrial membrane potential of exposed cells (Pan et al., 2021). In terms of genotoxicity, for all MP induced DNA damages, as shown by the COMET assay, however, the most pronounced effects were again detected for PS_{130}. Damage to the nuclear envelope might have led to DNA fragmentation, in particular, if concomitantly a release of lysosomal enzymes occurred.

As mentioned above, PS_{aged} display ROS on their surface, i.e., molecules that exert an adverse effect on several cellular processes in a time and concentration dependent-manner (Juan et al., 2021). The observed linear increase in the intracellular ROS accumulation for of $PS_{pristine}$ to PS_{86} treatments reaching a plateau for PS_{130} weathered MP can be ascribed to ROS present on the PS-MP (Rubio et al., 2020; Rubio et al., 2020). Since ROS accumulation was analysed using flow cytometry, we only measured the intracellular content of living cells (i.e., displaying an intact cell membrane). The stagnation of the intracellular ROS content in presence of PS_{130} might be a consequence of the loss of plasma membrane integrity concomitantly induced by these particles. ROS accumulation has been reported for pristine PS particles in various cell lines (Rudolph et al., 2021; Shengchen et al., 2021) and for phenol-formaldehyde particles with a translated ageing time of 18 and 37 days in lung epithelial cells (A549) (Zhu et al., 2020). ROS are known to have an impact on various biological pathways, e.g. cross-reactions with mitochondria, nucleophilic reactions with biomacromolecules, biomembranes and cytoskeleton or DNA (Valdivia et al., 2015; Haider et al., 2021; Marchi et al., 2012). Moreover, ROS accumulation leads to mitochondrial dysfunction resulting in a lower metabolic activity (Hu and Palić, 2020; Jeong et al., 2016; Zorov et al., 1757), which could be a reason for the reduction of the metabolic activity after PS_{130} treatment observed in our study. High ROS amounts can also influence the integrity of the membrane (Valdivia et al., 2015; Rosado et al., 2002). Finally, increased oxidative stress is known to contribute to DNA damages (Rubio et al., 2020a; Visalli et al., 2021). Hence, besides the morphology of the particle as discussed above, the accumulation of reactive groups and radicals on the surface of weathered MP could very well be responsible for the toxicity observed at the cellular level.

Since all assays demonstrated that the noxiousness of MP increased with weathering, similar findings were expected for the pro-inflammatory response, indicated by TNF-α secretion. Surprisingly, the concentration of TNF-α in the supernatant was significantly higher in case of cells challenged with $PS_{pristine}$ compared to PS_{130} ones. However, cells with damaged plasma membranes, i.e., those exposed to PS_{130}, were not able to produce TNF-α anymore, hence reducing the accumulation of TNF-α in the supernatant. Moreover, we cannot exclude that the impairment of various biological pathways in PS_{130} challenged cells, as discussed above, might in the end reduce the overall translational activity and hence TNF-α production. Importantly, TNF-α secretion is dependent on phagocytosis (Green et al., 1998; Shanbhag et al., 1994). PS_{aged} and especially the presumable more reactive fragments might enter the cells via non-biological pathways like piercing the plasma membrane due to their sharp edges. $PS_{pristine}$, which are assumed to be uptaken by the phagocytic pathway (Rudolph et al., 2021), might therefore show an induced inflammatory response. This finding is in accordance with a previous report, in which pristine microplastic was shown to induce a higher TNF-α production in human mast cells in direct comparison to mechanically fragmented and rougher particles (Choi et al., 2021).

The analysis of the transcriptome allows a tentative linking of various cellular responses with potential molecular pathways. The identification of downregulated genes located in enriched GOs terms, like "cellular respiration" and "ribosome", i.e., genes relevant for cellular metabolism and translation, are in line with the results of the detected biological adverse effects. The higher upregulation of genes associated with "uptake" for $PS_{pristine}$ supports the hypothesis, that more pristine MP enter the cells via phagocytosis compared to PS_{130}. The biological uptake of MP strongly depends on the nature of the protein corona (Banerjee and Shelver, 2021). Here, we can postulate that the weathering process, besides modifying the morphology of the PS-MP, also influences the surface topology, which in turn might change the composition of the protein corona (Chen et al., 2020). Moreover, $PS_{pristine}$ treatment allocated mainly pathogen-driven responses suggesting that the cells recognize $PS_{pristine}$ as some kind of biotic system. Finally, KEGG pathways prediction identified several signalling pathways implicated in inflammatory responses for $PS_{pristine}$ challenged cells, in particular, the TNF-α signalling pathway, which correlates well with the accumulation of this pro-inflammatory cytokine measured in the cell culture medium of $PS_{pristine}$ treated cells. Other studies found similar inflammation pathways after exposure to 5 μm PS-MP and < 2.5 μm environmental particulate matter (Li et al., 2021b, 2017).

5. Conclusion

To conclude, PS_{aged} showed coherent noxious effects on ImKC cells, indicating an increased cytotoxic potential for PS_{aged}, while $PS_{pristine}$ bears higher inflammatory potential (Scheme 1). Especially, fragmentation and formation of ROS are hereby assumed to contribute to the

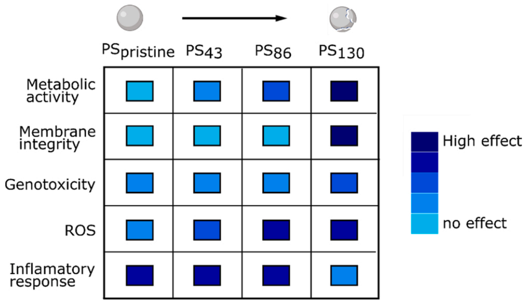

Scheme 1. Overview of detected biological/noxious effects of $PS_{pristine}$ and PS_{aged}.

high noxiousness. Comparison of the transcriptomic data revealed major differences between the effects of PS_{aged} and $PS_{pristine}$, giving first insights at a molecular level. Our results demonstrate for the first time that noxic effects of pristine and weathered MP induce different cellular responses at the transcriptional level. The proposed tentative identification of targeted biological pathways requires, however, some confirmations by proteomics analysis. Most importantly, it is urgently recommended to include accelerated-weathered MP in investigations in the microplastic field and to converge towards natural exposure models, as well as to investigate a broad range of biological effects when estimating a potential risk of microplastic.

Funding

This study was funded by the Deutsche Forschungsgemeinschaft (DFG, German Research Foundation, Germany) – SFB 1357 – 391977956.

Environmental implication

Microplastic, as a ubiquitously emerging, environmental contaminant, has become of high public and scientific interest. Despite various reports showing different biological effects on mammalian cells, investigations were mainly restricted to the use of pristine microplastic particles (MP). However, these laboratory particles might not be fully comparable to environmental particles. Therefore, our study used accelerated weathered particles and their pristine counterparts and compared the noxiousness on different biological levels using murine macrophages. We found significantly different cellular reactions to both particle types, stressing the importance of a more realistic approach when estimating the potential risk of microplastic.

CRediT authorship contribution statement

MV, VJ, AW, JJ, NM, PS, TS, and RF designed the experiments. MV performed most of the experiments. JJ provided particle characterization and confocal microscopy. NM prepared the weathered MP. AW analysed the RNA sequencing data. MV, AW and VJ analysed the data and created the Figures. MV, VJ, AW, PS, TS and RF wrote the manuscript. VJ, AW, TS, PS and RF reviewed and edited the manuscript and supervised during the experiments.

Declaration of Competing Interest

The authors declare that they have no known competing financial interests or personal relationships that could have appeared to influence the work reported in this paper.

Data availability

The raw RNA-Sequencing data were deposited at NCBI's Sequence Read Archive (SRA) under Bioproject number PRJNA785767.

Acknowledgments

Michaela Hochholzer supported this study by preparing RNA-Seq libraries for high-throughput sequencing. Jana Toepper and Sarah Taumann performed some of the COMET assays.

Appendix A. Supporting information

Supplementary data associated with this article can be found in the online version at doi:10.1016/j.jhazmat.2022.128955.

References

Amato-Lourenço, L.F., dos Santos Galvão, L., de Weger, L.A., Hiemstra, P.S., Vijver, M.G., Mauad, T., 2020. An emerging class of air pollutants: potential effects of microplastics to respiratory human health? Sci. Total Environ. 749, 1–7.

Amato-Lourenço, L.F., Carvalho-Oliveira, R., Júnior, G.R., Dos, S.G.L., Ando, R.A., Mauad, T., 2021. Presence of airborne microplastics in human lung tissue. J. Hazard. Mater. 416.

Banerjee, A., Shelver, W.L., 2021. Micro- and nanoplastic induced cellular toxicity in mammals: a review. Sci. Total Environ. 755, 142518.

Behzadi, S., Serpooshan, V., Tao, W., Hamaly, M.A., Alkawareek, M.Y., Dreaden, E.C., Brown, D., Alkilany, A.M., Farokhzad, O.C., Mahmoudi, M., 2017. Cellular uptake of nanoparticles: journey inside the cell. Chem. Soc. Rev. 46, 4218–4244.

Bindea, G., Mlecnik, B., Hackl, H., Charoentong, P., Tosolini, M., Kirilovsky, A., Fridman, W.-H., Pagès, F., Trajanoski, Z., Galon, J., 2009. ClueGO: a cytoscape plug-in to decipher functionally grouped gene ontology and pathway annotation networks. Bioinformatics 25, 1091–1093.

Campanale, C., Massarelli, C., Savino, I., Locaputo, V., Uricchio, V.F., 2020. A detailed review study on potential effects of microplastics and additives of concern on human health. Int. J. Environ. Res. Public Health 17.

Chen, B., Wu, Z., Tian, M., Feng, T., Yuanwei, C., Luo, X., 2020. Effect of surface morphology change of polystyrene microspheres through etching on protein corona and phagocytic uptake. J. Biomater. Sci. Polym. Ed. 31, 2381–2395.

Chen, H., Hua, X., Yang, Y., Wang, C., Jin, L., Dong, C., Chang, Z., Ding, P., Xiang, M., Li, H., Yu, Y., 2021. Chronic exposure to UV-aged microplastics induces neurotoxicity by affecting dopamine, glutamate, and serotonin neurotransmission in Caenorhabditis elegans. J. Hazard. Mater. 419.

Choi, D., Bang, J., Kim, T., Oh, Y., Hwang, Y., Hong, J., 2020. In vitro chemical and physical toxicities of polystyrene microfragments in human-derived cells. J. Hazard. Mater. 400, 123308.

Choi, D., Hwang, J., Bang, J., Han, S., Kim, T., Oh, Y., Hwang, Y., Choi, J., Hong, J., 2021. In vitro toxicity from a physical perspective of polyethylene microplastics based on statistical curvature change analysis. Sci. Total. Environ. 752, 142242.

Conkle, J.L., Báez Del Valle, C.D., Turner, J.W., 2018. Are we underestimating microplastic contamination in aquatic environments? Environ. Manag. 61, 1–8.

Coppack, S.W., 2001. Pro-inflammatory cytokines and adipose tissue. Proc. Nutr. Soc. 60, 349–356.

Deng, Y., Zhang, Y., Lemos, B., Ren, H., 2017. Tissue accumulation of microplastics in mice and biomarker responses suggest widespread health risks of exposure. Sci. Rep. 7, 1–10.

Frei, S., Piehl, S., Gilfedder, B.S., Löder, M.G.J., Krutzke, J., Wilhelm, L., Laforsch, C., 2019. Occurence of microplastics in the hyporheic zone of rivers. Sci. Rep. 9, 1–11.

Frostegård, J., Ulfgren, A.-K., Nyberg, P., Hedin, U., Swedenborg, J., Andersson, U., Hansson, G.K., 1999. Cytokine expression in advanced human atherosclerotic plaques: dominance of pro-inflammatory (Th1) and macrophage-stimulating cytokines. Atherosclerosis 145, 33–43.

Gewert, Berit, Plassmann, Merle M., MacLeod, Matthew, 2015. Pathways for degradation of plastic polymers floating in the marine environment. Environ. Sci. 17, 1513–1521.

Green, T.R., Fisher, J., Stone, M., Wroblewski, B.M., Ingham, E., 1998. Polyethylene particles of a 'critical size' are necessary for the induction of cytokines by macrophages in vitro. Biomaterials 19, 2297–2302.

Guimarães, A.T.B., Charlie-Silva, I., Malafaia, G., 2021. Toxic effects of naturally-aged microplastics on zebrafish juveniles: a more realistic approach to plastic pollution in freshwater ecosystems. J. Hazard. Mater. 407, 124833.

Haider, M.S., Jaskani, M.J., Fang, J., 2021. Overproduction of ROS: underlying molecular mechanism of scavenging and redox signaling, in: Biocontrol Agents and Secondary Metabolites. Elsevier,, pp. 347–382.

Han, S., Bang, J., Choi, D., Hwang, J., Kim, T., Oh, Y., Hwang, Y., Choi, J., Hong, J., 2020. Surface pattern analysis of microplastics and their impact on human-derived cells. ACS Appl. Polym. Mater. 2, 4541–4550.

Hesler, M., Aengenheister, L., Ellinger, B., Drexel, R., Straskraba, S., Jost, C., Wagner, S., Meier, F., von Briesen, H., Büchel, C., Wick, P., Buerki-Thurnherr, T., Kohl, Y., 2019. Multi-endpoint toxicological assessment of polystyrene nano- and microparticles in different biological models in vitro. Toxicol. Vitr. 61, 104610.

Hu, M., Palić, D., 2020. Micro- and nano-plastics activation of oxidative and inflammatory adverse outcome pathways. Redox Biol. 37, 101620.

Hu, X.-M., Li, Z.-X., Lin, R.-H., Shan, J.-Q., Yu, Q.-W., Wang, R.-X., Liao, L.-S., Yan, W.-T., Wang, Z., Shang, L., Huang, Y., Zhang, Q., Xiong, K., 2021. Guidelines for regulated cell death assays: a systematic summary, a categorical comparison, a prospective. Front. Cell Dev. Biol. 9, 634690.

Huang, Y., Ding, J., Zhang, G., Liu, S., Zou, H., Wang, Z., Zhu, W., Geng, J., 2021. Interactive effects of microplastics and selected pharmaceuticals on red tilapia: role of microplastic aging. Sci. Total. Environ. 752, 142256.

Hwang, J., Choi, D., Han, S., Jung, S.Y., Choi, J., Hong, J., 2020. Potential toxicity of polystyrene microplastic particles. Sci. Rep. 10, 7391–7403.

Ibrahim, Y.S., Tuan Anuar, S., Azmi, A.A., Wan Mohd Khalik, W.M.A., Lehata, S., Hamzah, S.R., Ismail, D., Ma, Z.F., Dzulkarnaen, A., Zakaria, Z., Mustaffa, N., Tuan Sharif, S.E., Lee, Y.Y., 2021. Detection of microplastics in human colectomy specimens. JGH Open Open Access J. Gastroenterol. Hepatol. 5, 116–121.

Issac, M.N., Kandasubramanian, B., 2021. Effect of microplastics in water and aquatic systems. Environ. Sci. Pollut. Res. 28, 19544–19562.

Jeon, S., Lee, D.-K., Jeong, J., Yang, S.I., Kim, J.-S., Kim, J., Cho, W.-S., 2021. The reactive oxygen species as pathogenic factors of fragmented microplastics to macrophages. Environ. Pollut. 281, 117006.

Jeong, C.-B., Won, E.-J., Kang, H.-M., Lee, M.-C., Hwang, D.-S., Hwang, U.-K., Zhou, B., Souissi, S., Lee, S.-J., Lee, J.-S., 2016. Microplastic size-dependent toxicity, oxidative stress induction, and p-JNK and p-p38 activation in the monogonont rotifer (Brachionus koreanus). Environ. Sci. Technol. 50, 8849–8857.

Jiang, B., Kauffman, A.E., Li, L., McFee, W., Cai, B., Weinstein, J., Lead, J.R., Chatterjee, S., Scott, G.I., Xiao, S., 2020. Health impacts of environmental contamination of micro- and nanoplastics: a review. Environ. Health Prev. Med. 25, 1–15.

Jin, Y., Lu, L., Tu, W., Luo, T., Fu, Z., 2019. Impacts of polystyrene microplastic on the gut barrier, microbiota and metabolism of mice. Sci. Total Environ. 649, 308–317.

Juan, C.A., La Pérez de Lastra, J.M., Plou, F.J., Pérez-Lebeña, E., 2021. The chemistry of reactive oxygen species (ROS) revisited: outlining their role in biological macromolecules (DNA, lipids and proteins) and induced pathologies. Int. J. Mol. Sci. 22, 1–21.

Kurtz-Chalot, A., Villiers, C., Pourchez, J., Boudard, D., Martini, M., Marche, P.N., Cottier, M., Forest, V., 2017. Impact of silica nanoparticle surface chemistry on protein corona formation and consequential interactions with biological cells. Mater. Sci. Eng. C. 75, 16–24.

Lee, H.-S., Amarakoon, D., Wei, C.-i, Choi, K.Y., Smolensky, D., Lee, S.-H., 2021. Adverse effect of polystyrene microplastics (PS-MPs) on tube formation and viability of human umbilical vein endothelial cells. Food Chem. Toxicol. 154, 112356.

Li, S., Ma, Y., Ye, S., Tang, S., Liang, N., Liang, Y., Xiao, F., 2021. Polystyrene microplastics trigger hepatocyte apoptosis and abnormal glycolytic flux via ROS-driven calcium overload. J. Hazard. Mater. 417, 126025.

Li, S., Shi, M., Wang, Y., Xiao, Y., Cai, D., Xiao, F., 2021. Keap1-Nrf2 pathway up-regulation via hydrogen sulfide mitigates polystyrene microplastics induced-hepatotoxic effects. J. Hazard. Mater. 402, 123933.

Li, X., Bechara, R., Zhao, J., McGeachy, M.J., Gaffen, S.L., 2019. IL-17 receptor-based signaling and implications for disease. Nat. Immunol. 20, 1594–1602.

Li, Y., Duan, J., Yang, M., Li, Y., Jing, L., Yu, Y., Wang, J., Sun, Z., 2017. Transcriptomic analyses of human bronchial epithelial cells BEAS-2B exposed to atmospheric fine particulate matter PM2.5. Toxicol. Vitr. 42, 171–181.

Liang, B., Zhong, Y., Huang, Y., Lin, X., Liu, J., Lin, L., Hu, M., Jiang, J., Dai, M., Wang, B., Zhang, B., Meng, H., Lelaka, J.J.J., Sui, H., Yang, X., Huang, Z., 2021. Underestimated health risks: polystyrene micro- and nanoplastics jointly induce intestinal barrier dysfunction by ROS-mediated epithelial cell apoptosis. Part. Fibre Toxicol. 18, 1–19.

Lindeque, P.K., Cole, M., Coppock, R.L., Lewis, C.N., Miller, R.Z., Watts, A.J.R., Wilson-McNeal, A., Wright, S.L., Galloway, T.S., 2020. Are we underestimating microplastic abundance in the marine environment? A comparison of microplastic capture with nets of different mesh-size. Environ. Pollut. (Barking, Essex 1987) 265, 114721.

Liu, P., Zhan, X., Wu, X., Li, J., Wang, H., Gao, S., 2020. Effect of weathering on environmental behavior of microplastics: properties, sorption and potential risks. Chemosphere 242, 125193.

Liu, P., Shi, Y., Wu, X., Wang, H., Huang, H., Guo, X., Gao, S., 2021. Review of the artificially-accelerated aging technology and ecological risk of microplastics. Sci. Total Environ. 768, 144969.

Liu, S., Wu, X., Gu, W., Yu, J., Wu, B., 2020. Influence of the digestive process on intestinal toxicity of polystyrene microplastics as determined by in vitro Caco-2 models. Chemosphere 256, 1–9.

Lu, L., Wan, Z., Luo, T., Fu, Z., Jin, Y., 2018. Polystyrene microplastics induce gut microbiota dysbiosis and hepatic lipid metabolism disorder in mice. Sci. Total Environ. 631–632, 449–458.

Marchi, S., Giorgi, C., Suski, J.M., Agnoletto, C., Bononi, A., Bonora, M., de Marchi, E., Missiroli, S., Patergnani, S., Poletti, F., Rimessi, A., Duszynski, J., Wieckowski, M.R., Pinton, P., 2012. Mitochondria-ros crosstalk in the control of cell death and aging. J. Signal Transduct. 2012, 329635–329652.

Meides, N., Menzel, T., Poetzschner, B., Löder, M.G.J., Mansfeld, U., Strohriegl, P., Altstaedt, V., Senker, J., 2021. Reconstructing the environmental degradation of polystyrene by accelerated weathering. Environ. Sci. Technol. 55, 7930–7938.

Merkley, S.D., Moss, H.C., Goodfellow, S.M., Ling, C.L., Meyer-Hagen, J.L., Weaver, J., Campen, M.J., Castillo, E.F., 2021. Polystyrene microplastics induce an immunometabolic active state in macrophages. Cell. Biol. Toxicol. https://doi.org/10.1007/s10565-021-09616-x.

Osborn, L., Kunkel, S., Nabel, G.J., 1989. Tumor necrosis factor alpha and interleukin 1 stimulate the human immunodeficiency virus enhancer by activation of the nuclear factor kappa B. PNAS 86, 2336–2340.

Ostling, O., Johanson, K.J., 1984. Microelectrophoretic study of radiation-induced DNA damages in individual mammalian cells. Biochem. Biophys. Res. Commun. 123, 291–298.

Pan, L., Yu, D., Zhang, Y., Zhu, C., Yin, Q., Hu, Y., Zhang, X., Yue, R., Xiong, X., 2021. Polystyrene microplastics-triggered mitophagy and oxidative burst via activation of PERK pathway. Sci. Tot. Environ. 781, 146753.

Ramsperger, A.F.R.M., Narayana, V.K.B., Gross, W., Mohanraj, J., Thelakkat, M., Greiner, A., Schmalz, H., Kress, H., Laforsch, C., 2020. Environmental exposure enhances the internalization of microplastic particles into cells. Sci. Adv. 6, eabd1211.

Ramsperger, A.F.R.M., Jasinski, J., Völkl, M., Witzmann, T., Meinhart, M., Jérôme, V., Kretschmer, W.P., Freitag, R., Senker, J., Fery, A., Kress, H., Scheibel, T., Laforsch, C., 2021. Supposedly identical microplastic particles substantially differ in their material properties influencing particle-cell interactions and cellular responses. J. Hazard. Mater. 9, 127961.

Riedl, S.A.B., Völkl, M., Holzinger, A., Jasinski, J., Jérôme, V., Scheibel, T., Feldhaar, H., Freitag, R., 2021. In vitro cultivation of primary intestinal cells from Eisenia fetida as basis for ecotoxicological studies. Ecotoxicology. https://doi.org/10.1007/s10646-021-02495-2.

Rosado, J.A., González, A., Salido, G.M., Pariente, J.A., 2002. Effects of reactive oxygen species on actin filament polymerisation and amylase secretion in mouse pancreatic acinar cells. Cell. Signal. 14, 547–556.

Rozman, U., Kalčikova, G., 2021. Seeking for a perfect (non-spherical) microplastic particle – the most comprehensive review on microplastic laboratory research. J. Hazard. Mater. 14, 127529.

Rubin, A.E., Sarkar, A.K., Zucker, I., 2021. Questioning the suitability of available microplastics models for risk assessment – a critical review. Sci. Total. Environ. 788, 147670.

Rubio, L., Barguilla, I., Domenech, J., Marcos, R., Hernández, A., 2020. Biological effects, including oxidative stress and genotoxic damage, of polystyrene nanoparticles in different human hematopoietic cell lines. J. Hazard. Mater. 398, 122900.

Rubio, L., Marcos, R., Hernández, A., 2020. Potential adverse health effects of ingested micro- and nanoplastics on humans. Lessons learned from in vivo and in vitro mammalian models. J. Toxicol. Environ. Part B, Crit. Rev. 23, 51–68.

Rudolph, J., Völkl, M., Jérôme, V., Scheibel, T., Freitag, R., 2021. Noxic effects of polystyrene microparticles on murine macrophages and epithelial cells. Sci. Rep. 11, 1–16.

Shanbhag, A.S., Jacobs, J.J., Black, J., Galante, J.O., Glant, T.T., 1994. Macrophage/particle interactions: effect of size, composition and surface area. J. Biomed. Mater. Res. 28, 81–90.

Shengchen, W., Jing, L., Yujie, Y., Yue, W., Shiwen, X., 2021. Polystyrene microplastics-induced ROS overproduction disrupts the skeletal muscle regeneration by converting myoblasts into adipocytes. J. Hazard. Mater. 417, 125962.

Silva, M.T., 2010. Secondary necrosis: the natural outcome of the complete apoptotic program. FEBS Lett. 584, 4491–4499.

von Smoluchowski, M., 1906. Zur kinetischen Theorie der Brownschen Molekularbewegung und der Suspensionen. Ann. Phys. 326, 756–780.

Stepanenko, A.A., Dmitrenko, V.V., 2015. Pitfalls of the MTT assay: direct and off-target effects of inhibitors can result in over/underestimation of cell viability. Gene 574, 193–203.

Stock, V., Böhmert, L., Lisicki, E., Block, R., Cara-Carmona, J., Pack, L.K., Selb, R., Lichtenstein, D., Voss, L., Henderson, C.J., Zabinsky, E., Sieg, H., Braeuning, A., Lampen, A., 2019. Uptake and effects of orally ingested polystyrene microplastic particles in vitro and in vivo. Arch. Toxicol. 93, 1817–1833.

Surinlert, P., Kongthong, N., Watthanard, M., Sae-lao, T., Sookbangnop, P., Pholpramool, C., Tipbunjong, C., 2020. Styrene oxide caused cell cycle arrest and abolished myogenic differentiation of C2C12 myoblasts. J. Toxicol. 2020, 1–11.

Syranidou, E., Karkanorachaki, K., Amorotti, F., Franchini, M., Repouskou, E., Kaliva, M., Vamvakaki, M., Kolvenbach, B., Fava, F., Corvini, P.F.-X., Kalogerakis, N., 2017. Biodegradation of weathered polystyrene films in seawater microcosms. Sci. Rep. 7, 1–12.

Valdivia, A., Duran, C., San Martin, A., 2015. The role of Nox-mediated oxidation in the regulation of cytoskeletal dynamics. Curr. Pharm. Des. 21, 6009–6022.

Visalli, G., Facciolà, A., Pruiti Ciarello, M., de Marco, G., Maisano, M., Di Pietro, A., 2021. Acute and sub-chronic effects of microplastics (3 and 10 μm) on the human intestinal cells HT-29. Int. J. Environ. Res. Public Health 18, 1–12.

Vlacil, A.-K., Bänfer, S., Jacob, R., Trippel, N., Kuzu, I., Schieffer, B., Grote, K., 2021. Polystyrene microplastic particles induce endothelial activation. PloS One 16, e0260181.

Wang, Q., Wangjin, X., Zhang, Y., Wang, N., Wang, Y., Meng, G., Chen, Y., 2020. The toxicity of virgin and UV-aged PVC microplastics on the growth of freshwater algae Chlamydomonas reinhardtii. Sci. Total Environ. 749, 141603.

Wang, X., Zheng, H., Zhao, J., Luo, X., Wang, Z., Xing, B., 2020. Photodegradation elevated the toxicity of polystyrene microplastics to grouper (epinephelus moara) through disrupting hepatic lipid homeostasis. Environ. Sci. Technol. 54, 6202–6212.

Wang, Z.-Y., Burlak, C., Klaunig, J.E., Kamendulis, L.M., 2014. Development of a cytokine-producing immortalized murine Kupffer cell line. Cytokine 70, 165–172.

Weis, J.S., Palmquist, K.H., 2021. Reality check: experimental studies on microplastics lack realism. Appl. Sci. 11, 8529–8545.

Weithmann, N., Möller, J.N., Löder, M.G.J., Piehl, S., Laforsch, C., Freitag, R., 2018. Organic fertilizer as a vehicle for the entry of microplastic into the environment. Sci. Adv. 4, eaap8060.

Wu, B., Wu, X., Liu, S., Wang, Z., Chen, L., 2019. Size-dependent effects of polystyrene microplastics on cytotoxicity and efflux pump inhibition in human Caco-2 cells. Chemosphere 221, 333–341.

Wu, S., Wu, M., Tian, D., Qiu, L., Li, T., 2020. Effects of polystyrene microbeads on cytotoxicity and transcriptomic profiles in human Caco-2. Cells, Environl. Toxicol. 35, 495–506.

Yousif, E., Haddad, R., 2013. Photodegradation and photostabilization of polymers, especially polystyrene: review. SpringerPlus 2, 1–32.

Yu, X., Lang, M., Huang, D., Yang, C., Ouyang, Z., Guo, X., 2021. Photo-transformation of microplastics and its toxicity to Caco-2 cells. Sci. Total Environ., 150954

Zhao, C., Xu, T., He, M., Shah, K.J., You, Z., Zhang, T., Zubair, M., 2021. Exploring the toxicity of the aged styrene-butadiene rubber microplastics to petroleum hydrocarbon-degrading bacteria under compound pollution system. Ecotoxicol. Environ. Saf. 227, 112903.

Zhao, L., Shi, W., Hu, F., Song, X., Cheng, Z., Zhou, J., 2021. Prolonged oral ingestion of microplastics induced inflammation in the liver tissues of C57BL/6J mice through polarization of macrophages and increased infiltration of natural killer cells. Ecotoxicol. Environ. Saf. 227, 112882.

Zhu, K., Jia, H., Zhao, S., Xia, T., Guo, X., Wang, T., Zhu, L., 2019. Formation of environmentally persistent free radicals on microplastics under light irradiation. Environ. Sci. Technol. 53, 8177–8186.

Zhu, K., Jia, H., Sun, Y., Dai, Y., Zhang, C., Guo, X., Wang, T., Zhu, L., 2020. Enhanced cytotoxicity of photoaged phenol-formaldehyde resins microplastics: combined effects of environmentally persistent free radicals, reactive oxygen species, and conjugated carbonyls. Environ. Int. 145, 106137.

Zorov, D.B., Juhaszova, M., Sollott, S.J., 1757. Mitochondrial ROS-induced ROS release: an update and review. Biochim. Biophys. Acta Bioenerg. 2006, 509–517.

Zou, W., Xia, M., Jiang, K., Cao, Z., Zhang, X., Hu, X., 2020. Photo-oxidative degradation mitigated the developmental toxicity of polyamide microplastics to zebrafish larvae by modulating macrophage-triggered proinflammatory Responses and Apoptosis. Environ. Sci. Technol. 54, 13888–13898.

This article was published in the Journal of Hazardous Materials 2022, 435, 128955.

Supplementary material: `https://doi.org/10.1016/j.jhazmat.2022.128955`

9 Acknowledgments

First and foremost, I want to thank my supervisor Prof. Strohriegl, for having given me the opportunity to this position and the chance to do my PhD here at the Macromolecular Chemistry I department, as a lateral entrant, coming from a different field of environmental sciences. It is a great honor to be able to work on such a current topic and on a novel project, having the freedom to include my own ideas and creativity. Thank you for the confidence and trust, letting me work with all the freedom I had, while still supporting me on every end possible. I was able to learn so much, improve my work and scientific thinking, and grow through experience. I am very grateful to have had such a caring and kind supervisor. Thank you!

I also want to thank Prof. Senker, Prof. Altstädt, and Prof. Ruckdäschel as well as Teresa Menzel, Anika Mauel and Björn Pötzschner for the extremely productive and excellent cooperations in the past years. It was an honor to work with such motivated scientists! Our meetings were always productive, our discussions constructive, we were a great team and working with you was not only fruitful, but also fun! Thank you!

Further I want to thank all the other MC1-people, who made my working-life a lot easier: Sandra Opel, Jutta Failner, Alex Kern, Jonas Meyer, Christian Neuber. Martina Heider and Ulrich Mansfeld for REM measurements. Martina Fried, Daniel Wagner, Lisa Weber, Reiner Giesa for particle preparation. Irene Bauer, Francesco Rodella, and my former lab colleagues for any support in the lab. Petra Weiss and Christina Wunderlich were always there for administrative help. Thank you all for your work, advice and help! Francesco, Julian, Andi, Andi, Melina, Christina, and Flo for listening to my worries and doubts at any time, and giving your support! It really helped a lot! Finally: thank you also to the entire MC1 people I did not mention by name. I had a wonderful time with you during work and especially after work! Thank you to every one of you made this 'journey' very special!

Thank you also to my project/lunch/university friends: Johanna, Matze, Moritz, Dimi, Daniel, Hendrik, Basti, Lena: you gave me support, always! Thank you for lunch, coffee-breaks, and lots of fun on evening and weekend activities. You are the best!
Thank you also to my climbing partners Ruth, Valentin, Flo, and Anita. You always helped compensate work with outdoor and climbing prime-time!

Thank you to my family Mama, Papa, Marco, Natalie, Oma Brigitte, Oma Lotte, Opa Gerhard. Thank you for all your support and belief, always!

And finally, thank you to my boyfriend Linus, who did not hesitate to move to Bayreuth with me. Thank you for your support, belief, trust, and love.

(Eidesstattliche) Versicherung und Erklärung

(§ 9 Satz 2 Nr. 3 PromO BayNAT)
Hiermit versichere ich eidesstattlich, dass ich die Arbeit selbstständig verfasst und keine anderen als die von mir angegebenen Quellen und Hilfsmittel benutzt habe (vgl. Art. 64 Abs. 1 Satz 6 BayHSchG).

(§ 9 Satz 2 Nr. 3 PromO BayNAT)
Hiermit erkläre ich, dass ich die Dissertation nicht bereits zur Erlangung eines akademischen Grades eingereicht habe und dass ich nicht bereits diese oder eine gleichartige Doktorprüfung endgültig nicht bestanden habe.

(§ 9 Satz 2 Nr. 4 PromO BayNAT)
Hiermit erkläre ich, dass ich Hilfe von gewerblichen Promotionsberatern bzw. -vermittlern oder ähnlichen Dienstleistern weder bisher in Anspruch genommen habe noch künftig in Anspruch nehmen werde.

(§ 9 Satz 2 Nr. 7 PromO BayNAT)
Hiermit erkläre ich mein Einverständnis, dass die elektronische Fassung meiner Dissertation unter Wahrung meiner Urheberrechte und des Datenschutzes einer gesonderten Überprüfung unterzogen werden kann.

(§ 9 Satz 2 Nr. 8 PromO BayNAT)
Hiermit erkläre ich mein Einverständnis, dass bei Verdacht wissenschaftlichen Fehlverhaltens Ermittlungen durch universitätsinterne Organe der wissenschaftlichen Selbstkontrolle stattfinden können.

________________________ ____________________

Ort, Datum Unterschrift